Technische Universität München

TUM School of Natural Sciences

Li-Ion Battery Theory vs. Experiment: Parametrization of Porous Electrodes and Kinetic Fundamentals via Electrochemical Impedance Spectroscopy

Robert Morasch

Vollständiger Abdruck der von der TUM School of Natural Sciences der Technischen Universität München zur Erlangung des akademischen Grades eines

Doktors der Naturwissenschaften (Dr. rer. nat.)

genehmigten Dissertation.

Vorsitz: Prof. Dr. Tom Nilges

Prüfer*innen der Dissertation: 1. Prof. Dr. Hubert A. Gasteiger
                                                       2. Prof. Dr.-Ing Andreas Jossen
                                                       3. Prof. Dr. Miran Gaberšček

Diese Dissertation wurde am 28.11.2022 bei der Technischen Universität München eingereicht und durch die TUM School of Natural Sciences am 04.01.2023 angenommen.

Abstract

The porous nature of battery electrodes imposes an additional complexity to the understanding of performance limitations in high-energy Li-ion batteries. This thesis gives insight into the topics of porous electrode theory and active material kinetics parametrization using electrochemical impedance spectroscopy (EIS). First, to simplify the EIS measurements, a method to enable half-cell measurements via µ-reference electrodes was developed. To further understand the porous nature of electrodes, the effect of inhomogeneous ionic resistances in porous electrodes on their EIS-based tortuosity analysis is shown, which allows the detection of binder gradients. EIS measurements of graphite electrodes with various loadings serve as example to elucidate the effect of competing kinetic and ionic resistances in porous electrodes on the EIS analysis. An example for such kinetically and transport limited electrodes is given via a comparison of the temperature dependent performance of silicon and graphite electrodes. High transport resistances give rise to Li^+ concentration gradients within the porous electrode, which in turn affects the active material kinetics. Thus lastly the Li^+-concentration,- temperature,- and state-of-charge-dependent kinetics of $LiNi_{1/3}Mn_{1/3}Co_{1/3}O_2$ (NMC 111) and graphite were measured via EIS and compared to theoretical approaches used in battery modelling.

Kurzfassung

Die poröse Eigenart von Batterieelektroden fügt dem Verständnis der Leistungslimitierung in Hochenergieelektroden von Li-Ionen Batterien eine zusätzliche Komplexität hinzu. Diese Arbeit gibt Einblicke in die Themengebiete der Theorie poröser Elektroden und der Aktivmaterialparametrisierung durch Elektrochemische Impedanzspektroskopie (EIS). Um EIS Messungen zu vereinfachen wurde zu Anfang eine Methode entwickelt, welche Halbzell-Messungen mittels einer µ-Referenzelektrode ermöglicht. Um das Verständnis für poröse Elektroden auszubauen wurde der Einfluss von inhomogenen ionischen Widerständen in porösen Elektroden auf die EIS-basierte Tortuositätsanalyse aufgezeigt, welche das Detektieren von Bindergradienten ermöglicht. EIS Messungen an Graphitelektroden mit unterschiedlichen Beladungen dienen als Beispiel um den Effekt von konkurrierenden kinetischen und ionischen Widerständen in porösen Elektroden auf die EIS Analyse aufzuzeigen. Als Beispiel für solch kinetisch- und transportlimitierte Elektroden wird ein Vergleich der temperaturabhängigen Leistung von Silizium- und Graphitelektroden aufgezeigt. Hohe Transportwiderstände resultieren in Li^+-Konzentrationsgradienten innerhalb der porösen Elektrode, welche im Gegenzug die Kinetik der Aktivmaterialien beeinflusst. Daher wurden letztlich die Li^+-Konzentration-Temperatur- und Ladungszustandsabhängige Kinetik von $LiNi_{1/3}Mn_{1/3}Co_{1/3}O_2$ (NMC 111) und Graphit mittels EIS vermessen und mit den Ansätzen aus der Batteriemodellierung verglichen.

Contents

Contents

_____

Nomenclature

<u>Abbreviations</u>

Abbreviation	Description
BMS	Battery management system
CMC	Carboxymethyl cellulose
DMC	Dimethyl-carbonate
EC	Ethylene carbonate
ECM	Equivalent circuit model
EIS	Electrochemical impedance spectroscopy
EMC	Ethyl-methyl-carbonate
EV	Electric vehicle
FSG	Free-standing graphite
GEIS	Galvano electrochemical impedance spectroscopy
GWRE	Gold wire μ-reference electrode
HF	Hydrogen fluoride
LFP	$LiFePO_4$
LTO	$Li_4Ti_5O_{12}$
NMC	$Li(Ni_xMn_yCo_z)O_2$
NMP	N-Methyl-2-pyrrolidon
OCV	Open circuit voltage
PEIS	Potentio electrochemical impedance spectroscopy
PVDF	Polyvinylidene fluoride
SEI	Solid electrolyte interphase
SOC	State-of-charge
SOH	State-of-health
SPM	Single particle model
TLM	Transmission line model
VC	Vinylene carbonate

_____

List of Symbols

Symbol	Description [unit]
A	Electrode area [m²]
a	Specific interfacial area [m_{AM}^2/m_{geom}^3]
C	Capacitance [As]
c	Concentration of species [mol/l]
D	Diffusion coefficient [m²/s]
d	Distance or thickness [m]
F	Faraday constant [As/mol]
f	Frequency [Hz]
I_0	Current amplitude [A]
i_0	Exchange current density [A/m²]
I	Current (time domain) [A]
j	Imaginary unit [−]
J	Local current density [A/m²]
k	Reaction rate constant [mol/(m² × s)]
l	Diffusion length [m]
Q	Constant phase element [$Fs^{1-\alpha}$]
R_{ct}	Charge-transfer resistance [Ω]
$\overline{R}$	Gas constant [J/(mol × K)]
R_{ion}	Ionic resistance [Ω]
r_{ion}	Individual ionic resistance element in a TLM
R_{planar}	Solid diffusion resistance for a planar geometry [Ωm²]
R_{sphere}	Solid diffusion resistance for a spherical geometry [Ωm²]

_____

R	Resistance [Ω]
r	Particle radius [m]
t_+	Transference number of the positive species [−]
T	Temperature [K]
t	Time [s]
TDF	Thermodynamic factor [−]
U	Open circuit voltage [V]
V_0	Voltage amplitude [V]
V	Voltage [V]
$\boldsymbol{Z}$	Complex impedance [Ω]
z_s	Individual surface element in a TLM
α_a, α_c	Anodic and cathodic transfer coefficient [−]
α	Constant phase exponent [−]
ε	Porosity [−]
Θ_s	Free insertion site [−]
κ	Electrolyte conductivity [S/m]
σ	Electrical conductivity [S/m]
τ	Tortuosity
ϕ_1	Local solid potential [V]
ϕ_2	Local electrolyte potential [V]
ф	Phase shift [−]
ω	Angular frequency [1/s]

Descriptive subscripts:

_____

Subscript	Description
AM	Active material
diff	Diffusion
dl	Double layer
eff	Effective parameter
HF	High-frequency
LF	Low-frequncy
l	Liquid
s	Solid
sep	Separator
i	Index
part	Particle
ref	Reference value

1 Introduction

From early achievements in the development of rechargeable Li-ion batteries (LIBs) by Whittingham and Goodenough in the 70s and 80s and the transition to mass market by Sony in the 90s, Li-ion batteries have quickly penetrated consumer markets with their use in cell phones and laptop computers.[1,2] Further driven by the electrification of transport, most notably by Tesla, the production of Li-ion batteries has turned into a billion dollar industry.

The use in electric vehicles also comes with a shift in requirements. Energy density and cost are still at the forefront of the LIBs development, reaching 300 Wh/kg at a cost down to USD 200/kWh.[3] However, requirements for lifetime and fast-charging have challenged the cell development and driven the industry to make larger improvements in those areas, as the lifetime requirements for handheld devices are significantly shorter than the requirements for electric vehicle (EV) applications.[4] Tracking the cycling history of cells is important for the lifetime prediction of a cell via the battery management system (BMS).[5] Intelligent BMSs can be paired with a digital twin, i.e., some form of a model-based representation of a battery, e.g., through an equivalent circuit model (ECM) or a more complex version of a model based on the Newman model.[5–7]

The model developed for intercalation batteries by Doyle, Fuller and Newman[8,9] is almost as old as the Li-ion battery itself, but the mathematical backbone of the model has been unchanged since then. Necessary prerequisites for advancements in battery modelling are i) more accurate models which represent the physical phenomena in a cell more closely and ii) proper parametrization of the required physico-chemical kinetic and transport parameters.

Electrochemical Impedance Spectroscopy (EIS) can be a quite useful tool for such parametrization, as it is non-invasive and allows the user to discern between different forms of resistances like electrical or charge transfer resistance.[10,11] Thus it can be used to track the symptoms of degradation mechanisms, namely increases in cell resistance, to estimate a cell's state-of-health (SOH), state-of-charge (SOC) or temperature.[12–14]

1.1 Principle working mechanisms of Li-ion batteries

A Li-ion battery is broadly described as an insertion battery, where the anode and cathode active materials are host structures which allow the lithium to move in and out reversibly. It consists of two porous electrodes with a separator in between, filled with an ion conducting organic electrolyte.[15] During charging, the cathode material releases Li^+ into the electrolyte, where the ion moves through the separator to the anode and is inserted back into a host structure.

The most used anode material for a Li-ion battery is graphite, which achieves a high reversible capacity of ~350 mAh/g at a density of 2.1 g/cm³, thus achieving a volumetric capacity of 735 mAh/cm³. Graphite shows two main plateaus in its potential profile which are at 0.12 and 0.075 V vs Li^+/Li, and thus lie close to the lithium redox potential (-3.04 V vs a standard hydrogen electrode), which is among the lowest known redox potentials. Using Li-metal as anode material would significantly increase the cells energy density, but drawbacks like dendrite formation pose a significant safety risk.[16–18] Recently, silicon has been in the focus as active material as it is abundant and shows an extremely high theoretical specific capacitiy of 4200 mAh/g.[19–22] So far, silicon is only viable when not making up the majority of capacity of LiB anodes, as electrodes consisting of mainly silicon suffer from rapid capacity fading during cycling due to the extreme volume expansion of the material.[22–24]

The low operating potentials of the aforementioned anode materials are outside of the stability window of the electrolyte, which is partly being decomposed in the first charging cycle of the LiB.[25,26] Luckily, certain electrolytes form a stable, insulating

solid electrolyte interphase (SEI) layer which is also Li^+ conductive and allows the stable operation of the LiB.[27–29] Thus the Li-ion battery is kinetically stable and can be used for several years without significant capacity loss.

Commonly used cathode active materials are $LiFePO_4$ (LFP) or $Li(Ni_xMn_yCo_z)O_2$ (NMC) with x+y+z=1.[30] Materials from the NMC family give lower reversible capacities compared to graphite, viz., 150 to 220 mAh/g (with a theoretical limit of ~280 mAh/g if it could be fully delithiated), and can be reversibly cycled to potentials around 4.4 V vs Li^+/Li.[31–33] With a significantly higher density around 4.4 g/cm³, the volumetric capacity of NMCs lies around 700-970 mAh/cm³, comparable to graphite and thus results in both electrodes having similar thickness. Current collectors for the active materials are copper on the anode side and aluminium on the cathode side. While aluminium is much lighter and thus would be preffered, it forms an alloy with lithium and is not suitable to be used at the relevant anode potentials.[34] The surface of the aluminium current collector, usually made of Al_2O_3, is only stable up to 3.8 V vs Li^+/Li and should therefore not be usable for most cathode active materials. However, the Al surface forms AlF_3 from hydrogen fluoride (HF), which is found in $LiPF_6$ containing electrolytes due to water contamination, and renders the current collector stable up to 6 V vs Li^+/Li.[35–37]

To avoid a short circuit, a separator is placed between anode and cathode, usually made of one or more porous layers of polypropylene or polyethylene, with the pores filled with electrolyte.[38–40] The separator is a focal point in battery safety, as it prevents short circuits and thermal runaways. The safety aspects are in direct contrast to the cell performance, as thicker tri-layer separators improve safety but hinder the Li^+ transport across the separator.[40]

The electrolyte usually consists of a mix of ethylene carbonate (EC), ethyl-methyl-carbonate (EMC), and/or dimethyl-carbonate (DMC) solvents and $LiPF_6$ salt.[41] For this thesis mostly a mix of 1M $LiPF_6$ in EC:EMC 3:7 (wt.) was used. Newly emerging alternatives are all-solid-state electrolytes which can achieve conductivities close to that of liquid electrolyte.[42,43] Their thermal stability was recently shown to be similarly problematic as that of liquid electrolytes,[44] and they additionally can exhibit poor electrochemical stability.[45]

_____

To achieve high energy densities in the cells, Li-ion battery electrodes are produced as porous electrodes, i.e., the active material is packed as thick as possible on the current collector and its pores are filled with electrolyte to allow Li^+ transport within the electrode. Having a porous electrode requires knowledge of the electrode's microstructure and an understanding of the behavior of a porous electrode. This topic is a focal point of this thesis.

1.2 Relevant mathematical description of a Li-ion battery

The following mathematical equations are part of a homogenized pseudo-2D Li-ion battery model. This model was mainly developed by Doyle, Fuller and Newman [8,9] (generally referred to as "Newman model") in the early 1990s and is still regularly used today. The Newman model homogenizes the electrode, i.e., it superimposes aspects of the solid and liquid part of the electrode such that at any point in the electrode the insertion reaction, electrolyte- and electrical current are present. Once the reaction occurred, the model then, figuratively speaking, transports the lithium into an active material particle where the diffusion into the particle takes place. The two dimensions do not directly affect each other, i.e., the electrolyte or electric current can flow unobstructed and are not affected by any geometric obstacles but are instead described by the use of effective parameters, hence the description pseudo-2D. The following mathematical descriptions of the cell are derived for a binary electrolyte and with the assumptions of constant (i.e., concentration independent) electrolyte parameters.

The battery can be divided geometrically into 3 main parts, namely anode, separator and cathode. The separator only holds electrolyte and is otherwise inert. The change in electrolyte concentration in the separator can be described by

$$\varepsilon_{\text{sep}} \frac{\partial c}{\partial t} = \frac{\partial}{\partial x}\left[D_{\text{eff,sep}} \frac{\partial c}{\partial x}\right] \tag{1.1}$$

with c as the concentration of Li$^+$ in the electrolyte, ε_{sep} as the separator porosity and $D_{\text{eff,sep}}$ as the effective diffusion coefficient of the electrolyte in the separator, which includes the effects of the separator tortuosity and porosity. The current I across the separator is described by

$$I = \kappa_{\text{eff,sep}} \frac{\partial \phi_2}{\partial x} + \frac{2\kappa_{\text{eff,sep}} \overline{R} T}{F} (1 - t_+) \frac{\partial \ln c}{\partial x} \tag{1.2}$$

with $\kappa_{\text{eff,sep}}$ as the effective electrolyte conductivity in the separator, Φ_2 as the electrolyte potential representing the potential which would be measured at this point by a Li-metal reference electrode, $\bar{R}$ the universal gas constant, F as Faradays constant and t_+ as the transference number of the positively charged ions (Li⁺).

Equation (1.2) is also used to describe the current in the electrolyte within the pores of the porous cathode and anode electrodes, by replacing the effective conductivity and diffusion coefficient of the separator with the adjusted values for the respective electrodes. As the electrodes act as a sink/source of Li⁺ into/from the electrolyte, the material balance [eqn. (1.1)] is adjusted by a sink/source term:

$$\varepsilon_i \frac{\partial c}{\partial t} = \frac{\partial}{\partial x}\left[D_{\text{eff},i}\,\frac{\partial c}{\partial x}\right] + a_i(1 - t_+)J_i \qquad (1.3)$$

with i indicating either the positive or negative electrode, a as the specific interfacial area (in units $\text{m}^2_{\text{AM}}/\text{m}^3_{\text{geom}}$ where "AM" denotes the active material surface area and "geom" the geometric volume of the electrode) and J as the local current density. The interfacial current is governed by the kinetic reaction according to Butler-Volmer and is described as

$$\text{i} = i_0\left[\exp\left(\frac{\alpha_a F(\phi_1 - \phi_2 - U)}{\bar{R}T}\right) - \exp\left(-\frac{\alpha_c F(\phi_1 - \phi_2 - U)}{\bar{R}T}\right)\right] \qquad (1.4)$$

with i_0 as the exchange current density, α_a and α_c as the anodic and cathodic transfer coefficients (assumed as $\alpha_a + \alpha_c = 1$), ϕ_1 as the solid potential and U as the open circuit voltage of the interface. Thus $(\phi_1 - \phi_2 - U)$ effectively describes the overpotential of the reaction on the particle surface. Since Li-ion battery materials change their potential with SOC, U is described by an SOC-dependent function rather than a specific potential.

The intercalation reaction into a host structure not only requires Li⁺ and an electron for recombination but also a free site in the host structure (Θ_s), resulting in the equation for the Li-ion intercalation reaction:

$$\text{Li} - \Theta_s = \text{Li}^+ + \Theta_s + e^-$$

(1.5)

The free site now also plays a part in the kinetic reaction of the electrode, as a full or empty host structure limits the reaction. The resulting equation for the exchange current is given as

$$i_0 = Fk(T)\frac{(c_{s,max} - c_s)^{\alpha_c}(c_s)^{\alpha_a}}{c_{s,max}}\left(\frac{c_l}{c_{ref}}\right)^{\alpha_a}$$

(1.6)

where $k(T)$ represents the temperature dependent reaction rate constant, c_s the concentration of lithium in the solid active material, $c_{s,max}$ the maximum concentration of lithium in the solid, c_l the concentration of Li⁺ in the liquid phase and c_{ref} the liquid reference concentration. Comparing equation (1.5) with equation (1.6), the term $(c_{s,max} - c_s)$ represents the unoccupied sites in the active material (Θ_s), c_s represents the available lithium in the solid and c_l represents the Li⁺ in the electrolyte solution. The equation predicts an increase in resistance if the material is either approaching a full or empty state or if the electrolyte concentration is being depleted.

In the solid part of the porous electrode, the electrical current can be described by

$$I = -\sigma_{eff,i}\frac{\partial \phi_1}{\partial x}$$

(1.7)

and simply represents ohms law. Within a particle, generally diffusion models based on Fick's law are used. For spherical particles, the governing equation for the mass transport in the solid is given as

$$\frac{\partial c_{\mathrm{s}}}{\partial t} = \frac{1}{r^2}\frac{\partial}{\partial r}\left[r^2 D_{\mathrm{s}}\ \frac{\partial c_{\mathrm{s}}}{\partial r}\right] \tag{1.8}$$

The equations described above are of general interest, especially for the later described impedance measurements, as they describe phenomena which are prominently measured, such as kinetic or electrolyte resistances. Other parts of the model need adaptation to describe the different ways in which some materials or systems function. For example, certain battery materials are more closely described by a conversion reaction where the educt and product are two distinct materials with no intermediates, such as for LFP or parts of graphite. These materials exhibit a flat potential and the lithiated and delithiated phase coexist with little equilibration.[46,47] For such multiphase systems, Baker and Verbrugge[48] developed a model to adapt diffusion inside the material.

Other battery models are simplified versions of this model, such as the single particle model (SPM). In the SPM, the electrolyte phase in the electrode is neglected and it is assumed that all particles in the electrode behave the same, effectively having one particle to represent the entire electrode.[49,50] The model is mostly valid for low current applications, where the current across the electrode is more homogeneous. Further simplifications for models are to void the model of its geometric aspects and convert it into an equivalent circuit model (ECM).[51–53] Such an equivalent circuit can be parametrized and validated using electrochemical impedance spectroscopy.

To understand the importance of the liquid phase transport, and thus the necessity to describe the Li-ion electrode as a porous electrode, the following calculation of the number of moles contained in the liquid phase compared to the solid phase can be useful. Assuming the use of a graphite anode with 735 mAh/cm^3 and an arbitrary NMC cathode with 800 mAh/cm^3 (see section 1.1), a solid fraction of 70% (porosity 30%) on both sides and an areal capacity of 3mAh/cm^2 for the cathode and 3.3

mAh/cm^2 for the anode results in electrode thicknesses of 53 μm for the cathode and 64 μm for the anode. Further assuming a commercial separator of 20μm and 40% porosity (e.g. Celgard 2320)[54], results in a total void volume of ~3.5 μl/cm^2 in the electrodes combined and only ~0.8 μl/cm^2 in the separator. Using an electrolyte of a 1M salt concentration (e.g., LiPF$_6$, assuming total salt dissociation) results in total 4.3 μM/cm^2 of Li-ions in the electrolyte phase. Converting the cathode capacity of 3mAh/cm^2 into moles (using Faradays constant) yields about 112 μM/cm^2, i.e., a factor 26 difference to the total amount of Li-ions in the electrolyte and more than a factor 100 compared to only the separator. The physical constraint of electroneutrality prevents an increase in average Li$^+$ concentration in the electrolyte (local increases/decreases are possible), thus limiting the total amount of Li$^+$ which can be present in the electrolyte to about 4% of the total cell capacity. This highlights the importance of the liquid phase and the impact of the microstructure of an electrode on the cells performance.
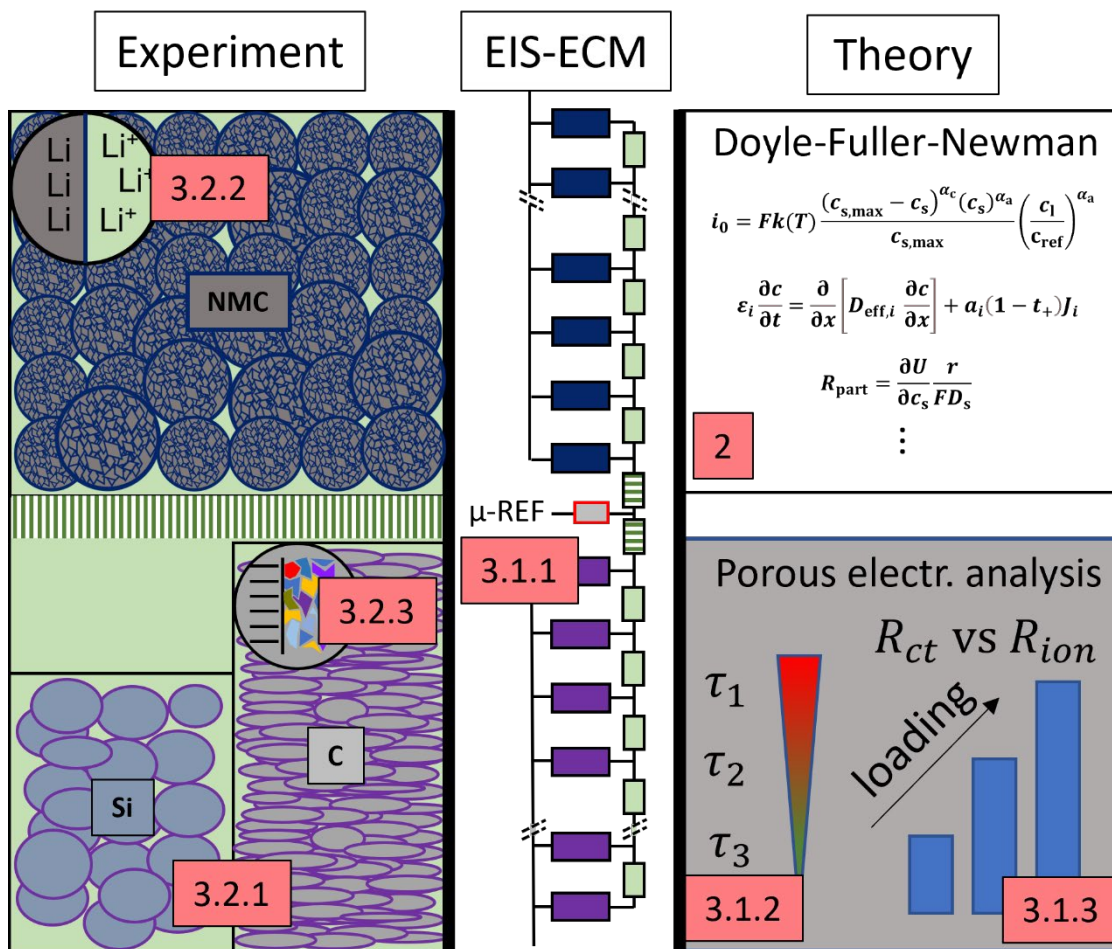
1.3 Dissertation overview

Figure 1.1 Overview over topics covered in this dissertation with chapter numbers: 2 gives an overview over existing battery fundamentals and EIS theory; 3.1.1 shows the origin of EIS artefacts when using a µ-reference electrode in half-cell measurements and a practical solution. 3.1.2 illustrates how binder migration causes inhomogeneities in tortuosity and the effect on the blocking EIS spectrum. 3.1.3 gives a detailed analysis of the impact of kinetic and ionic resistance on EIS spectra and how to properly analyze them. 3.2.1 compares graphite and silicon-based electrodes for their temperature dependent kinetic and ionic resistance with a detailed analysis on the resulting potential profile and charge rate performance. 3.2.2 explores NMC 111 fundamentals with measurements of the SOC-dependent and Li⁺-concentration-dependent reaction kinetics as well as NMC 111 diffusion resistance measurements. 3.2.3 analogously explores the graphite fundamentals, including the effects of the SEI on the graphite EIS spectrum and Li⁺-concentration-dependent kinetics.

2 Electrochemical Impedance Spectroscopy

2.1 General principles

In impedance spectroscopy, a sinusoidal current or potential at varying frequencies is applied to a system, generating an impedance spectrum which allows the user to identify a variety of impedances within a system. This analysis makes it possible to discern phenomena which happen on different time scales and since EIS is a non-invasive tool, it is very useful for tracking the evolution of impedances over the course of a LiB's lifetime. This chapter describes the mathematical background for the EIS technique and the useful ECMs for LiBs, which can be found in the pertinent literature.[55,56]

For a sinusoidally applied voltage of amplitude V_0 and angular frequency $\omega = 2\pi f$

$$V(t) = V_0 \, sin \, (\omega t) \tag{2.1}$$

the current response can be defined as

$$I(t) = I_0 \, sin \, (\omega t + \phi) \tag{2.2}$$

with I_0 as the current amplitude and ϕ the phase shift, resulting in the complex impedance

$$\boldsymbol{Z(\omega)} = \frac{V_0}{I_0} e^{j\phi(\omega)} \tag{2.3}$$

Two main requirements for successfully measuring EIS are i) linearity/reversibility and ii) steady state operations. The linearity and reversibility requirement practically means that within the excitation window, all measured circuit elements must not change their parameters, during or after the measurement. As shown later, NMC 111 shows a large SOC-dependent change in the charge transfer kinetics, which means that the excitation window must be chosen such that the change in SOC during the measurement is negligible. Also, the above-described Butler-Volmer kinetics become non-linear at higher overpotentials, but are comfortably linear for excitations around 10 mV, which was used throughout this thesis. The reversibility requirement (no memory effect) also prohibits measurements on non-reversible processes, which speaks against measurements conducted, e.g., during the SEI formation.

The steady state operations requirement practically means that the potential of the measured electrode must not change during the measurement (except due to the excitation), e.g., due to relaxation phenomena, electrode drift or temperature changes in the system. This requirement is easily satisfied by a sufficiently long open circuit period at constant temperature before each measurement or by holding the electrode at the desired potential before the measurement.

The potential of the electrode also dictates which excitation method should be used, Potentio Electrochemical Impedance Spectroscopy (PEIS), where the excitation comes from an applied potential, or Galvano Electrochemical Impedance Spectroscopy (GEIS), where the excitation is through an applied current. To avoid major changes in SOC, electrodes exhibiting perfectly flat potentials should be measured using GEIS, while in regions of non-flat potentials PEIS should be used. If the measurement is only conducted to frequencies down to around 0.1 Hz, PEIS measurements can be practically conducted for all electrodes, as the change in SOC is minimal due to the short measurement time. To discern the individual cathode and anode resistance, a gold wire μ-reference electrode (GWRE) developed by Solchenbach et al.[57] was used in large parts of this thesis.

2.2 Equivalent circuit elements and their use in Li-ion battery analysis

The analysis of basic equivalent circuit elements may seem trivial, but the information which is provided by a careful analysis of those can still be invaluable. While inductive elements are certainly important for commercial cell applications, their influence is not visible in the cell setups used in this work.[58,59]

2.2.1 R, C, Q elements

The simplest equivalent circuit element is a resistor, which is frequency independent and described by

$$\mathbf{Z}(\boldsymbol{\omega}) = R \tag{2.4}$$

It is used to represent a variety of resistances in a battery, e.g. electrical or kinetic resistances. There are also multiple sources of capacitive effects in Li-ion batteries, described by the capacitive element

$$\mathbf{Z}(\boldsymbol{\omega}) = \frac{1}{j\omega C} \tag{2.5}$$

with j as the imaginary unit and C as the capacitance. Usually the capacitive behavior is not ideal and the capacitance is replaced by a constant phase element $Q = C^{\alpha}$ with the complex resistance described as

$$\mathbf{Z}(\boldsymbol{\omega}) = \frac{1}{(j\omega)^{\alpha}Q} \tag{2.6}$$

There are multiple sources which give rise to capacitive behavior in a Li-ion battery. Most prominently, there are the double layer capacitance at the interface between the active material and the current collector[60,61] and the electrochemical double layer at the electrode/electrolyte interface.[62] The latter gives information about the

electrode surface area, however comparing measurements at different potentials is not advised, as the double layer capacitance also depends on the applied potential.
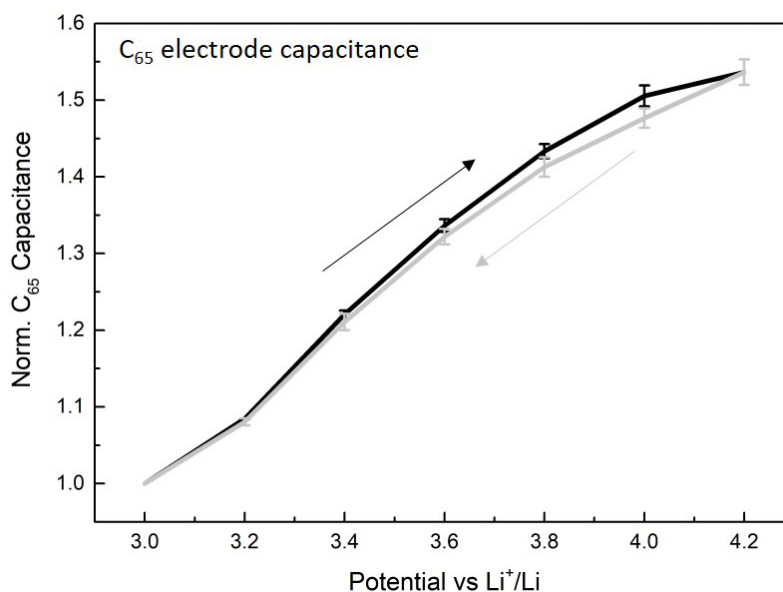

Figure 2.1 Double layer capacitance (Q) extracted from electrodes made of conductive carbon (Super C_{65}) on aluminium foil, measured at different potentials from 3 to 4.2 V vs Li+/Li. The capacitance was normalized to the value initially obtained at 3 V to show the potential dependent change in capacitance. Average of two individually normalized measurements, T-cell setup with GWRE, LP57 electrolyte.

Figure 2.1 shows the capacitance of an electrode made only of conductive carbon (Super C_{65}), extracted via EIS measurements (T-cell setup with GWRE and free-standing graphite on Li-metal counter electrode, PEIS measurement with 15min potential hold at each step), measured at different potentials between 3 and 4.2 V vs Li+/Li. As the electrode allows no charge transfer, it is constantly under blocking conditions and thus allows extracting the capacitance in the low-frequency part of the blocking EIS spectrum in the whole measured potential range. When normalizing the capacitance to the value obtained at 3 V, the electrode shows a 50% increase in capacitance with a reversible potential dependence of the capacitance. For electrodes which include active material, any potential dependent capacitance analysis is more complicated. The extracted information would include the potential dependent behavior of both passive and active materials. If the active material is suspected of "breathing", i.e., expanding and contracting with SOC, these SOC dependent changes cannot be distinguished from the potential dependent changes. However, an analysis of capacitance over the course of cycling should be possible and simply needs to be performed at the same potential (vs. Li+/Li),

regardless of SOC, as was done, e.g., for tracking of particle cracking in cathode active materials.[63–65]

Another source of capacitance is the extracted faradaic charge of a Li-ion battery, which is the main source of charge if the measurement is performed to frequencies below the apex frequency of the charge transfer reaction element (usually in the range of 10 Hz). To limit the extracted charge and avoid large SOC changes, small potential perturbations in the range of 5-10 mV are chosen for a PEIS measurement. The extracted charge is determined by the open circuit voltage (OCV) slope of the measured material at the point of measurement and the duration of the measurement, i.e., the lowest frequency point.

2.2.2 R/Q element

The most common element used to represent electrochemical systems is an R/C element, or practically more relevant an R/Q element, which is the parallel connection of a resistance and a capacitance. It is prominently used to describe the charge transfer interface with the resistance representing the kinetic resistance and the capacitance describing the double layer capacitance, but is, e.g., also used to describe the electrical contact resistance between battery electrodes and the current collector.[60] It can be described as follows:

$$\boldsymbol{Z(\omega)} = \frac{R}{RQ(j\omega)^\alpha + 1} \tag{2.7}$$

2.2.3 Electrolyte Warburg diffusion

Diffusion resistances play a major role in the performance of Li-ion battery electrodes. Diffusion in the liquid phase (e.g. within the separator) can usually be described as transmissive, i.e., the current source and sink allow drawing a constant current, and thus the behavior at steady state (low frequencies when the system does not change anymore) is that of a resistance. The diffusion impedance in the

liquid electrolyte within the pores of the separator can be described by the following equation:

$$Z(\omega) = R_{\mathrm{diff,l}} \frac{\tanh \sqrt{j\omega \frac{d^2}{D_{\mathrm{eff}}}}}{\sqrt{j\omega \frac{d^2}{D_{\mathrm{eff}}}}} \tag{2.8}$$

with

$$R_{\mathrm{diff,l}} = \frac{d}{\left(\frac{c_l D_{\mathrm{eff}} F^2}{2\bar{R}T(TDF)(1-t_+)^2} \right) A} \tag{2.9}$$

where d is the diffusion distance and A the geometric electrode area. The following calculation estimates the diffusion resistance across a pathway filled with electrolyte (no electrode involved) and can be found in more detail in section 3.2.2 (Manuscript Appendix):

Using Landesfeind et al.[66] for LP57 electrolyte parameters $TDF = 1.5$, electrolyte conductivity $\kappa = 8.9$ mS/cm, $D = 3 \times 10^{-10} \frac{m^2}{s}$ and $t_+ = 0.25$ at 298 K, a volume of 1 cm² area and 89µm thickness purely filled with electrolyte (no separator, simply electrolyte) would result in a 1 Ω high frequency resistance (resulting from the electrolyte conductivity and using the geometric relationship $R = \frac{d}{A \times \kappa}$). The diffusion resistance for such an electrolyte filled segment can be calculated using equation (2.9) with the above-mentioned parameters, resulting in 1.33 Ω. The resistance from the electrolyte conductivity (1 Ω) and the Warburg diffusion resistance (1.33 Ω) can now both be scaled by the porosity and tortuosity of the medium which is containing the electrolyte, e.g., a separator. Since both values scale equally with the geometric parameters, it can be stated that every 1 Ω in separator high frequency resistance results in an additional 1.33 Ω in diffusion resistance, i.e.,

measuring a 2 Ω separator high frequency resistance in an EIS measurement would then yield a 2.66 Ω separator diffusion resistance.

More practically measured are resistances on the order of 4 Ωcm² for a T-cell glass fiber separator resistance, resulting in 5.32 Ωcm² diffusion resistance. Using equation (2.8) and the values $R_{\mathrm{diff,l}} = 5.32$ Ω, separator thickness $d = 200\mu m$, $D_{eff} = D\frac{\varepsilon}{\tau} = 2.4 \times 10^{-10}\ \frac{m^2}{s}$ with tortuosity $\tau = 1$ and porosity $\varepsilon = 0.8$, Figure 2.2 shows the Nyquist plot of the resulting diffusion resistance expected from a T-cell setup. Usually, impedance spectra are obtained to a frequency of 0.1 Hz since i) below such a frequency the measurement time would significantly increase, ii) the mostly sought phenomena such as the electrodes kinetics are already present and iii) the spectra become increasingly dominated by solid diffusion phenomena (see Moškon et al.[10,11] for such measurements). The overlap with solid diffusion phenomena is also why the spectrum shown in Figure 2.2 is practically never measured and requires custom-made 4-electrode setups for electrolyte characterization to become visible. [67]

In measurements down to 0.1 Hz the electrolyte resistance can therefore mostly be neglected as the contribution of the electrolyte diffusion resistance in the separator to that point only contributes ~0.5 Ωcm². The Diffusion spectrum first follows a 45° line and transitions into a semi-circle below 0.01 Hz. The liquid diffusion resistance can thus be represented by a Q-element with an α coefficient of 0.5 for any measurement in such a frequency range. The spectrum will not change its shape if the geometry of the electrode stays planar, i.e., there is no deviation from the 45° angle under any circumstances and observing non-45° angles is usually the result of other phenomena overlapping, most prominently the aforementioned diffusion in the electrode solid material.
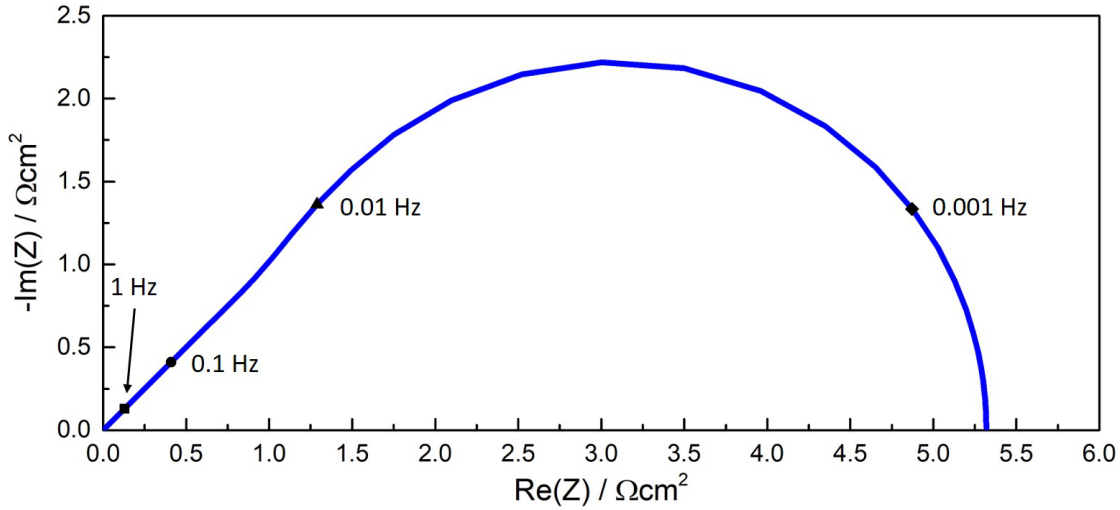
Figure 2.2 Calculated Warburg diffusion resistance for a T-cell glass fiber separator using electrolyte parameters of LP57 (D_{eff} of 3×10^{-6} cm^2/s) and a separator thickness of 200 μm (see section 3.2.2 for detailed parameter choices). The contribution of the liquid Warburg resistance to the EIS spectra could not be observed in this fashion in all cell setups of this thesis due to the overlapping with other phenomena and could thus only be described theoretically.

2.2.4 Active material solid Warburg diffusion

While the diffusion in the liquid can be described by transmissive boundary conditions, the diffusion in the active material is described by a reflective boundary condition. This means that the current source/sink are finite and ultimately result in a capacitive behavior. The reflective planar diffusion is described by

$$\boldsymbol{Z(\omega)} = R_{\text{planar}} \frac{\coth \sqrt{j\omega \frac{d^2}{D_s}}}{\sqrt{j\omega \frac{d^2}{D_s}}} \tag{2.10}$$

With the planar diffusion resistance R_{planar} derived by Ho et al.[68] as

$$R_{\text{planar}} = \frac{\partial U}{\partial c_s} \frac{l}{FD_s} \tag{2.11}$$

with l as the diffusion length.

However, usually active material particles are spherical, or close to spherical. The reflective diffusion for spherical particles can be described according to Meyers et al.[62] by

$$Z(\omega) = R_{\text{sphere}} \frac{\tanh \sqrt{j\omega \frac{r^2}{D_s}}}{\sqrt{j\omega \frac{r^2}{D_s}} - \tanh \sqrt{j\omega \frac{r^2}{D_s}}} \tag{2.12}$$

with r as the particle radius and R_{sphere} as the diffusion resistance in the spherical particle given as

$$R_{\text{sphere}} = \frac{\partial U}{\partial c_s} \frac{r}{F D_s} \tag{2.13}$$

with r as the particle radius. Figure 2.3 shows the difference in spectrum shape for the two resistances.
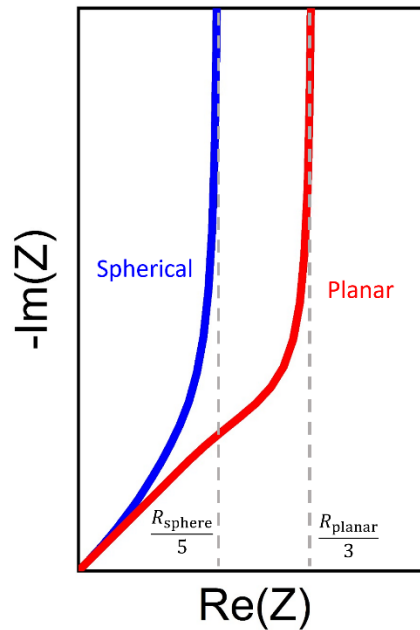

Figure 2.3 Qualitative comparison of the spectral shape of reflective planar and spherical diffusion resistances. While the planar diffusion (red) initially follows a 45° angle before reaching the 90° capacitive behavior, the spherical diffusion (blue) resistance is trending continuously upwards. The low-frequency intercept gives 1/5 of the spherical diffusion resistance and 1/3 of the planar diffusion resistance for the individual measurements.

The planar and spherical diffusion resistance differ in that the planar diffusion resistance at higher frequencies (bottom left graph for both spectra) starts in a 45° angle before reaching the capacitive upward trend at lower frequencies, while the spherical diffusion shows a more continuous upward trend. The low-frequency intercept (grey lines) gives 1/5 of the spherical diffusion resistance for the blue spectrum and 1/3 of the planar diffusion resistance for the red spectrum. The units of R_{planar} and R_{sphere} as described above are in $\Omega\mathrm{m}^2$, where the area is defined as the projected diffusion area of the particles, i.e., the surface area of the geometric particle if its surface roughness was 1 (perfectly smooth), since the particles surface roughness has no influence on the diffusion process.

Fundamentally, the diffusion resistance in the solid active material differs from diffusion in the liquid not only in the boundary condition, but also in its dependence on the OCV slope. From their mathematical description it can be followed that if the potential is not changing with a change in concentration of the solid species ($\frac{\partial U}{\partial c_{\mathrm{s}}} = 0$, i.e., a flat OCV profile) its diffusion resistance is zero and it will only reach its capacitive behavior at frequencies low enough to reach the boundaries of the measured plateau, which in the case of, e.g., LFP or $\mathrm{Li_4Ti_5O_{12}}$ (LTO) is when the electrode is empty or full. Some battery materials are effectively flat in only parts of their potential profile, e.g., graphite, which was prominently used in this thesis. Low frequency measurements (below 0.1 Hz) were only carried out for NMC, which does not show a plateau in its OCV profile (see section 3.2.2).

2.2.5 Transmission line model

A transmission line model (TLM) can be used to represent a variety of phenomena, including the above-described diffusion resistances, evident in the same equations describing both.[11,69–71] In this thesis the term is used to describe the equivalent circuit of a porous electrode, where depending on the measurement conditions certain simplifications can be made. Figure 2.4 shows the equivalent circuit of a simplified transmission line model.
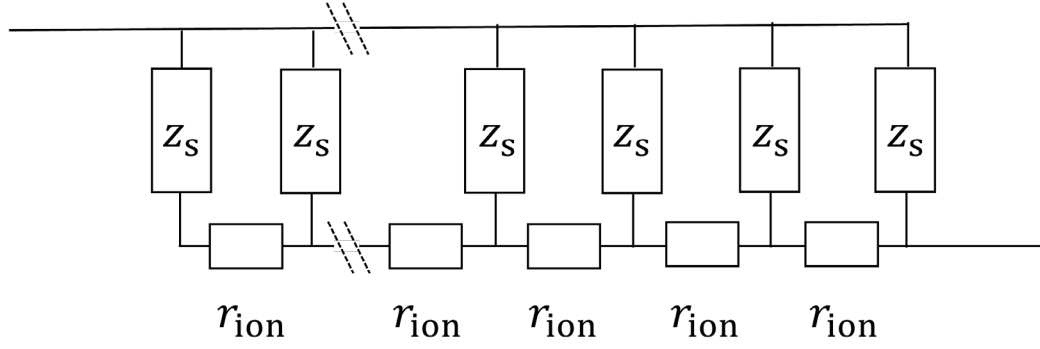
Figure 2.4 Simplified electrode transmission line model with z_s representing the individual electrode surface elements and r_{ion} representing the individual pore resistance elements. This simplification does not include electrical resistances (otherwise found in the upper backbone opposite to r_{ion}), separator resistance (otherwise found in the bottom right outward-bound connection) or the electrical contact resistance (otherwise found in the top left outward-bound connection)

This model is a geometric representation of the pores with two backbones for the electrical resistance through the solid (assumed negligible) and the ionic resistance through the liquid, connected via the material surface. z_s describes the individual surface elements, e.g., an R/Q element for the charge transfer reaction, while r_{ion} describes the ionic resistance from the electrolyte filled pores. In both cases any diffusion resistances in solid or liquid are neglected, as these only play minor roles for the majority of measurements conducted to a frequency down to 0.1 Hz. If the charge transfer resistance is infinitely large, the electrode is under so called "blocking conditions", and thus forms the simplest TLM with only capacitive elements on the surface. The blocking impedance spectra of the porous electrode gives the same spectrum as the reflective planar diffusion resistance as shown in Figure 2.3 and can be described by adjusting equation (2.10) to:

$$Z(\omega) = R_{ion} \frac{\coth \sqrt{(j\omega)^\alpha Q_{dl} R_{ion}}}{\sqrt{(j\omega)^\alpha Q_{dl} R_{ion}}} \tag{2.14}$$

with the electrolyte pore resistance R_{ion} and the electrochemical double layer capacitance Q_{dl}. Instead of the diffusion time constant $\frac{d^2}{D_s}$ from equation (2.10), here the equation includes the time constant of the circuit, $Q_{dl} R_{ion}$. The blocking impedance can be used to measure the ionic resistance since it is free of other influences and has been extensively studied.[54,69,72–79] Extending the model to

incorporate the electrochemical reaction, i.e., replacing the blocking Q-element on the particle surface with an R/Q-element, i.e., R_{ct}/Q_{dl}, where R_{ct} represents the electrochemical reaction, yields the following equation for the non-blocking transmission line model:

$$Z(\omega) = \sqrt{\frac{R_{ion}}{\left((j\omega)^\alpha Q_{dl} + \frac{1}{R_{ct}}\right)}} \coth\left(\sqrt{R_{ion}\left((j\omega)^\alpha Q_{dl} + \frac{1}{R_{ct}}\right)}\right) \qquad (2.15)$$

This equation does not incorporate any effects of the capacity limit in Li-ion batteries (solid diffusion elements) and can thus universally be used for any porous electrode which operates in the same geometric configuration (e.g., fuel cells). Its use is practically limited to the frequency range where additional capacitive or otherwise relevant diffusion effects are negligible.

All equations given above were derived under the assumption of homogeneity within the transmission line model, i.e., identical individual elements. Once an electrode becomes inhomogeneous in its resistance across the length of the electrode, the above solutions cannot be used anymore. This raises the question of the weighing of resistances. In a blocking impedance spectrum, the current flow is through the porous network and the current sinks are distributed across the electrode. Therefore, a locally increased resistance towards the separator interface is weighed more than an increase towards the current collector interface, as more current crosses the separator interface, and thus affects the measurement more. The effect of this is shown in section 3.1.2.
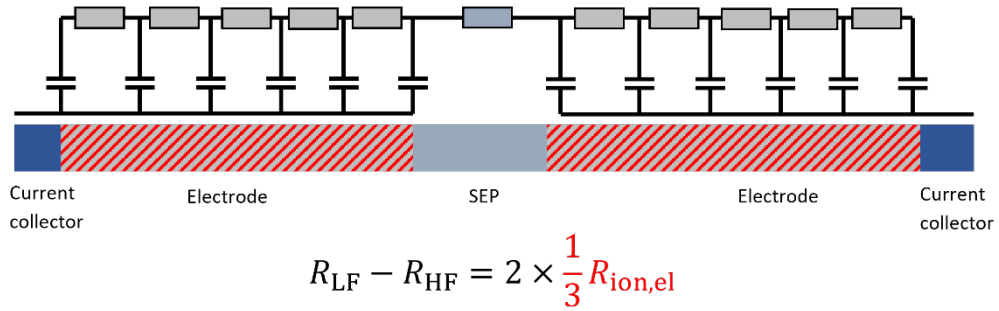
2.3 A practical approach to Transmissive EIS

If the porous network is measured in a transmissive setup, i.e., in a configuration where the electrode is not connected electrically but ionically on both sides (e.g., between two separators), with the current source/sink on the outside, there is no directional dependence of the measured resistance, since the current passes through the entire electrode. The impedance of a blocking electrode in a transmissive configuration can be described by

$$Z(\omega) = R_{\text{ion}} \frac{\tanh \sqrt{(j\omega)^\alpha Q_{\text{dl}} R_{\text{ion}}}}{\sqrt{(j\omega)^\alpha Q_{\text{dl}} R_{\text{ion}}}} \qquad (2.16)$$

which in essence is the same equation (and thus the same spectral shape) as the transmissive diffusion in equation (2.8) (when using $\alpha = 1$ for perfect capacitive behaviour). This is another example of how a Warburg diffusion resistance can be modeled via a transmission line model approach.[70] Practically, measuring an electrode's pore resistance under transmissive conditions requires significantly more effort. The measurement requires a current source/sink independent of the measured electrode (e.g., Li-metal electrodes on both sides) and reliable knowledge of their resistances. Alternatively, two reference electrodes can be employed to exclude the influence of the source/sink electrodes from the spectrum. Furthermore, an electrode without current collector (free-standing electrode) needs to be fabricated; an approach on how to easily do this is described in section 3.1.1. While in theory measuring a free-standing electrode sandwiched between two Li-metal electrodes (with separators in between) is possible, Li-metal electrodes can exhibit huge resistances (in the range of 50-200 Ωcm^2) and are generally not stable enough in their impedance over time to be used for such an analysis.[80] Since the use of Li-metal also requires the use of typical commercial electrolyte with a high conductivity, the pore resistance of one electrode is expected to be small (in the range of 10 Ωcm^2). Using two reference electrodes would simplify the analysis but complicate the cell construction significantly.

_____

A more practical approach would be to find another porous electrode under blocking conditions as source/sink electrodes, since their resistance is usually easy to measure. The outside (reflective) electrodes should have a low resistance and high surface area compared to the inner (transmissive) electrode to minimize their influence on the measurement. The theory for such a measurement is shown in Figure 2.5, which compares the reflective blocking impedance equivalent circuit (top) and the blocking transmissive setup (bottom). The equivalent circuit for the reflective setup comes from a standard symmetric cell with two transmission line models (red) and a separator in between. The transmissive setup includes three electrodes, two electrodes acting as current sink/source on the outside (purple) with a free-standing electrode (green) in between, insulated via separators. Even though this inner electrode is not electrically connected to any of the working- or counter electrode connections, it is ionically connected to the cell via the electrochemical double layer. Thus, the high frequency resistance R$_{HF}$ in both cases represents the separator resistance (one separator for the reflective setup, two for the transmissive). The low frequency resistance R$_{LF}$ for a reflective electrode additionally contains 1/3 $R_{\mathrm{ion,el}}$ for each electrode. In the transmissive configuration the ionic current goes through the entire transmissive electrode, similar to a separator, and therefore measures the full $R_{\mathrm{ion,el}}$ of said electrode. In this practical case, the symmetric reflective cell contains two electrodes, thus R$_{LF}$-R$_{HF}$ for the reflective setup equals $2 \times \frac{1}{3} R_{\mathrm{ion,el}}$. For the transmissive setup, R$_{LF}$-R$_{HF}$ gives $R_{\mathrm{ion,el}} + 2 \times \frac{1}{3} R_{\mathrm{ion,source}}$, i.e., a combination of transmissive and reflective measurements.

Reflective Setup

Current collector | Electrode | SEP | Electrode | Current collector

$$R_{\mathrm{LF}} - R_{\mathrm{HF}} = 2 \times \frac{1}{3} R_{\mathrm{ion,el}}$$

Transmissive Setup

CC | Thin, high surface-area sink/source electrode | SEP | Free standing electrode | SEP | Thin, high surface-area sink/source electrode | CC

$$R_{\mathrm{LF}} - R_{\mathrm{HF}} = R_{\mathrm{ion,el}} + 2 \times \frac{1}{3} R_{\mathrm{ion,source}}$$
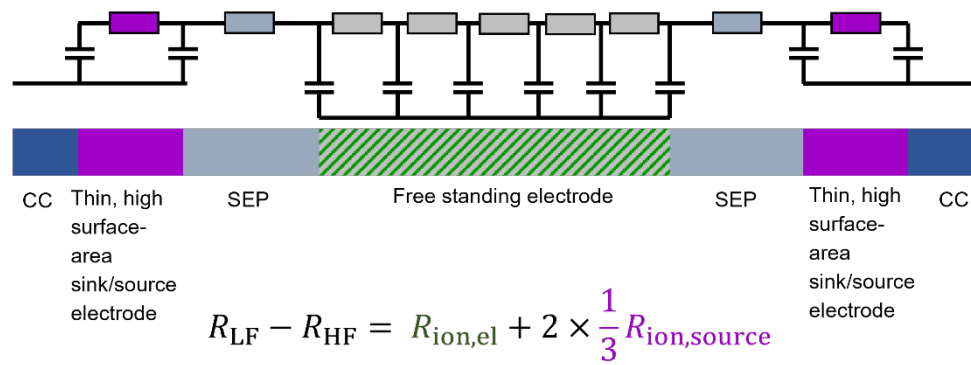
Figure 2.5 Configurations for blocking transmission line model measurements. Top: Reflective setup with the extrapolated resistance between high-and low frequencies of two electrodes corresponding to 2/3 R_{ion}. Bottom: Transmissive setup where the probed electrode is sandwiched between the separators and two thin, high-surface area electrodes on the outside, acting as current source/sink. The extrapolated resistance is the total $R_{\mathrm{ion,el}}$ and additionally the resistance of the outside source electrodes in reflective configuration, i.e., 2/3 $R_{\mathrm{ion,source}}$.

Figure 2.6a shows a simulated Nyquist plot of the reflective setup which points out the high- and low frequency resistance. In Figure 2.6b the calculated transmissive spectrum is plotted (green), which shows how a spectrum would look like if it was individually measured through the use of reference electrodes. As stated before, its shape is that of the Warburg liquid diffusion resistance (when α = 1). The blue spectrum showcases the spectral shape of a measurement which incorporates outer blocking electrodes (as current sink/source) which have a 10 times higher capacitance and a 10 times lower resistance compared to the transmissive electrode. The transmissive shape is still visible, but due to the ultimately blocking nature of the outer electrodes the spectrum shows a capacitive rise in resistance towards lower frequencies.
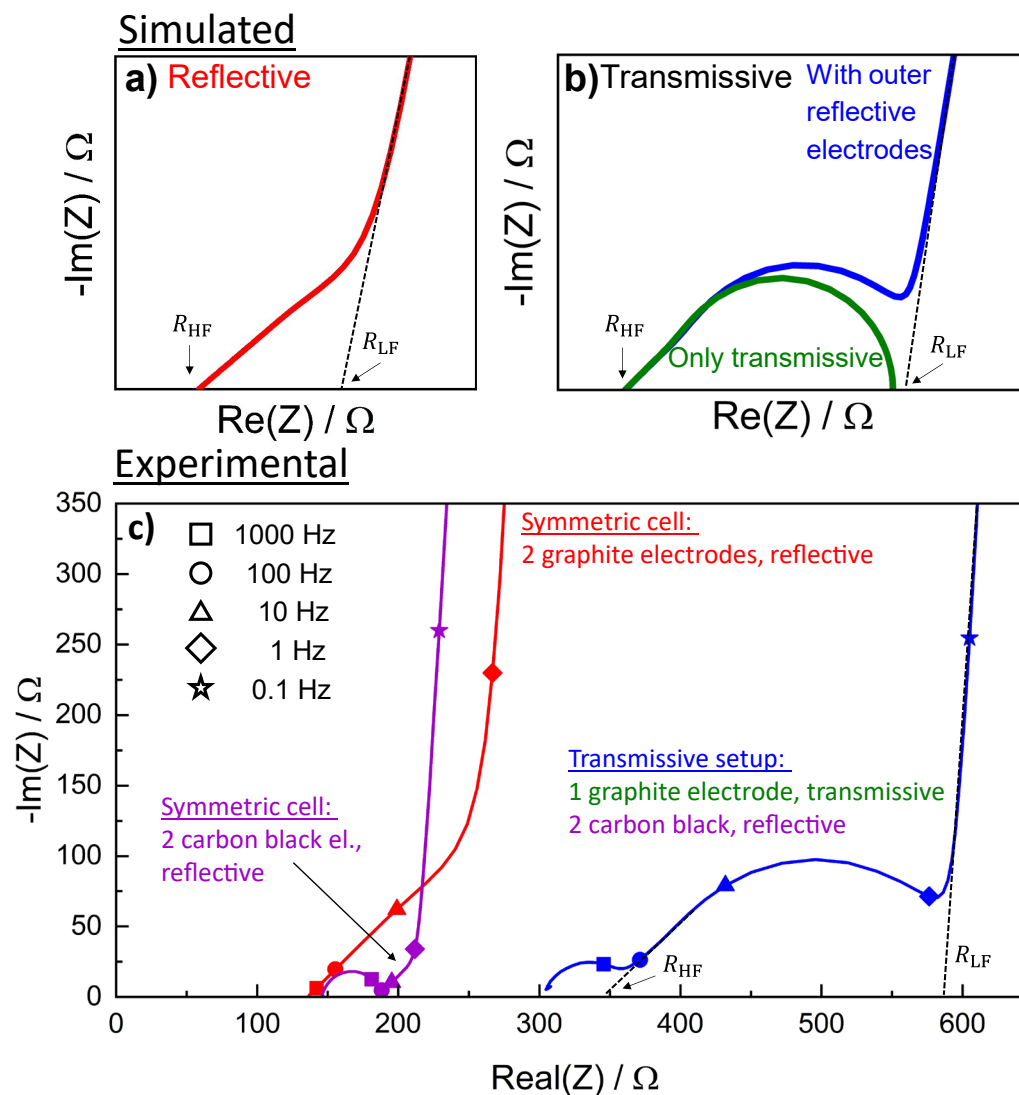
Simulated

a) Reflective

b) Transmissive — With outer reflective electrodes

R_{HF} R_{LF} — Only transmissive — R_{HF} R_{LF}

Experimental

c)
- □ 1000 Hz
- ○ 100 Hz
- △ 10 Hz
- ◇ 1 Hz
- ☆ 0.1 Hz

Symmetric cell:
2 graphite electrodes, reflective

Symmetric cell:
2 carbon black el.,
reflective

Transmissive setup:
1 graphite electrode, transmissive
2 carbon black, reflective

R_{HF} R_{LF}

Figure 2.6 a) and b) Nyquist plot of calculated EIS spectra for the reflective and transmissive setups shown in Figure 2.5. In b) the transmissive shape is shown individually in black and the spectrum, including outer blocking electrodes, is shown in blue. Calculation parameters: a) $R_{ion,el}$=100 Ω, C_{el}=1mF, α_{el}=0.9; b) Transm.: $R_{ion,el}$=100Ω, C_{el}=1mF, α_{el}=1, Refl. $R_{ion,source}$=10 Ω, C_{source}=10mF, α_{source}=0.9; c) experimentally obtained spectra regular symmetric cell for graphite (red curve) and carbon black electrodes (purple) and in a combined transmissive configuration (blue curve). Graphite electrodes ~9.9 mg/cm², ~108μm thickness, por. ~55%, Carbon black electrodes: ~0.6 mg/cm2, ~6μm thickness, por. ~50%. T-cell setup, 0.94 cm²

Figure 2.6c shows the experimentally obtained spectra. For the experiment, free-standing graphite electrodes (~9.9mg/cm², N-Methyl-2-pyrrolidon (NMP) based, T311 (SGL Carbon): polyvinylidene fluoride (PVDF, Kynar) 95:5) of ~110 μm thickness (uncompressed, porosity ~55 %) were measured using a low conductive electrolyte (0.35 mS/cm, ~20 mM TBAClO₄ in EC:EMC 3:7) in a symmetric cell setup with 2 glass fiber separators (red curve). The graphite electrodes were dried at room temperature (shown here) and 75°C for a later comparison of the tortuosity of the graphite electrodes with a homogeneous and an inhomogeneous ionic

resistance distribution within the electrode due to binder migration.[71] Additionally, electrodes with high surface area carbon (carbon black, 1500 m^2/g) were coated onto copper foil (Carbon black: PVDF, 1:1, dry thickness ~6 µm, 0.6 mg/cm^2) and measured symmetrically (purple curve). The graphite electrodes exhibit an R_{ion} of around 180 Ω per electrode and the carbon black electrodes around 45 Ω. From the 1 Hz datapoint of the red curve and the 0.1 Hz datapoint of the purple curve it is evident that the capacitance of the carbon black electrode is about 10 times larger than the capacitance of the graphite electrode. The carbon black electrode also shows a semi-circle at higher frequencies which can be explained by a contact resistance between the electrode and the copper foil. The free-standing electrodes were then measured according to the transmissive setup in Figure 2.5 and are shown in the blue curve in Figure 2.6c. The transmissive measurement uses carbon black electrodes as outer current sink/source electrode, 4 glass fiber separators (2 on each side) and one graphite electrode in transmissive configuration. The contact resistance semi-circle of the carbon black electrode is seen at the highest frequencies in the blue spectrum, followed by the expected diffusion shape which ends in the capacitive blocking branch. Comparing the 0.1 Hz datapoints of the purple and blue curve shows that this capacitive behavior comes from the outer carbon black electrodes, as expected.
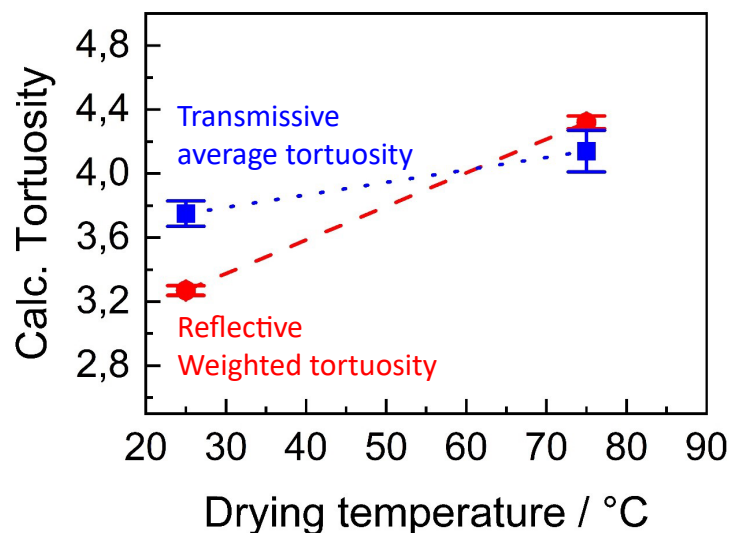

Figure 2.7 Tortuosity analysis of free-standing graphite electrodes in reflective and transmissive configuration as a function of their drying temperature.

Figure 2.7 shows the tortuosity analysis of the electrodes. The tortuosity was calculated as $\tau = \frac{R_{ion} \cdot A \cdot \varepsilon \cdot \kappa}{d}$ with A as the electrode area. For the room temperature dried electrodes, the transmissive measurement gives a bit higher tortuosity of around 3.8 compared to 3.3 for the reflective measurement. For electrodes dried at higher temperatures, both tortuosities increase to a value of around 4.0-4.2. Assuming no other source of influence, the difference between them can be traced back to the differences in measurement configuration. The transmissive measurement gives the cumulative sum of resistances and is directionally independent, while the reflective measurement is directionally dependent. Therefore, if the electrode is inhomogeneous, the transmissive measurement still gives the actual average tortuosity of the electrode and the reflective measurement gives a directionally weighted value where resistances at the separator side of the electrode are more significant than resistances at the current collector side of the electrode, as explained in more detail in section 3.1.2.[71] If the reflective measurement gives a smaller value, it can be assumed that the resistance at the separator side is below average, in this case, e.g., due to binder sedimentation during the long drying phase of NMP at room temperature. Vice versa it is not surprising that the reflective tortuosity increases for a higher drying temperature, as the binder migration blocks the electrode pores around the separator interface.[81–83] The increase in transmissive tortuosity with drying temperature can only be explained by an increase in average tortuosity. A likely origin of this effect is that the binder migration disproportionately increased the tortuosity of the separator interface more than it decreased the tortuosity towards the current collector interface. Ultimately both techniques give sufficiently similar information, and unless the user specifically requires knowledge of the average tortuosity, a reflective measurement would still be the preferred choice, as it is easier to execute and gives information about homogeneity.[71]

2.4 3D-structured electrode characterization

With increased electrode loading, the electrolyte transport within the electrode becomes increasingly important. To improve the electrode transport, 3D-structured electrodes can be manufactured, which shorten the diffusion pathway and thus improve the electrode performance.[84–93]

Figure 2.8a shows a cross-sectional sketch of a 3D-structured electrode, where the diffusion in the electrolyte-filled large pore (green center) is faster than the transport inside the (gray) electrode. Such a 3D structure introduces a new relevant parameter, the in-plane tortuosity, and can be measured using the method developed by Suthar et al.[94] In b) and c) scanning electron microscopy (SEM) images of laser-structured electrodes are shown with line and hexagonal hole structures, respectively. The laser-structuring was performed using the setup described by Habedank et al. [84]
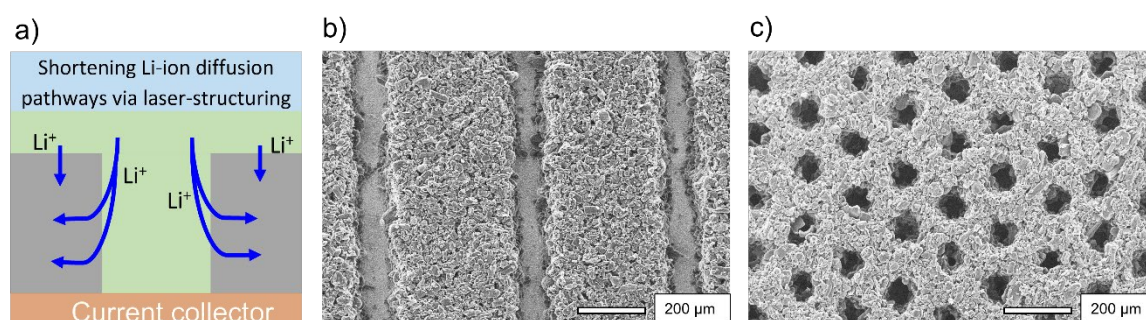

Figure 2.8 a) Sketch of the working principle of a 3D-structured electrode. The electrolyte-filled free space allows for a faster Li+ transport compared to the active material, where porosity and tortuosity increase the diffusion resistance. b) and c) show scanning electron microscopy top view images of laser-structured graphite electrodes in line pattern (b) and hexagonal hole pattern (c).

It is not surprising that opening the electrode structure improves the electrolyte transport and thus the electrode performance, especially in thick, higher-loading electrodes. The aim of this project was to i) understand if the electrode can be sensibly characterized by traditional tortuosity measurements and ii) understand the benefit of the type of structure and where their optimal improvements lie.

For tortuosity measurements, a set of graphite electrodes of around 3.4 mAh/cm^2 (~9.9 mg/cm^2 T311 (SGL):PVDF (Kynar), 95:5, ~110 µm thickness, porosity ~55%) were prepared. Some electrodes were measured in their pristine state via symmetric cells and evaluated for their tortuosity, while other electrodes were

laser structured with a hexagonal hole structure as shown in Figure 2.8c and examined via SEM for their geometry. Care was taken that the bottom of the holes showed the current collector, to allow a reconstruction of the electrode geometry in a COMSOL Multiphysics® (Comsol) model (otherwise the hole depth would not be defined, as the SEM images gives no depth information). The model was built in essence as described in section 3.1.2 but with the below specified geometries. The pristine through-plane electrode tortuosity was found to be 3.4, while the in-plane tortuosity was found to be 1.3. For the structured electrodes, three different geometries were prepared. All structures have the same hole size, as this was determined by the laser intensity parameters which were more practical to be kept constant. The average hole diameter was found to be 82 µm, with center-to-center hole distances of 140 µm, 170 µm and 200 µm, leading to a mass loss of around 30%, 20%, and 15%, respectively.

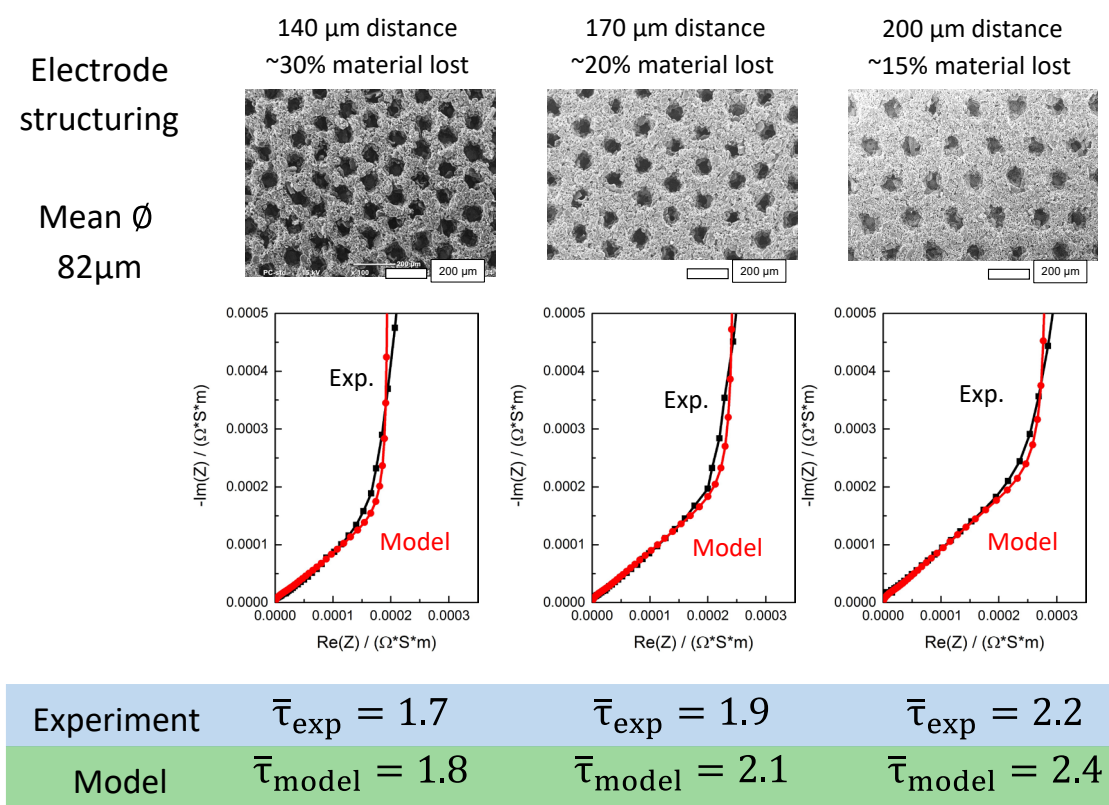|	140 µm distance ~30% material lost	170 µm distance ~20% material lost	200 µm distance ~15% material lost
Experiment	$\bar{\tau}_{exp} = 1.7$	$\bar{\tau}_{exp} = 1.9$	$\bar{\tau}_{exp} = 2.2$
Model	$\bar{\tau}_{model} = 1.8$	$\bar{\tau}_{model} = 2.1$	$\bar{\tau}_{model} = 2.4$

Figure 2.9 3D structured electrodes with mean hole diameter of 82µm. Top row: SEM images of the three different geometries with hole distances (center to center) of 140 µm, 170 µm, and 200 µm. Middle row: Nyquist plot of simulated and experimental symmetric cells showing a good agreement between the model and experiment for tortuosity determination. Bottom row: Average obtained tortuosity from both model and experiment, being in good agreement.

The 3D structures were then recreated in a 2D (lines) and 3D (hex. holes) Comsol model of the respectively identified unit cells of the geometries and evaluated for their tortuosities via simulated EIS analysis. The experimentally structured electrodes were similarly evaluated via EIS in symmetric cells. The middle row in Figure 2.9 shows the Nyquist plot of the model and experiment, which are in good agreement. The bottom row shows the obtained tortuosities which naturally are also in agreement. Since unstructured electrodes can be modeled in 1D, the tortuosity obtained of unstructured electrodes is also a 1D parameter. For the 2D and 3D geometries, the measured tortuosity becomes a form of apparent tortuosity, which combines effects of in-plane and through-plane transport.

After this validation, the model was used to identify the benefit of different geometries of 3D structures, most notably the before shown line structures and hexagonal hole structures. The hole structure was chosen as it appears to be the best structure geometrically, where a minimum of lost material might yield a maximum of performance increase. Unfortunately, the number of holes needed results in a long manufacturing time. The line structure is significantly faster, as the laser simply needs to cut through the coating in one motion and only needs to be turned off when the line ends, thus being the structure of choice for any practical applications. Also, for practical applications it is assumed that the 3D structured electrodes need to be of a specific areal capacity, which is why for the simulation the material loss was kept constant for varying 3D structure sizes.

Figure 2.10 shows the simulated mean tortuosity values for a (in a pristine state) 7.5 mAh/cm^2 graphite electrode. The high (simulated) loading was chosen since the 3D structuring works best at higher loadings, and thus differences between structures are visible more clearly.
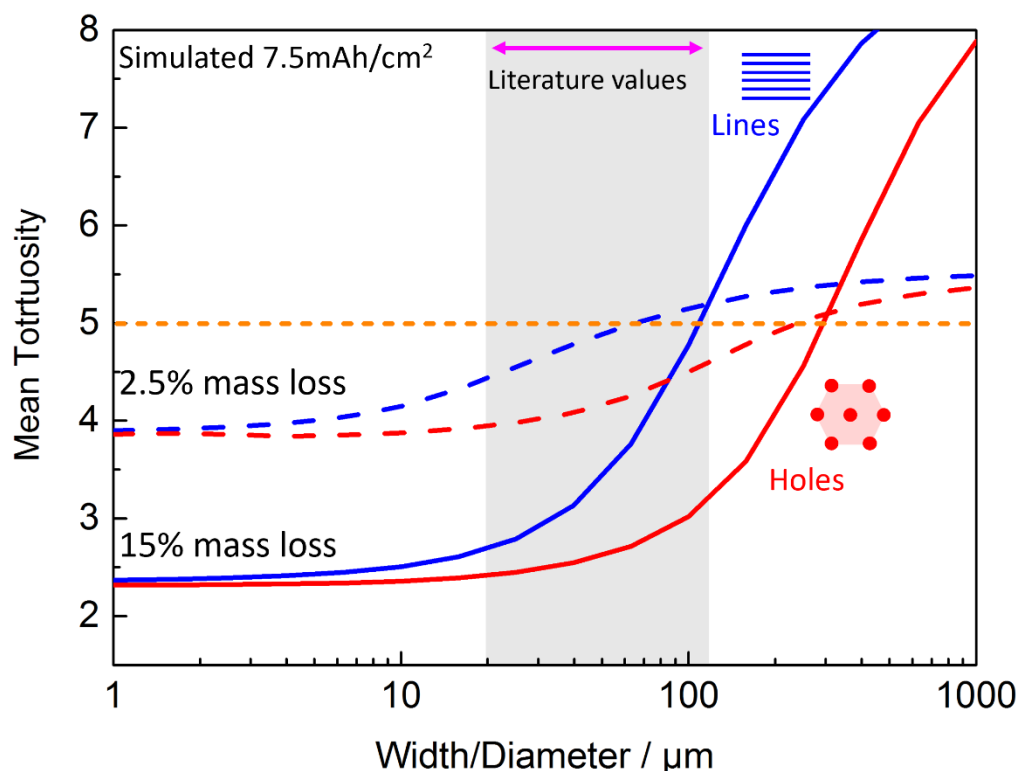
Figure 2.10 Simulated mean tortuosity values of 3D structured electrodes as a function of trench width for line structures or hole diameter for the hexagonal hole structure. For each subset, the mass loss was kept constant at either 2.5% (dashed lines) or 15% (solid lines). It is evident that to achieve similar improvements, the line structures must be finer compared to the hole structures, but both show a trend toward the same value for the finest structures which is only determined by the total mass loss. To improve the ion conduction even more, more active material must be removed from the structure.

The average through-plane tortuosity was set to 5 for the active material and the in-plane tortuosity to 1.3. The x-axis shows the channel width for line structured electrodes or the hole diameter for hole structured electrodes. Since the material loss was kept constant for each simulation subset, this practically results in a change in structure coarseness, i.e., the hole structure starts out with a few large holes and changes to many smaller holes with decreasing hole diameter. The results show that for hexagonally arranged holes the hole diameter can be significantly larger than the channel width of the lines to achieve the same improvement in average tortuosity. Since the channel width or hole diameter that can be achieved is a metric which heavily depends on the laser-quality, this is an important parameter when it comes to the practicalities of this process. The gray area indicates the range of structure size found in the literature. Assuming structure sizes of 20-50μm can be reproducibly produced, both structures could show an improvement, depending on the material lost. For practical applications, if both

electrodes are 3D structured the effect of alignment of the structures would need to be studied. Assuming only one side of the electrodes is structured, the effect of such an asymmetry in geometry on the electrochemical performance and unwanted reactions such as Li-plating needs to be studied carefully.
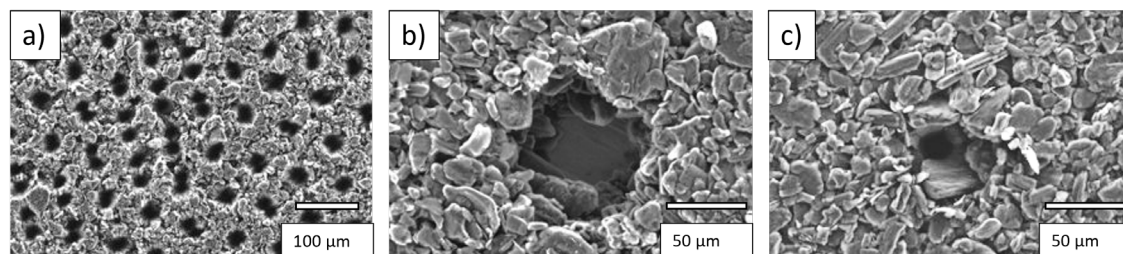

Figure 2.11 SEM images of laser structured electrodes. In a) a hexagonal shape was supposed to be visible, yet a movement of the sample due to heating from the laser caused a disorder in hole structures. b) and c) compares electrodes at ~55% and 30% porosity which were structured with the same settings. The difference in hole diameter shows the practical limit of the laser structuring process for electrodes of lower porosity.

Several practical limitations arose during the structuring process. Figure 2.11 shows SEM images of electrodes after laser structuring. In a) the electrode structure should exhibit a hexagonal structure, but the laser structuring heated the sample such that electrodes moved slightly (the copper current collector showed visible ripples on the backside, which appeared to happen due to the sample heating up) and thus ruined the pattern. Figure 2.11b and c compares two electrodes, where b) is an uncompressed electrode (~55% por.) and c) is the same type of electrode at ~30% porosity. Both electrodes were structured with the same laser settings, yet the difference in hole diameter and depth is enormous (no current collector visible in the second image). These two aspects, hole diameter and hole depth, appeared to be generally inseparable, i.e., the deeper the hole the larger the hole diameter, which makes it practically impossible to structure electrodes with varying diameter but same hole depth. The electrode loading/thickness and porosity both hugely influenced the resulting hole structure and any prolonged mild ablation led to a heating of the sample and to the effect seen in a). Thus an analysis, as it was done in Figure 2.10, was not possible to execute, as no two samples of equal capacity and differing electrode structure coarseness could be reliably manufactured.

2.5 Linking inhomogeneities in an electrode to EIS spectra

In section 3.1.2[71] the phenomenon of binder migration, causing inhomogeneous ionic resistances and the resulting effect on the EIS spectra has been studied. Following this, an effort has been made to understand if it was possible to get information on the underlying binder gradient by the appropriate fitting of the spectra of inhomogeneous electrodes. This works is based on analytical equations derived by Prof. Bharatkumar Suthar (currently at IITB, Mumbay) and are not yet published. The equations were incorporated into the MATLAB-based application ("EIS Breaker," © J. Landesfeind.). Figure 2.12 shows the different solutions.
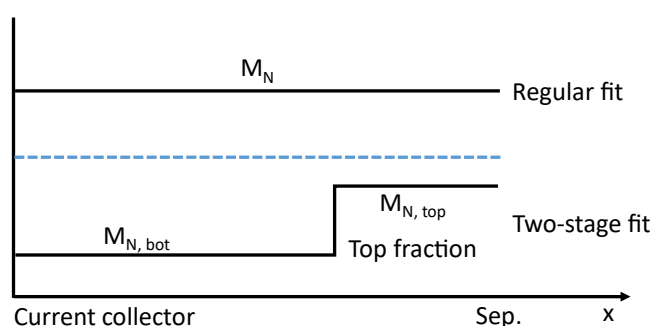

Figure 2.12 Available fit solutions for gradient electrodes to describe: a homogenous electrode (Regular fit) with only one parameter for the ionic resistance (M_N); the two-stage fit with three parameters, the separator and current collector sided resistance ($M_{N,\,top}$, $M_{N,\,bot}$, respectively) and the Top fraction which gives the fraction of the thickness of the top (separator) layer compared to the total electrode thickness.

The top of the figure gives the regular fit which only has one parameter for the MacMullin number. The two-stage fit, describes the EIS response of an electrode with two different ionic resistance regions. The solution introduces three parameters that replace the parameter of the ionic resistance, namely the top and bottom resistance as well as the top thickness fraction, i.e., the fraction of the top resistive layer thickness compared to the total electrode thickness. For example, if the top fraction is 0.25, the top 25% of the electrode exhibit the top resistance.

To test if the equations yields useful results in a practical setting, freestanding graphite electrodes with 3% PVDF binder and 12% PVDF binder with thicknesses around 270 and 55 μm and porosities of 53 and 43%, respectively, were fabricated. Since the porosities were unequal after coating, the MacMullin number, defined as $M_N = \frac{\tau}{\epsilon}$ was used as metric for the ionic resistance within the electrode. M_N was

determined as 6.2 ± 0.1 for the 3% PVDF containing electrode, which was measured for individual electrodes, and confirmed for an electrode stack of two electrodes on both sides to understand if the stacking of electrodes introduces any additional resistances. For the 12% PVDF electrodes, M_N was found to be 12.9 ± 0.5 for the single and 14.4 ± 0.1 for the double stacked electrode, showing a slight increase in resistance for electrode stacking, but not large enough to be of initial concern. The electrodes were then cross-stacked, with the 3% PVDF electrode at the bottom and the 12% PVDF electrode at the top (sep. side). This way the EIS fitting could be done on well-defined experimental data.
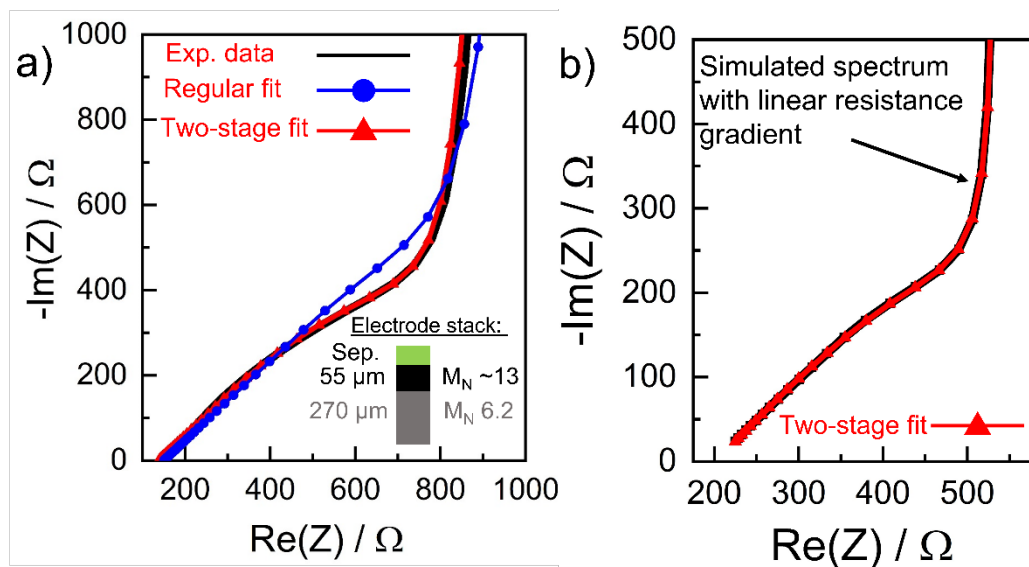

Figure 2.13 Nyquist plot of experimental and fitted symmetric cell data for a gradient electrode stack. The electrode stack is shown in the bottom right corner, with the high resistive, thinner electrode (~55 μm) at the separator interface (black box) and the lower resistive, thicker electrode (~270 μm) at the current-collector interface (grey box). The black data is the experimentally measured impedance, the blue data is a fit with a regular homogeneous TLM and the red data is the fitted spectrum with the two-stage TLM.

Figure 2.13a shows the experimental data of the electrode stack (black) with the ~270 μm thick bottom, low resistive electrode, and the ~55μm thick high resistive electrode at the top (sep. side). The blue data (circles) shows a fit made with a conventional transmission line model and gave a M_N of 9.8. The red data shows the fit with the two-stage solution, with the extracted parameters shown in Table 2.1.

Table 2.1 Electrode stack data giving the experimentally obtained values for the individual stack parts and the values obtained from the EIS data fit for the resistance at the electrode separator interface (M_N top) and the electrode current collector interface (M_N bottom) as well as the fraction of the top layer thickness compared to the total electrode thickness (Top fraction)

Variable	Exp. Measured	Two-stage fit	Error
M_N top	12.9-14.4	13	<10%
M_N bottom	6.2	6.7	8%
Top fraction	0.17	0.24	41%
$M_{N,top}/M_{N,bot}$	2.1-2.3	1.96	

The fitted resistance values are in good agreement with the experimentally obtained individual resistances, yet the top fraction data gives a large error and showed to be not sensitive enough to give reliable results, as the chosen frequency range had a significant influence on the extracted data. While the two-step gradient equation better represents the EIS data for inhomogeneous cells, it was ultimately not sensitive enough to yield reliable information on the underlying resistance gradient. This is evident in Figure 2.13b which shows a simulated linear resistance gradient (simulation performed as shown in 3.1.2[71]) and the corresponding two-stage fit which overlaps with the spectrum nicely. Thus, it is evident that the Nyquist spectra of gradient electrodes are not necessarily (practically) unique, and that the two-stage fit yields reasonably confident fit results for other types of inhogmogeneous data.

3 Results

This chapter contains the published work and manuscripts which are to be submitted, and is sectioned into two parts. Section 3.1 contains work designed to understand the practical and theoretical issues pertaining to the analysis of battery electrodes via EIS. Thus, 3.1.1 describes the artefacts that can arise when trying to determine the impedance of a Li-ion battery electrode in a half-cell configuration, and gives a practical solution to circumvent such artefacts. Another complexity in EIS analysis is presented when the assumption of homogeneity is not fulfilled, a topic which is discussed for the blocking-impedance analysis of porous electrodes in section 3.1.2. When the electrode is measured under faradaic (non-blocking) conditions, the relative size of the kinetic to the transport resistance plays a major role in the interpretation of the EIS data and the behavior of the current distribution within the electrode, which is described in detail in section 3.1.3.

Section 3.2 gives examples for a more practical use of EIS. In 3.2.1, silicon and graphite electrodes of practical areal capacities are compared for their impedances and their charge rate capability at different temperatures. To gain further understanding of the influence of Li^+ concentration gradients on the kinetics of active materials, section 3.2.2 and 3.2.3 examine the kinetics of a typical cathode active material NMC 111 and of the commonly used anode active material graphite, respectively. The NMC 111 kinetic analysis more closely follows a comparison to theoretical battery kinetics, while the graphite analysis is focused on a more fundamental phenomenological understanding of the kinetic behavior of the SEI.

3.1 Porous electrode impedance analysis

3.1.1 Simple Way of Making Free-Standing Battery Electrodes and their Use in Enabling Half-Cell Impedance Measurements via µ-Reference Electrode

The article entitled "Simple Way of Making Free-Standing Battery Electrodes and their Use in Enabling Half-Cell Impedance Measurements via µ-Reference Electrode" was submitted to the peer-reviewed Journal of the Electrochemical Society in March 2020 and published in June 2020 as an open-access article under the terms of the Creative Commons Attribution Non-Commercial No Derivates 4.0 License. The permanent web link can be found under: https://iopscience.iop.org/article/10.1149/1945-7111/ab9b93/meta.

The objective of the study was to enable the acquisition of impedance spectra of individual working electrodes in a half-cell configuration (i.e., with a lithium metal counter electrode) via µ-reference electrode, which had been observed to show artefacts. By measuring an equivalent circuit made of capacitors and resistors, which represents the general build-up of a three-electrode electrochemical cell, it was found that the artefacts arise due to the high impedance of the µ-reference electrode. It was assumed that this is a problem of the interplay between the cell and the potentiostat, as it was shown by Raijmaker et al.[95] that for high reference electrode impedances the working electrode impedance can be influenced by the counter electrode impedance. In the case of the µ-reference electrode based on a gold wire (GWRE), the artefacts only occur when the counter electrode impedance is significantly larger than the working electrode impedance, which is typically the case for half-cell designs compared to full-cells. To allow half-cell impedance measurements, the counter electrode impedance needs to be decreased.

This was achieved by developing and using free-standing graphite (FSG) electrodes which are attached to the Li-metal counter electrode. Free-standing electrodes can be made by coating a layer of carboxymethyl cellulose (CMC)-binder on top of a copper foil and then coating a PVDF-based electrode on top of the CMC film. Once dry, the coating is immersed in water or ethanol, the former dissolves the CMC film and the latter appears to help sever the electrode from the sheet, which can then simply be peeled off the electrode. In the half-cell, the FSG electrode attached to the

Li-metal is lithiated once in contact with electrolyte. The electrode then shows a low, stable impedance at 0 V vs. Li$^+$/Li, allowing for an artefact free impedance analysis of typical anode or cathode electrodes. For prolonged cycling, the Li/FSG counter electrode develops a contact resistance and thus can unfortunately not be used over prolonged periods of time.

Author contributions

R.M. conducted the measurements and evaluated the data. B.S. and R.M. developed the procedure to produce free-standing electrodes. R.M. wrote the manuscript. R.M., B.S. and H.A.G. discussed the results and revised the manuscript.

Simple Way of Making Free-Standing Battery Electrodes and their Use in Enabling Half-Cell Impedance Measurements via μ-Reference Electrode

Robert Morasch,[z] Bharatkumar Suthar,[*,a] and Hubert A. Gasteiger[**]

Chair of Technical Electrochemistry, Department of Chemistry and Catalysis Research Center, Technical University of Munich, Munich, Germany

Free-standing electrodes can be useful for a plethora of diagnostic measurements, as they allow transmissive measurements, stacking of electrodes, and/or measurements where the current collector would be disturbing the signal. Another advantage displayed in this publication is their use in Li-ion battery half-cells to decrease and stabilize the impedance of the counter electrode that is usually made of metallic lithium, allowing to conduct electrochemical impedance spectroscopy of a battery-type working electrode via μ-reference electrode which would otherwise show artefacts over a wide range of frequencies. Using measurements on an equivalent circuit mimicking a Li-ion battery half-cell with a μ-reference electrode we show how such artefacts arise from the large resistance in the μ-reference electrode and the imbalance in working and counter electrode resistance. We also show how the use of a free-standing graphite electrode attached to the Li-metal counter electrode (Li/FSG) reduces the counter electrode resistance and allows an artefact-free impedance measurement of the working electrode via a μ-reference electrode. Finally, we show the stability of the Li/FSG electrode and compare it to a Li-metal electrode.

The choice of battery cell configuration is important when evaluating the electrochemical properties of anode or cathode active materials with conventional electrolytes or with novel electrolytes/ additives for lithium-ion batteries. A convenient initial evaluation can be done using a so-called half-cell configuration with a metallic lithium (Li-metal) counter electrode (CE), providing direct information on the electrochemical properties of the working electrode (WE) active material while, at least ideally, minimizing the influence of the counter electrode on the active material under investigation. A drawback of this approach is that it complicates the analysis of electrochemical impedance spectroscopy (EIS) data, since the Li-metal CE surface morphology/area and, consequently, its impedance varies substantially over the course of cycling (particularly over the first few cycles) as well as over time when no current is applied.[1–3] Therefore, the cell impedance evolution obtained from half-cell measurements with a Li-metal CE does not allow for a rigorous determination of the working electrode impedance, as the impedance of the Li-metal CE cannot be reliably subtracted from the cell impedance. This can only be done by either assembling so-called symmetric cells[4–7] (i.e., cells built with nominally identical electrodes obtained after having subjected them to different charge/ discharge procedures) or by making use of a micro-reference electrode (μ-RE). While the former approach requires the experimentally cumbersome harvesting of cycled electrodes and their reassembly in symmetric cells, EIS measurements with μ-REs are non-invasive and more convenient.

In our recent work, Solchenbach et al. had demonstrated the use of a gold wire μ-RE (GWRE)[8] with which one can monitor the impedance evolution of each individual electrode in a full-cell;[8–10] however, so far we could not obtain artefact-free WE impedance spectra with the GWRE technique in a half-cell configuration with a Li-metal CE. As we will show here, this is related to the high impedance of μ-REs (on account of their small cross sectional area), which can result in measurement artefacts. Gómez-Cámer et al.[11] already demonstrated that artefacts can arise when using reference electrodes with high impedance and suggested that activation overpotentials play a role in successfully using a reference electrode for EIS measurements. In the case of battery full-cells consisting of NCM (LiNi$_a$Co$_b$Mn$_c$O$_2$, with $a + b + c = 1$) and graphite, Raijmakers et al.,[12] also showed that due to the interplay of the μ-RE impedance and internal impedances of the potentiostat, artefacts can occur at high frequencies (in the kHz regime). Studies done by other groups suggest additional artefacts caused by improper reference electrode positioning, which can produce inhomogeneities in current or potential response.[13–15] A review for Li-ion battery reference electrodes can be found in Ref. 16.

Table I summarizes the above-mentioned advantages and disadvantages of using symmetric cells and -μ-RE for EIS.

In this publication we investigated the source of error for artefacts in EIS measurements via a μ-RE when using a Li-metal counter electrode and developed a method that allows artefact-free EIS measurements of the WE via a μ-RE in a half-cell configuration (i.e., with a working electrode and a Li-metal counter electrode).

We will show that impedance spectra obtained with a μ-reference electrode in a half-cell configuration can show artefacts over a broad frequency range (kHz to mHz). In order to investigate their origin, we conducted comparative EIS measurements on model equivalent circuits composed of a set of actual resistors and capacitors that mimic the half-cell resistor and capacitor elements, but in the absence of any electrochemical reactions. EIS analysis of these model equivalent circuits shows that similar artefacts in the low-frequency region of the impedance spectra occur as observed for actual half-cell impedance spectra, indicating that these artefacts arise from an interplay of potentiostat impedances and cell impedances, whereby the former are generally unknown to the user. Based on the model equivalent circuit measurements, these low-frequency artefacts in half-cells with a Li-metal CE could be eliminated if one were able to substantially decrease the Li-metal impedance. We will show that this can be accomplished experimentally by inserting a free-standing graphite electrode (FSG) between the Li-metal CE and the separator, which establishes a low-impedance counter electrode at a stable Li-metal potential (referred to as Li/FSG). This allows for the acquisition of working electrode impedance spectra that are free of low-frequency artefacts in a cell configuration that essentially represents that of a half-cell with a Li-metal counter electrode.

*Electrochemical Society Member.
**Electrochemical Society Fellow.
aPresent address: Department of Chemical Engineering, Indian Institute of Technology Bombay, Mumbai 400076, India.
zE-mail: robert.morasch@tum.de

Table I. Overview of the cardinal advantages and disadvantages of electrochemical impedance measurements via symmetric cells and cells with a μ-RE (WE = working electrode; CE = counter electrode).

	Advantages	Disadvantages
symmetric cell	impedance determination of anode or cathode	requires electrode harvesting
μ-RE	operando impedance meas. of individual electrodes	measurement artefacts when using a Li-metal CE
μ-RE with modified Li-metal CE (this publication)	artefact-free measurements of the WE via the μ-RE	requires additional assembly step

Experimental

Preparation of free-standing electrodes.—The following describes an easy approach to produce free-standing PVDF-bonded electrodes. Other methods to produce free-standing electrodes can be found elsewhere.[17,18] The two here proposed methods (acc. to procedures A or B, see Fig. 1) are suitable to produce free-standing PVDF-bonded electrodes of both graphite and NCM (or other cathode active materials), whereby for the latter only procedure A can be used, as electrodes with cathode active materials generally should not be immersed in water. The first step in preparing free-standing electrodes is coating a thin layer of sodium carboxymethyl cellulose (CMC, Sigma Aldrich) binder onto a current collector foil. The CMC binder was mixed at a CMC to H_2O ratio of 1:25 (wt:wt) and coated at a wet film thickness of 30 μm onto a copper current collector foil (MTI, 12 μm) attached to a glass plate using a gap bar coater (RK PrintCoat Instruments, UK). To prepare a free-standing graphite electrode, graphite (T311 type from SGL, with 19 μm D50 and 3 $m^2 g^{-1}$) and polymer binder (polyvinylidene fluoride (PVDF), Arkema) at a ratio of 95:5 (wt:wt) were mixed with N-Methyl-2-pyrrolidone (NMP, Sigma Aldrich, anhydrous, 99.5%) at a solid to liquid ratio of 5:4 (wt:wt) in a planetary mixer (Thinky ARV-310) at 2000 rpm for five minutes. The prepared graphite slurries were coated onto the CMC-coated copper current collector at a wet film thickness of 200 μm. Free-standing cathode electrodes can be prepared analogously.

Since the CMC layer is not soluble in NMP, it serves to block the PVDF binder of the electrode coated on top of it from adhering to the current collector foil. The dried electrode is then put into a bath of ethanol (see panel A1 in Fig. 1, left-hand-side) or water (see panel B1 in Fig. 1, right-hand-side), whereby the latter is only recommended for materials stable in H_2O. Since CMC is not soluble in ethanol, the CMC film is not dissolved, but its surface becomes non-adherent and the electrode can be peeled or swiped off the surface with little effort (see panels A1-3 in Fig. 1). For graphite electrodes, the electrode sheet can also be immersed in a water bath in which the CMC layer dissolves, leaving the electrode detached from the surface, which can also easily be done with already punched electrodes (see panels B1-3 in Fig. 1). As CMC is commonly used in battery electrodes, residual CMC in the electrode is of little concern in battery tests; however, if necessary, it could be removed in an additional washing step. Additionally heating the water bath is possible to speed up the dissolution process of the CMC but no heat treatment was performed for this work. For the free-standing graphite (FSG) electrodes used in this study, only procedure A was used.

The thickness of the here prepared dried and uncompressed free-standing graphite electrodes and of conventional graphite working electrodes (prepared as above, but without the CMC interlayer) was ~105 μm (±2%), corresponding to graphite loadings of ~9.8 mg cm^{-2} (±2%) with an areal capacity of ~3.4 mAh cm^{-2} (calculated for a theoretical graphite capacity of 350 mAh g^{-1}). The electrodes were not further compressed/calendered, and their porosity was ~55% (based on thickness and areal weight measurements). The dried electrodes were punched out to a diameter of 10.95 mm (equating to an area of ~0.94 cm^2) using an electrode punch (Hohsen Corp. OSAKA, Japan). Alternatively, a carbon paper (5% hydrophobized ~360 μm thick Toray carbon fiber paper T120, Toray) was used as free-standing electrode and applied as received. The Carbon paper has a roughness factor of ~18 cm$^2_{BET}$ cm^{-2}, based on ~7 mg$_{carbon}$ cm^{-2} areal weight and ~0.25 m^2 g^{-1} BET area while the FSG electrode has a roughness factor of ~300 cm$^2_{BET}$ cm^{-2}, based on ~9.8 mg$_{graphite}$ cm^{-2} areal weight and ~3 m^2 g^{-1} BET area.

Equivalent circuit.—The equivalent circuit for the impedance measurements shown in Fig. 2b was soldered according to the circuit description of Fig. 2a, using carbon film resistors (Conrad Electronic
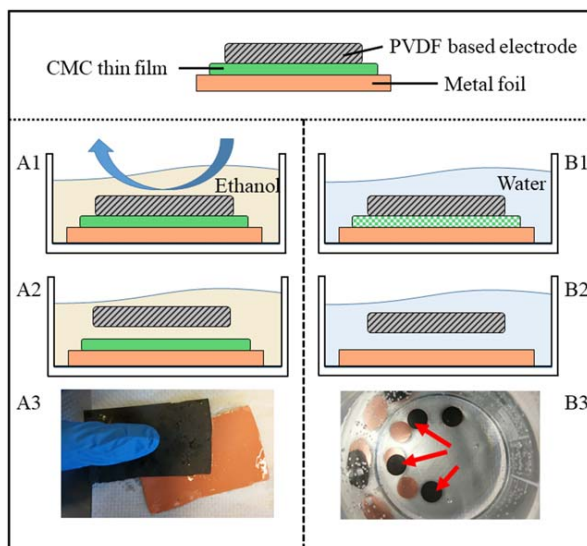

Figure 1. Depiction of the free-standing electrode preparation process based on a current collector foil (here copper foil) coated with a CMC layer onto which subsequently a PVDF-bonded electrode is coated (here graphite). Process A (left-hand-side): Immersion of the copper/CMC/graphite assembly into ethanol (A1), which causes a loss of adhesion between the graphite electrode and the CMC film, without dissolving the CMC film (A2). The electrode can then be swiped off the current collector with little effort, shown in panel A3 for a graphite electrode. Process B (right-hand-side): Alternatively, the electrode can be immersed in water (B1) to dissolve the CMC film, leading to the detachment of the electrode (B2), as seen in panel B3 for graphite electrodes punched at 10.95 mm diameter (red arrows indicate detached electrodes).

GmbH, Germany) and electrolyte (⩾1 μF) or film (1 nF) capacitors (Conrad Electronic GmbH, Germany).

Cell assembly, charge/discharge cycling, and impedance measurement.—For electrochemical impedance analysis, a three-electrode cell setup (Swagelok® T-cell) with a gold-wire reference electrode (GWRE, described in more detail in Fig. 1b in Ref. 8) was used. The cells were built inside an argon filled glove box (MBraun, 25 °C ± 1 °C, oxygen and water content <0.1 ppm, Ar 5.0, Westfalen). All cell parts were dried at 120 °C in a vacuum oven (Büchi, Switzerland) for 8 h before being transferred into an Ar-filled glovebox.

The cells were assembled with a graphite working electrode (areal capacity ~3.4 mAh cm^{-2}), two porous glass fiber separators with a diameter of 11 mm (VWR, 250 μm uncompressed thickness, 90% porosity), and a counter electrode consisting of either a metallic lithium foil (0.45 mm thickness and 11 mm diameter, Rockwood Lithium) or a free-standing graphite electrode firmly attached to the metallic lithium foil (referred to as Li/FSG). For cycling stability tests and impedance analysis of the Li-metal or the Li/FSG electrodes, symmetric cells in a three-electrode cell setup as described above were assembled. 80 μl of LP57 electrolyte (1 M LiPF$_6$ in EC:EMC 3:7 (wt:wt), battery grade, BASF) were added to the cells. Using a potentiostat (Bio-Logic Science Instruments, France), the gold-wire reference electrode was lithiated at 150 nA for 1 h via the Li-metal or Li/FSG counter electrode in a temperature-controlled chamber (25 °C, Binder).

The cycling protocol started with a 3 h open circuit voltage phase to allow for complete wetting of the electrodes and stabilization of the Li/FSG counter electrode. Lithiation of the graphite working electrode was performed galvanostatically (constant current lithiation) at C/10 to 40 mV vs Li$^+$/Li without prior formation. Potentiostatic electrochemical impedance measurements over the course of cycling were performed at open circuit voltage (OCV) at
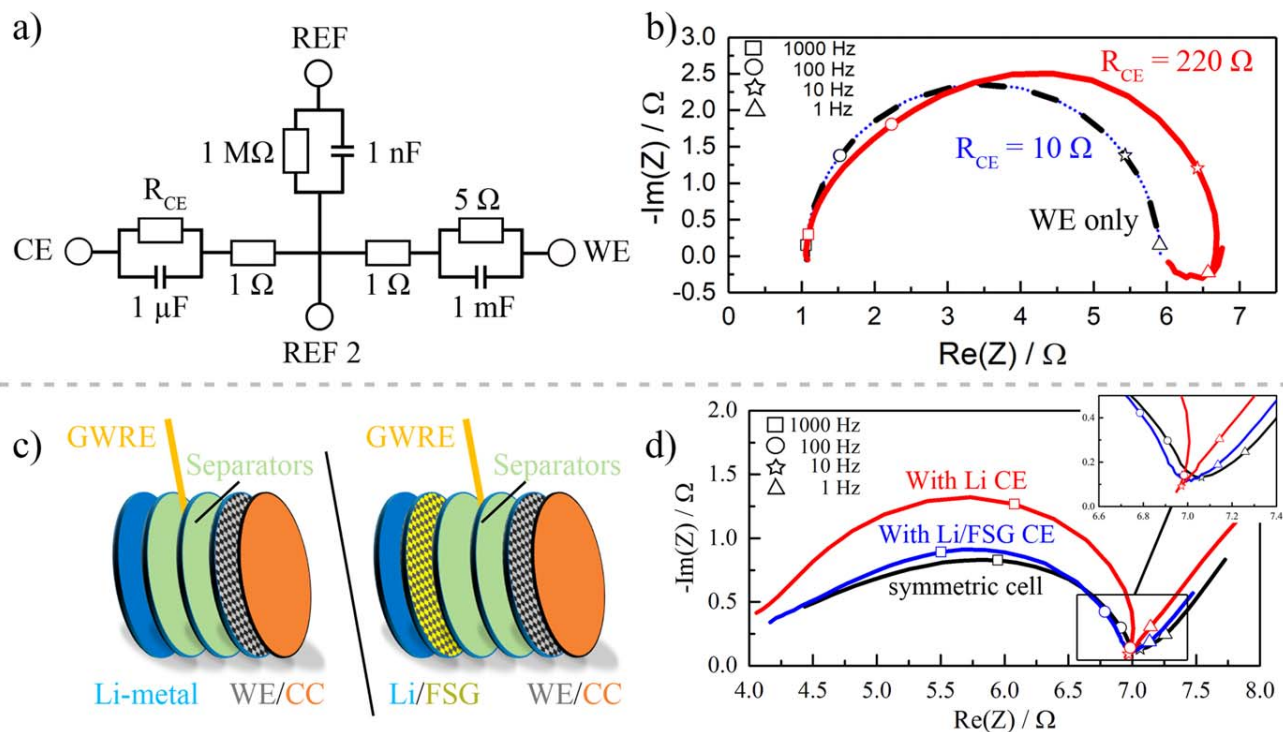
Figure 2. Comparison of the working electrode impedance (30 kHz to 0.1 Hz) of model equivalent circuits and of the graphite working electrode (at 100% SOC) in half-cells with a GWRE and with different counter electrodes. (a) Model equivalent circuit mimicking a lithium-ion battery half-cell with a gold-wire μ-RE with the indicated resistance and capacitance values (for choice of values see text), using a CE resistance (R_{CE}) of either 220 Ω or 10 Ω. (b) Impedance response of the WE of the model equivalent circuit with R_{CE} = 220 Ω (red) or R_{CE} = 10 Ω (dotted blue line), and comparison of the impedance responses to that of the individually measured WE (dashed black line; perfectly overlapping with the dotted blue line), where the RE and CE cables of the potentiostat are not connected to contacts CE and REF, respectively but are instead both connected to the contact marked as REF 2 in Fig. 2a). (c) Half-cell configuration with a graphite electrode (gray), a GWRE (yellow line) sandwiched between two separators (green), and either a Li-metal CE (blue; left sketch) or a Li-metal CE with an attached FSG electrode (yellow; right sketch). (d) Impedance response of the graphite WE obtained by either one of the two configurations shown in (c), i.e., either with a Li-metal CE (Li-CE, red line) or with an Li/FSG CE (blue line). For comparison, the black line shows the impedance response of the graphite WE in a symmetric cell (overall cell impedance divided by two).

100% state-of-charge (SOC) from 30 kHz to 0.1 Hz and with an excitation of 10 mV. For symmetric cell measurements, graphite electrodes prepared as mentioned above were charged to 40 mV, harvested, rinsed three times with 0.1 ml of diethylene carbonate (BASF SE, Germany), and re-assembled into symmetric cells using the above described assembly protocol but without a GWRE.

Results and Discussion

Impedance artefacts observed with model equivalent circuits.— There are multiple sources of error for impedance measurements, ranging from the potentiostat to artefacts that may arise from an individual cell design or cell chemistry.[11–15] To exclude any source of artefacts that may be caused by the three-electrode T-cell setup or from electrochemical phenomena in the half-cell, the cell setup was mimicked as a model equivalent circuit using actual resistors and capacitors, allowing us to probe whether the potentiostat controls circuitry might lead to impedance artefacts.

Figure 2a shows the simplified equivalent circuit that represents a lithium-ion battery half-cell with a gold wire μ-reference electrode. Each of the three electrodes is represented by a parallel resistor/capacitor element (further on referred to as R/C element) with approximate resistance and capacitance values that represent those of a lithium-ion battery half-cell composed of a μ-RE, a Li-metal CE, a conventional graphite WE, and a separator:

(1) The resistance and capacitance of the here used μ-RE (the GWRE) were measured to be on the order of 10^6 Ω and 1 nF, respectively, values which were used in the REF-branch of the model equivalent circuit (see top branch in Fig. 2a) and which

can be rationalized by the very small GWRE cross sectional area of $\sim 20 \times 10^{-6}$ cm^2 (this equates to a reasonable GWRE charge transfer resistance of 20 $\Omega \cdot$cm^2).

(2) The Li-metal CE resistance was measured to be on the order of 10^2 Ω (based on Li/Li symmetric cell measurements, see Fig. 3a, red and green lines) and its capacitance was measured to be on the order of 1 μF (calculated from the semicircle apex at 1077 Hz of the Li-metal impedance response, red line Fig. 3a);[8] both values are consistent with previous measurements.[8] Thus, the capacitance for the Li-metal CE part of the model equivalent circuit (left branch in Fig. 2a) was set to 1 μF, while its resistance was set to R_{CE} = 220 Ω. However, in order to investigate the effect of a lower CE resistance on the impedance response of the model equivalent circuit, we also conducted experiments with a resistor of R_{CE} = 10 Ω.

(3) The graphite working electrode resistance was approximated to be on the order of 5 Ω (see right branch in Fig. 2a), based on previous measurements with the same graphite material which showed overall graphite anode low-frequency resistances of ~ 2-4 Ω[8,10] for ~ 1.5-fold lower loadings. The capacitance was set to 1 mF, representing the large surface area of a standard battery electrode (the frequency of the data point closest to the apex in Fig. 2b [dashed black and dotted blue line] is 35 Hz).

(4) Finally, the commonly observed overall resistance for the separator of ~ 2 Ω[10] was divided into two 1 Ω resistances (see center part of the circuit in Fig. 2a).
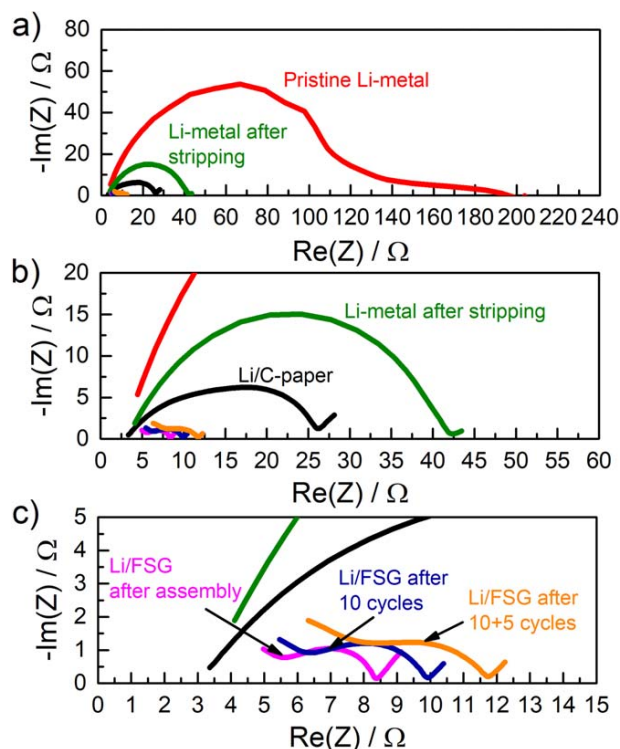
Figure 3. Nyquist plots at different levels of magnification, showing the WE impedance response obtained by means of a μ-RE in symmetric Li//Li, Li/FSG//Li/FSG, or Li/C-paper//Li/C-paper cells. (a) Impedance response of a pristine Li-metal WE, measured ~3 h after assembly, with a low-frequency resistance (LFR) of ~200 Ω (red lines). After Li-stripping at 0.32 mA cm^{-2}, the Li-metal LFR is significantly reduced to ~40 Ω (green lines). (b) Zoom of(a), illustrating the lowering of the LFR to ~25 Ω (corrected by the HFR) when a carbon fiber paper is attached to the Li-metal (Li/C-paper; black lines), measured ~3 h after assembly. (c) Zoom of (b), depicting the impedance response of the Li/FSG WE measured ~3 h after assembly (magenta lines) and showing an LFR of ~3–4 Ω (corrected for the HFR and R$_{contact}$); the LFR of the Li/FSG WE increases gradually after 10 cycles with 10 h of Li-stripping and Li-plating at ±0.21 mA cm^{-2} (blue lines), and after 5 additional cycles at ±0.42 mA cm^{-2} (orange lines).

The model equivalent circuit (Fig. 2a) was measured with two different resistance values for the counter electrode, namely with R$_{CE}$ = 220 Ω to represent the typical value of a Li-metal CE (see above), and with a substantially lower value of R$_{CE}$ = 10 Ω. Figure 2b shows the resulting Nyquist plots for the WE impedance measured via the reference electrode terminal (i.e., the RE cable of the potentiostat is connected to the contact marked REF in Fig. 2a; WE and CE cables are connected to the contacts marked WE and CE, respectively). For R$_{CE}$ = 220 Ω (red line), the WE impedance response (red line in Fig. 2b) shows an "overshoot" for frequencies below 110 Hz if compared to the expected semi-circle shape obtained when directly measuring the R/C circuit representing the working electrode (dashed black line; here, the RE and CE cables of the potentiostat are connected both to the contact marked REF 2 in Fig. 2a). Furthermore, a non-physical "back-looping" of the low-frequency branch is observed towards the lowest measured frequencies (i.e., near 0.1 Hz; see red line). Surprisingly, lowering the CE resistance to R$_{CE}$ = 10 Ω gives the correct response of the impedance measurement (compare dotted blue and dashed black line). This is unexpected, as the magnitude of the counter electrode impedance should not influence the impedance response of the WE measured via a reference electrode. The exact reason for this artefact is not known, but we presume this to be an effect caused by the large impedance of the reference electrode in combination with the

unknown internal impedances of the potentiostat, similarly to the descriptions in Ref. 12 Other explanations for the existence of impedance artefacts relating to the cell geometry and the reference electrode location[12–15] can be excluded, as the measurement on the model equivalent circuit is not affected by such influences. Hence, the correct impedance response with a high impedance μ-RE can be obtained by decreasing the value of the CE resistance, so that it is of a similar order of magnitude as that of the WE.

Graphite working electrode impedances in half-cells using a μ-RE.—The following section describes an approach to minimize and stabilize the impedance response of the Li-metal CE in order to allow for artefact-free EIS measurements of the WE using a μ-RE in a half-cell setup.

The impedance artefacts observed with the model equivalent circuit explain why artefact-free impedances can be obtained in full-cells with a μ-RE,[8–10] as there the WE and the CE have comparable impedances. On the other hand, it also explains why we so far had not been able to acquire artefact-free WE impedances in half-cells with a Li-metal CE, as there the impedance of the WE is typically $10^1 - 10^2$ times larger than that of the CE (see estimates above). The latter is illustrated by the graphite WE impedance response obtained for a half-cell with a GWRE and with a Li-metal CE (red line in Fig. 2d; cell configuration shown in the left panel of Fig. 2c), where a back-looping of the Nyquist plot near the low-frequency region occurs, rather similar to what was observed for the model equivalent circuit when R$_{CE}$ ≫ R$_{WE}$ (red line in Fig. 2b).

As mentioned in the introduction, half-cell measurements with a Li-metal CE provide valuable insights when evaluating new/modified anode or cathode active materials as working electrode, since the effect of a loss of cyclable lithium can be avoided by the large lithium excess and since the CE potential is well-defined (at least at low current densities, i.e., at low charge/discharge rates). However, in order to also enable an evaluation of the WE impedance with a μ-RE (i.e., in-situ, without the need to reassemble symmetric cells), the impedance of the Li-metal CE would need to be substantially reduced. This can be achieved by attaching a free-standing graphite electrode to the Li-metal surface, according to the cell configuration shown in the right-hand panel of Fig. 2c. Once the cell is filled with electrolyte, the free-standing graphite in contact with the metallic lithium (Li/FSG) is immediately lithiated and reaches a stable potential of 0 V vs Li$^+$/Li within ~3 h. At the same time, the largely increased interfacial surface area of the Li/FSG vs. the Li-metal CE leads to a drastic reduction of the CE impedance (as will be shown below), which should enable the acquisition of artefact-free WE impedances in a half-cell with a μ-RE and an Li/FSG CE. That this is indeed the case is shown by the graphite WE impedance response when using a GWRE and a low-impedance Li/FSG CE, and by comparing it to the symmetric cell measurement (blue and black line in Fig. 2d), where the back-looping of the Nyquist plot near the low-frequency region does not anymore appear, as expected on the basis of the model equivalent circuit experiments (blue line in Fig. 2b). This demonstrates that artefact-free in-situ WE impedance data can be obtained in a half-cell configuration, when a FSG is attached to a conventional Li-metal CE to lower its impedance. The apex frequency values of the measured graphite impedances for all three measurements in Fig. 2d (around 1 kHz) are more than one order of magnitude higher than the apex of the equivalent circuit measurements in Fig. 2b (around 35 Hz). This is the result of the more complex impedance of the graphite electrode which does not only include the charge transfer resistance, but also the pore resistances from the electrolyte within the pores of the graphite electrode as well as the solid electrolyte interphase. A detailed analysis of the graphite impedance will be shown in a later publication. In a recent work, we had also shown that the free-standing electrode concept can equally well be applied to determine the working electrode impedance in sodium-ion battery half-cells, using carbon paper attached to metallic sodium as the counter electrode.[19]

44

Impedances of Li-metal, Li/FSG, and Li/C-paper electrodes.— As the resistance of the CE is an important factor in enabling artefact-free EIS measurements of the WE via a μ-RE, we compared three different CE designs in order to give an overview over the range of resistance for different electrode designs: (i) lithium metal (referred to as Li-metal), (ii) carbon paper attached to Li-metal (referred to as Li/C-paper), and (iii) a FSG electrode attached to Li-metal (referred to as Li/FSG).

In order to obtain estimates for the impedance of a Li-metal electrode, a Li/FSG electrode, and a Li/C-paper, symmetric cells (i.e., Li//Li, Li/FSG//Li/FSG, and Li/C-paper//Li/C-paper cells) equipped with a GWRE were assembled. The impedance response (potentiostatic at OCV) of the working electrode (i.e., one of the two electrodes in the cell) was recorded using the GWRE. As shown in Fig. 3a, the low-frequency resistance (LFR, corrected by the high-frequency resistance (HFR)) of the pristine Li-metal electrode is ~200 Ω (red lines) and gets reduced substantially to ~40 Ω (green lines) after 5 h of Li-stripping at 0.32 mA cm^{-2} (for the graphite WE used in this study, this would correspond to a C-rate of ~0.1 h^{-1}). We attribute the drastic change in the lithium metal impedance to the change in lithium surface area after stripping, highlighting why cell impedance measurements of half-cells with a Li-metal CE and without a reference electrode do not allow to quantify the impedance of the WE. Figure 3b shows the impedance response of a Li/C-paper electrode (black line), which is a quick and easy alternative to a free-standing graphite electrode, as it is commercially available and can be applied as-received. While its LFR is lower than that of Li-metal (~25 Ω), it is still ~7 times larger compared to that of the pristine Li/FSG electrode (~3–4 Ω; see magenta lines in Fig. 3c), in part due to the roughly one order of magnitude smaller surface area of the C-paper (see experimental section).

Owing to the very low impedance of the Li/FSG electrode, the presence of a contact resistance ($R_{contact}$) can be discerned at high frequencies, which must be due to an imperfect lamination between the FSG and the Li-metal, so that the LFR for the Li/FSG electrode contains contributions from this contact resistance. Nevertheless, the overall LFR of the Li/FSG electrode is roughly an order of magnitude lower than that of Li-metal and rather similar to the LFR of a conventional graphite electrode (~8 Ω, see black line in Fig. 2d).

In order to evaluate the variation of the Li/FSG electrode impedance with cycling, the Li/FSG//Li/FSG cell was additionally cycled 10 times at ±0.21 mA cm^{-2} for 10 h (10 h stripping and 10 h plating per cycle). The blue line in Fig. 3c shows the impedance response after 10 cycles. The electrode impedance is slightly larger, with an additional shift to higher values attributed to an increase in electrical contact resistance between the FSG and the Li-metal (this could likely be suppressed by a higher cell compression, which in the current experiments is ~2 bar, set by a spring).[8] After 5 additional cycles at ±0.42 mA cm^{-2} for 5 h (i.e., 5 h stripping and 5 h plating per cycle), the impedance again shifts to the right, attributed to an additional increase in contact resistance. Overall, the Li/FSG electrode shows a slow increase in impedance for low current cycling; its impedance is independent of the state-of-charge of the working electrode, since on account of the quasi unlimited Li-supply from the Li-metal, the Li/FSG potential remains at 0 V vs Li$^+$/Li at OCV, where the impedance data are acquired. In this configuration, the WE impedance can in principle be estimated even from *cell* impedances acquired for half-cells with an Li/FSG CE and without a μ-RE over the course of a few cycles, if the impedance response of the Li/FSG electrode was measured independently beforehand, e.g., in symmetric cells. In this case, any reversibly measured changes in *cell* impedance can be attributed to changes of the working electrode impedance, allowing the user to extract useful information from a half-cell impedance measurement even without reference electrode. Such a setup was not used in this publication and it is of the discretion of the individual reader to determine its validity for individual setups.

Choosing the proper type of free-standing electrode.— As shown in this publication, the choice of CE affects the ability to perform artefact-free impedance analysis of the WE via a μ-RE. Two options of free-standing electrode to minimize the CE impedance and to enable the measurement of the WE impedance were presented here. First, the free-standing graphite electrode (FSG) attached to a Li-metal electrode (Li/FSG) shows the lowest impedance and is therefore best suited to allow the use of a μ-RE for any commercial Li-ion battery active materials known to the authors. This is true for a free-standing electrode of a reasonable loading of 1–3 mAh cm^{-2} comprised of commercially available graphite for Li-ion batteries. Its drawback, however, are the additional steps needed to produce the electrode and during cell assembly.

Using a carbon paper in contact with Li-metal (Li/C-paper) is more convenient, as carbon papers are commercially available and can be used as received. The drawback of the Li/C-paper configuration is its generally higher impedance (depending on the type of carbon paper), which is why it may not be suited for measurements of all types of working electrodes.

In all cases, however, the individual user needs to know the resistance range of the working electrode to be examined and should, for best practice, ensure that the counter electrode resistance is always equal or lower in resistance compared to the WE as the impedance ratio of WE and CE that marks the onset of artefacts is not know and may depend heavily on the cell setup and potentiostat.

Regarding the choice of Li-metal, any commercially available Li-metal films with thickness of 75 μm and above are sufficiently overbalanced to serve as Li-source for this setup.

Conclusions

This publication shows a simple approach to produce free-standing PVDF-bonded graphite electrodes, which in principle can also be extended to water-sensitive PVDF-bonded cathode active material electrodes.

We show how the use of free-standing graphite (FSG) electrodes attached to a metallic lithium electrode (referred to as Li/FSG) allows to determine the electrochemical impedance response of a battery-type working electrode (WE) in Li-ion battery half-cells equipped with a micro-reference electrode (μ-RE). This approach overcomes the impedance artefacts that are encountered over a wide frequency range when using a half-cell configuration with a conventionally used Li-metal counter electrode (CE), which we show to result from the large impedance difference between a typical Li-ion battery electrode as WE and a Li-metal CE in conjunction with a high-impedance μ-RE. That these artefacts are caused by the potentiostat controls circuitry is demonstrated by impedance measurements on a set of resistors and capacitors the mimick a Li-Ion battery half-cell.

Thus, the use of a Li/FSG counter electrode that is characterized by a very low impedance compared to a Li-metal CE allows for artefact-free measurements of the WE impedance in a half-cell configuration via a μ-reference electrode. The impedance response of the Li/FSG electrodes was found to be reasonably stable for low cycle numbers.

ORCID

Robert Morasch (iD) https://orcid.org/0000-0002-9931-1022

References

1. D. Aurbach, A. Zaban, A. Schechter, Y. Ein-Eli, E. Zinigrad, and B. Markovsky, *J. Electrochem. Soc.*, **142**, 2873 (1995).
2. A. Zaban, E. Zinigrad, and D. Aurbach, *J. Phys. Chem.*, **100**, 3089 (1996).
3. J. Y. Song, H. H. Lee, Y. Y. Wang, and C. C. Wan, *J. Power Sources*, **111**, 255 (2002).
4. J. C. Burns, L. J. Krause, D. B. Le, L. D. Jensen, A. J. Smith, D. Xiong, and J. R. Dahn, *J. Electrochem. Soc.*, **158**, A1417 (2011).
5. R. Petibon, C. P. Aiken, N. N. Sinha, J. C. Burns, H. Ye, C. M. VanElzen, G. Jain, S. Trussler, and J. R. Dahn, *J. Electrochem. Soc.*, **160**, A117 (2013).
6. N. Ogihara, S. Kawauchi, C. Okuda, Y. Itou, Y. Takeuchi, and Y. Ukyo, *J. Electrochem. Soc.*, **159**, A1034 (2012).
7. C. H. Chen, J. Liu, and K. Amine, *J. Power Sources*, **96**, 321 (2001).
8. S. Solchenbach, D. Pritzl, E. J. Y. Kong, J. Landesfeind, and H. A. Gasteiger, *J. Electrochem. Soc.*, **163**, A2265 (2016).
9. J. Landesfeind, D. Pritzl, and H. A. Gasteiger, *J. Electrochem. Soc.*, **164**, A1773 (2017).
10. D. Pritzl, J. Landesfeind, S. Solchenbach, and H. A. Gasteiger, *J. Electrochem. Soc.*, **165**, A2145 (2018).
11. J. L. Gómez-Cámer and P. Novák, *Electrochem. Commun.*, **34**, 208 (2013).
12. L. H. J. Raijmakers, M. J. G. Lammers, and P. H. L. Notten, *Electrochim. Acta*, **259**, 517 (2018).
13. M. Ender, J. Illig, and E. Ivers-Tiffée, *J. Electrochem. Soc.*, **164**, A71 (2017).
14. J. Costard, M. Ender, M. Weiss, and E. Ivers-Tiffée, *J. Electrochem. Soc.*, **164**, A80 (2017).
15. A. Battistel, M. Fan, J. Stojadinović, and F. La Mantia, *Electrochim. Acta*, **135**, 133 (2014).
16. R. Raccichini, M. Amores, and G. Hinds, *Batteries*, **5**, 1 (2019).
17. I. V. Thorat, D. E. Stephenson, N. A. Zacharias, K. Zaghib, J. N. Harb, and D. R. Wheeler, *J. Power Sources*, **188**, 592 (2009).
18. F. Pouraghajan, H. Knight, M. Wray, B. Mazzeo, R. Subbaraman, J. Christensen, and D. Wheeler, *J. Electrochem. Soc.*, **165**, A2644 (2018).
19. F. Linsenmann, D. Pritzl, and H. A. Gasteiger, *J. Electrochem. Soc.*, **166**, A3668 (2019).

3.1.2 Detection of Binder Gradients Using Impedance Spectroscopy and Their Influence on the Tortuosity of Li-Ion Battery Graphite Electrodes

The article entitled "Detection of Binder Gradients Using Impedance Spectroscopy and Their Influence on the Tortuosity of Li-Ion Battery Graphite Electrodes" was submitted to the peer-reviewed Journal of the Electrochemical Society in August 2018 and published in November 2018 as an open-access article under the terms of the Creative Commons Attribution Non-Commercial No Derivates 4.0 License. Robert Morasch presented the results of this work in a talk at the AiMES Meeting in October 2018 (Abstract No. MA2018-02 240). The permanent web link can be found under: https://iopscience.iop.org/article/10.1149/2.1021814jes/meta

In the production of Li-ion batteries, the active and passive solid materials are mixed with a solvent and coated on top of a metal current collector film. The coated film is then dried, which in the case of commercial production lines should happen quickly. The evaporation of the solvent from the top of the electrode (i.e., the coating/air interface) can drag binder dissolved in the liquid state to the top of the electrode, creating a gradient in binder distribution in the finished electrode.[81–83,96] As it was shown that an increase in binder leads to an increase in ionic resistance within the electrode,[97] the binder gradient leads to a gradient in ionic resistance in the electrode. From simulations it was shown that the gradient in resistance leads to a change in impedance spectra, most notably a deviation from the 45° line in a Nyquist plot usually observed in blocking impedance spectra, and can best be detected via a Bode phase plot which shows the phase angle of the EIS spectrum.

Temperature dependent drying experiments showed binder gradients for higher drying temperatures, measured by tracking the fluorine in the PVDF binder via energy dispersive X-ray spectroscopy on electrode cross sections. The electrodes with different degrees of binder gradients showed the same trend in impedance spectra as the simulated impedances with resistance gradients. An important aspect of the findings is the directional dependence of the impedance measurement, which is in a reflective setup, so that any increase in resistance towards the separator interface of the electrode is weighed significantly more than higher resistances towards the current collector interface. This was experimentally shown

by delaminating the electrodes dried at the highest drying temperature and flipping them in the EIS measurement, thus practically measuring an inverse resistance gradient. Comparing the normal and flipped electrodes showed significantly lower pore resistances for the flipped electrode due to the directional dependence of the measurement.

Author contributions

R.M. conducted the impedance measurements and the simulations and evaluated the data. R.M. performed the cross-section EDX measurements and J.L. aided their evaluation. R.M. and B.S. built the impedance model. R.M. wrote the manuscript. R.M., J.L, B.S., and H.A.G. discussed the results and revised the manuscript.

Detection of Binder Gradients Using Impedance Spectroscopy and Their Influence on the Tortuosity of Li-Ion Battery Graphite Electrodes

Robert Morasch, [ORCID]*,z **Johannes Landesfeind,** [ORCID] **Bharatkumar Suthar,** [ORCID]** **and Hubert A. Gasteiger***

Chair of Technical Electrochemistry, Department of Chemistry and Catalysis Research Center, Technical University of Munich, Munich, Germany

Drying battery electrodes at high rates leads to binder migration and has shown to affect the mechanical as well as the electrochemical properties of Li-ion battery electrodes. Up to now, little evidence has been shown as to why the performance suffers. Here, we investigate the influence of an inhomogeneous binder distribution on the total ionic resistance within an electrode. First, we model the impact that vertical inhomogeneities have on the impedance spectrum and the total resistance of an RC (resistor, capacitor) transmission line model. We show how different resistance profiles lead to characteristic changes in the impedance spectrum, in phase angle and magnitude, with high resistances close to the separator leading to a significantly increased overall resistance. We then show energy dispersive X-ray spectroscopy cross section data for electrodes dried at different temperatures and give experimental evidence for the formation and extent of the binder gradients. These electrodes are then measured using blocking electrolyte electrochemical impedance spectroscopy in a symmetric cell setup. It is demonstrated that, depending on the extent of the binder gradient, the phase angle changes and that just from impedance data one can detect binder gradients qualitatively without the need for other time-consuming analysis methods.

Understanding the influence of process parameters during Li-ion battery production on the electrode properties plays a pivotal role in the upscaling process from lab-scale electrodes to commercial-scale cells. The electrode film drying rate plays a vital role in electrode production, as it not only influences the cost of production but also the mechanical, electrical, and electrochemical properties of the electrode.[1–5] Jaiser et al.[1] investigated the adhesion and the rate capability of slow and fast dried graphite electrodes, showing that a faster drying process is detrimental for both adhesion and rate capability. Using energy dispersive X-ray spectroscopy (EDS), they show that when they apply higher drying rates, the polyvinylidene fluoride (PVDF) binder migrates toward the top of the electrode (i.e., toward the surface which constitutes the electrode/separator interface in an assembled cell). Their drying process was conducted at constant drying temperature (76.5°C) but at different ventilation speeds, highlighting that the observed binder migration is not an effect of temperature but rather of the overall drying rate. A more detailed study on the extent of binder gradients across the electrode thickness vs. drying rate was presented by Müller et al.,[2] based on EDS cross-sections of graphite anodes dried at different rates.

To understand the binder migration process, experimental as well as modelling approaches are discussed in the literature.[6–9] Hagiwara et al.[6] and Jaiser et al.[7] froze samples at different stages of the drying process and analyzed the composition of the electrode cross section. Hagiwara et al.[6] used Raman spectroscopy to determine the styrene-butadiene rubber (SBR)-distribution in water based graphite anodes. Their results showed that the binder gradient formation (i.e., strong enrichment of the binder at the free electrode surface) occurred at late stages of the drying process, i.e., when most of the water (>80%) had already evaporated. On the other hand, while Jaiser et al.[7] found a similar surface segregation of the binder upon drying of NMP based slurries of graphite and PVDF binder, they observed the formation of a binder gradient already at early stages of the drying process, initiating once only 14% of the solvent were evaporated.

As a result of the binder migrating away from the region of the electrode near the current collector (CC), the adhesion of the electrode was found to be reduced.[1,5] The loss in the rate performance of graphite anodes due to binder segregation to the free electrode surface was speculated to be due to the more extensive coverage of the graphite particles near the free electrode surface by the segregated binder, thereby increasing the resistance to Li-ion intercalation; as an alternative hypothesis, the authors also suggested that the simultaneous segregation of the conductive carbon to the free surface would lead to a high electrical resistance near the current collector, even though this seems unlikely in the case of graphite electrodes.[1] Ultimately, however, neither one of these hypotheses could be proven. A yet different hypothesis for the effect of binder gradients is that they influence the tortuosity of the electrode, i.e., that a binder-rich surface region might result in a high ionic resistance in the electrolyte phase near the electrode/separator interface. This is suggested by the recently observed strong effect of the type of binder on the tortuosity of graphite electrodes (quantified by AC impedance), even at low binder contents (≤ 5% by weight), whereby electrodes with a high tortuosity exhibited poor rate capability.[10]

To investigate the latter hypothesis, this work examines the influence of ionic resistivity gradients in the electrolyte phase normal to the electrode surface on the modeled electrochemical impedance spectroscopy (EIS) response, and compares it to the experimentally obtained EIS response of electrodes which exhibit binder gradients normal to the electrode surface. While inhomogeneities of the ionic resistance across the thickness of a porous electrode have been analyzed analytically in the past using a transmission line model, this phenomenon was not correlated at that time to binder migration induced by the drying of electrode ink coatings.[11–13] We therefore focus in our study on the effect of various ionic resistance distribution patterns across the thickness of a porous electrode on the modeled EIS response, and compare with the experimental EIS response of graphite electrodes dried at different temperatures. The resulting PVDF binder gradients will be determined experimentally by EDS analysis of resin embedded and polished electrode cross-sections. Lastly, we will show the impact of binder gradients on the rate performance of graphite anodes in half-cells with a lithium reference electrode.

*Electrochemical Society Student Member.
**Electrochemical Society Member.
***Electrochemical Society Fellow.
zE-mail: robert.morasch@tum.de

Experimental

*Impedance modelling.—*An impedance model was built in COM-SOL Multiphysics, using the included battery and fuel cell module which is based on the Newman model.[14,15] A 2D representation of two identical porous electrodes is used to mimic the experimental setup for symmetric cell EIS measurements (see below), even though a 1D representation would also be sufficient for the here pursued modelling approach. If not stated otherwise, the parameters described below are chosen arbitrarily, as the qualitative model results are independent of the chosen double layer capacity, electrode surface area, and geometry. The electrode dimensions were chosen to be 50 μm × 260 μm (width × thickness). The electrolyte bulk conductivity was set to 0.258 mS/cm, corresponding to the experimentally chosen electrolyte (see below), and the electrical conductivity of the solid phase was set to 10 S/cm, which is in the range of typically found values for graphite electrodes.[16] With this low ratio of electronic to ionic resistance in the electrolyte phase of the porous electrode (the latter being lower than the bulk conductivity due to electrode porosity and tortuosity), the resistance of the electronic path in the transmission line model becomes negligible, so that the changes in the EIS response depend solely on changes in the ionic resistance.[17] The electrode porosity ε_l was set to 55% and was considered uniform throughout the electrode, as the volume fraction of the binder for application relevant electrodes is generally negligible. This entails that the specific surface area of the graphite active material is also uniform throughout the thickness of the electrode. The separator thickness was set to 50 μm, and its porosity and tortuosity was set to one, as their value will only affect the high frequency resistance and not the shape of the observed transmission line model EIS response. For our reference case without binder gradient, the tortuosity was set at 5, which is a commonly observed value for graphite active materials.[18]

In the COMSOL modelling framework, faradaic reactions were disabled, leaving only the double layer capacity at the surface of the spherical particles (set to the default settings of $c_{dl} = 0.2$ F/m$_{BET}^2$ and a graphite particle radius of 10 μm; approximated specific surface area (particle surface area per electrode volume) $a_{dl} = 3 \times (1 - \varepsilon_l)/r_p = 1.35 \times 10^5$ m^2/m^3) as current sink/source. This represents the behavior of a graphite electrode in a so-called "blocking electrolyte", which is composed of ions which do not intercalate into graphite.[18] The ionic resistance within the porous electrodes (i.e., the tortuosity, since the porosity was set constant) was then varied linearly or stepwise as described later on. A harmonic perturbation of 20 mV was used in a frequency range from 0.01 Hz to 10 kHz. All of the shown EIS data have been corrected for the high frequency resistance, stemming from the ohmic contribution of the electrolyte in the separator. Changing any of the other parameters above will not change the qualitative outcome of the model. Again, the only prerequisite for this model to represent a porous graphite electrode in a non-intercalating electrolyte is that the electrical resistance be at least two orders of magnitude smaller than the ionic resistance of the electrolyte phase within the porous electrode.[17]

*Slurry preparation and drying.—*Graphite (T311, Timcal, 19 μm D50, 3 m^2/g) and polymer binder (polyvinylidene fluoride (PVDF), Arkema) at a ratio of 95:5 (wt:wt) were mixed with N-Methyl-2-pyrrolidone (NMP, Sigma Aldrich, anhydrous, 99.5%) at a solid:liquid ratio of 5:4 (wt:wt) in a planetary mixer (Thinky ARV-310) at 2000 rpm for five minutes. The prepared graphite slurries were coated onto a copper current collector foil (MTI, 12 μm) attached to a glass plate using a gap bar coater (RK PrintCoat Instruments, UK). The wet film thickness was either 150 μm for electrodes used for rate performance tests or 500 μm for EIS and EDS analysis; the resulting thicker electrodes for the latter was used to allow a better quantification of the binder gradients by EDS.

Electrode drying was performed using an infrared (IR) lamp (IH2000IR, ELV electronics, Germany, 1300 W) mounted in a fume hood. An aluminum plate was placed below the IR-lamp, and the temperature was controlled by the distance between the lamp and plate.

The temperature was measured by a thermocouple placed on top of the aluminum plate after temperature equilibration, and the glass plate with the freshly coated electrode was then placed onto the aluminum plate until the coating was dry. The time until the coating was visually observed to be dry was ∼2 min for the aluminum plate heated to 125°C (28 cm distance to lamp), ∼7 min when heated to 100°C (41 cm distance to lamp), ∼18 min when heated to 75°C (63 cm distance to lamp), ∼90 min when heated to 50°C (91 cm distance to lamp), and several hours for the room temperature (RT) dried sample (lamp turned off). For electrodes used for EDS measurements and EIS analysis, the thickness of the dried electrodes was ∼245 μm (±6%), corresponding to graphite loadings of ∼25.5 mg/cm^2 (±6%); for the rate capability tests, the thickness of the dried electrodes was ∼74 μm (±2%), corresponding to graphite loadings of ∼7.4 mg/cm^2 (±2%) with a capacity of ∼2.4 mAh/cm^2 (calculated for a theoretical graphite capacity of 350 mAh/g). The electrodes were not further compressed/calendered, and their porosity was ∼55% (based on thickness and areal weight measurements). The dried electrodes were punched out to a diameter of 10.95 mm (equating to an area of ∼0.94 cm^2) using an electrode punch (Hohsen Corp. OSAKA, Japan).

*Tortuosity determination.—*The impedance measurements for the determination of the electrodes' tortuosity were performed at 25°C in a symmetric cell setup (T-cells; two electrode configuration; measured at open circuit voltage) using 100 μL of a non-intercalating electrolyte as described previously,[18] viz., a 3:7 (wt:wt) mixture of ethylene carbonate (EC, BASF, anhydrous, 99.99%) and ethyl methyl carbonate (EMC, BASF, anhydrous, 99.99%) containing ∼10 mM tetrabutyl-lammonium perchlorate (TBAClO$_4$, Sigma Aldrich, ≥99.0%). The conductivity was measured using a conductivity sensor (SI-Analytics, LF 1100 T+) to be 0.258 mS/cm at 25°C.

*SEM/EDS.—*Cross-sectional EDS mapping was conducted with the above described thick electrodes. The current collector was manually peeled off the electrodes, taking care not to damage the electrode (easily possible for such thick electrodes), followed by placing each of them between two aluminum plates (1 × 1 × 0.1 cm) and fully immersing the stacked up electrode into a liquid resin (EpoThin 2, BUEHLER, USA). With the resin still liquid, the sample stack was placed into a desiccator, which was then evacuated to ensure complete filling of the pores by the resin. After the resin had hardened, the sample stack was polished with SiC paper (CarbiMet S, P320, Buehler Ltd.) until the electrode cross section was fully exposed. Afterwards the electrode was polished using a finer SiC paper (CarbiMet S, P1200, Buehler Ltd.) and lastly with a diamond solution (MetaDi Supreme, Polycristalline Diamond Suspension, 9 μm, Buehler Ltd.) applied onto a micro cloth (TexMet C, Buehler Ltd.). Elemental analysis was performed using a JCM-6000 (JEOL, Japan) scanning electron microscope (SEM), imaging an area of ∼600 × 300 μm. Fig. 1 shows an optical microscope image of polished electrode cross sections, embedded in resin and mounted between aluminum sheets. For a better quantification of the EDS data, the signal from each electrode sample was split into five segments of equal length (i.e., five horizontally aligned segments in Fig. 1, representing the top, the bottom, and three middle sections across the electrode thickness), determining the average fluorine concentration in each segment. The background correction was done by taking the spectrum signal for the entire measured electrode area (separately for each electrode) and subtracting one fifth of the total background signal from the five individual segments, as the software did not allow to reliably correct the background for the five individual segments separately.

*Rate capability test.—*For electrochemical analysis, rate tests were performed using a three-electrode cell setup (Swagelok T-cell) with a Li-metal reference electrode (described in more detail in Fig. 1a in Ref. 19). The cells were built inside an argon filled glove box (MBraun, 25°C ± 1°C, oxygen and water content < 0.1 ppm, Ar 5.0, Westfalen). The cells were assembled with a graphite working-electrode (areal capacity ∼2.4 mAh/cm^2), a Li-metal counter-electrode (0.45 mm
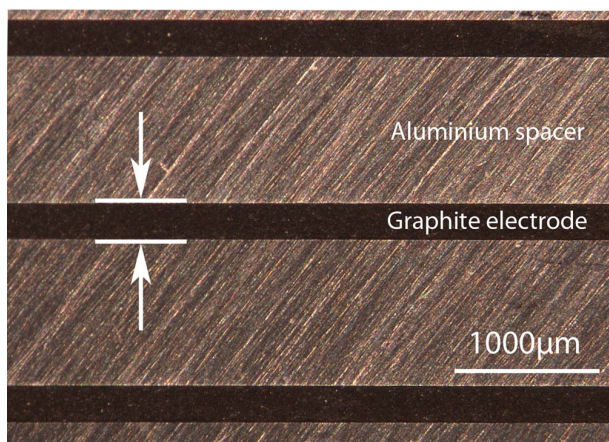
Figure 1. Optical microscope image of graphite electrodes stacked between aluminum sheets, vacuum filled with resin, and polished after hardening of the resin. Shown are the cross sectional areas for several embedded electrodes which are used for EDS measurements.
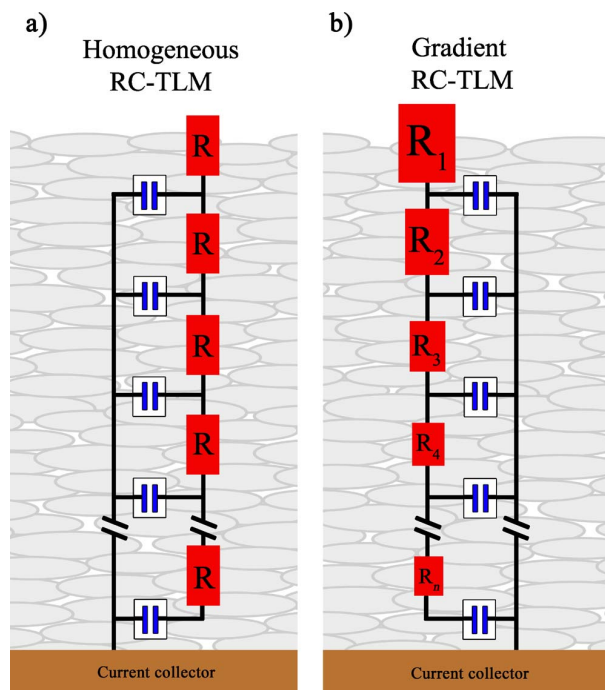

Figure 2. RC- Transmission line models (TLMs) where the resistances represent the ionic resistance of infinitesimal element and the capacitors the electrochemical double layer capacity in the electrode; a) Homogeneous RC-Transmission line model with resistive elements of equal value throughout the electrode; b) Gradient RC-Transmission line model showing a gradient in resistance with a higher resistance toward the top (separator interface) of the electrode. Capacitive elements throughout both equivalent circuits are of equal capacitance.

thickness and 11 mm diameter, Rockwood Lithium), and two porous glass fiber separators with a diameter of 11 mm (VWR, 250 μm uncompressed thickness, 90% porosity).

All cell parts were dried at 120°C in a vacuum oven (Büchi, Switzerland) for 8 h before being transferred into an Ar-filled glove box. 80 μL of LP57 electrolyte (1 M LiPF$_6$ in EC:EMC 3:7 (wt:wt), battery grade, BASF) were added to the main compartment and 50 μL were added to the reference electrode compartment. Using a potentiostat (Maccor, Cambridge (UK)) the cells were cycled in a temperature-controlled chamber (25°C, Binder) between 0.01–1.5 V vs. Li$^+$/Li, controlled and measured against the Li-metal reference electrode. The cycling protocol started with a 3 h open circuit voltage phase to allow for complete wetting of the electrodes. Lithiation of the graphite working-electrode was performed galvanostatically (CC lithiation) without any preceding formation cycles at various C-rates: first 4 cycles at C/10, followed by five cycles each at C/5, C/2, 1 C, 1.5 C, 2 C, 2.5 C, 3 C, 5 C, and 10 C; on the other hand, delithiation cycles were performed using a constant current phase followed by a constant voltage phase (CCCV) at the same C-rates as the corresponding lithiation, but not faster than 0.5 C. For every electrode type, three cells were measured and the plotted values represent the average and the standard deviation of the measured capacities (note that this procedure is very similar but not identical to that described previously by our group).[10]

Results and Discussion

Modeled EIS response of porous electrodes with different R$_{ion}$ profiles.—To examine numerically how the EIS response of a porous electrode is affected by gradients in the ionic resistance in the electrolyte phase (R_{ion}), which we hypothesize to be caused by binder segregation during the drying process, we will be considering the five different R_{ion} distributions across the thickness of a porous electrode shown in Fig. 3 (note that the total ionic resistance across the entire electrode thickness is equal in all cases). Their EIS response in a blocking electrolyte is then calculated based on a simplified transmission line model (TLM) using RC elements, R representing infinitesimal elements of R_{ion} and C the double-layer capacitance of the graphite electrode, shown exemplary in Fig. 2a without resistance gradient and Fig. 2b with gradient. As stated above, the electronic resistance contribution in this RC-TLM can be neglected (discussed in detail in Ref. 17).

In modelling the EIS response, the selected ionic resistance value (on the order of R_{ion} = 1 kΩ cm^2) is representative of what we

obtained for our thick electrodes in the blocking electrolyte. However, the imaginary and real resistances in the shown Nyquist plots were normalized by (R_{ion}/1.5), so that they are more generally applicable, i.e., so that the Nyquist plots would look identical for electrodes with different average R_{ion} values. The frequency range needed to probe across the entire electrode thickness will be different for different electrodes, since it depends on the double-layer capacity and the ionic resistance of the electrode, so that the modeled Bode plots are specific to a given modeled electrode. The qualitative features of the Bode plots, however, are independent of these values, as long as the above-mentioned condition of low electronic resistance compared to ionic resistance is fulfilled.

Figs. 4a and 4b show the Nyquist and the phase angle plots for the EIS response of electrodes with different R_{ion} profiles. The modeled RC-TLM impedance response for a homogeneous R_{ion} profile (see black curve labeled *ng* ("no gradient") in Fig. 3,), subsequently referred to as reference case, is shown by the black lines in Fig. 4. This reference case first exhibits an initial 45° line in the high frequency region of the Nyquist plot (Fig. 4a), which is represented by a plateau at 45° extending from high toward low frequencies in the phase angle plot (Fig. 4b). There, it is followed by a small dip to a lower phase angle (∼43.4°) before increasing to higher phase angle values, due to the predominantly capacitive behavior of the RC-TLM at lower frequencies. The difference between the high frequency x-axis intercept (here set to zero) and the linear extrapolation from low frequencies toward the x-axis (dashed black line in Fig. 4a for case *ng*) when normalizing the impedances by (R_{ion}/1.5) corresponds to the ionic resistance in the electrolyte phase of one porous electrode in the symmetric cell, namely to 2/3 × Re(Z) in the symmetric cell. While this represents the ideal case for a macro-homogeneous resistance distribution across the thickness of a porous electrode, which one would expect for a
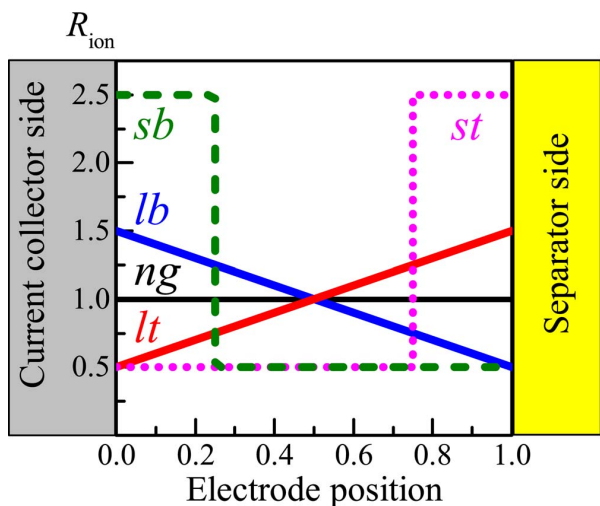
Figure 3. Chosen ionic resistance distributions in the electrolyte phase across the thickness of a porous electrode used for modeling its EIS response with a blocking electrolyte. Here, and furtheron, "bottom" refers to the interface between the current collector and the electrode, and "top" refers to the electrode/separator interface. The various shown profiles are described as follows. *ng* ("no gradient"): represents a uniform resistance profile, i.e., without gradient, and is given for reference (black curve),. *lb* ("linear bottom") represents a linear R_{ion} profile with higher resistance ($1.5 \times R_{ion}$) at the bottom (CC-side, blue curve); *lt* ("linear top") represents a linear R_{ion} profile with higher resistance ($1.5 \times R_{ion}$) at the top (separator-side, red curve); *sb* ("step bottom") represents a step function profile with a higher resistance in the bottom quarter of the electrode ($2.5 \times R_{ion}$, dashed green curve); *st* ("step top") represents a step function profile with a higher resistance in the top quarter of the electrode ($2.5 \times R_{ion}$, dotted magenta curve). Note that the total ionic resistance summed up over the entire electrode thickness is the same in all cases.

homogeneous binder distribution, we will now explore the effect of an inhomogeneous resistance profile on the EIS response of a porous electrode.

The EIS response for a linear R_{ion} gradient across the thickness of the electrode, with a maximum value at the bottom (CC-side) of the electrode (profile *lb* ("linear bottom"), see blue line in Fig. 3) is shown by the blue lines labeled *lb* in Fig. 4. Here, we chose a 1.5-fold higher resistance at the current collector side of the electrode and a 0.5-fold lower resistance at the separator side of the electrode, both referenced to the average R_{ion} value across the electrode thickness (the latter being the same as that for the homogeneous R_{ion} distribution, case *ng*). Such a distribution decreases the apparent ionic resistance by ~25% compared to the reference value (see Fig. 4a). In this case, however, the phase angle plot (blue line in Fig. 4b) shows a constantly increasing phase angle from the 45° value at high frequencies to an intermediate maximum of ~48.6° at ~0.3 Hz, before increasing again as the frequency goes below ~0.3 Hz. Reversing the linear resistance distribution so that the maximum R_{ion} value is at the top of the electrode (i.e., at the separator-side; see red line in Fig. 3), the modeled impedance response (profile *lt* ("linear top"), red curves) shows the opposite trend: a ~25% higher apparent R_{ion} value compared to the reference case (see red vs. black lines in Fig. 4a) and a comparably more pronounced phase angle minimum of ~40.3° at a frequency of ~0.1 Hz (see red line in Fig. 4b). Thus, linear R_{ion} gradients across the thickness of a porous electrode affect the apparent R_{ion} values, and their presence and direction is indicated by characteristic maxima/minima in modeled phase angle plots.

To further explore these impedance characteristics, we also modeled a second set of resistance distribution profiles, namely modeled stepped profiles with either the bottom quarter of the electrode (CC-side) or the top quarter of the electrode (separator-side) exhibiting a
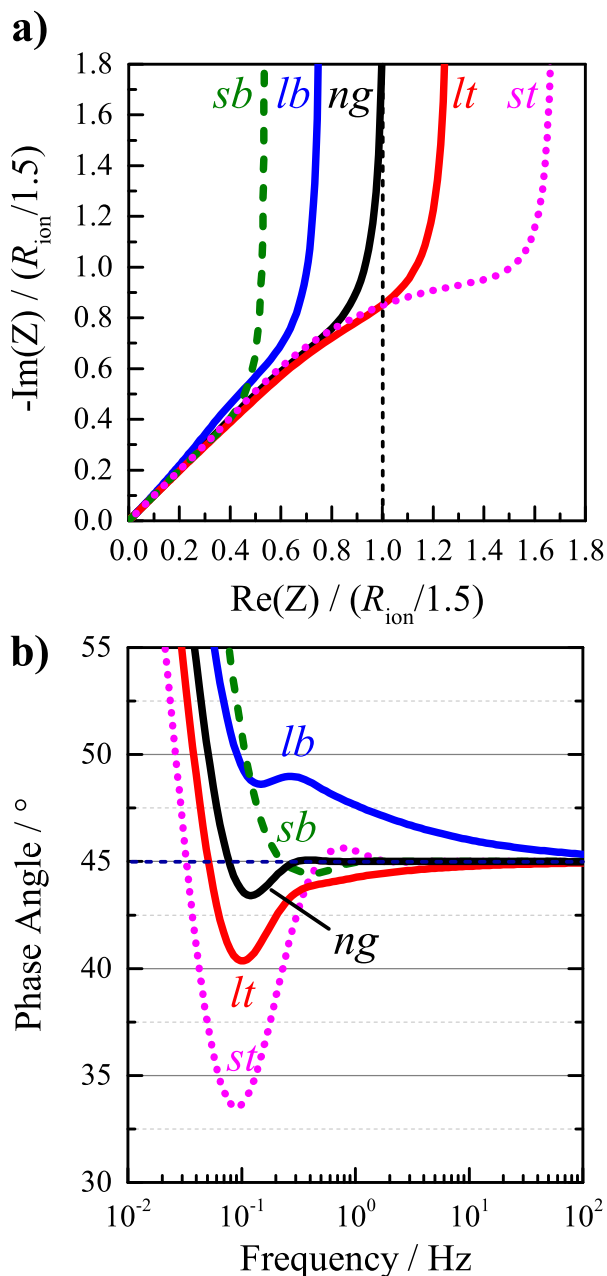
Figure 4. Modeled EIS response (high frequency corrected) for a porous electrode with a blocking electrolyte (RC-TLM model) for a constant ionic resistance in the electrolyte phase (R_{ion}) across the electrode thickness (*ng*, black lines) as well as various resistance distributions as shown in Fig. 3. The latter are linear resistance gradients with a maximum resistance either at the top of the electrode (*lt*, red) or at the bottom of the electrode (*lb*, blue) as well as step functions with a maximum resistance either at the top (*st*, magenta, dotted line) or at the bottom of the electrode (*sb*, green, dashed line); here, "top" refers to the separator side of the electrode and "bottom" to the current collector side of the electrode. a) Nyquist plot of the scaled negative imaginary part of the impedance vs. the scaled real part of the impedance;. b) corresponding phase angle plot (Bode plot). The chosen model parameters resemble those of the experiments conducted with the thick electrodes shown in Fig. 6: electrode thickness 260 μm; electrolyte conductivity 0.258 mS/cm; porosity 55%; tortuosity 5; the double-layer capacity is based on the area of spherical particles ($r_p = 10$ μm, approximated by the specific surface area (particle surface area per electrode volume) $a_{dl} = 3 \times (1-0.55)/r_p = 1.35 \times 10^5$ m²/m³) and a double layer capacitance of 0.2 F/m².

high ionic resistance (2.5-times of the average R_{ion} value), whereby the average R_{ion} value across the electrode thickness was again chosen to be the same as that of the homogeneous case. These distributions are shown in Fig. 3, labelled as *sb* ("step bottom", green dashed curve) or as *st* ("step top", magenta dotted curve), respectively. The modeled EIS response for these R_{ion} profiles is shown in Fig. 4. For the profile with a higher resistance at the CC-side (*sb*, green dashed lines), the apparent R_{ion} value is ∼46% lower than that of the reference case with a homogenous R_{ion} profile (see Fig. 4a). In the phase angle plot, the *sb* profile starts with a 45° value at high frequencies and passes through a very shallow minimum of ∼44.5° at low frequencies. In analogy with the above discussed linear R_{ion} profiles, a stepped profile with the maximum R_{ion} value at the top (separator-side) shows a reversed trend (*st* profile, magenta dotted lines in Fig. 4): the apparent R_{ion} value increases by ∼66% compared to the reference case and shows a significantly more pronounced phase angle minimum of ∼39.1° at low frequencies.

The change in the apparent resistance for inhomogeneous resistance profiles stems from the directionally dependent weighing of the ionic resistance profile of the electrolyte phase. For such a case, assuming the current sink (capacitive elements) is homogeneously distributed throughout the electrode, higher current flows through the resistances near the separator region than the current collector region (reflective boundary condition case).[20] This is analogous to the transport phenomena involved in a Li-ion battery, where the ionic current, all of which passes through the electrode/separator interface, must be consumed (intercalated) along the thickness of the electrode. No ionic current passes through the current collector. Hence a resistance at the top (electrode/separator interface) is weighed higher than a resistance at the bottom. This is in contrast to a setup with transmissive boundary condition, where the measured apparent resistance is directionally independent, as the resistances through the electrode are weighed solely by their thickness fraction of the electrode.[20–22] In such systems, all of the resistance profiles shown in Fig. 3 would yield the same apparent resistance (hence the same apparent tortuosity). The above mentioned description of the system using the RC-TLM is valid for a two-phase system, here the binder and graphite active material. In a system incorporating conductive carbon or other additives, as would be necessary for most cathode active materials, the above mentioned prerequisites (e.g. low electrical resistance) might not hold true anymore and could lead to data misinterpretation.[17]

***Preparation and EIS analysis of graphite electrodes with binder gradients.*—**While the above numerical analysis reveals that R_{ion} gradients across the thickness of a porous electrode can be detected by the electrode's EIS response, no direct proof has yet been provided that R_{ion} gradients may be caused by binder gradients. This would not necessarily be obvious for the here examined electrodes, since the PVDF binder only accounts for ∼6% of the solids volume (graphite and PVDF), corresponding to only ∼2.7% of the electrode volume (calculated from the 95/5 graphite/PVDF mass ratio, the graphite and PVDF densities of ∼2.2 and ∼1.8 g/cm³, respectively, and the electrode porosity of ∼55%). Thus, for the following analysis, we first prepared electrodes with different binder gradients, then quantified the binder gradients by EDS cross sectional mapping, and finally examined their EIS response. The binder distribution was affected by drying electrodes at different temperatures, which was shown to result in different extents of binder migration.[6] The graphite electrodes examined in the following were dried between 50–125°C using an IR-lamp as well as at room temperature (RT, ∼23°C), as described in the experimental section. It is emphasized that the intrinsic driving force to generate different binder gradients is not the drying temperature, but rather, as mentioned above, the drying rate, for which reason we have provided the visually observed drying time in the experimental section and in Fig. 6c.

To quantify the extent of binder migration and to directly correlate it to the impedance obtained from the dried graphite electrodes, we analyzed the electrode cross section of electrodes dried at temperatures from RT up to 125°C using EDS. An exemplary line scan of the
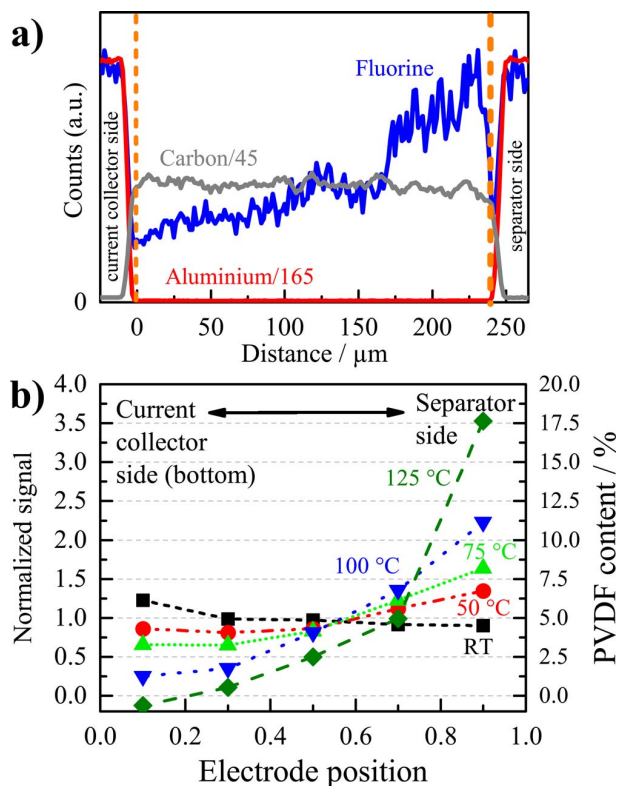

Figure 5. EDS cross section line scans for electrodes dried at different temperatures with a final thickness of ∼245 μm (±6%), coated at a wet film thickness of 500 μm. a) Example of the EDS raw signals for carbon (gray, signal divided by 45), fluorine (blue), and aluminum (red, signal divided by 165) of an electrode dried at 100°C. Carbon and Aluminium signals indicate the beginning and end of the electrode (marked by vertical orange dashed lines). b) Background corrected fluorine signal stemming from the PVDF binder for electrodes dried between RT and 125°C; the fluorine signals were averaged over five evenly spaced segments across the electrode thickness, with the x-axis values of 0 and 1.0 corresponding to the bottom (CC-side) and the top (separator-side) of the electrodes, respectively (for details see Experimental section). The left axis was normalized to show the expected average fluorine signal of 1.0, corresponding to 5% binder (right axis).

measured aluminum, carbon, and fluorine signal is shown in Fig. 5a for the sample dried at 100°C. The aluminum signal stems from the two aluminum spacers at the top (separator-side of the electrode, right side in Fig. 5) and bottom (CC-side, left side in Fig. 5) of the electrode (also compare Fig. 1). The decrease in the aluminum signal and the intermediate carbon signal plateau marks the top and bottom of the electrode, seen on the right and left side of Fig. 5a (marked by the vertical dashed orange lines), respectively. The fluorine signals (blue line) between the vertical dashed orange lines stem from the PVDF binder, whereas the EDS signals at the fluorine energy before/after the dashed orange lines are caused by an interference with the EDS signals from aluminum.

The fluorine signals across the thickness of electrodes dried at different temperatures are shown in Fig. 5b. The signal was split into five parts of equal length (from bottom to top of the electrode), corrected for the background signal, and averaged (see experimental section); the average fluorine signal for each segment is marked at the mid-point of each segment by the symbols in Fig. 5b, connected with dashed lines serving as a guide-to-the-eye. The black symbols depict the fluorine signals for the RT dried electrode across the electrode thickness. While it is reasonably constant, indicating a rather homogeneous binder profile across the electrode thickness, there is a slightly stronger fluorine signal toward the bottom of the electrode, which
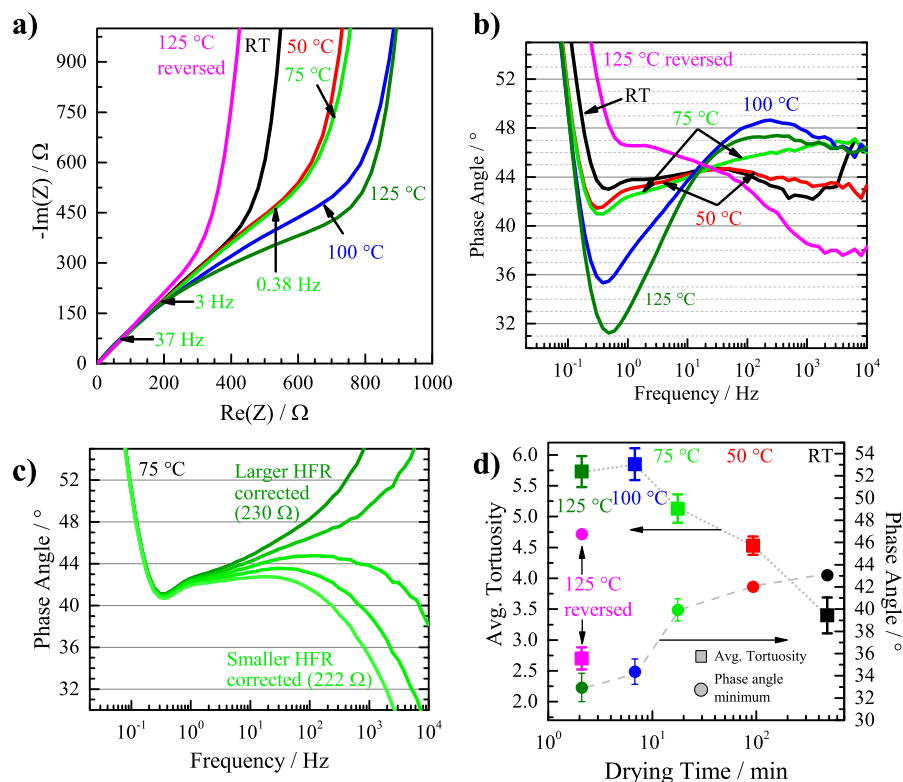
Figure 6. Experimental EIS response of graphite electrodes dried between 25 and 125°C and with a final thickness of ~245 μm (±6%), coated at a wet film thickness of 500 μm; the electrode labeled "125°C reversed" was dried at 125°C, removed from the current collector, and re-assembled such that the original CC-side of the electrode becomes the separator-side in the re-assembled cell. EIS measurements (20 mV amplitude, between 10 mHz and 200 kHz) were conducted in a symmetric cell setup (T-cells, ø = 10.95 mm) using a non-intercalating electrolyte (10 mM TBAClO$_4$ in EC:EMC 3:7, with κ = 0.258 mS/cm). a) High frequency resistance (HFR) corrected Nyquist plots with frequencies marked for the 75°C sample. b) HFR-corrected phase angle plots. c) Phase angle plot of the 75°C dried electrode corrected for the experimentally determined HFR of 226 Ω, but adding small deviations of ± 2 Ω (i.e., ca. ± 1%) and ± 4 Ω (i.e., ca. ± 2%) to the HFR correction, which are considered to be within the error of HFR quantification. d) Apparent tortuosities for the electrodes vs. the observed drying time (left axis, cubes) as well as minimum phase angles (right axis, circles; the value for the "125°C reversed" sample was taken at the last visible plateau at low frequencies (~1 Hz) in the phase plot). Error bars indicate the standard deviation of four separate measurements; drying times were observed by eye, whereby the room temperature drying time was taken as 8 h (overnight). The two gray dashed lines were added as guide-to-the-eye for the changes in tortuosity and phase angle minima for the differently dried electrodes (excluding the data for the reversed electrode).

could possibly be caused by a small degree of binder sedimentation due to the extremely slow drying process at room temperature (several hours). The 50°C dried sample however already shows first signs of binder migration to the top of the electrode (separator-side) and a concomitant slight depletion of binder at the bottom of the electrode (current collector-side), as reported in the literature for higher drying temperatures and the associated faster drying rates.[1,2,6,8] The extent of binder migration to the top surface of the electrode clearly increases with drying temperature (i.e., with increasing drying rate), so that the electrode dried at 75°C (light green line) already shows a binder gradient which resembles a linearly increasing binder distribution toward the separator-side. For higher drying temperatures, this gradient buildup continues, showing the strongest gradient formation for the sample dried at the highest temperature (125°C, dark green line). The fact that the fluorine signal at the bottom of the electrode goes slightly below 0 is caused by background correction errors related to the extremely small fluorine signal at this position; the low binder content at the CC-side for the electrode dried at 125°C is also reflected by the very poor adhesion of the electrode coating to the current collector, which allowed us to also prepare freestanding electrodes in this case.

Having characterized the PVDF binder distribution across the thickness of electrodes dried at different temperatures, we will now examine their EIS response in symmetrical cells with non-intercalating electrolyte, and then compare them to the modeled EIS response for

electrodes with different R_{ion} profiles. It should be noted that the direct comparison of ionic resistances of individual measurements is only of qualitative nature, as the measurement is dependent on (among others) the electrode thickness (standard deviation ± 6%). Averaged values for the tortuosities of four separate measurements per sample set are depicted in Fig. 6d. Figs. 6a and 6b show exemplary data of the experimentally determined Nyquist and phase angle plots, respectively, corrected for the high frequency resistance (HFR), as was done for the modeled EIS responses shown in Fig. 4. The lowest apparent R_{ion} value for the as-prepared electrodes is obtained for the RT dried sample (black line in Fig. 6a), i.e., for the electrode with the most homogeneous binder distribution across the electrode thickness (black symbols in Fig. 5a). The apparent R_{ion} value increases ~1.4-fold for electrodes dried at 50°C (red line) and 75°C (light green line) and by ~1.7-fold for electrodes dried at 100°C (blue line) and 125°C (dark green line). Quite clearly, the apparent R_{ion} value increases with an increasing extent of binder migration to the electrode top surface (separator-side; see Fig. 5b). Comparing this trend with the modeled Nyquist plots (Fig. 4a) for electrodes with increasing R_{ion} values from the electrode bottom (CC-side) to the electrode top (separator-side) suggests that the experimentally observed binder gradients indeed cause an analogous R_{ion} gradient, despite the rather small volume fraction of binder (~6% of the solids volume or ~2.7% of the electrode volume). Thus, even small amounts of binder can substantially influence the apparent ionic resistance through a porous electrode,

either by differences in binder distribution affected by the drying process as shown, or by the chemical nature of the binder as we had observed previously.[10]

Additional insight can be gained when examining the experimental HFR-corrected phase angle plots shown in Fig. 6b. Following the above indication that the observed binder gradients reflect analogous gradients in the electrode's R_{ion} values, the EIS models shown in Fig. 4 would predict (i) 45° phase angles at high frequency, and, (ii) increasingly pronounced phase angle minima with increasing binder gradients, i.e., with increasing drying temperatures. The latter can be clearly observed in the experimental data shown in Fig. 6b: the phase angle minimum is rather small for the RT dried electrode (black line) with its nearly homogeneous binder distribution (see Fig. 5b), while it becomes increasingly more pronounced as the drying temperature and thus the binder gradient increases. At the same time, however, the high frequency phase angles do not seem to approach the expected 45° phase angle. Apart from phase changes due to inhomogeneity within the electrode, this may also have to do with the fact that even minute errors in the HFR correction lead to large errors in the high frequency phase angle, as is demonstrated exemplarily in Fig. 6c for the EIS data obtained for the electrode dried at 75°C. Here, the impedance data were corrected for the experimentally determined HFR of 226 Ω, but adding small deviations of ± 2 Ω (i.e., ca. ± 1%) and ± 4 Ω (i.e., ca. ± 2%) to the HFR correction, which we consider rather small errors in the quantification of the HFR. Quite clearly, this results in dramatic variations of the phase angle plot in the high frequency region beyond the phase angle minima (i.e., at frequencies higher than ~1–2 Hz), so that from an experimental point of view no reliable information can be obtained from the high frequency region. The sensitivity is evident when examining the Nyquist plot (Fig. 6a), where the first marked frequency of 37 Hz is close to the origin of the Nyquist plot, but spans almost 50% of the phase angle plot. On the other hand, at lower frequencies the curves start to overlap, illustrating that the extent of the phase angle minima is not affected by small errors in the HFR and can thus be used to deduce the presence/absence of binder gradients.

The above observed correlations can be further confirmed by examining an electrode configuration, for which the binder gradient goes into the opposite direction, i.e., for which the binder concentration is highest at the bottom of the electrode (i.e., at the CC-side) and the lowest at the top of the electrode (i.e., at the separator-side). Such a reversed binder gradient can be mimicked by using a freestanding electrode dried at 125°C, as it easily detached from the current collector foil (see above), so that these freestanding electrodes could be re-assembled into symmetric T-cells now with the separator-sides of the original electrodes facing the current collectors. Symmetric cells assembled in this reversed configuration now have a binder profile which is a mirror image of that shown for the 125°C dried electrode (i.e., mirroring the dark green line in Fig. 5b around the $x = 0.5$ value). Its experimental impedance response is given by the magenta line in Fig. 6, with the Nyquist plot (Fig. 6a) showing a reduced apparent R_{ion} value compared to the reference case with homogeneous binder distribution (black line), and with the phase angle plot (Fig. 6b) now revealing a characteristic local minimum at a phase angle of ~47°, i.e., well above that of the reference case. The lower apparent R_{ion} value and the shift of the phase angle minimum to above the reference case value is perfectly consistent with the EIS model for electrodes with a linear R_{ion} gradient, where the same behavior is observed upon reversing the liniear R_{ion} profile with a maximum resistance at the top of the electrode (red line labelled *lt* in Fig. 6) so that the profile is reversed (blue line labelled *lb* in Fig. 6).

As described above, the apparent R_{ion} value for the different electrodes was obtained from the HFR-corrected Nyquist plots in Fig. 6a by interpolating the low frequency data to the Re(Z)-axis. From this, electrode resistance tortuosities (τ) were determined using the electrolyte bulk conductivity (κ = 0.258 mS/cm), the electrode porosity (ε = 0.55), and the measured electrode thickness (ranging from 245 to 260 μm), as described in Ref. 18. Fig. 6d shows the thus determined apparent tortuosities together with the characteristic phase angle minima (obtained from Fig. 6b) of the various electrodes vs. the ap-

proximate drying time. The trend to higher apparent tortuosities with decreasing drying time, i.e., with increasing drying rates, is evident: as the drying time is reduced at higher drying temperature, leading to more pronounced binder migration toward the top (separator-side) of the electrode, the apparent tortuosity increases. On the other hand, the electrodes dried at the highest temperature of 125°C but re-assembled in reverse configuration (i.e., the separator-side during drying now facing the current collector for the measurement) show a very low apparent tortuosity of ~2.7, even lower than that of the RT dried sample, consistent with what one would expect based on Fig. 4a for an electrode with very little binder content at the separator. As discussed above, the best qualitative indicator for the extent and the direction of binder gradients are the phase angle minima observed in the phase angle plots (Fig. 6b), which are therefore plotted also in Fig. 6d (right axis). The angle shown for the "125°C reversed" (magenta) sample was obtained by taking the phase angle values of the last plateau at low frequencies (~1 Hz), before the phase angle increased continuously due to the capacitive behavior at low frequencies. Clearly, the decreasing values for the characteristic phase angle minima with shorter drying times (i.e., for higher drying temperatures) is consistent with what one would expect based on the experimentally observed binder profiles (Fig. 5b); furthermore, while the 100°C and the 125°C dried electrodes show similar tortuosities, the phase angle minimum of the latter is still lower, suggesting a stronger binder gradient, as indeed can be seen from the EDX based binder profiles (see dark green vs. blue lines in Fig. 5b).

Charge rate capability of differently dried graphite electrodes.— Previous studies on the rate capability of graphite/NMC full-cells have shown that cells with graphite anodes dried at a high drying rate are inferior to those with graphite anodes dried at low drying rate, which the authors related to binder gradients formed at high drying rate. Similarly, the effect of various binder types on the charge rate capability of graphite anodes was observed recently by Landesfeind et al.,[10] monitoring the onset of lithium plating upon the lithiation of graphite electrodes in half-cells by means of a reference electrode. In the following, we will therefore examine whether there is a correlation between the charge rate capability of graphite anodes dried at different temperatures (i.e., at different drying rates) and the extent of binder gradients indicated by their EIS response. For this charge rate capability tests, we examine graphite electrodes with industrially relevant areal capacities of ~2.4 mAh/cm^2 (corresponding to graphite loadings of ~7.4 mg/cm^2 (±2%) and thicknesses of ~74 μm (±2%)) and dried at 75°C or 125°C.

The results from the EIS characterization of these electrodes in symmetric cells with non-intercalating electrolyte of these electrodes can be seen in Fig. 7a. Both electrodes have similar apparent tortuosities (4.4–4.6), but the electrodes dried at 125°C show a significantly more pronounced minimum in the phase angle plot, suggesting that the binder is significantly more inhomogeneously distributed, namely with significant binder enrichment at the top of the electrode (separator-side), as one would expect based on the above discussed data with thicker electrodes. The charge (i.e., lithiation) rate capability is depicted in Fig. 7b, showing the inferior performance of electrodes dried at 125°C, analogous to what was shown by Jaiser et al. for slow- vs. fast-dried graphite anodes.[1] These authors had suggested that the most likely reasons for the poor rate capability of fast-dried anodes would be either the suppression of the charge transfer resistance by thick binder films covering the graphite particles near the separator-side of the electrode or poor conductivity near the CC-side of the electrode due to the migration of carbon black. The latter clearly can be ruled out in the present case. On the other hand, since our impedance model based on R_{ion} gradients across the thickness of the electrode (Fig. 4) very well describes the experimental EIS response for electrodes with binder gradients (see Fig. 5b and Figs. 6a, 6b), our study suggests that the underlying reason for the inferior rate capability of electrodes with strong binder migration to the top of the electrode may be caused by a high ionic resistance in the electrolyte phase near the anode/separator interface. Under this hypothesis, the
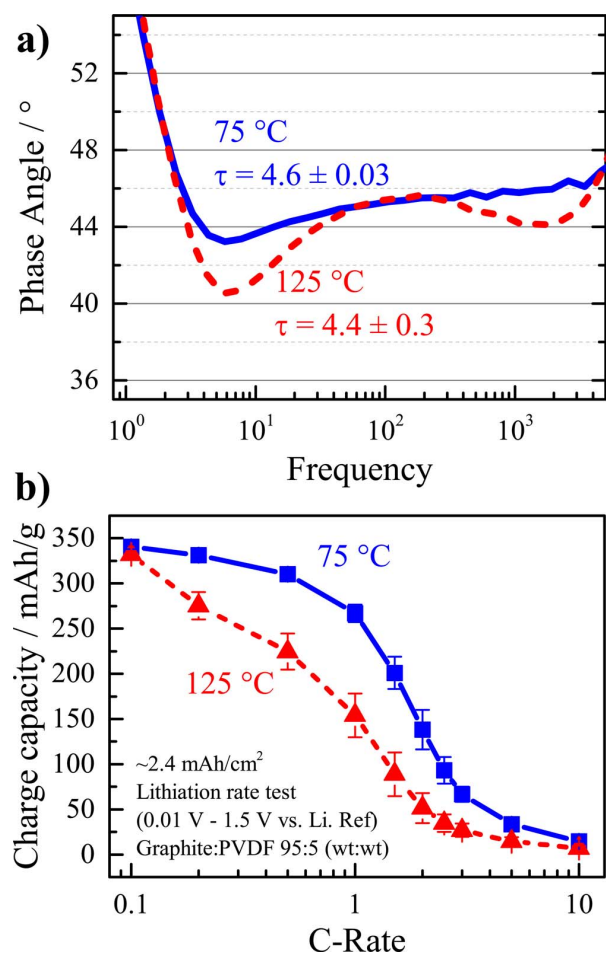
Figure 7. Impedance characteristics and charge rate capability of graphite electrodes with areal capacities of ∼2.4 mAh/cm^2 (corresponding to ∼7.4 mg$_{graphite}$/cm^2 (±2%) and electrode thicknesses of ∼74 μm (±2%)) dried at either 75°C (blue lines/symbols) or 125°C (red dashed lines/symbols). a) HFR-corrected phase angle plots and tortuosity values obtained from symmetric cell measurements with non-intercalating electrolyte (∼10 mM TBAClO$_4$ in EC:EMC 3:7). b) Charge (i.e., lithiation) capacity vs. C-rate for cycling the graphite electrodes between 1.5 V and 0.01 V vs. a Li-metal reference electrode. The error bars show the standard deviation of independent measurements with three nominally identical electrodes.

explanation for the inferior charge rate capability of the graphite anode dried at 125°C would be an inferior access of lithium ions into the bulk of the anode due to a partially pore-blocking binder layer at/near the anode/separator interface.

Summarizing the above analysis, we would like to point out that it is not yet possible to quantitatively correlate binder gradients with R_{ion} gradients, even though it is quite clear from the above comparison that the EIS response calculated for different R_{ion} profiles behaves analogous to the EIS response measured for electrodes with experimentally determined binder gradients. Entirely unclear at this point is the distribution of the migrated binder within the plane of the electrode (parallel to the current collector), as it could either deposit as a homogeneous binder layer over the graphite particles or deposit in a web-like form which could span across the (sub-)μm-sized pores between the graphite particles, thereby preventing a homogeneous influx of lithium ions into the interior of the graphite electrode. The latter phenomenon was observed for fuel cell electrodes, where depending on the catalyst ink's solvent type large ionomer patches were observed, covering large cross-sectional areas of the electrode paral-

lel to the electrode surface.[23] Quite clearly, an electrode performance model would have to consider the in-plane distribution on the binder near the anode/separator interface. Similar effects may also be the origin of the so-called "rollover" failure reported by Burns et al., who suggested that during extended battery cycling, the pores at the top of the electrode (separator-side) are becoming clogged and thereby cause the "rollover" failure, i.e., the point when batteries quickly lose their capacity over a short amount of cycles.[24] Such a mechanism resembles the modeled behavior above (Fig. 3, profile *st*). As it is possible to measure impedance in blocking condition in-situ using a three electrode setup,[25,26] this failure mechanism could be detected by analyzing the phase angle plot of the impedance spectrum.

The effect of binder migration may be one of the reasons for the discrepancies between EIS and X-Ray tomography measurements when it comes to tortuosity determination. Recently Landesfeind et al.[17] showed that an at least partially unresolved binder distribution in 3D reconstructed electrodes causes an underestimation of tortuosity values compared to impedance measurements, an effect which exacerbates the dilemma faced by groups using 3D reconstruction techniques to model transport in porous battery electrodes. However, additional care also has to be taken when determining tortuosities from impedance data, as this approach usually uses homogeneous transmission line models and would thus misinterpret the extracted R_{ion} and tortuosity values, which only have a well-defined meaning in a macro-homogeneous battery model in the absence of strong binder gradients. Conversely, in the presence of strong binder gradients (i.e., for fast-dried electrodes or electrodes dried at high temperature), the tortuosities extracted from impedance analysis are apparent tortuosities which obviously cannot be directly applied to a macro-homogeneous battery model.

The here provided EIS analysis approach is most useful when comparing electrodes of the same composition and loading, but with different drying/aging history. A quick impedance measurement in blocking condition (in situ[26] or in a symmetric cell with a blocking electrolyte)[18] is sufficient to collect the necessary data. Comparing the phase angle plots, one can quickly draw qualitative conclusions about the presence of any binder gradients and on the expected performance of the electrodes (see Fig. 7) and whether the obtained tortuosity value is suitable for use in a macro-homogeneous electrode model. Hence the phase angle minimum in the phase angle plot is an extremely important criterion to determine the presence of significant binder gradients and should not be neglected in the analysis of impedance data.

Conclusions

Up to now, visualizing binder migration required extensive and time consuming experimental effort, such as EDS. The analysis method in this publications gives the reader an additional tool to quickly screen electrodes for their homogeneity. Impedance model results show how high resistances toward the separator side of the electrode increase the overall resistance of the electrode significantly. This was verified by experimentally inducing binder migration by drying electrodes at low and high drying rates. EDS and impedance measurements combined confirmed that changes in the impedance spectrum give qualitative information on the extent of the binder gradient. Simple phase angle minimum analysis together with ionic resistances gathered from the same measurement give information about the presence of binder gradients and therefore the expected electrochemical performance. The ionic resistances gathered have to be considered with caution when applying them to an electrochemical model. Any calculated tortuosity is a mere apparent tortuosity and is, in the case of strong binder gradients, not representative for the entire electrode. Electrodes of similar apparent tortuosity but different degrees of binder gradients show significant differences in performance. While the exact mechanism of the poor performance of fast dried electrodes is still not clear, this analysis gives additional insight into the resistances within an electrode and help explain this phenomenon.

ORCID

Robert Morasch ⓘ https://orcid.org/0000-0002-9931-1022
Johannes Landesfeind ⓘ https://orcid.org/0000-0003-0333-2185
Bharatkumar Suthar ⓘ https://orcid.org/0000-0002-8612-9483

References

1. S. Jaiser, M. Müller, M. Baunach, W. Bauer, P. Scharfer, and W. Schabel, *J. Power Sources*, **318**, 210 (2016).
2. M. Müller, L. Pfaffmann, S. Jaiser, M. Baunach, V. Trouillet, F. Scheiba, P. Scharfer, W. Schabel, and W. Bauer, *J. Power Sources*, **340**, 1 (2017).
3. B. G. Westphal, H. Bockholt, T. Günther, W. Haselrieder, and A. Kwade, *ECS Trans.*, **64**, 57 (2015).
4. C.-C. Li and Y.-W. Wang, *J. Electrochem. Soc.*, **158**, A1361 (2011).
5. S. Jaiser, A. Friske, M. Baunach, P. Scharfer, and W. Schabel, *Dry. Technol.*, **35**, 1266 (2017).
6. H. Hagiwara, W. J. Suszynski, and L. F. Francis, 8 (2013).
7. S. Jaiser, J. Kumberg, J. Klaver, J. L. Urai, W. Schabel, J. Schmatz, and P. Scharfer, *J. Power Sources*, **345**, 97 (2017).
8. F. Font, B. Protas, G. Richardson, and J. M. Foster, *J. Power Sources*, **393**, 177 (2018).
9. M. Stein, A. Mistry, and P. P. Mukherjee, *J. Electrochem. Soc.*, **164**, A1616 (2017).
10. J. Landesfeind, A. Eldiven, and H. A. Gasteiger, *J. Electrochem. Soc.*, **165**, A1122 (2018).
11. G. Paasch and P. H. Nguyen, *Electrochem. Appl.*, **1**, 1 (1997).
12. P. H. Nguyen and G. Paasch, *J. Electroanal. Chem.*, **460**, 63 (1999).
13. H. Keiser, K. D. Beccu, and M. A. Gutjahr, *Electrochim. Acta*, **21**, 539 (1976).
14. T. F. Fuller, M. Doyle, and J. Newman, *J. Electrochem. Soc.*, **141**, 1 (1994).
15. M. Doyle, T. F. Fuller, and J. Newman, *J. Electrochem. Soc.*, **140**, 1526 (1993).
16. M. Ender, A. Weber, and E. Ivers-Tiffée, *Electrochem. commun.*, **34**, 130 (2013).
17. J. Landesfeind, M. Ebner, A. Eldiven, V. Wood, and H. A. Gasteiger, *J. Electrochem. Soc.*, **165**, A469 (2018).
18. J. Landesfeind, J. Hattendorff, A. Ehrl, W. A. Wall, and H. A. Gasteiger, *J. Electrochem. Soc.*, **163**, A1373 (2016).
19. S. Solchenbach, D. Pritzl, E. J. Y. Kong, J. Landesfeind, and H. A. Gasteiger, *J. Electrochem. Soc.*, **163**, A2265 (2016).
20. S. J. Cooper, A. Bertei, D. P. Finegan, and N. P. Brandon, *Electrochim. Acta*, **251**, 681 (2017).
21. I. V. Thorat, D. E. Stephenson, N. A. Zacharias, K. Zaghib, J. N. Harb, and D. R. Wheeler, *J. Power Sources*, **188**, 592 (2009).
22. D. Kramer, S. A. Freunberger, R. Flückiger, I. A. Schneider, A. Wokaun, F. N. Büchi, and G. G. Scherer, *J. Electroanal. Chem.*, **612**, 63 (2008).
23. S. A. Orfanidi, P. J. Rheinländer, N. Schulte, and H. A. Gasteiger, *Submitted* (2018).
24. J. C. Burns, A. Kassam, N. N. Sinha, L. E. Downie, L. Solnickova, B. M. Way, and J. R. Dahn, *J. Electrochem. Soc.*, **160**, A1451 (2013).
25. J. Landesfeind, D. Pritzl, and H. A. Gasteiger, *J. Electrochem. Soc.*, **164**, A1773 (2017).
26. D. Pritzl, J. Landesfeind, S. Solchenbach, and H. A. Gasteiger, *J. Electrochem. Soc.*, **165**, A2145 (2018).

3.1.3 Methods—Understanding Porous Electrode Impedance and the Implications for the Impedance Analysis of Li-Ion Battery Electrodes

The article entitled "Methods—Understanding Porous Electrode Impedance and the Implications for the Impedance Analysis of Li-Ion Battery Electrodes" was submitted to the peer-reviewed Journal of the Electrochemical Society in May 2021 and published in July 2021 as an open-access article under the terms of the Creative Commons Attribution Non-Commercial No Derivates 4.0 License. The permanent web link can be found under: https://iopscience.iop.org/article/10.1149/1945-7111/ac1892/meta

The analysis of porous electrodes posts its own challenges, as there are several resistances which influence the impedance spectrum of electrodes, most notably the charge transfer resistance, R_{ct}, and the resistance of the electrolyte in the pores, R_{ion}. Other resistances such as, e.g., the electrical resistance of the electrode can usually be neglected. The impedance response of a porous electrode changes in spectral shape and in the required simplified analysis equation, depending on the ratio of R_{ct} and R_{ion}. For $R_{ct} \gg R_{ion}$, the impedance is dominated by the R_{ct} semi-circle with a 45° line at higher frequencies representing the pore resistance. The electrode's low-frequency resistance can then be described by $R_{LF} = R_{ion}/3 + R_{ct}$. Extracting both resistances from such a spectrum is possible as both show unique features within the spectrum (the 45° straight line and the semi-circle). For $R_{ct} \ll R_{ion}$, the spectrum and the necessary analysis method changes. While the spectrum still shows a 45° line at higher frequencies and ends in a semi-circle at lower frequencies, the low-frequency resistance must be defined by a new simplified equation, namely $R_{LF} = \sqrt{R_{ct}R_{ion}}$. From the equation it becomes clear that changes in electrode loading do not change the low-frequency resistance as R_{ct} scales inversely with loading and R_{ion} scales linearly with the electrode loading. Thus, any number of combinations of R_{ct} to R_{ion} can give the same spectrum. The analysis practically becomes impossible without a separate measurement of R_{ion} or R_{ct}, demonstrated in an analysis of simulated and experimentally fitted impedance spectra, which showed that the fitting residuals between different simulated

spectra are smaller than the residuals of practically fitted spectra, effectively preventing the user to differentiate between them.

The reason for the apparently invariant electrode resistance with loading is the limitation in probing depth into the electrode. Once the pore resistance is high enough, the EIS measurement effectively only probes the top of the electrode. This also means that, if the electrode resistances are not homogeneously distributed, the measurement is only representative for the top part of the electrode, i.e., the part near the separator interface.

The publication additionally contains instructions on the analysis of porous electrode impedances and gives practical boundaries, showing which ratio of R_{ct} to R_{ion} constitutes a kinetically or transport limited electrode.

Author contributions

R.M. conducted the electrochemical measurements and evaluated the data. J.K. conducted preliminary electrochemical measurements. B.S. provided the current-distribution analysis. R.M. and B.S. developed the analysis guidelines and error analysis. R.M. wrote the manuscript. R.M., J.K, H.A.G. and B.S. discussed the results and revised the manuscript.

Methods—Understanding Porous Electrode Impedance and the Implications for the Impedance Analysis of Li-Ion Battery Electrodes

Robert Morasch,[1,z] Josef Keilhofer,[1,2] Hubert A. Gasteiger,[1] and Bharatkumar Suthar[3]

[1]*Chair of Technical Electrochemistry, Department of Chemistry and Catalysis Research Center, Technical University of Munich, Munich, Germany*
[2]*current address: Department of Mechanical Engineering, Institute for Machine Tools and Industrial Management (iwb), Technical University of Munich, Munich, Germany*
[3]*Department of Chemical Engineering, Indian Institute of Technology Bombay, Mumbai 400076, India*

Two of the main factors influencing the performance of Li-ion battery (LIB) electrodes are the kinetic losses due to the charge transfer resistance of the active material (R_{ct}) and the ionic transport resistance in the electrolyte phase within the electrode pores (R_{ion}). Seeking to increase the energy density of LIBs, ever higher active material loadings are applied, resulting in thicker electrodes for which R_{ion} becomes dominant. As electrochemical impedance spectroscopy is commonly used to quantify R_{ct} of electrodes, understanding the impact of R_{ion} on the impedance response of thick electrodes is crucial. By use of a simplified transmission line model (TLM), we simulate the impedance response of electrodes as a function of electrode loading. This will be compared to the impedance of graphite anodes (obtained using a micro-reference electrode), demonstrating that their impedance response varies from purely kinetically limited at 0.6 mAh cm^{-2} to purely transport limited at 7.5 mAh cm^{-2}. We then introduce a simple method with which R_{ct} and R_{ion} can be determined from the electrode impedance, even under transport limited conditions. Finally, we show how the initially homogenous ionic current distribution across porous electrodes under kinetically limited conditions becomes severely inhomogeneous under transport limited conditions.

Analyzing the electrochemical impedance spectroscopy (EIS) spectra of electrochemical cells and electrodes requires an in-depth knowledge of the underlying kinetic and transport processes and their appropriate representation via an equivalent circuit model. The perhaps most commonly used circuit element to describe the response of electrochemical systems is the so-called R/C element, i.e., the parallel arrangement of a resistor and a capacitor. This element can be used to describe a multitude of interfaces, most prominently the electrochemical interface between an electrode and an ionically conductive electrolyte, e.g., the interface between a battery active material and the electrolyte. When describing the electrochemically active surface area of the active material with an R/C element, the resistor represents the kinetic resistance for the faradaic charge transfer reaction and the capacitor models the capacitive effect arising from the electrochemical double layer forming at the interface of the electrochemically responsive electrode material surfaces (i.e., the active material and the conductive carbon) and the ion conducting electrolyte.[1] The resulting spectrum for such an R/C circuit element in a Nyquist plot is a semicircle, with a diameter that corresponds to the resistance R and that spans over a frequency range that is in part also defined by the capacitive element C. As actual electrochemical systems generally do not show a perfect capacitive behavior and are generally better described by a so-called constant phase element Q, the R/C element (resulting in a semicircle in a Nyquist plot) is typically replaced by an R/Q element that results in a slightly depressed semicircle.

In addition to the charge transfer resistance (R_{ct}) and the electrode capacitance (Q_{dl}), the electrode impedance of porous Li-ion battery electrodes also depends on the ionic resistance within the electrolyte phase contained in the pores of the electrode (R_{ion}). For this reason, the quantification of the charge transfer resistance of a LIB electrode and its change over the course of cycling from impedance measurements is not straightforward and requires a more refined equivalent circuit model. A commonly used representation of the impedance of a porous electrode is given by the so-called transmission line model (TLM), which in its simplified form is here composed of a resistive path (with R_{ion} as the sum of the resistance elements r_{ion}, stemming from the electrolyte in the pores of the electrode) as well as of r_{ct}/q_{dl} elements that act as local current source or sink to the resistive path (see top part of Fig. 1). The r_{ct}/q_{dl} elements cumulatively give rise to the overall charge transfer resistance (R_{ct}) and the overall double layer capacitance (Q_{dl}), as described in the caption of Fig. 1. Other possible contributions to the electrode impedance are not being considered for the following reasons: (i) electrical resistances across the electrode are typically negligible compared to ionic resistances, particularly for graphite anodes that are in the focus of this study[2]; (ii) solid and electrolyte Warburg diffusion elements (in the electrodes and in separator) are not expected to influence the impedance spectra within the here examined frequency region[3,4]; (iii) the separator resistance, since it only results in a constant high-frequency offset of the spectra. A review of EIS applications including different circuit elements can be found in Ref. 5.

Driven by the demand to increase the energy density of LIBs, increasingly higher active material (AM) loadings (in units of mg$_{AM}$ cm^{-2}), corresponding to higher areal capacities (C_{areal}, in units of mAh cm^{-2}, not to be confused with the previously defined capacitance C), are being employed, since this leads to a lower mass fraction of inactive materials (current collectors, separators, current tabs) and therefore also lower cost.[6,7] Conceptually, a doubling of the areal capacity, assuming the same electrode composition and morphology (i.e., porosity and tortuosity), has the following consequences: (i) a doubling of the material surface area that is in contact with the electrolyte, thus a doubling of the electrode capacitance (i.e., $Q_{dl} \propto C_{areal}$); (ii) a doubling of the active material surface area, resulting in a halving of the charge transfer resistance (i.e., $R_{ct} \propto 1/C_{areal}$); and, (iii) a doubling of the electrode thickness, resulting in a doubling of the ionic resistance (i.e., $R_{ion} \propto C_{areal}$). Figure 1 shows a schematic of how the increase in active material loading (i.e., of areal electrode capacity C_{areal} which in turn scales with electrode thickness) affects the two resistances. Starting at an arbitrary active material loading (referred to as "Loading 1") with a

zE-mail: robert.morasch@tum.de

ratio of the charge transfer resistance over the ionic resistance of $R_{ct}/R_{ion} \equiv A/B$, doubling the loading effectively doubles the ionic resistance and halves the charge transfer resistance, resulting in $R_{ct}/R_{ion} = (1/2)/2 \times A/B$ for the electrode with a two-fold higher active material loading ("Loading 2"). Further increasing the active material loading by a factor of 3 and 4 results in $R_{ct}/R_{ion} = (1/3)/3 \times A/B$ and $R_{ct}/R_{ion} = (1/4)/4 \times A/B$, respectively. In other words, a 4-fold increase in areal capacity is expected to lead to a 16-fold decreased R_{ct}/R_{ion} value.

As Li-ion batteries make use of an intercalation reaction, i.e., the lithium is stored in the active material, lithium ions eventually have to reach the interface of the electrode with the current collector (CC) (right-hand side of Fig. 1) during the lithiation of the active material particles, or have to be transported through the electrode and the separator to the opposing separator/electrode interface (left-hand side) during delithiation. For *very thin electrodes* (i.e., for very low active material loadings and areal capacities), R_{ion} is negligible and the electrode impedance is dominated by R_{ct} (furtheron referred to as *kinetically limited*). On the other hand, for high loaded *thick electrodes* (i.e., for high areal capacities), R_{ion} will dominate the electrode impedance due to the increased ion conduction path length through the electrode and the simultaneously decreased R_{ct} (furtheron referred to as *transport limited*). Which of the two limiting cases become dominant for a given active material loading (or areal capacity) is a question addressed in this work. The impact of the ion conduction resistance through the porous electrodes on EIS spectra has previously been studied, but these earlier studies neglected the influence of low R_{ct}/R_{ion} values on the mathematical response of the transmission line model,[8–12] so that these findings are only relevant for low active material loadings. Therefore, we have extended this analysis to the low R_{ct}/R_{ion} regime that, as we will show, is relevant for LIB graphite anodes with currently used areal capacities of ~3 mAh cm^{-2} and beyond.

To understand the transition of the impedance response of a LIB electrode from the kinetically limited regime at low active material loadings (i.e., at high R_{ct}/R_{ion} values) to the transport limited regime at high active material loadings (i.e., at low R_{ct}/R_{ion} values), we first simulate the EIS spectra using the transmission line model shown in Fig. 1 for different R_{ct}/R_{ion} values. We will show how the impedance spectrum changes from exhibiting an R_{ct}-dominated semicircle at high R_{ct}/R_{ion} values to a non-semicircle shaped spectrum at low R_{ct}/R_{ion} from which the determination of the charge transfer resistance requires additional considerations. We then compare these simulated spectra to experimentally obtained impedance spectra of LIB graphite anodes with widely varying graphite loadings, corresponding to areal capacities of C_{areal} = 0.6–7.5 mAh cm^{-2}, showing that their impedance response indeed varies from purely kinetically limited (for 0.6 mAh cm^{-2}) to purely transport limited (for 7.5 mAh cm^{-2}). An additional current distribution analysis gives insight into the change in current homogeneity throughout the electrode. Lastly we demonstrate how to analyze these impedance spectra without the need for a fitting software to give the user the ability to analyze and deconvolute R_{ct} from the electrode impedance spectrum.

Experimental

Slurry preparation and drying.—Graphite (T311, Timcal, 19 μm D50, 3 m^2 g^{-1}) and polymer binder (polyvinylidene fluoride (PVDF), Kynar, Arkema) at a ratio of 95:5 (wt:wt) were mixed with N-Methyl-2-pyrrolidone (NMP, Sigma Aldrich, anhydrous, 99.5%) at a solid:liquid ratio of 5:4 (wt:wt) in a planetary mixer (Thinky ARV-310) at 2000 rpm for five minutes. The prepared graphite slurries were coated onto a copper current collector foil (MTI, 12 μm) attached to a glass plate using a gap bar coater (RK PrintCoat Instruments, UK) at wet film thicknesses of 30 μm, 100 μm, 200 μm, and 450 μm to achieve areal capacities of 0.6, 1.5, 2.9, and 7.5 mAh cm^{-2}, respectively (referenced to a nominal

graphite capacity of 350 mAh g$_G^{-1}$), and dried in an oven at 50 °C. The dried electrodes were punched out to a diameter of 10.95 mm (equating to an area of ~0.94 cm^2) using an electrode punch (Hohsen Corp. OSAKA, Japan), and compressed in a press using a pressure of ~100 MPa. The specifications of the graphite electrodes with regards to graphite loading (in mg$_G$ cm^{-2}), electrode thickness, and electrode porosity are summarized in Table I. Densities used for the porosity calculations were 2.26 g cm^{-3} for graphite and 1.77 g cm^{-3} for PVDF.

Cell assembly, formation and impedance measurement.—For electrochemical impedance analysis, a three-electrode cell setup (Swagelok® T-cell) with a gold-wire reference electrode (GWRE; described in more detail in Fig. 1b in Ref. 13) was used. The cells were built inside an argon filled glove box (MBraun, 25 °C ± 1 °C, oxygen and water content <0.1 ppm, Ar 5.0, Westfalen). All cell parts were dried at 120 °C in a vacuum oven (Büchi, Switzerland) for 8 h before being transferred into the glovebox.

The cells were assembled with a graphite working electrode, two porous glass fiber separators with a diameter of 11 mm (VWR, 250 μm uncompressed thickness, 90% porosity), and a counter electrode consisting of a free-standing graphite electrode that was firmly attached to the metallic lithium foil (0.45 mm thickness and 11 mm diameter, Rockwood Lithium), as described in Ref. 14 80 μl of LP57–2 electrolyte (1 M LiPF$_6$ in EC:EMC 3:7 (wt:wt) + 2 wt% VC, battery grade, BASF) were added to the cells.

Using a potentiostat (Bio-Logic Science Instruments, France), the gold-wire reference electrode was lithiated at 150 nA for 1 h via the counter electrode in a temperature-controlled chamber (25 °C, Binder). The cycling protocol started with a 3 h open circuit voltage phase to allow for complete wetting of the electrode. Two formation cycles for the graphite working electrode were performed galvanostatically at C/10 (referenced to a nominal specific capacity of 350 mAh g$_G^{-1}$) between 2V and 40 mV vs Li$^+$/Li. The electrode was then brought to 50% state of charge (SOC) at C/10. Potentiostatic electrochemical impedance measurements were performed at open circuit voltage (OCV) from 30 kHz to 0.1 Hz and with an excitation of 10 mV; the use of the micro-reference electrode (i.e., the GWRE) allowed for a rigorous determination of the impedance response of the graphite electrode.

Current distribution analysis.—The theoretical background for the current distribution analysis can be found in the Appendix.

Data simulation and fitting.—Impedance simulation and fitting was performed with a MATLAB-based application ("EIS Breaker," © J. Landesfeind) based on the fminsearch MATLAB function using a Nelder-Mead simplex algorithm and modulus weighing. For all data fitting, only the value of R_{ion} was fixed, while the remaining parameters (R_{ct}, Q_{dl} and α) were fitted.

Results and Discussion

Aspects of this work in the context of literature.—Previous studies have shown impedance analyses conducted with changing ratios of R_{ct}/R_{ion}, most prominently done by Ogihara et al.,[8–11] who built a baseline theory for porous electrode impedance analysis. Their analysis is based on a simplification for the low-frequency impedance that, as we will show here, is only valid for larger values of R_{ct}/R_{ion}, a fact that is not specified in any of their publications. While these publications study a large range of R_{ct}/R_{ion}, the experimental and simulated spectra analysis stops short of reaching transport limited impedances and are thus in a range where the error made from their simplifications are still lowsmall. This is due to the fact that their studies are concerned exclusively with the impedance response of cathode electrodes, which for practical areal capacities still have high R_{ct}/R_{ion} values. On the other hand, as will be shown in the following, this is not true for graphite electrodes, which at
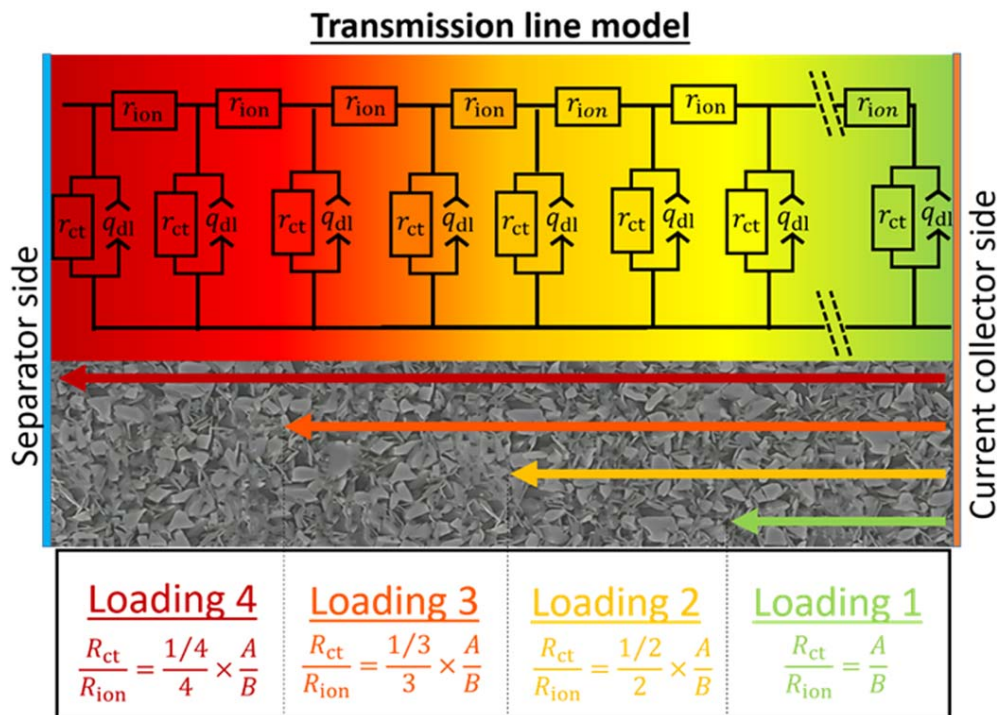
Transmission line model

Figure 1. Middle panel: schematic representation of a porous LIB electrode, extending between the separator/electrode interface (left) and the electrode/current collector interface (right). Top panel: simplified transmission line model (TLM) equivalent circuit with pore resistance element r_{ion}, charge transfer resistance element r_{ct}, and capacitive elements q_{dl}, whereby $\sum r_{ion} = R_{ion}$, $\sum 1/r_{ct} = 1/R_{ct}$, and $\sum q_{dl} = Q_{dl}$. Bottom panel: Influence of loading changes on the ionic resistance R_{ion} and the charge transfer resistance R_{ct}. Starting at an arbitrary active material loading where R_{ct} takes the value A and R_{ion} takes the value B, so that $R_{ct}/R_{ion} = A/B$ ("Loading 1"), a 2-fold increase of the loading (i.e., of the areal capacity) increases the pore resistance by a factor of 2 due to the increase in electrode thickness (assuming constant porosity and tortuosity) and decreases the charge transfer resistance by a factor of 2 due to the increased electrochemically active surface area, resulting in a 4-fold lower R_{ct}/R_{ion} value ("Loading 2"). Increasing the loading by 3- or 4-fold, changes the resistances and R_{ct}/R_{ion} accordingly.

practical areal capacities have R_{ct}/R_{ion} values of $\ll 1$. To the best of our knowledge, we therefore show for the first time how to analyze and understand porous electrode impedance spectra over the full range of R_{ct}/R_{ion}. (from $\gg 1$ to $\ll 1$).

Simulated and experimental impedances of porous electrodes.—This subsection discusses the mathematical background of the transmission line model shown in Fig. 1 and examines the simulated electrode impedance spectra for different fictitious areal capacities. The simulated spectra are then compared to experimentally obtained impedance spectra of graphite anodes (acquired using a micro-reference electrode) of various areal capacities (see Table I). A subsequent analysis of the simulated current distribution vs fictitious areal capacity in the following subsection will give insights into the possible ramifications of increasing areal capacities for the charging/discharging behavior of LIB electrodes.

The equivalent circuit model shown in Fig. 1 is represented mathematically by the following equation (see Refs. 15, 16 for the general derivation)):

$$\mathbf{Z} = \sqrt{\frac{R_{ion}}{\left((j\omega)^{\alpha} Q_{dl} + \frac{1}{R_{ct}} \right)}} \coth\left(\sqrt{R_{ion}\left((j\omega)^{\alpha} Q_{dl} + \frac{1}{R_{ct}} \right)} \right) \quad [1]$$

where **Z** [Ω] is the complex impedance of the electrode, ω [rad/s] is the radial frequency, R_{ct} [Ω] and R_{ion} [Ω] are the charge transfer resistance of the entire electrode, and j is the imaginary unit. Furthermore, the ideal double layer capacitor element (C_{dl}) is replaced in Eq. 1 by a constant phase element, defined as $(j\omega)^{\alpha} Q_{dl}$ with $\alpha (0 < \alpha \leqslant 1)$. The impedance given by Eq. 1 neglects the electronic resistance of the solid phase (usually negligible for practical electrodes),[2,17] the diffusion phenomena of electroactive species in both electrolyte and electrode (usually appearing at very low frequencies), and the ionic resistance of the electrolyte in the separator. As Eq. 1 represents the porous electrode only (as the separator resistance is not included), its limiting case for infinitely high frequencies is **Z** = 0 (also clear from Eq. 1 that as $\omega \to \infty$,

Table I. Properties of the various here used graphite electrodes with different areal capacities by varying the graphite mass loading. The accuracy of the thickness measurement is ±3 μm (Lifematic VL-50, Mitutoyo, Japan), and the here listed electrode coating thicknesses were obtained by subtracting the thickness of the current collector. Porosities were determined by dividing the theoretical bulk volume of the graphite and PVDF components (using bulk densities of 2.26 g cm^{-3} and 1.77 g cm^{-3}, respectively) by the total electrode volume determined by the measured electrode thickness.

Areal Capacity [mAh cm^{-2}]	Graphite Mass Loading [mg$_G$ cm^{-2}]	Thickness [μm]	Porosity [%]
7.5	21.5	165	42
2.9	8.2	65	43
1.5	4.3	36	46
0.6	1.7	14	46

$Z \rightarrow 0$). For the low-frequency resistance, i.e., as $\omega \rightarrow 0$, Eq. 1 simplifies to:

$$L \equiv \mathbf{Z}_{\omega \rightarrow 0} = \sqrt{R_{ion} \cdot R_{ct}} \ \coth(\sqrt{R_{ion}/R_{ct}}) \qquad [2]$$

This equation represents the low-frequency resistance (L [Ω]) that would be obtained from an impedance measurement for a porous electrode, not taking into account the separator or the solid or liquid diffusion Warburg resistance. Next, we define $\vartheta \equiv R_{ct}/R_{ion}$ in order to simplify Eq. 2 as follows:

$$\frac{L}{R_{ion}} = \sqrt{\vartheta} \ \coth(1/\sqrt{\vartheta}) \qquad [2a]$$

In the following, we will describe the limiting cases, when either the charge transfer resistance (R_{ct}) dominates the impedance response, further on referred to as *kinetically limited*, or when the ionic resistance (R_{ion}) in the electrolyte phase within the electrode pores dominates the impedance response, further on referred to as *transport limited*. The former occurs for $R_{ion} \ll R_{ct}$, in which case the term $\sqrt{R_{ion}/R_{ct}}$ in the coth function in Eq. 2 becomes very small, so that the coth function can be approximated by:

$$\lim_{y \rightarrow 0} \coth(y) = \frac{1}{y} + \frac{y}{3} + \text{higher order terms} \qquad [3]$$

Simplifying Eq. 2 by this approximation of the coth function (neglecting the higher order terms), the kinetically limited value of the low-frequency electrode impedance ($L|_{(R_{ion} \ll R_{ct})}$) becomes:

$$L|_{(R_{ion} \ll R_{ct})} = R_{ct} + \frac{R_{ion}}{3} \qquad [4]$$

Similar to Eqs. 2a, 4 can also be expressed in terms of $\vartheta \equiv R_{ct}/R_{ion}$ as follows:

$$\frac{L}{R_{ion}} \bigg|_{(R_{ion} \ll R_{ct})} = \vartheta + \frac{1}{3} \qquad [4a]$$

On the other hand, in the transport limited regime, where $R_{ion} \gg R_{ct}$, the term $\sqrt{R_{ion}/R_{ct}}$ in the coth function in Eq. 2 becomes very large, so that the coth function approaches 1 (i.e., $\lim_{y \rightarrow \infty} \coth(y) \rightarrow 1$) and Eq. 2 simplifies to the expression for the transport limited low-frequency impedance ($L|_{(R_{ion} \gg R_{ct})}$, also see Refs. 3, 15 for derivation):

$$L|_{(R_{ion} \gg R_{ct})} = \sqrt{R_{ion} R_{ct}} \qquad [5]$$

Expressing Eq. 5 via the ϑ variable leads to the following equation:

$$\frac{L}{R_{ion}} \bigg|_{(R_{ion} \gg R_{ct})} = \sqrt{\vartheta} \qquad [5a]$$

In summary, in the kinetically limited regime ($R_{ion} \ll R_{ct}$), Eq. 4 shows that R_{ct} constitutes the major fraction of the low-frequency resistance, so that the low-frequency resistance is a reasonably close measure of R_{ct}. On the other hand, in the transport limited regime ($R_{ion} \gg R_{ct}$), Eq. 5 shows that R_{ct} cannot be evaluated directly from the low-frequency resistance.

Figures 2a and 2b show the simulated impedance spectra of electrodes for which the effect of varying active material loadings was simulated by varying R_{ion} and R_{ct}. As outlined in the discussion of Fig. 1 and as shown in the bottom panel of Fig. 1, it was assumed that a doubling of the active material loading and thus of the areal capacity would result in a halving of the charge transfer resistance (i.e., $R_{ct} \propto 1/C_{areal}$) and in a doubling of the ionic resistance (i.e.,

$R_{ion} \propto C_{areal}$). Thus, the simulated R_{ct} values that are decreasing from 16 to 0.5 Ω (in steps of factors of 2) represent an increase in the simulated active material loading (or areal capacity) by an overall factor of 32; this is accompanied by a 32-fold increase of R_{ion} from 1 to 32 Ω (also in steps of factors of 2). Since the double layer capacitance is expected to increase with the active material loading (or areal capacity), the Q_{dl} value was scaled from an initial value of 0.25 mF for the lowest loading (represented by $R_{ct} = 16 \ \Omega$ and $R_{ion} = 1 \ \Omega$) by 0.25 mF $\times \dfrac{R_{ion}}{1\Omega}$ for higher loadings (assuming that $Q_{dl} \propto C_{areal}$ and that $\alpha = 1$). As will be shown later, the here chosen values for R_{ct}, R_{ion}, and Q_{dl} fall within the range of those obtained for graphite anodes with areal capacities of 0.6–7.5 mAh cm^{-2} (see Table III).

As an idealized reference case, we start our discussion of the simulated impedance spectra for a hypothetical electrode with a low active material loading that does not have any pore resistance (i.e., $R_{ct} = 16 \ \Omega$ and $R_{ion} = 0 \ \Omega$, with $Q_{dl} = 0.25$ mF). In this case, the simulated impedance spectrum only consists of a semicircle, represented by the dashed red line in Fig. 2a. Adding a 1 Ω ionic resistance (i.e., $R_{ct} = 16 \ \Omega$ and $R_{ion} = 1 \ \Omega$) barely changes the spectrum (orange line), except for the appearance of a short 45°-line region at high frequencies that represents the ionic resistance in the electrode pores (clearly visible in Fig. 2b). The 45°-line extends from Re(Z) = 0 Ω until ~0.33 Ω, corresponding to 1/3 R_{ion}, followed at lower frequencies by a semicircle with a diameter of 16 Ω, summing up to an overall low-frequency resistance of $L = 16.33 \ \Omega$, as predicted by Eq. 4. A spectrum exhibiting such clear features allows the user to directly extract the numerical values of both R_{ct} and R_{ion} from the spectrum, as both components are represented by unique features (viz., by the diameter of the semicircle and by the real axis extension of the 45°-line, respectively).

In order to simulate the increase of the active material loading by a factor of 2, the ionic resistance is being doubled (from 1 to 2 Ω) and the charge transfer resistance is being halved (from 16 to 8 Ω). The simulated impedance spectrum then shows a low-frequency resistance of 8.66 Ω, but still exhibits a clear 45°-line feature with an extension along the real axis of $R_{ion}/3$ (=2/3 Ω) as well as a pronounced semicircle with a diameter corresponding to R_{ct} (8 Ω; see yellow lines in Figs. 2a and 2b). A further simulated doubling of the active material loading by further increasing R_{ion} to 4 Ω and decreasing R_{ct} to 4 Ω, yields a low-frequency resistance of 5.33 Ω (green line) that is still well described by Eq. 4, even though R_{ct}/R_{ion} is now 1/1. Deviations from Eq. 4 are observed upon a further two-fold increase of the simulated active material loading (represented by $R_{ct} = 2 \ \Omega$ and $R_{ion} = 8 \ \Omega$; blue line), for which the simulated low-frequency resistance of 4.15 Ω (based on Eq. 1) differs from the 4.66 Ω predicted by Eq. 4 (kinetically limited regime) as well as from the 4.0 Ω predicted by Eq. 5 (transport limited regime). Hence, the electrode impedance response lies in the transition zone between the two limiting cases, and retrieving the values of R_{ct} and R_{ion} requires a more complex analysis, as described later in this publication.

Further increasing the simulated loading yields a, on the first glance, surprising result. The impedance spectra for higher simulated loadings (here R_{ct}/R_{ion} with 1/16 and 0.5/32, see dark purple line and light purple square symbols) not only have the same low-frequency resistance and fully overlap, but are also very similar to that obtained for $R_{ct}/R_{ion} = 2/8$ (blue line). This can be understood when looking at Eq. 5 that describes the transport limited regime, where a doubling of R_{ion} and a halving of R_{ct} simulates a doubling of the active material loading and results in the identical low-frequency resistance. Thus, in the transport limited regime, the impedance spectrum does not anymore provide any information on the individual values of R_{ion} and R_{ct}, as any combination of these two resistances will yield the same low-frequency resistance and, as a matter of fact, exhibit the practically identical impedance spectrum in a Nyquist plot. To determine R_{ion} and R_{ct} from an impedance
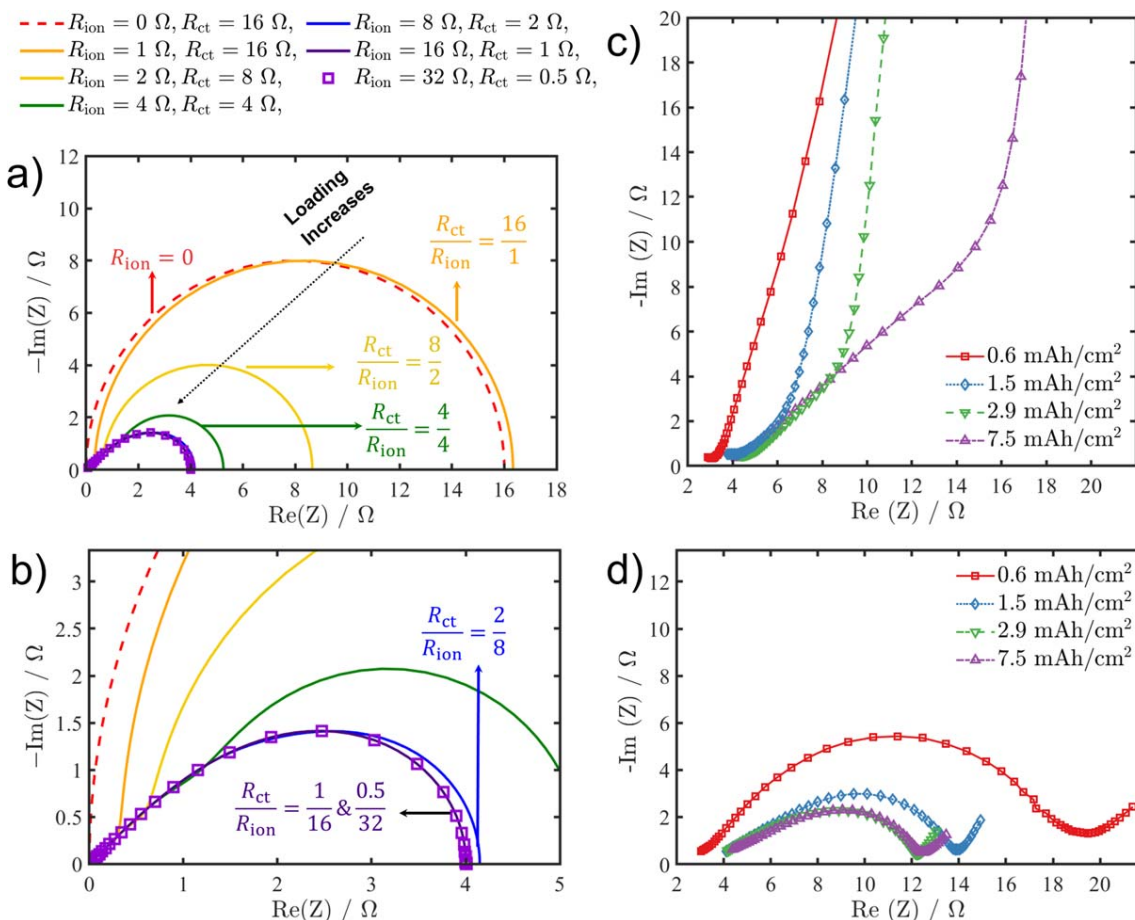
Figure 2. Electrode impedance spectra simulated acc. to Eq. 1 and measured for graphite anodes with different areal capacities. (a) Simulated electrode impedance spectra (Eq. 1). Parameters Q_{dl} = 0.25 mF with α for the constant phase element set to 1; Spectra are simulated for the frequency range of 100 kHz to 0.1 Hz. (b) Zoom into the high-frequency region of panel a. For decreasing R_{ct}/R_{ion} ratios (higher active material loadings), the distinct features of the 45°-line and the semicircle disappear and the spectrum merges into a single feature. (c) Experimentally obtained impedance spectra of graphite electrodes (measured via micro-reference electrode) with different areal capacities, recorded at 2 V vs Li$^+$/Li before formation (i.e., under blocking conditions). (d) Impedance spectra of the graphite electrodes at 50% SOC after two formation cycles, showing first a decrease in the low-frequency resistance (from 0.6 to 2.9 mAh cm^{-2}) and then a constant low-frequency resistance for 2.9 and 7.5 mAh cm^{-2}. The graphite anode impedance data between 30 kHz and 0.1 Hz were obtained by using a micro-reference electrode. The semicircle apex frequency for the experimental data is between 110 Hz (0.6 and 1.5 mAh cm^{-2}) and 139 Hz (2.9 and 7.5 mAh cm^{-2}).

spectrum in this regime, either one of these two resistances needs to be known or to be determined independently. For example, R_{ion} could be simply acquired via measurements in blocking conditions (i.e., conditions where no faradaic reaction is possible).[8,18–21] A more detailed description of how to analyze impedance spectra in the transport limited regime will be shown later on.

To understand whether the impedance spectra of practical Li-ion battery electrodes fall into the kinetically or transport limited regime, we measured impedance spectra of graphite anodes with different active material loadings, i.e., with areal capacities ranging from 0.6–7.5 mAh cm^{-2} (see Table I). Impedance spectra were acquired both before formation at 2 V vs Li$^+$/Li, corresponding to 0% SOC (representing blocking conditions, due to the very high R_{ct} of a pristine graphite electrode at this potential), as well as after two formation cycles and a partial charge to 50% SOC, as shown in Figs. 2c and 2d, respectively. The spectra of the pristine graphite electrodes acquired at 2 V vs Li$^+$/Li (= 0% SOC) exhibit the 45°-line feature (see Fig. 2c), as expected for blocking conditions,[8,18,19] in which case the extension of the 45°-line along the real axis corresponds to $R_{ion}/3$ (this will be further discussed in the context of Fig. 4a). Thus, a preliminary inspection of Fig. 2c shows that R_{ion} clearly increases with increasing areal capacity (i.e., with active material loading and electrode thickness), which was the basis for our interpretation of the simulated impedance spectra

(Figs. 2a and 2b). A quantitative analysis of our assumed relationship of $R_{ion} \propto C_{areal}$ will follow towards the end of this work.

The spectra in Fig. 2d show the graphite electrode impedances at 50% SOC after formation. The graphite electrode with the lowest areal capacity of 0.6 mAh cm^{-2} (red line/squares) exhibits a negligible ionic resistance, as indicated by the very short 45°-line at high frequencies, but shows a large kinetic resistance, as indicated by the large diameter of the semicircle that follows at lower frequencies. This impedance spectrum is qualitatively very similar to the simulated impedance spectra for R_{ct}/R_{ion} ratios of 16/1 and 8/2 (orange and yellow lines in Figs. 2a and 2b), except that the semicircle of the experimental spectrum is somewhat suppressed, indicating a lower α value (note that α = 1 was used for the simulated spectra). Upon increasing the areal capacity of the graphite electrode to 1.5 mAh cm^{-2} (blue line/diamonds in Fig. 2d), the electrode resistance is reduced substantially and the impedance spectrum exhibits a now continuous transition from a high-frequency ~45°-line feature to a suppressed semicircle feature. The experimental spectrum thus resembles the simulated spectra with R_{ct}/R_{ion} ratios somewhere in between 4/4 and 2/8 (green and blue lines in Figs. 2a and 2b). Finally, increasing the areal capacity of the graphite electrodes to 2.9 and 7.5 mAh cm^{-2} (green line/inverted-triangles and purple line/triangles in Fig. 2d), essentially identical impedance spectra are obtained, with an electrode resistance that is only

marginally smaller than that for the 1.5 mAh cm^{-2} electrode. Furthermore, the impedance spectra of the 2.9 and 7.5 mAh cm^{-2} graphite electrodes resemble the spectra simulated for R_{ct}/R_{ion} ratios somewhere in between 2/8 and 1/16 (blue and purple lines in Figs. 2a and 2b), indicating that their impedance response represents the transport limited regime. The 0.6 mAh cm^{-2} electrode also shows that the assumption of the simplified TLM with one kinetic R/C element is valid, as the sample shows only one semi-circle feature associated with the kinetics. It cannot be determined from these measurements whether this spectral feature also contains contributions from the solid electrolyte interphase (SEI) formed during the first charge of the anodes, as the SEI is generally also associated with a semi-circle feature.[22] This, however, should not influence the impedance analysis outlined in this publication.

In summary, upon increasing the areal capacity (i.e., the active material loading) of graphite electrodes, their low frequency electrode resistance does not significantly decrease for areal capacities above 1.5 mAh cm^{-2}, suggesting a compensation of the decreasing R_{ct} by the increasing R_{ion} as the areal capacity being increased, consistent with Eq. 5 that describes the transport limited regime of the electrode impedance. Prior to presenting a methodology by which R_{ct} can be obtained even under these conditions, we will first examine the current distribution at frequencies close to where the low-frequency resistance is being determined and will show the changing sampling depth into a porous electrode at that frequency.

Current distribution across an electrode in the R_{ct} and R_{ion} dominated domain.—The ratio of R_{ct}/R_{ion} strongly affects the way the current distributes over the electrode. Figure 3a shows the current density distribution for a given applied current, normalized to its maximum local value at the separator/electrode interface for electrodes with different R_{ct}/R_{ion} ratios. The expression for the normalized complex current density along with its associated equivalent circuit is shown in the Appendix (see Fig. A·1 and Eq. A·9) and it is valid only under the condition that R_{ct} and R_{ion} are dominating the current response, i.e., only within the frequency range where the double layer capacitance effect has become negligible (in this case below ~10^1 Hz) and where the diffusion in the solid and electrolyte phase is not yet significant (here above ~10^0 Hz). Practically, Eq. 9 and Fig. 3a describe the scaled complex current density distribution in the vicinity of the imaginary impedance minimum after the (suppressed) semicircle of the spectrum

of an electrode, i.e., near the point that marks the low-frequency resistance; based on the impedance data of the graphite electrodes shown in Fig. 2d, this occurs in the vicinity of ~1 Hz. This current distribution can thus be understood as the charging/discharging current toward the end of a short (on the order of 10^0 s) current pulse applied to the electrode and it is independent of the absolute current magnitude (provided that we are in the linear range of Butler-Volmer kinetics). Thus, this scaled current distribution across the electrode only depends on the R_{ct}/R_{ion} ratio and would be essentially identical for a C/10 or a 1C current pulse, so that it should closely reflect the current distribution after a short DCIR (direct current internal resistance) pulse, which is a commonly used diagnostic tool in Li-ion battery research.[23,24]

For a dominating R_{ct}, the current density distribution is mostly homogeneous throughout the electrode (lines in the red/orange shaded region, Fig. 3a). In such an electrode, the charge transfer reaction takes place (mostly) homogeneously throughout the electrode, and the active material particles would be charged or discharged uniformly across the electrode. Increasing R_{ion}, i.e., decreasing ϑ, leads to significantly lower currents towards the electrode/separator interface (i.e., near $x = 1$) and results in a less homogeneous current density distribution (green/blue shaded regions). In this case, active material particles at/near the separator/electrode interface (left side in Figs. 3a and 3b) are charged/discharged more extensively than particles at/near the electrode/CC interface. Ultimately, upon further decreasing ϑ (purple shaded region), the current distribution becomes so skewed that parts of the electrode are practically not participating in the reaction anymore during the impedance measurement (in the frequency range on the order of ~10^0 Hz). In such a case, the impedance response of the electrode is in the transport limited regime, and active material particles at/near the electrode/CC interface are not charged/discharged during the measurement.

The latter aspect is further illustrated in Fig. 3b, where the current distribution across electrodes with three different active material loadings (viz., δ_1, $\delta_2 = 2 \cdot \delta_1$, and $\delta_3 = 3 \cdot \delta_1$) and thicknesses is being examined, whereby the x-axis represents the electrode thickness at which a given loading is reached. For the lowest loaded electrode (δ_1), an R_{ct}/R_{ion} ratio of 1/16 was assumed, that according to Figs. 2a/2b and Fig. 3a falls within the transport limited regime. Consequently, the current density at the electrode/CC interface (at δ_1) is essentially zero (red circles in Fig. 3b). Increasing the loading by a factor of 2 to δ_2 and reducing R_{ct}/R_{ion} to 0.5/32 (blue
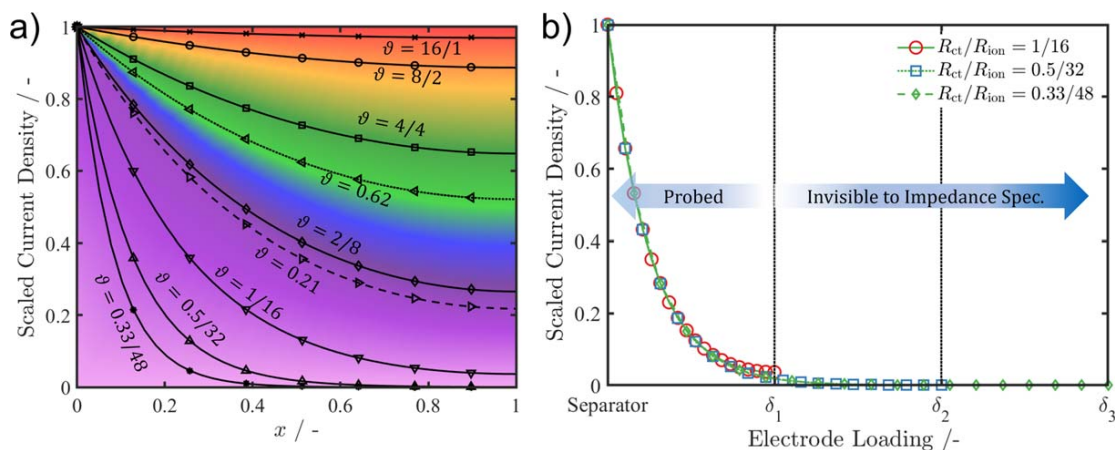
Figure 3. Ionic current density distribution across an electrode (scaled to the maximum current density at the separator/electrode interface) based on Eq. A·9 in the Appendix. (a) Scaled current density for different ratios of $\vartheta = R_{ct}/R_{ion}$ vs the normalized electrode thickness x, with $x = 0$ being the separator/electrode interface and $x = 1$ being the electrode/CC interface. (b) Scaled current density distribution for conceptual electrodes with three different active material loadings (and thicknesses). For the lowest loading electrode (δ_1), an R_{ct}/R_{ion} value of 1/16 was chosen, representing a transport limited electrode, and the scaled current distribution between the separator/electrode and the electrode/CC interface is shown by the red circles. For a 2-fold and 3-fold higher electrode loading and a concomitant reduction of R_{ct}/R_{ion}, the essentially identical current profile is obtained (blue squares).

squares), or by factor of 3 to δ_3 and reducing R_{ct}/R_{ion} to 0.33/48 (green diamonds), does not significantly change the current distribution anymore, as the current has already dropped to a negligible value at the electrode/CC interface even for the lowest loading (point marked δ_1), and since the current distributions for all three loadings are therefore overlapping. Hence, the additionally added active material mass for the loadings δ_2 and δ_3 is not visible to the impedance measurement. For a real battery (as opposed to the simplified representation shown in Fig. 1), the additional loading will be visible at very low frequencies (on the order of mHz), where the electrode will again exhibit a capacitor-like behavior due to the limited Li storage capacity in the particles.

These insights are important to consider when analyzing aged electrodes via impedance spectroscopy, since aged electrodes may have high ionic resistances due to pore blocking by SEI (solid electrolyte interphase) products and may exhibit an increased ionic resistance near the separator/electrode interface (produced, e.g., by lithium plating at the separator/electrode interface caused by fast-charging).[25] In these cases, only the part of the electrode near the separator/electrode interface may be probed by impedance measurements. This could lead to an incorrect interpretation of the impedance spectra, as the measured resistance would only be representative for the region of the electrode near the separator/electrode interface. It is also noteworthy that the R_{ct}/R_{ion} ratio of 1:1 ($\vartheta = 4/4$ in Fig. 3a) is still described as kinetically limited rather than being in the transition zone between the kinetically and the transport limited regimes. This is because the kinetic resistances are connected in parallel (see Figs. 1 and A·1), i.e., all current must eventually pass through a kinetic resistive element so that the contribution of R_{ct} is larger compared to that of R_{ion}, as not all current passes through the entire ionic resistance of the electrode. This is most clearly seen in Eq. 4 where the ionic contribution is 1/3 of the total ionic resistance and the kinetic resistance is represented in full.

While the terminology of kinetically or transport limited behavior of an electrode is directly applicable for reactions that are at steady-state (as, e.g., applies to the half-cell reactions in fuel cells or electrolyzers), in which case the electrode utilization attains a steady-state value (i.e., a constant overpotential for an applied current), this terminology is more complicated in the case of battery electrodes. Intercalation reactions in finite sized particles are transient processes (no steady-state), where not all particles may participate in the reaction at the same time and where the liquid electrolyte may continuously change its concentration profile (leading to changing overpotentials) throughout the charging/discharging process. While the measured R_{ion} value is only a function of the electrolyte conductivity and the electrode pore structure, the total electrolyte overpotential during an applied current is also a function of the additional Warburg element[26] that incorporates diffusion coefficient, thermodynamic factor, and transference number, all of which may vary greatly between different electrolyte compositions and temperatures.[27] In addition, the charge transfer resistance is also a function of the lithium concentration in the electrolyte as well as in the solid phase of the active material, further complicating the analysis. Nevertheless, some fundamental statements can be made.

An important factor (other than the ratio of R_{ct}/R_{ion}) in determining the homogeneity in lithiation/delithiation of the active material particles in an electrode for Li-ion batteries is the open circuit voltage (OCV) profile of the active material. Very steep OCV profiles, i.e., spanning over a wide potential range (e.g., NMC materials that span an OCV range of ~1.1 V within their operating window, viz., from ~3.3-4.4 V vs Li$^+$/Li) generally charge more homogeneously compared to active materials that charge/discharge over a narrow OCV range, especially if the overpotential is small compared to the OCV window. For the former materials, the thermodynamic potential (i.e., the OCV) becomes the deciding factor in determining the particle SOC. On the other hand, for active materials with a narrow OCV range (e.g., graphite with its two

main lithiation stages, Li$_4$Ti$_5$O$_{12}$ (LTO), or LiFePO$_4$ (LFP)), the degree of lithiation of the electrode is only weakly dependent on the electrode OCV. In such cases of narrow OCV ranges, the R_{ct}/R_{ion} ratio can be a deciding factor determining the current distribution, even for longer current applications, resulting in a current "front" moving from the separator interface to the current collector interface for severely transport limited electrodes. Other factors like the active material particle size distribution also need to be considered. As small particles would generally lithiate faster, the current distribution of a transport limited electrode would not only move from the separator to the current collector interface but also from small to large particles.

Impedance analysis guidelines for porous electrodes.—The following subsection gives a guideline on how to determine R_{ct} and R_{ion} from the low-frequency resistance (L) obtained from individual electrode impedance data using the TLM represented by Eq. 1 and its low-frequency solution given by Eq. 2. For this, it is important to understand whether the impedance response of a given electrode falls within the kinetically or the transport limited regime, which depends on the R_{ct}/R_{ion} ratio that in turn depends on the actual active material and electrolyte as well as on the active material loading. Since the impedance response in the transport limited regime becomes independent of the active material loading or areal capacity (see Fig. 2), a deconvolution of R_{ct} and R_{ion} in this regime requires an independent measurement of one of the two resistances (i.e., even a fit of Eq. 1 to the impedance data will practically not yield a unique solution anymore, as indicated also by Eq. 5 and discussed in a later section). The practical implications of analyzing transport limited electrode impedance spectra are detailed later on.

Table II shows the regions that we define as the kinetically or transport limited regimes. At one extreme, when $R_{ct} \ll R_{ion}$ (i.e., $\vartheta \to 0$), the impedance response becomes transport limited and the low-frequency resistance (L) can be described by Eqs. 5 or 5a. At the other extreme, when $R_{ct} \gg R_{ion}$ (i.e., for $\vartheta \to \infty$), the impedance spectrum can be visually separated into its transport resistance contribution and R_{ct}; here, the low-frequency resistance is described by Eqs. 4 or 4a. Even though Eqs. 4/4a and 5/5a are only strictly correct under the limiting conditions of $R_{ct}/R_{ion} = \vartheta \to \infty$ and $R_{ct}/R_{ion} = \vartheta \to 0$, respectively, they still provide a good approximation for the low-frequency resistance L over a rather wide R_{ct}/R_{ion} range. For a given low-frequency resistance L that can be determined from the impedance response of an electrode, we define the error ($\epsilon_\vartheta \equiv |(\vartheta_{true} - \vartheta_{approx})|/\vartheta_{true}$) in the prediction of ϑ, using the full solution (Eqs. 2 or 2a) vs the simplified solutions for the kinetically limited regime (Eqs. 4 or 4a) or the transport limited regime (Eqs. 5 or 5a). Tolerating 5% error in the determined ϑ value, the range of validity of the simplified solutions is given in Table II. It shows that use of Eqs. 4/4a will only give rise to $\leqslant$5% error (overprediction) in the value of ϑ compared to the full solution given by Eqs. 2/2a for $L/R_{ion} \leqslant 0.46$ (corresponding to $\vartheta \leqslant 0.21$); similarly Eqs. 5/5a will produce $\leqslant$5% error (underprediction) in the value of ϑ for $L/R_{ion} \geqslant 0.92$ (corresponding to $\vartheta \geqslant 0.62$). These values give the practical boundaries which henceforth are considered to be kinetically limited ($L/R_{ion} \geqslant 0.92$), transport limited ($L/R_{ion} \leqslant 0.46$), or being in the transition zone.

In the following, we will describe how the value for R_{ct} can be determined from electrode impedance measurements, even if it is not known a priori whether R_{ct} or R_{ion} is dominant. The outlined procedure is expected to yield accurate results for electrodes that have not yet undergone extensive cycling; for aged electrodes, the above discussed restrictions apply. Figure 4 depicts the analysis process to determine the charge transfer resistance for porous electrodes which have an either kinetically or transport limited impedance response, or whose impedance response falls within the transition region. For each step described below, please refer to the respective step described in Fig. 4.

Step #1: determine R_{ion}.—In the most general case, the pore resistance stemming from the electrolyte filled pores needs to be measured under blocking conditions that can be achieved by recording the impedance spectrum either at a potential where no faradaic reaction can take place (as shown in Fig. 2c; ideally conducted prior to electrode formation) or by using an electrolyte that does not contain any reacting species (a so-called "blocking electrolyte").[19–21] Such measurements can either be done using a symmetric cell setup (as shown by Landesfeind et al.[19]) or in a full-cell when using a micro-reference electrode to determine the impedance of each individual electrode (as done in Fig. 2c). From the thus obtained impedance spectra, R_{ion} can be extracted by taking the difference between the low- and high-frequency intercepts which equals $R_{ion}/3$, as illustrated in Fig. 4a (in case of symmetric cell measurements, R_{ion} of an individual electrode would then be a half of the $R_{ion}/3$ value obtained from the cell).

Step #2: determine L.—The low-frequency electrode resistance L is the resistance difference between the low- and high-frequency region of the spectrum (see Fig. 4b). The value of L excludes the high-frequency contributions by the separator resistance and by electrical contact resistances (both of them are accounted for in the high-frequency intercept value). Moreover, we also assume that the diffusion processes (both in the electrolyte and in the solid phase) are slow enough that their contribution to the value of L can be neglected. An example of how to assign different phenomena to different parts of the spectra can be found in Refs. 20, 21 Additionally, the apex frequency (f_{apex}) and the imaginary resistance Im_{apex} (taken as the modulus, since Im_{apex} is a negative number) can be evaluated by taking the frequency and imaginary resistance of the highest point of the impedance spectrum (the apex of the (suppressed) semicircle feature of the spectrum). Both values are later needed to determine the α coefficient of the constant phase element that represents the double layer capacitance (see Fig. 1), as described in the subsequent sections.

Step #3: use L/R_{ion} to classify the electrode impedance response.—The ratio between the electrode low-frequency resistance L and the pore resistance R_{ion} marks whether the electrode impedance response is kinetically or transport limited, or whether it is in the transition region. As outlined in Table II, if $L/R_{ion} \geqslant 0.92$, the system can be treated as kinetically limited (region marked in the upper right-hand corner of Fig. 4c), and Eq. 4 can be used (see step #4a below). If the ratio $L/R_{ion} \leqslant 0.46$, the system can be considered as transport limited (region marked in the lower left-hand corner of Fig. 4c), and Eq. 5 can be used (see step #4b below). In between these two values ranges, the impedance response of the electrode falls within the transition region (gray shaded field in Fig. 4c) and the spectrum can be analysed according to step #4c below and the description of Fig. 5.

Step #4a: R_{ct} and R_{ion} quantification in the kinetically limited regime.—The kinetically limited regime allows for the simplest and certainly most commonly known way to analyze the impedance data of an electrode, as the features of the individual resistances are clearly discernible (see yellow, orange, and green lines in Figs. 2a/2b). In this regime, one can simply use the semicircle in the spectrum to determine the charge transfer resistance and then use the low-frequency resistance L to determine R_{ion} via Eq. 4 (the blue dashed line in Fig. 4c corresponds to Eq. 4a). Alternatively, if R_{ion} was determined from an impedance measurement under blocking conditions (see step #1), R_{ct} can be determined via Eq. 4. Note that blocking conditions constitutes a state of the electrode where R_{ct} is significantly larger than R_{ion}, and is therefore a limiting case of the kinetically limited regime.
The double layer capacitance can be determined from the apex frequency of the semicircle (f_{apex}) using the equation provided in the

lower blue shaded field in Fig. 4c (labeled Step 4a) after determination of the α coefficient of the constant phase element. To determine the latter, we refer the user to Fig. 5. Alternatively, as the spectrum in the kinetically limited regime shows a pronounced semicircle, the semicircle features can also be fitted using an R/Q element to directly get α and Q_{dl}, which can be done with most impedance fitting software. Figure 4c shows the comparison between the simplified expression for the low-frequency resistance scaled by R_{ion} (Eq. 4a, blue dashed line) and the full solution (Eq. 2a, red line). Finally, it should be noted that in the kinetically limited regime, a fit of the electrode impedance data to Eq. 1 would also allow for an unambiguous quantification of R_{ct}, R_{ion}, and Q_{dl}.[9,20]

Step #4b: R_{ct} and R_{ion} quantification in the transport limited regime.—Electrode impedance spectra representing the transport limited regime can be just as easily evaluated as those in the kinetically limited regime, just using a different set of equations. In this regime, however, R_{ion} must be determined a priori (acc. to step #1), since the low-frequency resistance L contains the product of R_{ion} and R_{ct} (Eq. 5), and since the features representing each of the two resistances cannot anymore be discerned in the spectrum (see blue and purple lines in Figs. 2a/2b). Also, the apex frequency of the spectrum can be used to determine the double layer capacitance using the same equation as for the kinetically limited regime except for an additional α–dependent correction factor P_α, as shown in in the lower green shaded field in Fig. 4c (labeled Step 4b) and in Fig. 5b. To determine the α coefficient, we refer the user to Fig. 5a. Figure 4c shows the comparison between the simplified expression for the low-frequency resistance in the transport limited regime (Eq. 5a, green dashed curve) and the full solution (Eq. 2a, red curve).
Finally, it should be noted that in the transport limited regime a fit of the impedance spectrum to the TLM described by Eq. 1 practically cannot yield a unique solution for R_{ct} and R_{ion} anymore (see section below), so that an independent determination of R_{ion} is required (acc. to step #1).

Step #4c: R_{ct} and R_{ion} quantification in the transition region.—If the electrode's impedance response is neither kinetically limited nor transport limited, the impedance analysis cannot be conducted using the simplified expressions (Eqs. 4 and 5), and the full solution (Eq. 2) must be used. One approach will be to use the full complex impedance solution (Eq. 1) to fit the experimental data to obtain R_{ct}, R_{ion}, and Q_{dl}, but in general a unique fit requires an independent quantification of R_{ion} under blocking condition, either as described in step #1 or by driving the electrode into blocking condition during a cell cycling protocol, as shown by Landesfeind et al.[20,21]
Here, we aim to simplify that procedure and present a graphically based method to determine R_{ct} with in the transition region. It is in principle identical to the above described approach for the transport limited regime, except that Eq. 2a (i.e., the red line in Fig. 4c) is used to determine R_{ct}/R_{ion}: (i) R_{ion} is obtained acc. to step #1; (ii) R_{ct}/R_{ion} is obtained from the measured value of L/R_{ion} using the red solid curve in Fig. 4c (corresponding to the full solution as expressed in Eq. 2).
From the thus obtained R_{ct}/R_{ion} ratio, one can refer to Fig. 5a to determine the constant phase exponent α from the measured values of the low-frequency resistance L and the modulus of the imaginary impedance at the apex frequency Im_{apex}. With ϑ and α known, the value of the scaled peak frequency ($\hat{f}_{apex}$) can be obtained from Fig. 5b, from which together with the above determined values of R_{ct} and α and the measured value of the apex frequency f_{apex}, the value of the double layer capacitance Q_{dl} can be determined from Eq. 6. It should be noted that Fig. 5 is generated using Eq. 1 in order to facilitate a graphical extraction of the α exponent (for values of 1–0.7) and the double layer capacitance. The following definition ($\hat{f}_{apex}$) can be used to calculate the double layer capacitance (Q_{dl}).
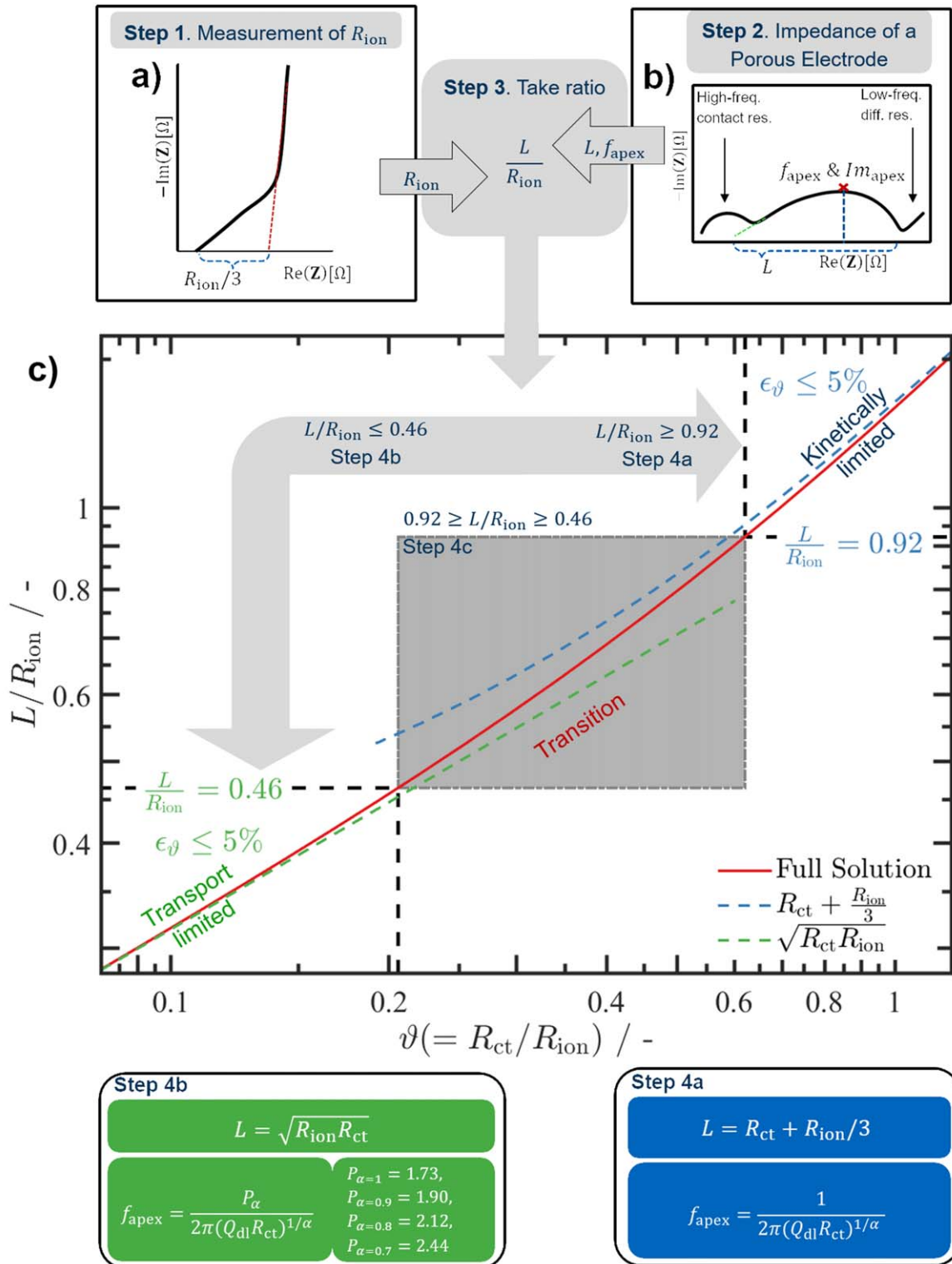
Figure 4. Step-by-step guidelines for the deconvolution of the charge transfer resistance (R_{ct}) from the impedance response of a battery electrode. (a) Recording of the electrode impedance spectrum under blocking conditions, which allows the extraction of the electrode pore resistance (R_{ion}) (b) Recording of the electrode impedance spectrum at a given SOC (≠ 0% SOC), from which the low-frequency electrode resistance (L) can be determined as well as the apex frequency (f_{apex} [Hz]) and the imaginary impedance at the apex frequency (Im_{apex} [Ω]). (c) Plot of the low-frequency resistance L normalized to the pore resistance R_{ion} vs $R_{ct}/R_{ion} \equiv \vartheta$, showing the precise relationship given by Eq. 2a (red line) that can be approximated in the kinetically limited regime (i.„e, for **$L/R_{ion} \geqslant 0.92$ or $\vartheta \geqslant 0.62$**) by Eq. 4a (blue dotted line and blue shaded panel) and in the transport limited regime (i.„e, for $L/R_{ion} \leqslant 0.46$ or $\vartheta \leqslant 0.21$) by Eq. 5a (green dashed line and green shaded panel).
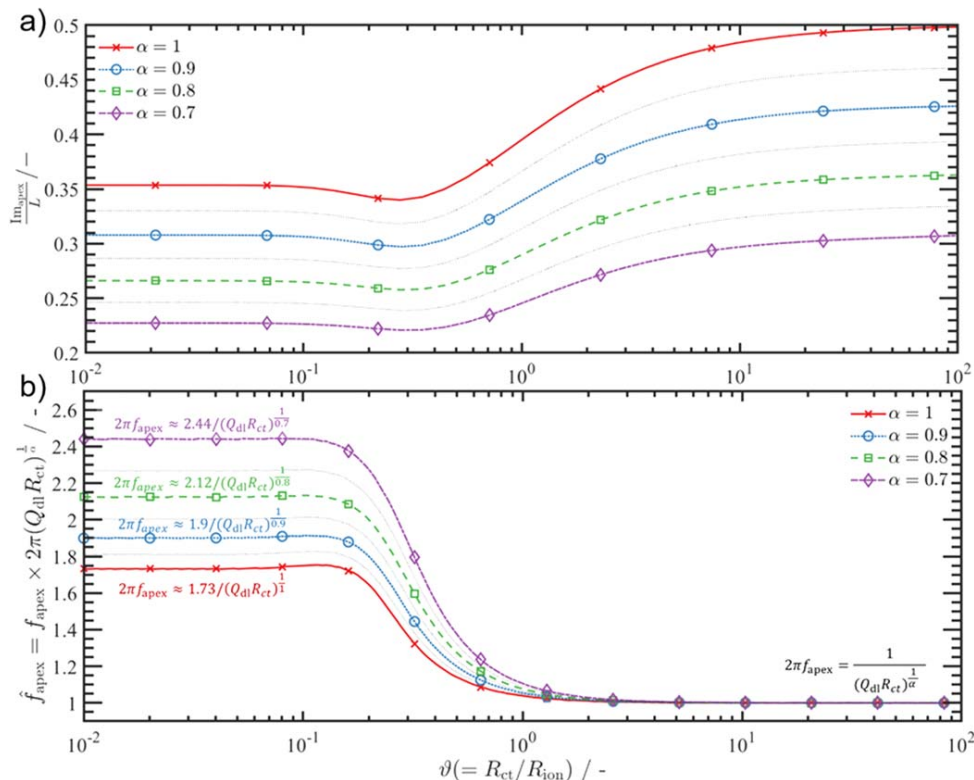
Figure 5. (a) Graphical representation of Im_{apex}/L vs ϑ to allow the extraction of the constant phase element exponent α between values of 1–0.7 in steps of 0.05. (b) Scaled apex frequency ($\hat{f}_{apex}$) for values of the constant phase exponent α of 1 to 0.7 in steps of 0.05. The graph allows to extract all information necessary to determine the electrode capacitance value Q_{dl} as described in Eq. 6.

$$\underbrace{\hat{f}_{apex}}_{\substack{\text{determined} \\ \text{from Fig. 5b}}} = \underbrace{f_{apex}}_{\substack{\text{experimentally} \\ \text{measured}}} \times 2\pi \left(\underbrace{R_{ct}}_{\substack{\text{from} \\ \text{Fig. 4c}}} \times \underbrace{Q_{dl}}_{\text{unknown}} \right)^{\frac{\frac{1}{\alpha}}{\text{from} \\ \text{Fig. 5a}}} \qquad [6]$$

The values for α are given between 1 and 0.7. Values above 1 are considered not physically viable, whereas values below 0.7 should be treated with caution, since such low α values may be a result of diffusion phenomena that are not considered in Eq. 1 (a 45°-line resulting from diffusion phenomena can be described by a Q element with an exponent of $\alpha = 0.5$).

Example impedance analysis.—The following subsection gives an example on the use of the above described method to determine R_{ct}, R_{ion}, and Q_{dl} from the experimentally obtained impedance data for the graphite electrode with an areal capacity of a 2.9 mAh cm^{-2}, whose impedance response under blocking and non-blocking conditions is shown in Figs. 2c and 2d, respectively. Subsequently, the analysis results are shown for all four graphite electrodes and the results are compared to the simulated impedance responses shown in Figs. 2a/2b.

Figure 6a re-plots the impedance data for a graphite electrode with an areal capacity of 2.9 mAh cm^{-2} under blocking conditions from Fig. 2c, acquired at 2 V vs Li$^+$/Li before formation. The procedure outlined above as Step #1 describes how to retrieve R_{ion} from the measurement by determining the difference between the projected high-frequency intercept (HFR) and the projected low-frequency intercept, as indicated by the green dashed lines. For this single dataset, this difference amounts to 9 Ω − 4.45 Ω = 4.55 Ω and corresponds to $R_{ion}/3$, yielding a value of $R_{ion} = 13.7$ Ω. Following

Step #2, we next determine the low-frequency electrode resistance L from the impedance spectrum recorded at 50% SOC (green line in Fig. 2d, replotted in Fig. 6b), which corresponds to the difference between the projected HFR intercept and the projected low-frequency intercept, as shown in Fig. 6b. This results in $L = 12.2$ Ω −3.25 Ω = 8.95 Ω. Here, one must be careful to exclude Warburg-like diffusion phenomena arising at the low-frequency end of the spectrum. Additionally, the apex frequency value (f_{apex}) and the modulus of the imaginary impedance at the apex frequency (Im_{apex}) can be determined, which for this example amount to $f_{apex} = 139$ Hz and $Im_{apex} = 2.29$ Ω.

As described in Step #3, the L/R_{ion} ratio determines whether the impedance response of the electrode is in the kinetically limited, transport limited, or the in the transition regime. In case of the here examined 2.9 mAh cm^{-2} graphite electrode, $L/R_{ion} = 0.66$, i.e., acc. to Table II, the impedance response of the electrode is in the transition regime, as can also be seen from Fig. 4c.

Therefore, the analysis should proceed acc. to Step #4c, determining the x-axis value of the red line in Fig. 4c that corresponds to the y-axis value of $L/R_{ion} = 0.66$, resulting in $R_{ct}/R_{ion} \approx 0.37$. Thus, based on the above value of $R_{ion} = 13.7$ Ω determined under blocking conditions, the resulting R_{ct} value is 5.05 Ω. To accurately determine the capacitance of the interface, the value of the α coefficient needs to be known. Usually this can be done by analyzing the blocking low-frequency spectrum via an R/Q element. Alternatively, Fig. 5a allows to determine the α coefficient from the spectrum. In this case, the blocking spectrum was measured before SEI formation with an $\alpha = 0.95$ whereas the analysis of the data at 50% SOC (assuming $R_{ion} = 13.7$ Ω) gave a value of $\alpha = 0.78$, meaning that the change in surface by the SEI changed the α coefficient. Therefore Fig. 5 allows for the determination of α from the non-blocking spectrum.

Table II. Overview of the applicability of the simplified Eqs. 4/4a for the kinetically limited regime and Eqs. 5/5a for the transport limited regime to predict the value of $\vartheta \equiv R_{ct}/R_{ion}$ from the low-frequency resistance (L) obtained from the impedance response of an electrode. The range of L/R_{ion} giving ⩽5% error in the prediction of ϑ shows that the expressions are valid for a much broader range of ϑ and not just in the extremes ($\vartheta \ll 1$ and $\vartheta \gg 1$).

$\vartheta \equiv R_{ct}/R_{ion}$	kinetically limited	for any value of ϑ	transport limited
applicable eqn. for L	$L = R_{ct} + \dfrac{R_{ion}}{3}$ [4] $\dfrac{L}{R_{ion}} = \vartheta + \dfrac{1}{3}$ [4a]	$\dfrac{L}{R_{ion}} = \sqrt{\vartheta}\coth\left(1/\sqrt{\vartheta}\right)$ [2a]	$L = \sqrt{R_{ion}R_{ct}}$ [5] $\dfrac{L}{R_{ion}} = \sqrt{\vartheta}$ [5a]
5% error in ϑ ($\epsilon_\vartheta \leq 5\%$)	$L/R_{ion} \geq 0.92$ $\vartheta \geq 0.62$	n.a.	$L/R_{ion} \leq 0.46$ $\vartheta \leq 0.21$

For $\vartheta = 0.37$ and $Im_{apex}/L = 0.26$, Fig. 5a gives $\alpha = 0.8$. Thus Fig. 5b gives $\hat{f}_{apex} = 1.35$ Hz. Next, Eq. 6 will be used to get the value of Q_{dl} as shown below.

$$1.35 = 136\,\text{Hz} \times 2\pi (5.05 \times Q_{dl})^{\frac{1}{0.78}}$$

This yields a constant phase element capacitance value of $Q_{dl} = 1.29$ mFs$^{\alpha-1}$.

Table III shows the analysis of the individual experimental data points from Figs. 2c/2d and gives a comparison to the values from a fit to Eq. 1. To fit the impedance spectra, the pore resistance is measured separately under blocking conditions prior to cycling the electrode (see Fig. 2c) and kept constant for the fitting process. This is necessary, as Eq. 5 shows that different combinations of R_{ct} and R_{ion} can give the same low-frequency impedance intercept. The fitted data are in good agreement with the manually obtained datapoints. Table III also shows the main finding of this work: if the low-frequency electrode resistance (L) were to be interpreted as

charge-transfer resistance for the graphite electrode with an areal capacity of 7.5 Ah cm^{-2}, i.e., if one were to assume incorrectly that the experimental impedance spectrum were to represent a suppressed semicircle (contrary to our above presented analysis), one woud estimate a charge transfer resistance of 9.28 Ω (entire value of L) as opposed to the true R_{ct} value of ~2.37 Ω.

To evaluate whether our initial assumptions outlined in Fig. 1 are correct, namely that R_{ct} scales inversely and that R_{ion} scales proportionally with the areal capacity, Table IV shows the experimentally determined areal capacity-scaled values for R_{ion} and R_{ct}. For all of the here examined graphite electrodes (0.6–7.5 mAh cm^{-2}), R_{ion}/C_{areal} is practically constant (see 3rd column of Table IV), as expected for electrodes of constant porosity (see Table I) if the tortuosity is independent of the areal capacity, i.e., of the graphite loading. The latter point can be checked by calculating the tortuosity of the electrodes via $\tau = \frac{R_{ion}\cdot\epsilon\cdot\kappa\cdot A}{d}$, with ϵ being the electrode porosity, A the geometric electrode area (0.94 cm^2), κ the electrolyte conductivity (8.9 mS cm^{-1}), and d the electrode thickness
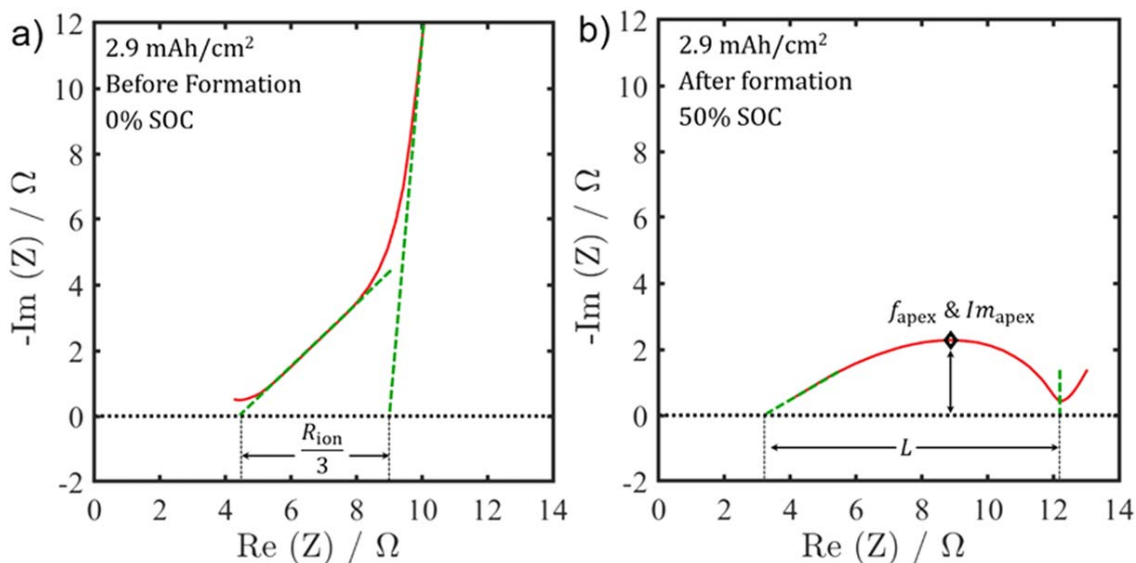
Figure 6. Exemplary analysis of the experimentally obtained impedance data of the graphite electrode with an areal capacity of 2.9 mAh cm^{-2} (spectra re-plotted from Figs. 2c and 2d). (a) Impedance spectrum under blocking condition, acquired at 2 V vs Li$^+$/Li prior to formation (data from Fig. 2c). The difference between the projected low- and high frequency intercepts (see dashed green lines) corresponds to $R_{ion}/3$. (b) Impedance spectrum acquired at 50% SOC after two formation cycles (data from Fig. 2d). The low-frequency electrode impedance L corresponds to the difference between the projected high- and low-frequency intercepts of the spectrum (see dashed green lines). Also f_{apex} and Im$_{apex}$ are determined from the point of the spectrum with the highest imaginary value.

Table III. Parameter values determined using the method described in this publication (R_{ct}, α, and Q_{dl}) and parameters from a spectra fit ($R_{ct,fit}$, α_{fit}, and $Q_{dl,fit}$) for the experimental impedance data shown in Figs. 2c/2d. The data were fitted to the complex impedance solution represented by Eq. 1, keeping the R_{ion} value determined under blocking conditions prior to cycling (see Fig. 2c) constant, and then fitting the remaining variables in the impedance spectrum.

C_{areal} [mAh/cm^2]	R_{ion} [Ω]	L [Ω]	R_{ct} ($R_{ct,fit}$) [Ω]	f_{peak} [Hz]	Im_{apex} [Ω]	α (α_{fit}) [--]	Q_{dl} ($Q_{dl,fit}$) [mFs$^{\alpha-1}$]
7.5	36.3	9.28	2.37 (2.27)	139	2.29	0.76 (0.74)	3.84 (5.03)
2.9	13.7	8.95	5.05 (5.01)	139	2.29	0.80 (0.78)	1.14 (1.35)
1.5	6.70	10.7	8.50 (8.70)	110	3.00	0.80 (0.74)	0.75 (0.97)
0.6	2.80	16.8	15.8 (16.2)	110	5.41	0.76 (0.74)	0.44 (0.51)

(see Table I). The thus calculated tortuosity values are indeed essentially identical ($\tau = 7.4 \pm 0.3$, see 4th column in Table IV), whereby the absolute tortuosity values are are slightly higher than those reported previously for similar graphite electrodes ($\tau \approx 5.0$–5.5, see Refs. 17, 19). Overall, however, the initially assumed scaling relationship of $R_{ion}/C_{areal} =$ constant is confirmed by the experimental data.

The capacity-scaled R_{ct} (i.e., $R_{ct} \times C_{areal}$), expected to also be constant, shows an increase by a factor of $\sim$1.8 as the areal capacity increases by a factor of 12.5, i.e., as the graphite loading of the electrodes increases by a factor 12.5. This implies that, the experimentally determined charge transfer resistance is $\sim$1.8 times higher than expected based on the initially assumed scaling law of $R_{ct} \times C_{areal} =$ constant for the highest loading. One reason for the deviation could be possible differences in the formation of a thin kinetically limited electrode and a thick transport limited electrode: A kinetically limited thin electrode is charged homogeneously during the formation cycle, and the individual active material particles all see the C/10 homogeneous current throughout the formation. On the other hand, the thick electrodes are likely charged more inhomogeneously (as explained via Fig. 3), with higher local currents as the active material particles are being charged successively starting at the separator/electrode interface towards the electrode/current collector interface. This may influence the SEI formation and thus the electrode kinetics, as the active material particles are effectively undergoing formation at a higher C-rate. An alternative explanation might be related to the effect of binder migration during the drying of electrode inks, resulting in an inhomogenous distribution of pore resistances across the electrode thickness that can cause a locally higher calculated R_{ct} (see Refs. 28, 29). A locally higher R_{ion} compared to the average R_{ion} of the electrode would lead to a greater measured electrode impedance (L), hence leading to increased calculated (i.e., overestimated) values for the charge transfer resistance. Analyzing the phase angle of the experimental impedance spectra shown in Fig. 2 (acc. to Ref. 29, phase angle analysis not shown) suggests that this might indeed be

the case here for the 7.5 mAh cm^{-2} electrode. This ties in with the aforementioned caution of evaluating data of aged and potentially inhomogeneous electrodes, as R_{ct} is calculated based on the assumption of a homoegenous electrode via a measurement which can be distorted by inhomogeneities in the electrode.

Lastly, Table IV also shows the experimentally determined ratio of R_{ct}/R_{ion} for the different graphite electrodes, from which the impedance regime for a given electrode can be determined based on Table III or Fig. 4c. Here, only the highest loaded electrode (7.5 mAh cm^{-2}) is fully transport limited, whereas the 2.9 mAh cm^{-2} electrode is in the transition regime. The two lowest loaded electrodes with areal capacities of 1.5 mAh cm^{-2} and 0.6 mAh cm^{-2} are both kinetically limited. This shows that Li-ion battery electrodes of relevant loadings above 1.5 mAh cm^{-2} can show significant transport resistances, visible in the invariable impedance response with increasing areal capacity shown in Fig. 2. Thus, an interpretation of the impedance spectra of graphite electrodes with practically relevant areal capacities requires a careful analysis of their transport resistance contribution to the impedance spectrum.

Accuracy of impedance fits in the transition or transport limited regime.—The following subsection gives an overview over the accuracy when fitting porous electrode impedance spectra (utilizing Eq. 1) using both simulated and experimental data. We compare a simulated spectrum for a given set of R_{ion}, R_{ct}, Q_{dl}, and α that are chosen to represent the transport limited regime (i.e., $R_{ct}/R_{ion} < 0.21$, see Fig. 4c) with various impedance fits conducted with different fixed values for R_{ion} (with R_{ct}, Q_{dl}, and α as fitting parameters), examining the fitting errors when fitting the simulated spectrum with incorrect R_{ion} values. This illustrates that fixed R_{ion} values that are different by factors of 2 from the actual R_{ion} value that was used to generate the simulated spectrum still yield rather small errors in the impedance fit. We then show a chosen experimental impedance spectrum from an electrode in the transition regime (i.e., the 2.9 mAh cm^{-2} electrode, see Table IV) and give the fitting residuals calculated by fitting the experimental spectrum with

Table IV. Experimentally obtained electrode resistances R_{ion} and R_{ct} for graphite electrodes with different areal capacities (data from Table III), which are then used to calculate the values for R_{ion}/C_{areal}, the tortuosity (τ), $R_{ion} \times C_{areal}$, and R_{ct}/R_{ion}. The latter ratio then allows to classify the impedance response regime, based on Table II.

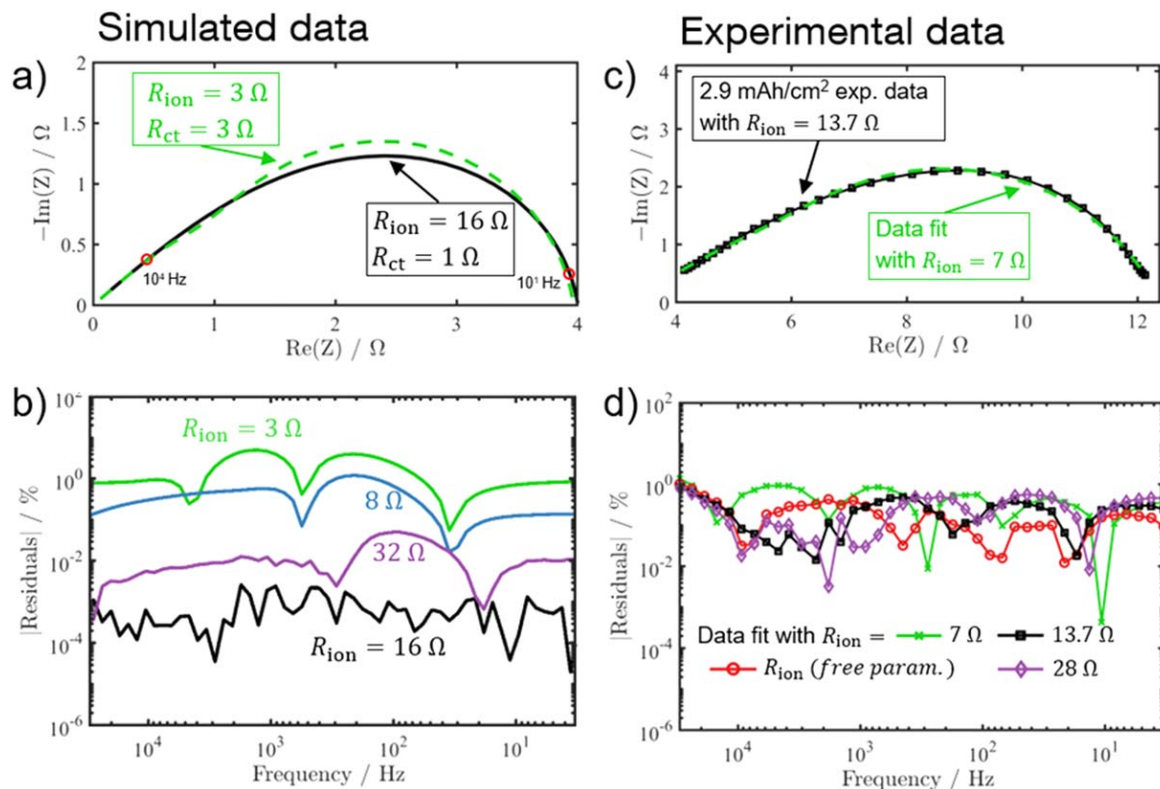| C_{areal} [$\frac{mAh}{cm^2}$]	R_{ion} [Ω]	R_{ion}/C_{areal} [$\Omega/\frac{mAh}{cm^2}$]	τ [—]	R_{ct} [Ω]	$R_{ct} \times C_{areal}$ [$\Omega\frac{mAh}{cm^2}$]	R_{ct}/R_{ion} [—]	Impedance regime
7.5	36.3	4.8	7.7	2.27	17.3	0.06	transport limited
2.9	13.7	4.7	7.5	5.01	14.5	0.37	transition regime
1.5	6.70	4.5	7.1	8.70	13.1	1.30	kinetically limited
0.6	2.80	4.7	7.7	16.2	9.7	5.79	kinetically limited

Figure 7. Comparison of impedance fits of simulated and of experimental impedance spectra. (a) Simulated impedance data calculated from Eq. 1 with $R_{ion} = 16\ \Omega$, $R_{ct} = 1\ \Omega$, $Q_{dl} = 2$ mF, and $\alpha = 0.9$ (corresponding to the transport limited spectrum, black line). The green dashed spectrum was fitted using Eq. 1 while keeping R_{ion} fixed to 3 Ω, resulting in a fitted value of $\boldsymbol{R_{ct}} = 3\ \Omega$ (i.e., R_{ct}/R_{ion} indicates the kinetically limited regime) (b) Residuals of fits of the simulated spectrum (black curve in a) when fixing R_{ion} to the different values marked in the figure. (c) Experimental data of the 2.9 mAh cm^{-2} electrode (black squares; data taken from Fig. 2d), fitted with a fixed value of $R_{ion} = 7\ \Omega$ (green dashed line) that is 2-fold lower than the value determined under blocking conditions (13.7 R_{ion}). (d) Residuals of the fit in c (green line) as well as the residuals for various fixed values of R_{ion} that differ by factors of 2 from the value determined under blocking conditions. That the residuals are within the same range for all fits (indicating the same quality of fit) highlights the difficulty when fitting experimental spectra without the prior determination of $\boldsymbol{R_{ion}}$.

different fixed R_{ion} values that are centered around the R_{ion} value obtained under blocking conditions, illustrating that the fit quality is essentially independent of the chosen R_{ion} value, while resulting in different values of R_{ct}, Q_{dl}, and α. This demonstrates that R_{ion} must be known when trying to extract R_{ct} values from impedance spectra in the transition or the transport limited regime.

Figure 7a shows a simulated porous electrode impedance spectrum in the transport limited regime (black line), calculated from Eq. 1 with $R_{ion} = 16\ \Omega$, $R_{ct} = 1\ \Omega$, $\alpha = 0.9$, and $Q_{dl} = 2$ mF (note that the main difference to the simulated spectrum for $R_{ion} = 16\ \Omega$ and $R_{ct} = 1\ \Omega$ in Figs. 2a/2b (orange lines) is that here a more realistic value of $\alpha = 0.9$ was chosen). The green dashed line shows a spectrum fitted to the black spectrum where R_{ion} is fixed falsley to a much lower value of 3 Ω, giving the remaining parameters best fitted to be $R_{ct} \approx 3.0\ \Omega$, $\alpha \approx 0.90$, and $Q_{dl} \approx 0.35$ mF, which would correspond to a spectrum in the kinetically limited regime (i.e., $R_{ct}/R_{ion}<0.62$, see Fig. 4c). The Nyquist plot representing this fit (green dashed line) overlaps closely for higher ($>10^4$ Hz, left side of the spectrum) and lower frequencies ($<10^1$ Hz, right side), but deviates visibly at intermediate frequencies.

To better quantify the differences between the simulated spectrum (black line) and the spectra fitted with different fixed R_{ion} values, Fig. 7b shows the magnitude of the residuals vs frequency, i.e., the scaled difference between the simulated data and fit vectors $\left(\frac{|\,Z(f_i)\,| - |\,Z_{fit}(f_i)\,|}{|\,Z_{fit}(f_i)\,|} \right)$ at the same frequency f_i (in %). The thus determined residuals for the fit with a fixed $R_{ion} = 3\ \Omega$ (green line in Fig. 7b) are a quantitative measure of the difference between the

simulated spectrum (black line in Fig. 7a) and the thus fitted spectrum (dashed green line in Fig. 7a), with maximum values of the residuals of ~5%. A sudden dip in residuals followed by a semi-circle shaped features (e.g., between 10^4 to 10^2 Hz for the green line in Fig. 7b) are points where the fitted spectrum deviates from the simulated/experimental data over wider frequency ranges. Ideally, a perfectly fitted spectrum gives low residuals which can be described as noise around the fitted datapoints, whereas constant deviations over a wider frequency range can be the result of more systematic errors in the analysis (as seen, e.g., in the green residuals).

As expected, fitting the data using the correct R_{ion} value (i.e., fixing $R_{ion} = 16\ \Omega$ while fitting) gives the lowest residuals (~10^{-3}%; see black line in Fig. 7b) and yields the correct values for R_{ct}, α, and Q_{dl} (i.e., the values that were used to generate the simulated spectrum). Since the simulated spectrum can be described as transport limited ($R_{ct}/R_{ion}\ll0.21$, see Fig. 4c), fixing R_{ion} to 32 Ω (purple line in Fig. 7b) and fitting the simulated spectrum still gives very low residuals (~10^{-2}%). In this case, the fit gives values for R_{ct} of 0.5 Ω, $\alpha \approx 0.9$, and $Q_{dl} \approx 1$mF (i.e., a 2-fold lower R_{ct} value, as expected from the discussion of the spectra in Fig. 2), showing that while these two transport limited spectra (i.e., for $R_{ion} = 16\ \Omega$ and for $R_{ion} = 32\ \Omega$) are theoretically not identical, they very closely match each other. Fitting the simulated spectrum with a lower fixed R_{ion} value of 8 Ω still gives reasonably small residuals on the order of 1% (with $R_{ct} \approx 1.9\ \Omega$, $Q_{dl} \approx 0.95$ mF, and $\alpha \approx 0.9$), suggesting that the spectrum is in the transition region ($R_{ct}/R_{ion} \approx 0.48$, see Fig. 4c). In summary, while the fit of simulated, perfectly noise-free impedance data in the transport controlled regime would still yield the correct

values of R_{ion}, R_{ct}, Q_{dl}, and α, the residuals that are obtained when fixing an R_{ion} value that is different by a factor of 2 are still very small (below 1%). Therefore, owing to the noise in experimental impedance data, a unique fitting result cannot any more be obtained, as will be illustrated in the following.

Figure 7c shows the experimentally obtained impedance spectrum for the electrode with an areal capacity of 2.9 mAh cm^{-2} (black squares; same data as in Fig. 2c) to 3 Hz, since datapoints below 3 Hz are dominated by diffusion phenomena. Based on the R_{ion} value of 13.7 Ω that was determined for the pristine electrode under blocking conditions (see Fig. 2d), the fit of the impedance spectrum using Eq. 1 (with an additional resistance element in series for the high frequency separator resistance) and fixing R_{ion} at 13.7 Ω yields $R_{ct} = 5.0$ Ω (also $Q_{dl} = 1.35$ mF and $\alpha = 0.78$, see Table III). Thus, based on $R_{ct}/R_{ion} \approx 0.36$, this impedance spectrum fit suggests that the impedance response of this electrode falls within the transition regime (see Fig. 4c). As shown in Fig. 7d (black squares), the residuals for this fit are at ≤1% over the entire frequency range. On the other hand, if R_{ion} is treated as a fitting parameter (i.e., the software was allowed to alter all four parameters to find the best fit, an approach that would be used if R_{ion} was unknown), the fitted values are $R_{ion} = 11.0$ Ω and $R_{ct} = 5.7$ Ω (also $Q_{dl} = 1.1$ mF and $\alpha = 0.78$). Based on $R_{ct}/R_{ion} \approx 0.52$, the impedance spectrum still falls within the transition regime. The maximum residuals (red circles) are also ≤1% and thus essentially identical with those obtained when using the R_{ion} value determined for the pristine electrode under blocking conditions.

Fitting the experimental spectrum using an R_{ion} value that is arbitrarily fixed to 7.0 Ω results in a spectrum that is represented by the green dashed line in Fig. 7c. The corresponding fitted value of R_{ct} is now 7.0 Ω (also $Q_{dl} = 1$ mF and $\alpha = 0.71$), i.e., the spectrum can now be described as kinetically limited, since $R_{ct}/R_{ion} \approx 1$. The residuals for this fit (green crosses in Fig. 7d) are also ≤1% over the entire frequency range and only marginally higher than for the fits where R_{ion} is either fixed at the value obtained for the pristine electrode under blocking conditions or where R_{ion} is treated as a fitting parameter (see above). Fixing R_{ion} at 28 Ω, i.e., at a 2-fold higher value than suggested by the blocking condition measurements, also yields residuals of ≤1% (purple diamonds); with the fitted R_{ct} value of 2.9 Ω (also $Q_{dl} = 3.3$ mF and $\alpha = 0.76$), the impedance response of the electrode would now fall into the transport limited regime ($R_{ct}/R_{ion} \approx 0.11$, see Fig. 4c).

The above analysis illustrates that a fit of the impedance spectrum of a graphite electrode with a pore resistance that is similar in value to the charge transfer resistance, as is the case for large areal capacitances (i.e., for areal capacitances of near/above 3 mAh cm^{-2}), does not allow for a reliable determination of R_{ct}, since the difference in the residuals is rather negligible. For example, for the 2.9 mAh cm^{-2} graphite electrode examined here, assuming R_{ion} values between 7–28 Ω yields essentially identical residuals, while the fitted R_{ct} values differ by a factor of ~2.5 (2.9–7 Ω). The low α-value of real electrodes also plays a role in this, since the transition between the straight line at high frequencies (having slope of 45° × α) to the depressed semi-circle feature is a less pronounced feature for lower α-values. This is seen in the impedance fit for a fixed R_{ion} of 7 Ω (green dashed line in Fig. 7c), where the fit gives an α-value of 0.71 compared to 0.78 when using the R_{ion} value of 13.7 Ω that is obtained under blocking conditions. Lowering the α-value makes for a more seamless transition between the initial straight line feature to the depressed semi-circle, making it difficult to distinguish it from a spectrum with a higher R_{ion}. Therefore, in view of the inevitable noise in experimental impedance spectra, the quantification of R_{ct} from the impedance spectra of high areal capacity graphite electrodes requires an independent measurement of R_{ion}, which, as shown here, can be obtained under blocking conditions for a pristine electrode. While the thus determined R_{ion} may increase over extended charge/discharge cycling, it is expected to remain constant over the first few cycles.[21]

Conclusions

This work shows how the ratio of the charge transfer resistance to the resistance stemming from the electrolyte filled porous path inside a porous electrode (R_{ct}/R_{ion}) influences the electrode impedance spectra of Li-ion battery electrodes. We use a simplified transmission line model (TLM) with the ionic resistance R_{ion} in the electrolyte and the faradaic reaction charge transfer resistance R_{ct} as the only contributions to the spectrum, neglecting the electronic resistance of the solid phase or diffusion resistances in both the electrolyte and in the solid phase that only appear at very low frequencies, to model the influence of areal capacity (or mass loading) on the spectrum shape and the low-frequency resistance L.

Simulating changes in electrode loading by considering that $R_{ct} \propto \frac{1}{C_{areal}}$ and $R_{ion} \propto C_{areal}$, the porous electrode impedance spectra show a change in shape when changing the ratio $\vartheta \equiv R_{ct}/R_{ion}$. For $\vartheta \gg 1$, the electrode is described as *kinetically limited* and the impedance spectrum is dominated by a semicircle that represents R_{ct}. For $\vartheta \ll 1$, the electrode is described as *transport limited*, where any change in active material loading barely affects the shape of the impedance spectra and where the low-frequency intercept becomes practically independent of the active material loading. Hence the transport limited regime requires prior knowledge of R_{ion} to quantify R_{ct} from an impedance fit.

We then provide practical boundaries to describe the kinetically and transport limited regime. For $\vartheta \geqslant 0.62$, the electrode impedance can be calculated as $L = R_{ct} + \frac{R_{ion}}{3}$, whereas for $\vartheta \leqslant 0.21$, the electrode is transport limited and the low-frequency electrode resistance is described by the $L = \sqrt{R_{ion}R_{ct}}$. For in-between values of ϑ, no simplified solution can be determined. The loading independent impedance spectra for transport limited electrodes is explained by the limited measurement penetration depth (smaller than the thickness of the electrode). As R_{ion} becomes dominating, only the electrode side close to the separator contributes to the measurement, and thus parts of the electrode (near the current collector) are invisible to the measurement. The findings of the simulation were confirmed by experimentally obtained impedance spectra of graphite electrodes of different areal capacities. Graphite electrodes between 0.6–7.5 mAh cm^{-2} were measured and found to be ranging from kinetically limited to transport limited.

To analyze the impedance spectra without prior knowledge of its limitation (i.e., transport vs kinetically limited electrodes), we provide a tool and a step by step description of a porous electrode impedance analysis without the need for a fitting software. This analysis requires measurement of the pore resistance under blocking conditions to accurately determine the charge transfer resistance from impedance measurements. While analyzing transport limited electrodes (in non-blocking conditions), care should be taken in interpreting the values of charge transfer resistance values obtained from this analysis, since the measurement of R_{ct} is obtained only by partial probing of the electrode (due to the limited signal penetration depth). The impedance of an electrode having an inhomogeneous distribution of charge-transfer resistance (i.e., in the transport limited regime) will only provide information of the charge transfer resistance that lies within the penetration depth. An analysis of graphite electrodes with widely varying areal capacities showed that our assumption of a direct proportionality of R_{ion} with electrode loading holds true. On the other hand, experimentally observed relationship between R_{ct} and areal capacity deviated somewhat from the assumed inverse proportionality of R_{ct} with areal capacity. Possibilities for such a deviation could be the local probing of the electrode when its response becomes transport limited or might arise from the more inhomogeneous formation of a transport limited electrode.

Lastly, we show that fitting simulated spectra (devoid of any noise) of transport limited electrodes without prior knowledge of their pore resistance is theoretically possible and results in the

extraction of the correct parameters. However, the differences between simulated transport limited impedance spectra (simulating changes in loading/areal capacity) are minute. The fits of experimentally obtained spectra of transport limited electrodes or those in the transition region are practically indistinguishable from other transport limited spectra, highlighting the need for the separate measurement of R_{ion}.

Acknowledgments

Appendix

The section below describes the mathematical background for the current distribution analysis shown in Fig. 3.

Figure A·1 shows the equivalent circuit for which we write the charge conservation equation for the electrolyte phase:

$$\underset{[\text{A m}^{-3}]}{\left(\frac{\underset{[\text{V}]}{E}}{\underset{[\Omega \text{ m}^3]}{\hat{r}_{ct}}} \right)} = \underset{[\text{A m}^{-3}]}{-\nabla \cdot \underset{[\text{A m}^{-2}]}{(-\kappa_{eff} \nabla E)}} \qquad [\text{A·1}]$$

The right-hand side represents the change in the flux of ionic current, whereas the left-hand side represents the current due to the charge transfer reaction. Here E [V] is the potential in the time domain, $\hat{r}_{ct} [\Omega \text{ m}^3]$ is the charge transfer resistance of the small volume element, and κ_{eff} is the effective conductivity of the electrolyte. Since we are dealing with a 1-dimensional system, Eq. A·1 can be simplified. We take the Laplace transform and the resulting Eqn. is shown in Eq. A·2:

$$\frac{E}{\hat{r}_{ct}} = \kappa_{eff} \frac{d^2 E}{dX^2} \qquad [\text{A·2}]$$

where X [m] is the axial direction going from 0 to the thickness of the electrode d [m]. Introducing $x = X/d$, we get the following equation:

$$\frac{E}{\hat{r}_{ct}} = \frac{\kappa_{eff}}{d^2} \frac{d^2 E}{dx^2} \qquad [\text{A·3}]$$

Rearranging Eq. A·3 to introduce the total charge transfer resistance (R_{ct}) and the ionic resistance (R_{ion}) as follows:

$$E = \frac{\hat{r}_{ct}}{d} \frac{A}{A} \frac{\kappa_{eff}}{d} \frac{d^2 E}{dx^2} \qquad [\text{A·4}]$$

Notice that $\frac{\hat{r}_{ct}}{Ad} = R_{ct} [\Omega]$ and $\frac{A \kappa_{eff}}{d} = \frac{1}{R_{ion}}$, whereby A is the geometric area. We get Eq. A·5 as a second-order differential equation:

$$E = \frac{R_{ct}}{R_{ion}} \frac{d^2 E}{dx^2} = \vartheta \frac{d^2 E}{dx^2} \qquad [\text{A·5}]$$

To solve Eq. A·5, the two boundary conditions in the Laplace domain are: $\mathbf{E}(x = 0) = 1$ and $\left. \frac{d\mathbf{E}}{dx} \right|_{x=1} = 0$ (no electrolyte current leaves the current collector). We then introduce $\vartheta = \frac{R_{ct}}{R_{ion}}$, to make
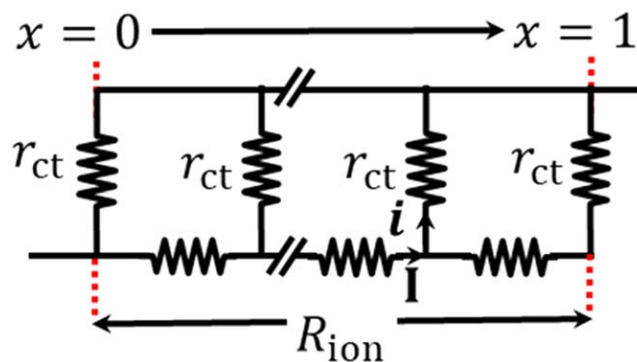

Figure A1. Simplification of the transmission line model presented in Fig. 1 for the case when the frequency is sufficiently low so that the current contributed by the double layer capacitance becomes negligible. Note that this TLM also excludes the effect of diffusion of lithium in electrolyte and solid phase that becomes significant at very low frequencies. Only the charge transfer reaction acts as a source or a sink for the current, the double-layer capacitance is inactive at such a low frequency.

the expression more compact. The solution to Eq. A·5 with the above specified boundary conditions can be expressed as follows (a modified version of Eq. A·6 can be found in Lasia, chapter 9):

$$\mathbf{E} = \frac{\cosh((1-x)/\sqrt{\vartheta})}{\cosh(1/\sqrt{\vartheta})} \qquad [\text{A·6}]$$

From Eq. A·6, we get the following equation for the current in the pore of the porous electrode (using Ohm's law for electrolyte):

$$\mathbf{I} = -\frac{1}{R_{ion}} \frac{d\mathbf{E}}{dx} = \frac{1}{R_{ion} \sqrt{\vartheta}} \frac{\sinh((1-x)/\sqrt{\vartheta})}{\cosh(1/\sqrt{\vartheta})} \qquad [\text{A·7}]$$

Here $\mathbf{I}$ is the complex current in the pore, x is the axial coordinate in the direction of the electrode thickness going from the separator/electrode interface ($x = 0$) to the electrode/current collector interface($x = 1$). We then define the complex current density $i(x) = -d\mathbf{I}/dx$, which represents the change in current at any point (due to charge transfer reaction only, as we have specified that the frequency is zero). A uniform $i(x)$ will mean a uniform reaction and a full utilization of the electrode.

$$i(x) = -\frac{d\mathbf{I}}{dx} = \frac{1}{R_{ct}} \frac{\cosh((1-x)/\sqrt{\vartheta})}{\cosh(1/\sqrt{\vartheta})} \qquad [\text{A·8}]$$

Finally, we define the scaled complex current density as the current density scaled with the current density at $x = 0$:

$$i_s(x) = \frac{i(x)}{i|_{x=0}} = \frac{\cosh((1-x)/\sqrt{\vartheta})}{\cosh(1/\sqrt{\vartheta})} \qquad [\text{A·9}]$$

The scaled current density at the current collector can be calculate by substituting $x = 1$, in Eq. A·9.

$$i_s(x = 1) = \frac{1}{\cosh(1/\sqrt{\vartheta})} \qquad [\text{A·10}]$$

During charging, all electrodes attained their full capacity at the cutoff of 40 mV vs Li$^+$/Li with the exception of the 7.5 mAh cm^{-2} electrode which reached ~5.6 mAh cm^{-2} due to the exceptionally high loading. During discharge, all electrodes reach the previously charged capacity as the measurement is conducted as a half-cell with a Li-FSG counter electrode.

List of Symbols

Symbol	Description [unit]
A	Geometric area [m^2]
α	Constant phase exponent [−]
C	Arbitrary capacitance value
C_{dl}	Double layer capacitance [F]
δ_j	Loading unit ($\delta_2 = 2 \times \delta_1$ and $\delta_3 = 3 \times \delta_1$) [−]
d	Thickness of the electrode [m]
E	Potential (time domain) [V]
$\mathbf{E}$	Complex potential (Laplace domain) [V]
ϑ	Ratio of charge-transfer to ionic resistance (R_{ct}/R_{ion}) [−]
ϑ_{approx}	Approximated ϑ using simplified expressions [−]
ϑ_{true}	True ϑ using full solution [−]
ε	Porosity of the electrode [−]
ϵ_ϑ	Error in approximating ϑ [−]
f	Frequency [Hz]
f_{peak}	Peak frequency, where the imaginary resistance attains its peak value [Hz]
$\hat{f}_{peak}$	Scaled peak frequency [−]
$\mathbf{I}$	Complex current in Laplace domain [A]
$\boldsymbol{i}$	Complex current density ($=-d\mathbf{I}/dx$) in Laplace domain [A]
$\boldsymbol{i}_s$	Scaled complex current density ($\boldsymbol{i}(x)/\boldsymbol{i}|_{x=0}$) in Laplace domain [−]
Im_{peak}	Peak value of the imaginary resistance [Ω]
j	Imaginary unit
κ	Conductivity of the bulk electrolyte [S/m]
κ_{eff}	Effective conductivity of electrolyte in porous media ($\kappa_{eff} = \kappa\varepsilon/\tau$) [S/m]
L	Difference between low and high frequency intercept [Ω]
Q_{dl}	Double layer constant phase element capacitance of entire electrode [Fs$^{1-\alpha}$]
q_{dl}	Double layer constant phase element capacitance of electrode segment [Fs$^{1-\alpha}$]
R	Arbitrary resistance value
R_{ion}	Ionic resistance ($=d/(A\kappa_{eff})$) [Ω]
r_{ion}	Ionic resistance of a small element in the TLM [Ω]
R_{ct}	Charge-transfer resistance of an entire electrode [Ω]
r_{ct}	Charge-transfer resistance of a small element in the TLM [Ω]
$\hat{r}_{ct}$	Charge-transfer resistance of a small volume element ($=R_{ct}Ad$) [Ωm^3]
τ	Tortuosity of the electrode [−]
ω	Angular frequency ($=2\pi f$) [Rad s^{-1}]
x	Scaled axial length [−]
X	Axial coordinate [m]
$\mathbf{Z}$	Complex impedance [Ω]

Descriptive subscripts:

AM	Active Material
Areal	Relating to the geometric area
Fit	Parameter obtained by a spectrum fit
true	Parameter ϑ obtained using the full impedance solution (Eq. 2)
approx	Parameter ϑ obtained using the simplified solution (Eqs. 4 and 5)
peak	Relating to the peak of the "semicircle"
eff	Relating to the effective parameter
dl	Relating to the double layer capacitance
G	Relating to the graphite active material
ion	Relating to the ionic resistance
ct	Relating to the charge transfer resistance
s	Scaled parameter

ORCID

Robert Morasch https://orcid.org/0000-0002-9931-1022
Josef Keilhofer https://orcid.org/0000-0002-5092-1567
Hubert A. Gasteiger https://orcid.org/0000-0001-8199-8703
Bharatkumar Suthar https://orcid.org/0000-0002-8612-9483

References

1. A. Zaban, E. Zinigrad, and D. Aurbach, *J. Phys. Chem.*, **100**, 3089 (1996).
2. M. Ender, A. Weber, and E. Ivers-Tiffée, *Electrochem. Commun.*, **34**, 130 (2013).
3. M. Cronau, M. Kroll, M. Szabo, F. Sälzer, and B. Roling, *Batter. Supercaps*, **3**, 611 (2020).
4. J. Huang and J. Zhang, *J. Electrochem. Soc.*, **163**, A1983 (2016).
5. N. Meddings et al., *J. Power Sources*, **480**, 228742 (2020).
6. D. Schreiner et al., *J. Electrochem. Soc.*, **168**, 030507 (2021).
7. J.-H. Schunemann, H. Dreger, H. Bockholt, and A. Kwade, *ECS Trans.*, **73**, 153 (2016).
8. N. Ogihara, S. Kawauchi, C. Okuda, Y. Itou, Y. Takeuchi, and Y. Ukyo, *J. Electrochem. Soc.*, **159**, A1034 (2012).
9. N. Ogihara, Y. Itou, T. Sasaki, and Y. Takeuchi, *J. Phys. Chem. C*, **119**, 4612 (2015).
10. N. Ogihara and Y. Itou, *R&D Rev. Toyota CRDL*, **48**, 17 (2017).
11. Y. Itou, N. Ogihara, and S. Kawauchi, *J. Phys. Chem. C*, **124**, 5559 (2020).
12. A. N. Mistry and P. P. Mukherjee, *Phys. Chem. Chem. Phys.*, **21**, 3805 (2019).
13. S. Solchenbach, D. Pritzl, E. J. Y. Kong, J. Landesfeind, and H. A. Gasteiger, *J. Electrochem. Soc.*, **163**, A2265 (2016).
14. R. Morasch, B. Suthar, and H. A. Gasteiger, *J. Electrochem. Soc.*, **167**, 100540 (2020).
15. A. Lasia, "Electrochemical Impedance Spectroscopy and its Applications." *Modern Aspects of Electrochemistry* (Springer, Boston, MA) 32, p. 1 (2002).
16. S. G. Compton, S. G. Beesley, and D. A. Jones, *Heredity (Edinb).*, **61**, 235 (1988).
17. J. Landesfeind, M. Ebner, A. Eldiven, V. Wood, and H. A. Gasteiger, *J. Electrochem. Soc.*, **165**, A469 (2018).
18. I. V. Thorat, D. E. Stephenson, N. A. Zacharias, K. Zaghib, J. N. Harb, and D. R. Wheeler, *J. Power Sources*, **188**, 592 (2009).
19. J. Landesfeind, J. Hattendorff, A. Ehrl, W. A. Wall, and H. A. Gasteiger, *J. Electrochem. Soc.*, **163**, A1373 (2016).
20. J. Landesfeind, D. Pritzl, and H. A. Gasteiger, *J. Electrochem. Soc.*, **164**, A1773 (2017).
21. D. Pritzl, J. Landesfeind, S. Solchenbach, and H. A. Gasteiger, *J. Electrochem. Soc.*, **165**, A2145 (2018).
22. P. Lu, C. Li, E. W. Schneider, and S. J. Harris, *J. Phys. Chem. C*, **118**, 896 (2014).
23. J. H. Kim, S. J. Lee, J. M. Lee, and B. H. Cho, *7th Internatonal Conference on Power Electronics, ICPE'07*(IEEE, Piscataway, NJ) p. 1173 (2007).
24. S. Zhao, F. Wu, L. Yang, L. Gao, and A. F. Burke, *Electrochem. Commun.*, **12**, 242 (2010).
25. T. Waldmann, B. I. Hogg, and M. Wohlfahrt-Mehrens, *J. Power Sources*, **384**, 107 (2018).
26. M. Doyle, T. F. Fuller, and J. Newman, *J. Electrochem. Soc.*, **140**, 1526 (1993).
27. J. Landesfeind and H. A. Gasteiger, *J. Electrochem. Soc.*, **166**, A3079 (2019).
28. J. Jaiser, J. Kumberg, J. Klaver, J. L. Urai, W. Schabel, J. Schmatz, and P. Scharfer, *J. Power Sources*, **345**, 97 (2017).
29. R. Morasch, J. Landesfeind, B. Suthar, and H. A. Gasteiger, *J. Electrochem. Soc.*, **165**, A3459 (2018).

3.2 Li-Ion Battery Electrode performance and Material Kinetics

3.2.1 Comparison of Silicon and Graphite Anodes on their Temperature-Dependent Impedance and Rate Performance

The article entitled "Comparison of Silicon and Graphite Anodes on their Temperature-Dependent Impedance and Rate Performance" was submitted to the peer-reviewed Journal of the Electrochemical Society in November 2022.

Silicon is an emerging anode material for Li-ion batteries due to its ten times higher specific capacity (3579 mAh/g) compared to graphite (372 mAh/g). Additionally, the OCV potential of silicon is higher compared to graphite, which allows for higher overpotentials before the onset of Li-plating, but in turn also decreases the specific energy of the cell. The higher specific capacity means less active material is required in practical electrodes to achieve the same capacity, which results in significantly thinner electrodes and decreases the electrode's mass transport resistance. On the other hand, the electrode also has a reduced surface area, which increases the interface resistance. Thus, when comparing the performance of electrodes of practical loadings, the graphite electrode is expected to show higher transport resistances but lower interfacial resistances, while the silicon electrode shows the opposite features.

In this study silicon and graphite electrodes with areal capacities of 2.7 mAh/cm^2 are analyzed for their electrode properties, specifically the pore resistance and the charge transfer resistance, and compared with respect to their temperature dependent behavior. The ~2-fold thicker graphite electrodes show a greater pore resistance than the silicon electrodes but lower charge transfer resistance. Since the charge transfer resistance shows a significantly higher activation energy than the pore resistance, the former becomes negligible at high temperatures and the pore resistance dominates the electrode's resistance. At lower temperatures, this trend inverses and the kinetic resistance becomes dominating. As the two materials exhibit significantly different OCV profiles, simply comparing the capacities reached by the electrodes does not yield an accurate description of the electrode's resistive properties, as the silicon electrode would reach higher capacities even if both electrodes were otherwise equal simply due to its different OCV profile. Thus, the

shape of the electrode potential is analyzed for charge rate capability on both silicon and graphite electrodes. These show that the graphite electrodes are strongly limited by the mass transport in the pores across all temperatures, while the silicon electrodes are mostly kinetically limited, due to their higher specific capacity that results in thinner electrodes and thus lower mass transport overpotential.

Author contributions

R.M. conceptualized the measurement plan. C.B. conducted the measurements. R.M. and C.B. evaluated the data. R. M. wrote the manuscript. R.M., C.B., M.G. and H.A.G. discussed the results and revised the manuscript.

Comparison of Silicon and Graphite Anodes: Temperature-Dependence of Impedance Characteristics and Rate Performance

Clara Berg[=], Robert Morasch[=]*, Maximilian Graf and Hubert A. Gasteiger

Chair of Technical Electrochemistry, Department of Chemistry and Catalysis Research Center, Technical University of Munich, Munich, Germany

*Corresponding author
[=]equal contribution

Abstract

A meaningful benchmarking of battery active materials with inherently different properties requires knowledge of both their intrinsic electrochemical properties as well as of the differences in the resulting porous electrode structures for equal, practically relevant areal capacities. Here we compare graphite and silicon anodes with practical areal capacities of 2.8 mAh/cm^2 for lithium-ion batteries with regard to their temperature-dependent kinetic charge-transfer resistances (R_{ct}) and their ion transport resistances through the electrolyte phase within the pores of the electrodes (R_{ion}), measured via impedance spectroscopy. We deconvolute the kinetic resistance from the impedance spectra by individually measuring the temperature-dependent pore resistance between −5 and +45°C, showing that the charge-transfer resistance dominates at low temperatures, while at high temperatures the pore resistance dominates for both electrode types due to the significantly higher activation energy of R_{ct}. An analysis of the potential profile of the electrodes at different lithiation rates shows how the thinner silicon electrode is significantly less affected by R_{ion}-induced transport losses compared to a thicker graphite electrode, resulting in lower overpotentials when fast-charging at high temperatures, despite similar kinetic resistances. Overall the silicon electrodes could be charged up to two times faster than graphite before reaching 0 V vs Li$^+$/Li.

Introduction

Silicon is a promising anode active material for next-generation high energy density lithium-ion batteries.[1,2] By electrochemically alloying silicon with lithium, the $Li_{15}Si_4$ phase can be obtained, which equates to a theoretical capacity of 3579 mAh/g_{Si} (2194 Ah/L).[3–5] Compared to the state-of-the-art graphite anode material which intercalates lithium to a composition of LiC_6 (372 mAh/g, 719 Ah/L), the use of silicon-rich anodes can significantly improve the gravimetric and volumetric capacity of a lithium-ion battery (LIB). However, a major drawback of silicon is its large volumetric change of up to 280% during a full charge/discharge cycle,[5] which leads to a pulverization of μm-sized silicon particles when they are cycled to high degrees of lithiation due to the mechanical strain upon extensive volume expansion.[6,7] As shown by Jantke et al.,[8] pulverization of μm-scale crystalline silicon can be avoided by only partially lithiating the silicon particles, whereby a partial lithiation to ~30% (corresponding to ~1200 mAh/g_{Si}) enables the reversible cycling of silicon-rich anodes (70%$_{wt}$) in full-cells for up to 250 cycles without particle pulverisation and with little initial irreversible capacity losses.[8,9] For this limited degree of lithiation, the microscale silicon particles retain their crystalline core over cycling,[9,10] and the electrode-level specific capacity of such silicon electrodes (~840 mAh/$g_{electrode}$) is still ~2.5-fold higher than that of typical graphite electrodes (~340 mAh/$g_{electrode}$). Therefore, the silicon electrodes used in the present study were made with microscale silicon (70%$_{wt}$) and were partially lithiated to 1200 mAh/g_{Si}.

Fast-charging of lithium-ion batteries is predominantly limited by lithium plating on the anode, which is possible once the anode potential drops below 0 V vs Li^+/Li. If the total overpotentials of graphite and silicon electrodes were to be identical, silicon anodes would allow for higher lithiation rates, as the average lithiation potential of amorphous silicon is

2

substantially higher than that of graphite, particularly in case of the partial lithiation concept, where the lithiation potential of silicon electrodes is at least 100 mV higher compared to that of graphite over the entire state-of-charge (SOC) range (Fig. 1a). In addition, when comparing anodes with the same areal capacity, the higher specific capacity of silicon results in anode electrodes that are substantially thinner than graphite based electrodes, so that the reduced path length of the ions in the electrolyte phase within the pores of the anode electrodes should result in lower mass-transport overpotentials (assuming comparable electrode porosities and tortuosities). Finally, the alloying of silicon can occur in three dimensions, whereas the intercalation into the graphite planes is two-dimensional.

Fig. 1b shows the cross-section scanning electron microscopy (SEM) image of an electrode with 70%wt microscale silicon (left) and of a graphite electrode (right) with 95.8%wt graphite. Both electrodes have a reversible areal capacity of 2.8 mAh/cm^2, which in the case of the silicon electrode is based on a ~30% utilization of the theoretical silicon capacity (i.e., 1200 mAh/g$_{Si}$), but the electrodes differ in thickness by more than a factor of two (~40 μm for the silicon vs. ~95 μm for graphite electrode).
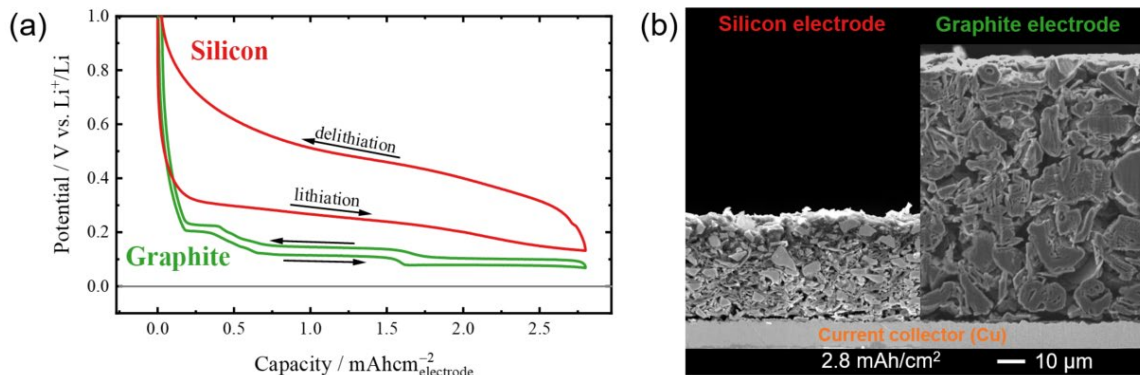
Fig. 1. (a) Potential profiles of microscale silicon (red) and graphite (green) working electrodes vs. capacity during galvanostatic cycling at C/10 (5th cycle) of electrodes with an areal capacity of 2.8 mAh/cm^2, calculated by referring to the reversible capacities of 1200 mAh/g$_{Si}$ for silicon (i.e., using ~30% of the theoretical capacity of Si) and 350 mAh/g$_{Gra}$ for graphite. The potentials are referenced to a lithium metal

reference electrode and the counter electrode is composed of metallic lithium and a free-standing graphite (FSG) electrode (see Experimental section). **(b)** Scanning electron microscopy (SEM) images, showing the cross-sections of a silicon and a graphite electrodes with 2.8 mAh/cm^2, illustrating the reduced thickness of the silicon electrode (~40 µm) compared to that of the graphite electrode (~95 µm) .

Since the pore resistance is a major factor that affects the electrode performance, we will first compare the resistance contributions of the ionic pore resistance (R_{ion}) and the kinetic charge-transfer resistance (R_{ct}, here assumed to also contain the SEI resistance) of both silicon and graphite electrodes of practical areal capacities (2.8 mAh/cm^2) via electrochemical impedance spectroscopy (EIS). The EIS analysis is done using a transmission line model approach as shown in Refs. [11] and [12]. As R_{ion} is influenced by the structure and morphology of the electrodes (i.e., thickness, porosity, and tortuosity), and since R_{ct} is dependent on the type of active material and its specific surface area, we show how silicon and graphite electrodes exhibit different contributions from each of these two resistances. This results in different temperature-dependent behavior of the electrodes due to the significantly higher activation energy of R_{ct} compared to R_{ion} (shown, e.g., for NCA cathode electrodes[13] as well as graphite anode electrodes[14,15]), rendering R_{ion} as the dominating resistance at high temperatures.

In a second part, we will compare the effect of the differences in R_{ct} and R_{ion} on the lithiation rate capability of silicon and graphite anodes. As the lithiation potential of silicon (especially when operating it at partial lithiation of only ~30%) is higher than that of graphite over the entire state-of-charge (SOC) region, directly comparing the lithiation capacities reached at 0 V vs Li$^+$/Li is not sufficient to deduce the effect of R_{ct} and R_{ion} on the lithitaion rate capability. Thus, we analyze the potential profiles of the electrodes at different lithiation rates (expressed as C-rates) and at different temperatures in order to disentangle the electrode performance from the potential profile, showing how R_{ct} causes a downshift in the potential, while R_{ion} causes a constant increase in electrode

4

overpotential with SOC, ultimately limiting the graphite electrode performance. Lastly, we compare the silicon and graphite rate performance at different temperatures and show how silicon electrodes show a performance improvement by a factor of two.

Experimental

Silicon electrode preparation.— The targeted weight percentages of the electrode were 70%$_{wt}$ silicon, 25%$_{wt}$ conductive graphite additive, and 5%$_{wt}$ acrylate binder. First, 7.0 g of silicon (d_{50} = 4.5 µm, A_{BET} = 2.9 m^2/g, Wacker Chemie AG, Germany), 12.5 g of an aqueous 4%$_{wt}$ LiPAA solution (prepared by neutralizing a polyacrylic acid (PAA; M_v = 459k, Sigma Aldrich) solution with LiOH to pH 7), and 5.1 mL of deionized water (18 MΩcm, Merck Millipore) were added to a mixing beaker (125 mL). After mixing the materials in a dissolver mixer (Dispermat LC30, VMA-Getzmann) at 4500 rpm for 5 min, 2.5 g of graphite (KS6L, A_{BET} = 23.2 m^2/g, Imerys) were added in small portions by gently stirring the mixture using a spatula, followed by another mixing step at 4500 rpm for 5 min and finally at 12000 rpm for 30 min. In a last step, the ink was degassed by mixing it in a planetary orbital mixer (Thinky Corp., USA) for 5 min at 2000 rpm. The slurry was coated onto copper foil (MTI, 12 µm) with a box-type coating bar (Erichsen, Hemer, Germany) using an automated coater (RK PrintCoat Instruments). Wet-film thicknesses of 110 µm resulted in the desired capacity loading of ~2.8 mAh/cm^2 based on the reversible capacity of 1200 mAh/g$_{Si}$. After drying the coating at room temperature for 12 h, electrodes were punched out to a diameter of 10.95 mm (equating to an area of ~0.94 cm^2) using an electrode punch (Hohsen Corp. OSAKA, Japan), and then dried overnight under vacuum

in a glass oven (Büchi, B-585) at 120°C and transferred into the glove box (note that the electrodes were not calendered or compressed).

The punched-out electrodes were individually characterized by weight (Sartorius Cubis I MSA225S) and thickness (Mitutoyo, Japan), with estimated absolute measurement errors of ± 0.015 mg and ± 1 µm, respectively. The cupper foil areal weight (8.57 ± 0.02 mg/cm^2) and thickness (10 ± 1 µm) were determined from cupper foil sampled in close proximity to the punched-out electrodes and subtracted from the measured electrode weight and thickness. The capacities of all analyzed electrodes ranged between 2.83 ± 0.08 mAh/cm^2 (based on 1200 mAh/g$_{Si}$), and for each of the studied electrodes the areal capacity was determined with a calculated measurement error of ± 0.02 mAh/cm^2. From the determined electrode thickness, the areal weight of all electrode components, and the bulk densities of the electrode components ($\rho_{Si} \approx 2.34$ g/cm^3, $\rho_{KS6L} \approx 2.26$ g/cm^3, and $\rho_{LiPAA} \approx 1.5$ g/cm^3), an average porosity of 62.0% with a maximum deviation of ± 0.5 percentage points was obtained. Here the resulting absolute error from the uncertainties in weight and thickness measurement was estimated as ± 2.2 percentage points.

Graphite electrode preparation.— The targeted weight percentages were 95.8%$_{wt}$ graphite, 1%$_{wt}$ carbon black, 1%$_{wt}$ sodium carboxymethyl cellulose (CMC), and 2.2%$_{wt}$ polystyrene-co-butadiene rubber (SBR). First, 0.2 g of CMC (MAC200HC, D.o.S = 0.85 – 0.95 mol/C$_6$, SUNROSE) were added to 10 mL of DI water and mixed twice for 10 min until the CMC was well dissolved. 19.16 g of surface-modified graphite (SMG, $A_{BET} = 3.1$ m^2/g, BASF SE, Germany) and 0.2 g of carbon black (Super C65, $A_{BET} = 62$ m^2/g, TIMCAL, Switzerland) were mixed in a separate beaker for 10 min at 1500 rpm. The resulting powder mixture was added to the CMC solution and everything was mixed in three steps in a

planetary orbital mixer (Thinky Corp., USA): (1) 10 min at 1000 rpm, (2) 10 min at 1500 rpm, (3) 5 min at 1500 rpm, and (4) 5 min at 2000 rpm. Before the second and third mixing step, water (2 x 3.75 mL) was added. The cup was weighed before and after each mixing step and any water vapour losses were compensated for. Finally, 0.88 g of SBR (Sigma-Aldrich, Germany) were added and all was mixed for 5 min at 500 rpm. Wet-film thicknesses of 140 μm resulted in a loading of ~2.8 mAh/cm^2 based on a reversible capacity of graphite of 350 mAh/g$_{Gra}$. The coating was dried and electrodes were punched to 10.95 mm diameter. Subsequently, they were dried overnight under vacuum in a glass oven (Büchi, B-585) at 120°C (note that the electrodes were not calendered or compressed) and transferred into the glove box.

Electrodes with an average capacity of 2.82 mAh/cm^2 (based on a reversible capacity of 350 mAh/g$_{Gra}$) with a maximum deviation of ± 0.05 mAh/cm^2 were obtained. Each electrode's capacity was determined with a calculated measurement error of ± 0.01 mAh/cm^2. From the determined electrode thickness, the areal weight of all electrode components, and the bulk densities of the electrode materials ($\rho_{Gra} \approx 2.26$ g/cm^3, $\rho_{C65} \approx 2.26$ g/cm^3, $\rho_{CMC} \approx 1.6$ g/cm^3, and $\rho_{SBR} \approx 1.04$ g/cm^3), an average porosity of 59.0% with a maximum deviation of ± 0.2 percentage points was obtained. Here the resulting absolute error from errors in weight and thickness measurements was estimated as ± 0.9 percentage points for each electrode.

The free-standing graphite (FSG) electrodes used on the counter electrode were prepared analogously to the method described in our previous publication.[16] The ~105 μm thick FSG electrodes were composed of 95%$_{wt}$ graphite (T311 type from SGL) and 5%$_{wt}$ polymer binder (polyvinylidene fluoride (PVDF), Arkema); they had a graphite loading of ~10.31 mg/cm^2.

Test cell assembly. — For electrochemical impedance analysis (EIS) and rate capability tests, three-electrode cell setups (Swagelok® T-cell) with reference electrodes were used, either with a gold-wire reference electrode (GWRE) for EIS measurements[17] or with a lithium metal reference electrode for rate capability tests. The cells were built inside an argon-filled glove box (MBraun, $25 \pm 1°C$, oxygen and water content <0.1 ppm, Ar 5.0, Westfalen). All test cell components were dried at 80°C overnight in an oven (Binder, Germany), while the glass fiber (GF) separators (11 mm diameter, 250 μm thickness, ~90% porosity; VWR) were dried overnight under vacuum in a glass oven (Büchi, B-585) at 300°C. The here used electrolytes were LP57 (1 M $LiPF_6$ in EC:EMC 3:7 (w:w), BASF, Germany), and 1 M $LiPF_6$ in a 1:4 mixture (v:v) of fluoroethylene carbonate (FEC, Gotion, USA) and diethyl carbonate (DEC, Gotion, USA).

Test cells for the electrochemical impedance measurements were assembled with a working electrode (silicon or graphite), four glass fiber separators, and a counter electrode consisting of a free-standing graphite electrode firmly attached to the metallic lithium foil (11 mm diameter, 0.45 mm thickness; Rockwood Lithium, 99.9% battery grade). 160 μL electrolyte were added to the four separators between the working and counter electrode.

Cells for rate capability tests were assembled analogously to the cells used for the impedance measurements (i.e., with a lithium counter electrode attached to a FSG electrode). Instead of the GWRE, metallic lithium was used as a reference electrode (6 mm diameter) and an additional 30 μL were added to the separator at the reference electrode.

8

Cell formation, impedance measurements, and rate capability tests.— Before electrochemical testing, all cells were left for 3 h at open circuit voltage (OCV) after assembly in order to allow for complete wetting of the electrode. Formation cycles and rate tests at 25 and 45°C were performed in climate chambers (Binder, Germany). Temperature-dependent impedance measurements and rate tests at –5°C were performed in a programmable low-temperature cabinet (ESPEC, LU-114, Japan). Electrochemical cycling and impedance measurements were conducted using a potentiostat (Bio-Logic Science Instruments, France). For cells with a gold wire reference electrode, the GWRE was lithiated by applying 150 nA for 1 h at 25°C via the counter electrode.

Figure 2 schematically illustrates the formation of the silicon and graphite electrodes and the procedure for the impedance analysis. The same formation procedure was carried out for all cells, i.e., also for those that were used for rate capability tests. Two galvanostatic (constant current (CC) (de-)lithiation) formation cycles were performed at C/10, with the first cycle at 25°C and the second cycle at 45°C. For the graphite electrodes, formation cycling was done between 30 mV and 1.5 V vs. Li^+/Li. The working electrode potentials were measured against the reference electrode whereby the GWRE potential was determined as 0.311 V vs. Li^+/Li.[17] For simplicity, all potentials are given with respect to the Li^+/Li potential. In case of the silicon electrodes, a partial lithiation of the microscale silicon was achieved by capacitively limiting the lithiation to 1200 mAh/g_{Si}, while for the delithiation a potential cutoff of 1 V vs. Li^+/Li was chosen.
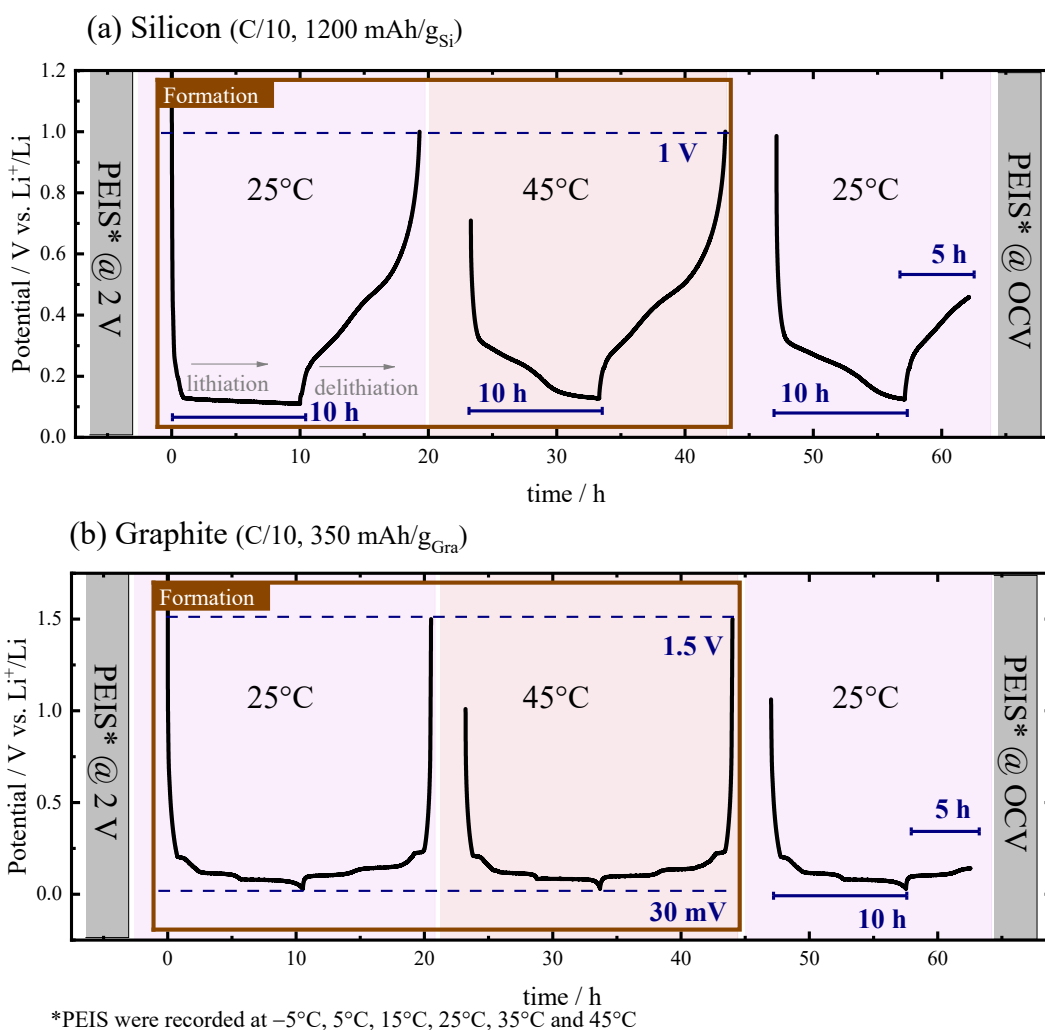
Fig. 2. Illustration of the potential curves during the formation procedure done for all cells (1st cycle at 25°C and 2nd cycle at 45°C) and during setting of the 50% SOC point (in delithiation direction) for the EIS measurements in T-cells with a GWRE (right-most segments) for: **(a)** silicon; **(b)** graphite. Galvanostatic cycling was performed at C/10, based on specific capacities of 1200 mAh/g$_{Si}$ and 350 mAh/g$_{Gra}$ for silicon and graphite electrodes, respectively (for details see text).

Potentiostatic electrochemical impedance spectra (PEIS) were recorded by applying a sinusoidal voltage perturbation of 10 mV at frequencies in the range of 30 kHz – 0.1 Hz. Before formation, PEIS was measured under blocking conditions (2 V vs Li$^+$/Li). After formation, the working electrodes were lithiated once more (to 1200 mAh/g$_{Si}$ in the case of silicon and to 350 mAh/g$_{Gra}$ in the case of graphite) and then delithitated to 50% SOC (600 mAh/g$_{Si}$ and 175 mAh/g$_{Gra}$) at a rate of C/10 at 25°C. Then, PEIS was recorded at OCV at 50% SOC (see right-most segments in Fig. 2). All PEIS measurements (i.e., before

10

formation and at 50% SOC) were performed in the following sequence: 25°C, −5°C, 5°C, 15°C, 25°C, 35°C, 45°C, 25°C. Before each impedance measurement, the cell was left to adapt to the respective temperature for 2 h. All impedance spectra were fitted to a simplified, reflecting, transmission line model (TLM, see e.g. Pritzl et al.[11]) using the software RelaxIS (rhd instruments, Version 3.0.20). The ionic pore resistances (R_{ion}) were determined from a fit of the spectra recorded in blocking conditions before formation. The charge-transfer resistances (R_{ct}) at 50% SOC were obtained from a non-blocking TLM fit with the variable for R_{ion} fixed to the values determined before formation.

For half-cell rate capability tests, the working electrode (silicon or graphite) was lithiated using a CC procedure, applying the current corresponding to each respective rate until the total capacity equaled 1200 mAh/g_{Si} or 350 mA/g_{Gra}. The CC delithiation was performed to a cut-off voltage of 1 V and 1.5 V versus the Li$^+$/Li reference electrode for silicon and graphite electrodes, respectively. This was followed by a constant voltage (CV) step until the measured current dropped below C/40. After formation (Fig. 2), three lithiation/delithiation cycles were carried out for each lithiation rate: C/10, C/5, C/2, 1 C, 1.33 C, 1.66 C, 2 C, 2.5 C, 3 C, and 4 C. The delithiation was performed at C/10 for the C/10 cycles and at C/5 for all other cycles. These rate capability tests were performed at −5, 25, and 45°C using two cells at each temperature.

Electrolyte conductivity measurements.— The ionic conductivities of the electrolytes were determined in a commercially available Pt microelectrode setup consisting of a Pt beaker and electrode (rhd Instruments, TSC 1600 closed, Germany). 0.9 mL of electrolyte were added to the Pt beaker inside the glovebox. The setup was then transferred to a programmable low-temperature cabinet (ESPEC, LU-114, Japan) and connected to a

potentiostat (Bio-Logic Science Instruments, France). Cell impedances were measured after a thermal equilibration for 2 h at the temperatures −5°C, 5°C, 15°C, 25°C, 35°C, and 45°C. The obtained cell resistances were converted to conductivity values using the calibration constant $k_c = 1370 \pm 20$ Ω mS cm^{-1} which was previously determined for a KCl calibration solution (Mettler Toledo, conductivity standard, 12.88 mS/cm).

Results and Discussion

Quantification of R_{ion} and R_{ct} for graphite and silicon electrodes.— This section describes the impedance analysis and the thereby determined differences in the ionic pore resistance (R_{ion}) as well as the charge-transfer resistance (R_{ct}) between the graphite and silicon electrodes. As this analysis is done for electrodes with practically relevant areal capacities of 2.8 mAh/cm^2 that have a significant thickness, R_{ion} is of the same order as R_{ct} near room temperature (illustrated for graphite anodes in Reference [12]) and thus will have a strong impact on electrode performance. For a better comparison, LP57 was used as electrolyte for both Si and graphite electrodes. However, since Si electrodes are typically used with FEC-based electrolyte, the Si electrodes were also examined using FEC:DEC 1:4 (v:v) with 1 M LiPF$_6$; for any analyses pertaining to the silicon electrode measured with this electrolyte, we denote the electrode as Si$_{FEC}$.

Fig. 3a and b show exemplary impedance spectra of a graphite electrode in LP57 (green) and of silicon electrodes in either LP57 (red) or in the FEC-based electrolyte (orange), acquired at 25°C prior to formation as well as at 50% SOC (after two formation cycles). R_{ion} and R_{ct} were determined by an EIS analysis that was performed according to Ref. 12: i) first, the value of R_{ion} was determined under blocking conditions (i.e., prior to

formation), using a transmission line model (TLM) with only capacitive and ionic resistance elements (neglecting electrical resistances) as well as a resistor representing the separator resistance (including electrical contact resistances); ii) subsequently, the value of R_{ct} was determined at 50% SOC (see right-most segments of Fig. 2), using the above TLM but including charge-transfer resistance elements, whereby the TLM was fitted using the R_{ion} value determined under blocking conditions (a necessary step for low values of R_{ct} compared to R_{ion} as described in Ref. 12). The shift in the high-frequency resistance (HFR) for the Si electrode impedance spectra in FEC-based electrolyte (Si$_{FEC}$) in Fig. 3a/b is a result of the lower ionic conductivity of the FEC-based electrolyte (6.8 ± 0.1 mS/cm) compared to the LP57 electrolyte (9.1 ± 0.1 mS/cm) at 25°C.
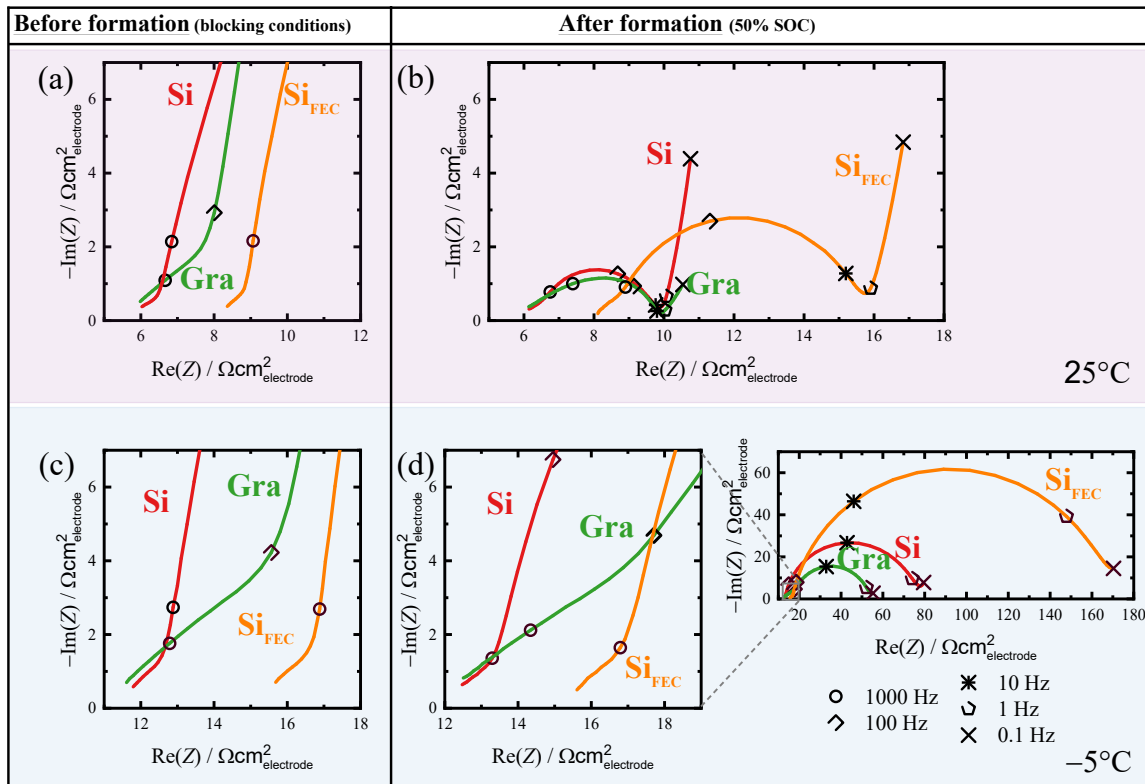
Fig. 3. Nyquist plots of the impedances of silicon and graphite working electrodes with areal capacities of 2.8 mAh/cm², measured by means of a micro-reference electrode (GWRE) in half-cells with a lithium metal counter electrode attached to a free-standing graphite electrode (Li/FSG): **(a)** measured at 25°C before formation at 2 V vs. Li⁺/Li, i.e., under blocking conditions; **(b)** measured at 25°C after formation at 50% SOC (see Fig. 2). The graphite electrode was measured with LP57 electrolyte (green), while the Si electrode

was measured with both LP57 (red) and with an FEC-based electrolyte (orange; 1M LiPF$_6$ in FEC:DEC 1:4 (v:v)). **(c)** and **(d)**: Same type of EIS data, but acquired at −5°C.

Fig. 3a shows the 25°C impedance spectra under blocking conditions of the electrodes prior to electrode formation, allowing the determination of R_{ion}, as, e.g. described in the literature.[13,18] The R_{ion} value obtained from Fig. 3a for the graphite electrode is 6.9 Ωcm$^2_{electrode}$, whereas R_{ion} for the Si electrode measured in the same LP57 electrolyte is 2.3 Ωcm$^2_{electrode}$ (see Table 1). These differences can be understood by considering the most general mathematical description of R_{ion}:

$$R_{ion} = \frac{\tau \cdot t}{\varepsilon \cdot A \cdot \kappa} \qquad [1]$$

where τ is the tortuosity, t is the electrode thickness, ε is the porosity (here ~60% for all electrodes, see Table 1), A is the geometric surface area of the electrodes (0.94 cm^2), and κ is the electrolyte conductivity. The most apparent factor that would lower R_{ion} of the Si electrodes is their nearly 2.5-fold lower thickness (~40 vs. ~95 μm, see Table 1 and Fig. 1). Additionally, particle shape, binder type, and electrode preparation can be an important factor influencing the electrode tortuosity values,[18–20] which can be determined from equation 1 using the measured values of R_{ion}, the geometric parameters of the electrodes (ε, t, and A), and the electrolyte bulk conductivities. The resulting tortuosity values for silicon (~3.2) are roughly 20% smaller than those obtained for graphite (~3.9), indicating that the structure of the silicon electrodes offers slightly better intrinsic ionic transport properties. Ultimately, the major effect responsible for the ~3-fold lower R_{ion} of the silicon compared to the graphite electrodes in the LP57 electrolyte (see green and red highlighted segments in Table 1) is simply their difference in electrode thickness.

Table 1. Structural characterization of the graphite and silicon electrodes that were analyzed by impedance spectroscopy for their electrochemical properties in LP57 electrolyte and, in the case of the silicon electrodes,

14

also in FEC-based electrolyte (1 M LiPF$_6$ in FEC:DEC 1:4 (v:v); the corresponding data are referred to as Si$_{FEC}$). The table lists the reversible capacities, electrode thicknesses ($t_{coating}$), calculated porosities (ε), the ionic pore resistances (R_{ion}) obtained at 25°C from the impedance spectrum in blocking conditions, and the tortuosity (τ) determined from eq. 1. For each electrode/electrolyte combination, two independent samples were measured and analyzed (labelled as #1 and #2) and the ionic conductivites (κ) at 25°C are 9.1 ± 0.1 mS/cm for LP57 and 6.8 ± 0.1 mS/cm for the FEC-based electrolyte. The errors correspond to the measurement errors for each sample, including the error propagation in case of ε and τ.

System		Capacity	$t_{coating}$	ε	R_{ion}	τ
		[mAh/cm$^2_{electrode}$]	[μm]	[%]	[Ωcm$^2_{electrode}$]	[-]
Gra (LP57 electrolyte)	#1	2.85 ± 0.01	94 ± 1	59 ± 1	6.9 ± 0.10	3.9 ± 0.1
	#2	2.86 ± 0.01	95 ± 1	59 ± 1	6.8 ± 0.05	3.8 ± 0.1
Si (LP57 electrolyte)	#1	2.86 ± 0.02	40 ± 1	62 ± 2	2.3 ± 0.09	3.2 ± 0.2
	#2	2.84 ± 0.02	39 ± 1	62 ± 2	2.2 ± 0.05	3.2 ± 0.2
Si$_{FEC}$ (FEC-based electrolyte)	#1	2.78 ± 0.02	39 ± 1	62 ± 2	2.9 ± 0.10	3.1 ± 0.2
	#2	2.92 ± 0.02	40 ± 1	62 ± 2	3.0 ± 0.10	3.2 ± 0.2

Fig. 3b shows the impedance of the graphite and silicon electrodes after formation at 50% SOC (for conditions, see right-most segments in Fig. 2a/b). Both silicon measurements show an initial 45°-slope at high frequencies of above 1 kHz (for frequency assignments see legend given in the lower right-hand corner of Fig. 3), followed by a transition into a semicircle (between 1 kHz and 1 Hz), and a final diffusive branch (below 1 Hz).

Assuming that the value for R_{ion} does not change significantly upon formation (e.g., via volumetric expansion), the data in Fig. 3b yield charge-transfer resistances in LP57 electrolyte at 25°C of 2.7 Ωcm$^2_{electrode}$ for graphite and 3.4 Ωcm$^2_{electrode}$ for silicon. On the other hand, when using the FEC-based electrolyte, the charge-transfer resistance of the Si electrodes is approximately twice as high, at 7.0 Ωcm$^2_{electrode}$, which is presumably due to the formation of an SEI with different composition and/or more resistive solid electrolyte interphase (SEI).[21,22] To move this analysis from the electrode level to the material level, one would need to consider the intrinsic charge-transfer resistance of the different active materials, i.e., the charge-transfer resistance normalized to the electrochemically active

surface area which, a zero-order estimate would be the BET surface area of the active material. With this assumption, the electrode roughness factor multiplied with the above given charge-transfer resistance referenced to the geometric surface area yields the intrinsic charge-transfer resistance. The graphite electrode roughness factor is calculated as ~250 $cm^2_{BET}/cm^2_{electrode}$ (based on the graphite BET surface area of 3.1 m^2/g and the graphite loading), while that of the silicon electrodes with ~70 $cm^2_{BET}/cm^2_{electrode}$ (based on a BET surface area of 2.9 m^2/g and the silicon loading) is more than 3-fold smaller. This yields intrinsic charge-transfer resistances in LP57 of 675 Ωcm^2_{BET} for graphite, which is ~3-fold larger than the 238 Ωcm^2_{BET} for silicon. However, since the silicon surface area is subject to change over cycling[23] and since the graphite basal planes are not expected to be electrochemically active, this comparison of the active materials intrinsic charge-transfer resistances needs to be studied in more detail to yield further understanding. It should be noted that, while the silicon electrodes contain graphite as conductive additive, the potential of the silicon electrode at 50% SOC (450 mV vs. Li^+/Li) lies above the threshold at which intercalation into the graphite is possible and we expect no notable influence of the graphite on the charge-transfer analysis of the silicon electrodes (i.e., the graphite is under blocking conditions).

Fig. 3c depicts the blocking impedance measurement of the electrodes at −5°C, showing the roughly twofold increase in R_{ion} due to the temperature-induced decrease in electrolyte conductivity. Comparing the impedance responses at 50% SOC obtained at −5°C (Fig. 3d) with those obtained at 25°C reveals a drastic increase in the charge-transfer resistance of the electrodes. The strong temperature dependence of R_{ct} (discussed further in the section below) results in a more rapid increase of R_{ct} compared to R_{ion} with decreasing temperatures. As this leads to a better separation of the contributions of R_{ion} and R_{ct} in the

frequency domain (i.e., to a clearly visible 45°-line at high frequencies followed by a well-pronounced semicircle at lower frequencies), R_{ion} can be determined in a straightforward manner even from measurements under non-blocking conditions.[12] This allows for comparison of R_{ion} obtained under blocking conditions before formation (Fig. 3c) and obtained under non-blocking conditions after formation at 50% SOC (left plot in Fig. 3d). For all the here analyzed cells, the R_{ion} value obtained at −5°C either from blocking conditions before formation (see Fig. 3c) or at 50% SOC after two formation cycles (see Fig. 3d) deviated by less than 15%. This means that our above stated assumption used to determine R_{ct}, namely that R_{ion} does not change significantly over the course of the two formation cycles, is reasonably accurate, i.e., that fixing the value for R_{ion} to that obtained before formation is reasonable. The change of the individual resistances with temperature is discussed in more detail in the following section.

Temperature-dependent impedance.— This section describes the temperature-dependent behavior of the two resistances, R_{ct} and R_{ion} . The resistances were extracted by individually measuring R_{ion} before formation at all temperatures and then analyzing the spectra at 50% SOC to extract the charge-transfer resistance.

As described above, the main differences in electrode properties between the graphite and silicon electrodes is their difference in pore resistance, which is lower for the much thinner silicon electrodes, as well as in charge-transfer resistance, which is slightly higher for the silicon electrodes in the same electrolyte (i.e., in LP57) and substantially higher when using an FEC-based electrolyte that is commonly used for silicon electrodes. This difference plays a key role when it comes to the temperature-dependent behavior of the electrode

performance. Fig. 4 shows the temperature dependence of the two resistances, R_{ion} and R_{ct}, which were extracted from the EIS measurements.

First, Fig. 4a shows the temperature-dependence of R_{ion} of the different electrodes as well as of the resistivity ($\rho_{electrolyte} = 1/\kappa$) of the pure electrolytes (i.e., of LP57 and the FEC-based electrolyte), together with the thereof calculated activation energies. For the graphite electrodes in LP57, the activation energy for R_{ion} of 14.1 kJ/mol (Fig. 4a, green text/symbols) is in very good agreement with the activation energy determined for the ionic resistivity of LP57 of 13.8 kJ/mol (dark blue text/symbols; reasonably close to the 13.2 kJ/mol determined by Solchenbach et al. from Swagelok® T-cell measurements[15]), as one would expect on the basis of equation 1. On the other hand, for the silicon electrode in LP57, the activation energy for R_{ion} (15.6 kJ/mol, red text/symbols) is ~13% higher than the activation energy of the ionic resistivity of LP57. This deviation is likely due to a non-negligible error in the analysis of the impedance data R_{ion}, since the ~3.5-fold lower R_{ion} value for the silicon electrodes in LP57 makes it difficult to accurately analyze the spectra (this is especially the case at higher temperatures, which in turn may lead to an apparently higher slope). For the silicon electrodes with the FEC-based electrolyte, the same discrepancy between the activation energy for R_{ion} (15.4 kJ/mol, orange text/symbols) and for $\rho_{electrolyte}$ (13.6 kJ/mol, blue text/symbols) is observed, presumably for the same reason. Overall, however, it can be stated that the activation energies for R_{ion} are rather low and, as expected, very close to the activation energy for $\rho_{electrolyte}$.

Fig. 4b shows the change of the charge-transfer resistance with temperature. The graphite and the Si electrodes with LP57 electrolyte show activation energies for R_{ct} of 61.8 and 64.4 kJ/mol, respectively. The Si$_{FEC}$ electrodes show a slightly higher activation energy for

the charge-transfer reaction (68.0 kJ/mol), but reasonably similar to that of the silicon electrodes with LP57 electrolyte, despite an expected difference in SEI composition.[21,22]
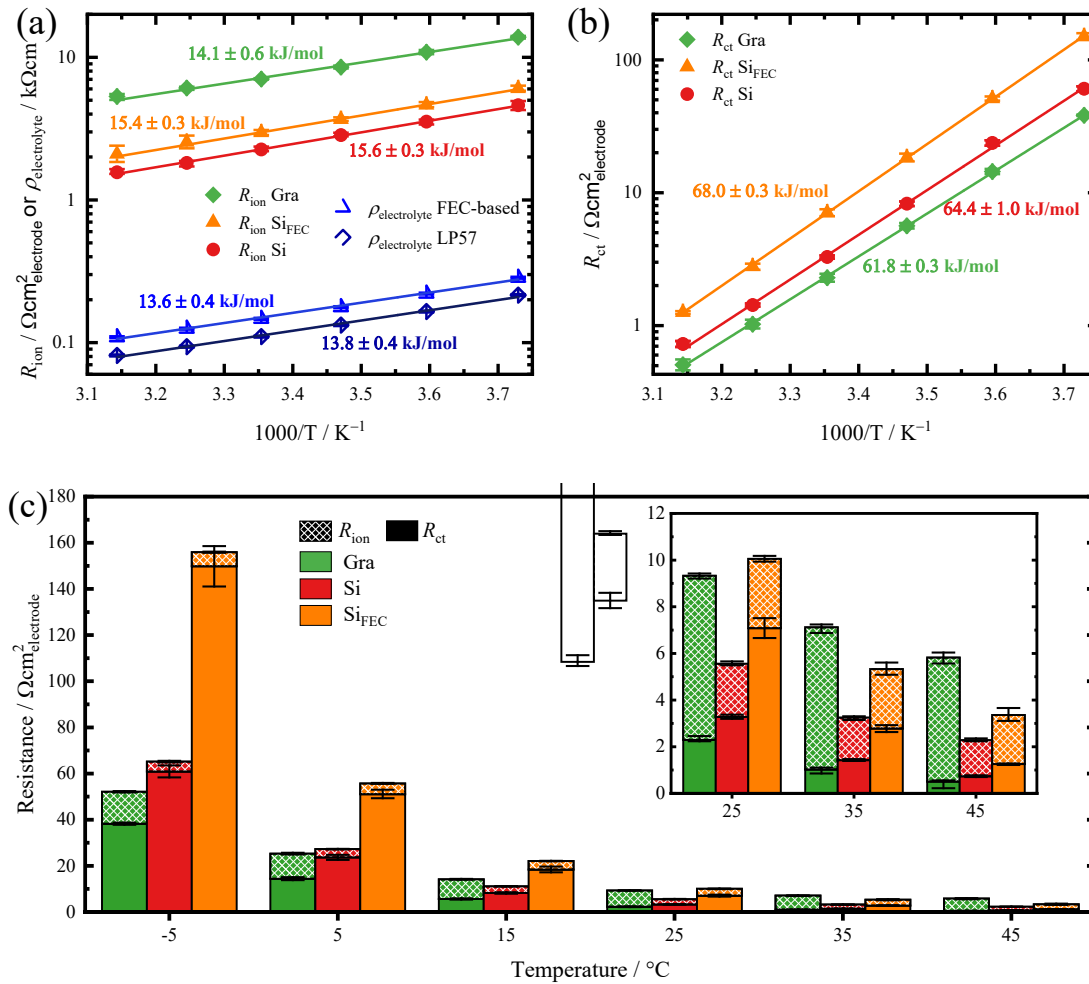

Fig. 4. The obtained values for R_{ct} and R_{ion} from the impedance analysis conducted at -5 to +45°C with graphite and silicon electrodes (2.8 mAh/cm^2) in LP57 and with silicon electrodes in 1 M LiPF$_6$ in FEC:DEC 1:4 (referred to as Si$_{FEC}$). **(a)** Arrhenius plots for R_{ion} and the electrolyte resistivities ρ; **(b)** Arrhenius plot for R_{ct}; **(c)** Bar chart showing the absolute contributions of R_{ion} and R_{ct} for each system and temperature, with R_{ct} represented by the lower part of the bar and R_{ion} represented by the upper hatched part of the bar. The data shows the change of resistance contribution, with R_{ct} dominating at lower temperatures and R_{ion} dominating at higher temperatures. The average obtained from two measurements in separate cells is plotted. The plotted error bars span the deviation of each resistance value from the mean plus the error obtained from each impedance fit.

To better highlight the differences in electrode resistances, Fig. 4c shows the sum of R_{ct} (fully colored lower part of the bars) and R_{ion} (hatched upper part of the bars) at each temperature. At −5°C, R_{ct} is the dominating resistance for all electrodes/electrolytes, most prominently for the Si electrodes, for which the ratio of R_{ct}/R_{ion} is ~13 (LP57) and ~25

97

(FEC), whereas it is only ~2.8 for the graphite electrodes. With increasing temperature, the charge-transfer resistance change drastically due to their higher activation energy, so that the ratio of R_{ct}/R_{ion} at 45°C decreases to 0.47, 0.58, and 0.11 for the Si, Si$_{FEC}$, and graphite electrodes, respectively. At these elevated temperatures, the dominating resistance is now R_{ion}, i.e., the material is expected to be limited by the lithium ion transport in the electrolyte phase within the pores of the electrodes rather than by the reaction resistance. While at −5°C the sum of R_{ct} and R_{ion} was lowest for the graphite electrode, at 35°C and 45°C this is reversed and the graphite electrode shows the largest total resistance compared to Si in either one of the electrolytes. This is explained by the difference in activation energies and the differences in R_{ct} and R_{ion} for the graphite and silicon electrodes. At low temperatures, R_{ct} is increased significantly and the silicon electrodes show larger resistances compared to graphite. At high temperatures, R_{ct} is significantly reduced, so that the differences between the kinetic resistances become negligibly small, leaving R_{ion} as the dominating resistance, which is smallest for the thin silicon electrodes.

***Electrode potential profile comparison in lithiation rate tests.*—** This section describes the observed influence of the two resistances R_{ct} and R_{ion} on the potential profile and the performance of the electrodes. While the resistances shown in the previous section were measured during delithiation and only show the resistance at 50% SOC, they can still be used as guidelines and reference points to understand the behavior of the potential curves of the electrodes under load, even though they are not necessarily representative of the overpotentials of the electrodes at all SOCs. Additionally, the diffusion overpotentials from Li$^+$ concentration gradients in the electrodes and the separator, which are not part of the measured R_{ion}, will contribute to the measured overpotential.[24,25]

98   20

The effects of the resistances R_{ct} and R_{ion} on the potential profile are expected to be different. The charge-transfer resistance is a resistance connected in series to the reaction path, i.e., every Li$^+$-ion has to overcome the reaction resistance to be intercalated (in case of graphite) or alloyed (in case of silicon). The kinetics may change as a function of SOC (assuming e.g. Doyle-Fuller-Newman (DFN) - type kinetics[26]), but between C-rates the difference in overpotential from faradaic reactions should result in the electrode potential being shifted downward, as changes in the applied current correspond to changes in Butler-Volmer (BV) type overpotential. The linear region of the BV kinetics, where the kinetic overpotential equates to the product of R_{ct} and the current density, extends to overpotentials of up to roughly one third of the Tafel slope. Assuming a kinetic transfer coefficient of $\alpha = 0.5$, the Tafel slope (*TS*) at room temperature is ~120 mV (based on TS = 2.303·R·T/(α·F), with R being the ideal gas constant, F the Faraday constant, and T the temperature in Kelvin), so that the linear region should extend to up to roughly ± 40 mV.[27] At 25°C, the R_{ct} of the silicon electrode with LP57 is ~3 Ωcm^{2}electrode, resulting in a kinetic overpotential of ~8 mV at a rate of 1C (i.e., at a current density of 2.8 mA/cm^{2}electrode), i.e., still being in the linear BV region. At −5°C however, the charge-transfer resistance of the silicon electrode with LP57 increases to R_{ct} ~60 Ωcm^{2}electrode, resulting in a linearly extrapolated kinetic overpotential at 1C of ~170 mV; as the latter is outside the linear region, the actual kinetic overpotential would be lower. In either case (i.e., whether in the linear or non-linear BV region), higher rates will lead to an increased down-shift of the potential curve (i.e., of E vs. SOC). Furthermore, if R_{ct} does not vary strongly with the SOC, the potential curve retains its specific shape. The change in R_{ct} with SOC is not shown in this work but has been measured to be below a factor 2 for most parts

of the SOC window measured in LP57, similarly to the DFN model which predicts a max. change of factor 2 in kinetics between 10 – 90% SOC.[26,28]

In contrast, the electrolyte ionic resistance in the pores of the electrode is connecting the active material particles through the electrode, and not all ions have to pass through the entire electrode for the reaction to occur. For example, only 10% of the total Li^+ exchanged needs to reach the bottom 10% of the electrode near the electrode/current collector interface. Thus, one might assume that it is less important compared to the charge-transfer resistance. However, high currents can lead to concentration gradients across the electrode and thus to an inhomogeneous use of the electrode, i.e., it is more difficult for Li^+ to reach the region of the electrode near the current collector versus the region of the electrode near the separator, which is reflected in a downward-sloping potential profile.[25] Additionally, R_{ion} is only a representation of the electrolyte conductivity, whereas during operation of a battery cell additional diffusion resistances will contribute to the mass transport overpotential. These diffusion overpotentials not only play a role in the porous electrodes but also across the separator. The concentration difference across the separator can be estimated via

$$\frac{\partial c}{\partial x} = -\frac{I(1 - t_+)\varepsilon}{D\tau F} \qquad [2]$$

with c being the electrolyte concentration, x being the path length (e.g., the separator thickness), F being the Faraday constant, I being the applied current (in A/m^2), t^+ being the transference number, and D being the salt diffusion coefficient (in m^2/s). Combined with the equation

$$\frac{\partial \phi}{\partial x} = \frac{\frac{2RT}{F}(\text{TDF})(1 - t_+)}{c}\frac{\partial c}{\partial x} \qquad [3]$$

with R being the ideal gas constant, T the electrolyte temperature (in Kelvin), and TDF being the thermodynamic factor, the potential drop ϕ across the separator can be estimated.[29] The path length of ions through the separator x can be estimated from the thickness of the separator and its tortuosity. The tortuosity of the separator can be calculated using equation 1 assuming $\varepsilon = 0.8$, separator thickness $\sim 2 \times 200$ μm (two separators measured from the reference electrode to the working electrode), electrolyte conductivity 9.1 mS/cm and a resistance of ~ 6 $\Omega \text{cm}^2_{\text{electrode}}$ (HFR), giving $\tau \approx 1$. From there, using electrolyte values for 25°C measured by Landesfeind et al.[30] for LP57, ($D = 3 * 10^{-10} m^2/s$, $t^+ = 0.25$, TDF = 1.5), the overpotential at C/5 ($\equiv 0.56$ mA/cm$^2_{\text{electrode}}$) across two glass fiber separators is estimated to be ~ 2.7 mV, which corresponds to an areal resistance of ~ 4.8 $\Omega \text{cm}^2_{\text{electrode}}$. The Warburg diffusion resistance is dependent on the same geometric and electrolyte properties as the HFR, meaning that an increase in HFR would directly follow an increase in the Warburg diffusion resistance, with the Warburg resistance giving 0.8× HFR. This means that under load the separator exhibits a resistance 1.8 times the measured HFR. Following this, the factor 1.8 can be used with any resistance stemming from the electrolyte under load, including R_{ion}. It should be mentioned that changes in Li$^+$ concentration in the electrolyte are also assumed to have an effect on the kinetics, with a locally decreased Li$^+$ concentration increasing the local R_{ct}, as, e.g., expected during fast-charging on the anode side. This highlights the importance of the porous aspect of the electrode, as it has an effect on local current homogeneity,[12,25] kinetic resistances, as well as transport resistances. In summary, electrodes which are mostly limited by kinetic resistances are expected to keep the shape of their potential profile, with the potential

versus SOC curve only being shifted downward (assuming no drastic changes in SOC-dependent kinetics). In contrast, electrodes which show strong transport limitations in the electrolyte phase are subject to inhomogeneous current distributions in the electrode and show time dependent concentration gradients, which are expected to increase the electrode overpotential over time, i.e., over SOC when conducting a constant-current charge or discharge curve.

To show the influence of R_{ct} and R_{ion} on the electrode performance, the electrodes were tested for their rate capability during lithiation (corresponding to the charging of a battery cell). Fig. 5 shows the potential profiles of the graphite and silicon electrode measured with LP57 electrolyte at different temperatures and C-rates, whereby the graphite and silicon electrode potentials are measured versus the reference electrode in the cell. The silicon electrode (red colored lines) shows the expected behavior of electrodes that are limited by their charge-transfer kinetics, where the electrode potential versus SOC curve retains its shape but is shifted downward, visible most clearly for the −5°C data at C/5 (Fig. 5a) and C/2 (Fig. 5b). Only at a rate of 1C at −5°C, the silicon electrode shows an increase in overpotential with SOC (i.e., with lithiation time) and the electrode potential ultimately falls below 0 V vs Li$^+$/Li, where lithium plating can occur.
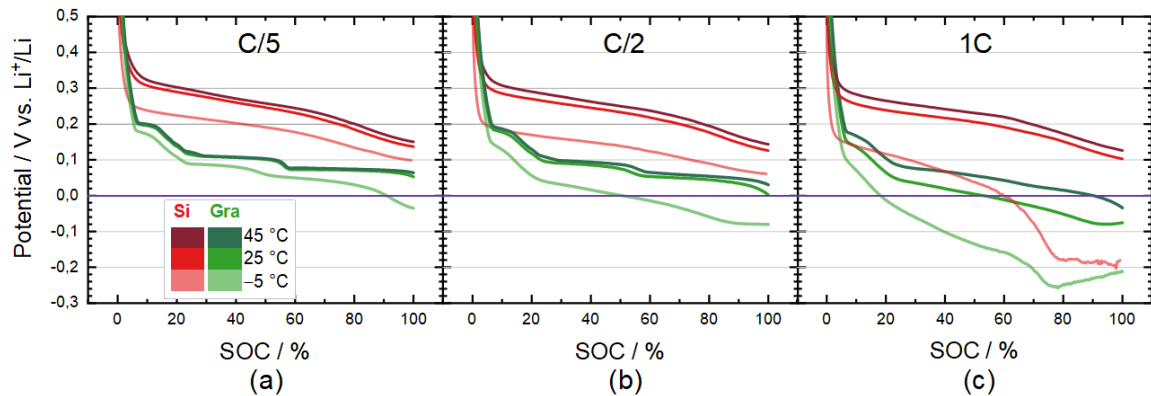

Fig. 5. Lithiation potentials versus SOC for silicon (red colored line) and graphite electrodes (green colored lines) in LP57 at 45°C, 25°C and −5°C at various C-rates: **(a)** C/5, **(b)** C/2, and **(c)** 1C. The silicon and

graphite electrode potentials are referenced to the reference electrode in Swagelok® T-cells, with graphite or silicon as working electrodes (2.8 mAh/cm²) and a lithium metal foil with a free-standing graphite electrode as counter electrode. Note that the silicon in the silicon electrodes is utilized only partially, i.e., only up to 1200 mAh/g$_{Si}$.

The graphite electrodes only retain the shape of their open circuit potential versus SOC profile for C/5 and C/2 at 25°C and 45°C, suggesting a constant overpotential over the entire SOC range under these conditions. However, while the graphite potential profile at −5°C is downshifted at C/5 in a similar fashion at low SOCs (see Fig. 5a), it starts to become more sloped at higher SOCs (around 80% SOC), suggesting stronger concentration overpotentials at high SOCs. This effect is even more pronounced at C/2 and −5°C (see Fig. 5b), where a substantial sloping and smearing out of the plateaus of the different lithiation stages can be observed already beyond ~20% SOC. At 1C (see Fig. 5c), the graphite electrodes show a constantly increasing overpotential over all temperature ranges and even at the highest temperature of 45°C, the electrode cannot be fully charged before reaching 0 V vs Li$^+$/Li. The resistances derived from the impedance data (Fig. 4c) between 25°C and 45°C show that the graphite and silicon charge-transfer resistances (for LP57) are similar, and that the electrodes differ most prominently in their ionic pore resistance which are ~3-fold smaller for the silicon electrodes. This results in a poor lithiation performance at 1C of the graphite electrode, but does not yet limit the performance of the thinner silicon electrode. Analyzing the electrode potential at 100% SOC, the effect of the difference in ionic pore resistance becomes apparent: at 45°C, the potential difference between C/5 and 1C for the silicon electrodes is ~30 mV at 100% SOC, while it is ~100 mV for the graphite electrode, i.e., ~3-fold larger.

The comparison of the effect of temperature and of the individual resistances (i.e., R_{ct} and R_{ion}) on the potential versus SOC profile is important when comparing the performance of different materials, as it allows to deconvolute the influence of their open circuit potentials

from the influence of their charge-transport and ionic pore resistances on the rate performane of the electrodes. By virtue of having a potential profile which lies significantly higher than graphite, silicon electrodes (particularly silicon electrodes where the silicon is utilized only partially, as is the case here) allow higher overpotentials than graphite before reaching the lithium plating potential of 0 V vs. Li$^+$/Li. The above analysis shows that it is not only the potential versus SOC profile, but also the reduced ionic pore resistance that allows higher rate capabilities of the material.

To give an overview over the lithiation rate capability of the graphite (in LP57) and of the silicon (in LP57 and the FEC-based electrolyte) electrodes, Fig. 6 shows the SOC values of the electrodes at which their potential reaches 0 V vs. Li$^+$/Li (determined by the lithium metal reference electrode), i.e., the SOC beyond which the plating of lithium becomes possible. This analysis shows the combined effect of the higher potential of the silicon electrode (based on a ~30% silicon utilization) as well as its lower ionic pore resistance (i.e., its lower transport overpotential) on its lithiation rate capability. The graphite electrode (Fig. 6a) shows a performance improvement of a factor ~4 from the lowest (−5°C) to the highest (+45°C) temperature, with 50% SOC reached for C/2 at −5°C and for ~1.8C (interpolated C-rate) at 45°C. The silicon electrode measured in LP57 (Fig. 6b) generally allows for higher C-rates, giving 50% SOC at ~1.2C when measured at −5°C. At higher temperatures, the electrode limitation is ultimately expected to be also caused by ionic transport limitations, as kinetic resistances are very low at high temperatures, and at 45°C the silicon electrode reaches 50% of its capacity at ~3.2C (i.e., a factor of ~2.5 improvement from −5°C to 45°C). The silicon electrode with the FEC-based electrolyte (Si$_{FEC}$, see Fig. 6c) shows a very similar behavior.

Comparing the lithiation rate capabilities of the various electrodes at a given temperature, one can see that at −5°C it is similar for the silicon electrodes in the two different electrolytes and ~2-fold higher than that of the graphite electrode (i.e., 50% SOC are reached for the silicon electrodes at ~1C and for the graphite electrode at ~0.5C; see Fig. 6d). The overall electrode resistance of the silicon electrode in FEC-based electrolyte at −5°C is dominated by R_{ct} and is ~3-fold higher than that of the graphite electrode (see Fig. 4c), yet it still performs clearly better than the graphite electrode. Thus, the higher OCV of silicon compensates for the high kinetic overpotentials at low temperatures. Comparing graphite and silicon at 25°C (Fig. 6e) and 45°C (Fig. 6f), the temperature-induced reduction in kinetic overpotential strongly improves the rate capability of the silicon electrodes in both electrolytes, which only show a reduced capacity above 2C at 25°C and 2.5C at 45 °C. In contrast, graphite is limited above ~0.75 C at both 25 and 45°C, which can be explained by the kinetics becoming negligible at higher temperatures. As the pore resistance is significantly less affected by changes in temperature, it becomes the dominant factor in determining the electrodes limitation at higher temperatures.
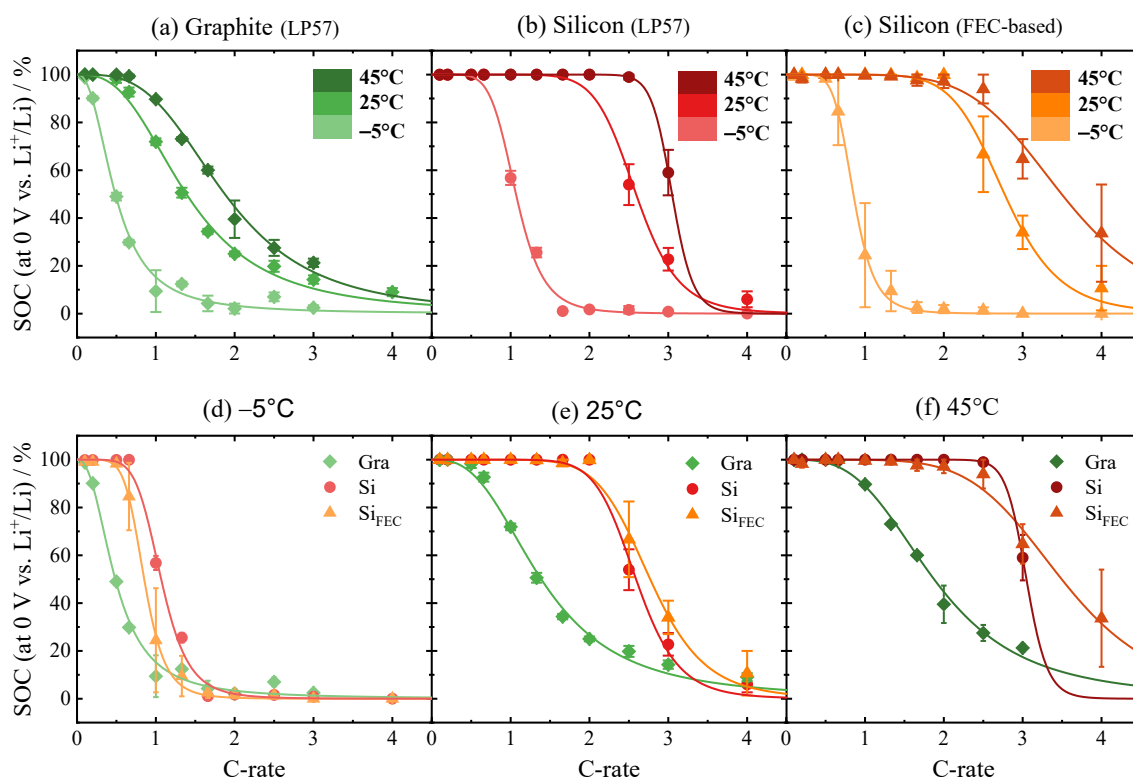
Fig. 6. SOC obtained at 0 V vs. Li$^+$/Li for silicon and graphite electrodes at different temperatures and C-rates. **(a)-(c)** Lithiation rate versus SOC at which 0 V vs. Li$^+$/Li are reached for graphite in LP57, silicon in LP57, and silicon in FEC-based electrolyte (Si$_{FEC}$), acquired at −5°C, 25°C, and 45°C. **(d)-(f)** Lithiation rate test data for the three sets of electrodes/electrolytes at each of the three temperatures. Error bars indicate the standard error of the mean of two independent measurements with electrodes of identical composition. A sigmoidal fit was added as a guide-to-the-eye according to the mathematical description described in Ref. [1]. Measurements were conducted with Swagelok® T-cells equipped with a GWRE, with graphite or silicon as working electrodes (2.8 mAh/cm^2), and a lithium metal foil with a free-standing graphite electrode as counter electrode. Note that the silicon in the silicon electrodes is utilized only partially, i.e., only up to 1200 mAh/g$_{Si}$.

Conclusions

In this publication we analyzed and compared graphite and silicon electrodes of practical areal capacities (2.8 mAh/cm^2) for their kinetic and transport resistances at temperatures between −5 to 45°C via electrochemical impedance spectroscopy (EIS) with a micro-reference electrode to quantify the anode (graphite or silicon) impedance. For the here studied silicon elecrodes (70%$_{wt}$ silicon), only ~30% of the full capacity of silicon was utilized (i.e., 1200 mAh/g$_{Si}$). LP57 was used as reference electrolyte for both graphite and

28

silicon, the latter also being measured in an FEC-based electrolyte which is generally used for silicon electrodes.

Using EIS we showed that the graphite anode has a ~2.5 times higher ionic resistance (R_{ion}) for lithium ion conduction in the electrolyte phase within the pores of the electrode, mostly due to its ~2.5-fold larger electrode thickness at the same areal capacity as the silicon-based electrode. Furthermore, the graphite electrode exhibits only slightly lower kinetic resistances (R_{ct}) compared to silicon when measured in LP57 at 25°C. The temperature-dependent impedance analysis showed how the ratio of R_{ct} to R_{ion} changes from predominantly kinetically limited at lower temperatures to transport limited at higher temperature, due to high activation energies for R_{ct} of ~62 – 68 kJ/mol compared to the ionic resistance R_{ion} of ~14 – 16 kJ/mol.

We subsequently explored the lithiation rate limiting properties of the graphite and silicon electrodes by comparing the resulting potential profiles at different C-rates to the findings from the EIS analysis. We showed how the kinetically dominated silicon electrodes mostly retain their potential shape, as the kinetic overpotential only generates an offset in overpotential, while the graphite electrodes, which show a much greater transport limitation, show a smearing of the potential profile and an increase in overpotential over SOC when cycled at higher C-rates. Only at −5°C, the graphite electrode exhibited a kinetic limitation at C/5 but already showed additional transport overpotentials starting at C/2. At 1C the graphite potential showed transport limitations even at 45°C and did not reach the full capacity before reaching 0V vs. Li$^+$/Li. In contrast, the thinner silicon electrodes only showed transport overpotentials at −5°C for a 1C lithiation. Comparing the end-of-charge overpotential of the two electrode types at 45°C and 1C, the graphite overpotential of ~100 mV was three times greater than that of the silicon (~30 mV), highlighting how the silicon

electrodes' decreased transport resistance is contributing significantly to its greater lithiation rate capability. This potential profile analysis showed that the better performance of silicon is not only due to its higher reversible potential, which allows for higher overpotentials before the onset of Li-plating, but also due to its significantly smaller thickness.

Additional analysis of the temperature-dependent lithiation rate tests gave insight into the overall performance of the electrodes. While the graphite electrodes could not reach the full capacity at 1C and 45°C, the silicon electrodes allowed a lithiation at 2C already at 25°C and still reached the full capacity at 2.5°C and 45°C. Overall the silicon electrodes showed a roughly 2-fold increase in lithiation rate capability compared to graphite.

Acknowledgments

References

1. M. N. Obrovac, Si-alloy negative electrodes for Li-ion batteries, *Current Opinion in Electrochemistry*, **9**, 8–17 (2018) https://doi.org/10.1016/j.coelec.2018.02.002.

2. O. Gröger, H. A. Gasteiger, and J.-P. Suchsland, Review—Electromobility: Batteries or Fuel Cells?, *Journal of The Electrochemical Society*, **162**, A2605–A2622 (2015)

https://iopscience.iop.org/article/10.1149/2.0211514jes.

3. M. N. Obrovac and L. Christensen, Structural Changes in Silicon Anodes during Lithium Insertion/Extraction, *Electrochemical and Solid-State Letters*, **7**, A93 (2004) https://iopscience.iop.org/article/10.1149/1.1652421.

4. J. Li and J. R. Dahn, An In Situ X-Ray Diffraction Study of the Reaction of Li with Crystalline Si, *Journal of The Electrochemical Society*, **154**, A156 (2007) https://iopscience.iop.org/article/10.1149/1.2409862.

5. M. N. Obrovac, L. Christensen, D. B. Le, and J. R. Dahn, Alloy Design for Lithium-Ion Battery Anodes, *Journal of The Electrochemical Society*, **154**, A849 (2007) https://iopscience.iop.org/article/10.1149/1.2752985.

6. J. Christensen and J. Newman, Stress generation and fracture in lithium insertion materials, *Journal of Solid State Electrochemistry*, **10**, 293–319 (2006) http://link.springer.com/10.1007/s10008-006-0095-1.

7. U. Kasavajjula, C. Wang, and A. J. Appleby, Nano- and bulk-silicon-based insertion anodes for lithium-ion secondary cells, *Journal of Power Sources*, **163**, 1003–1039 (2007) https://linkinghub.elsevier.com/retrieve/pii/S037877530602026X.

8. D. Jantke et al., Silicon-Dominant Anodes Based on Microscale Silicon Particles under Partial Lithiation with High Capacity and Cycle Stability, *Journal of The Electrochemical Society*, **166**, A3881–A3885 (2019) https://iopscience.iop.org/article/10.1149/2.1311915jes.

9. S. Haufe, R. Bernhard, and J. Pfeiffer, Revealing the Failure Mechanism of Partially Lithiated Silicon-Dominant Anodes Based on Microscale Silicon Particles, *Journal of The Electrochemical Society*, **168**, 080531 (2021) https://iopscience.iop.org/article/10.1149/1945-7111/ac1491.

10. M. Graf et al., Effect and Progress of the Amorphization Process for Microscale Silicon Particles under Partial Lithiation as Active Material in Lithium-Ion Batteries, *Journal of The Electrochemical Society*, **169**, 020536 (2022) https://iopscience.iop.org/article/10.1149/1945-7111/ac4b80.

11. J. Landesfeind, D. Pritzl, and H. A. Gasteiger, An Analysis Protocol for Three-Electrode Li-Ion Battery Impedance Spectra: Part I. Analysis of a High-Voltage Positive Electrode, *Journal of The Electrochemical Society*, **164**, A1773–A1783 (2017) http://jes.ecsdl.org/lookup/doi/10.1149/2.0131709jes.

12. R. Morasch, J. Keilhofer, H. A. Gasteiger, and B. Suthar, Methods—Understanding Porous Electrode Impedance and the Implications for the Impedance Analysis of Li-Ion Battery Electrodes, *Journal of The Electrochemical Society*, **168**, 080519 (2021) https://iopscience.iop.org/article/10.1149/1945-7111/ac1892.

13. N. Ogihara et al., Theoretical and Experimental Analysis of Porous Electrodes for Lithium-Ion Batteries by Electrochemical Impedance Spectroscopy Using a Symmetric Cell, *Journal of The Electrochemical Society*, **159**, A1034–A1039 (2012) http://jes.ecsdl.org/cgi/doi/10.1149/2.057207jes.

14. J. Illig, M. Ender, A. Weber, and E. Ivers-Tiffée, Modeling graphite anodes with serial and transmission line models, *Journal of Power Sources*, **282**, 335–347 (2015) https://linkinghub.elsevier.com/retrieve/pii/S037877531500261X.

15. S. Solchenbach, X. Huang, D. Pritzl, J. Landesfeind, and H. A. Gasteiger, Monitoring

SEI Formation on Graphite Electrodes in Lithium-Ion Cells by Impedance Spectroscopy, *Journal of The Electrochemical Society*, **168**, 110503 (2021) https://iopscience.iop.org/article/10.1149/1945-7111/ac3158.

16. R. Morasch, B. Suthar, and H. A. Gasteiger, Simple Way of Making Free-Standing Battery Electrodes and their Use in Enabling Half-Cell Impedance Measurements via µ-Reference Electrode, *Journal of The Electrochemical Society*, **167**, 100540 (2020) https://iopscience.iop.org/article/10.1149/1945-7111/ab9b93.

17. S. Solchenbach, D. Pritzl, E. J. Y. Kong, J. Landesfeind, and H. A. Gasteiger, A Gold Micro-Reference Electrode for Impedance and Potential Measurements in Lithium Ion Batteries, *Journal of The Electrochemical Society*, **163**, A2265–A2272 (2016) http://jes.ecsdl.org/lookup/doi/10.1149/2.0581610jes.

18. J. Landesfeind, J. Hattendorff, A. Ehrl, W. A. Wall, and H. A. Gasteiger, Tortuosity Determination of Battery Electrodes and Separators by Impedance Spectroscopy, *Journal of The Electrochemical Society*, **163**, A1373–A1387 (2016) http://jes.ecsdl.org/lookup/doi/10.1149/2.1141607jes.

19. J. Landesfeind, A. Eldiven, and H. A. Gasteiger, Influence of the Binder on Lithium Ion Battery Electrode Tortuosity and Performance, *Journal of The Electrochemical Society*, **165**, A1122–A1128 (2018) http://jes.ecsdl.org/lookup/doi/10.1149/2.0971805jes.

20. R. Morasch, J. Landesfeind, B. Suthar, and H. A. Gasteiger, Detection of Binder Gradients Using Impedance Spectroscopy and Their Influence on the Tortuosity of Li-Ion Battery Graphite Electrodes, *Journal of The Electrochemical Society*, **165**, A3459–A3467 (2018) http://jes.ecsdl.org/content/165/14/A3459.abstract.

21. K. U. Schwenke, S. Solchenbach, J. Demeaux, B. L. Lucht, and H. A. Gasteiger, The Impact of CO_2 Evolved from VC and FEC during Formation of Graphite Anodes in Lithium-Ion Batteries, *Journal of The Electrochemical Society*, **166**, A2035–A2047 (2019) https://iopscience.iop.org/article/10.1149/2.0821910jes.

22. S. K. Heiskanen, J. Kim, and B. L. Lucht, Generation and Evolution of the Solid Electrolyte Interphase of Lithium-Ion Batteries, *Joule*, **3**, 2322–2333 (2019) https://doi.org/10.1016/j.joule.2019.08.018.

23. M. Wetjen et al., Morphological Changes of Silicon Nanoparticles and the Influence of Cutoff Potentials in Silicon-Graphite Electrodes, *Journal of The Electrochemical Society*, **165**, A1503–A1514 (2018) https://iopscience.iop.org/article/10.1149/2.1261807jes.

24. J. Moškon and M. Gaberšček, Transmission line models for evaluation of impedance response of insertion battery electrodes and cells, *Journal of Power Sources Advances*, **7**, 100047 (2021) https://linkinghub.elsevier.com/retrieve/pii/S2666248521000020.

25. S. Malifarge, B. Delobel, and C. Delacourt, Experimental and Modeling Analysis of Graphite Electrodes with Various Thicknesses and Porosities for High-Energy-Density Li-Ion Batteries, *Journal of The Electrochemical Society*, **165**, A1275–A1287 (2018) https://iopscience.iop.org/article/10.1149/2.0301807jes.

26. T. F. Fuller, M. Doyle, and J. Newman, Simulation and Optimization of the Dual Lithium Ion Insertion Cell, *Journal of The Electrochemical Society*, **141**, 1–10 (1994) http://jes.ecsdl.org/cgi/doi/10.1149/1.2054684.

27. J. Newman and K. E. Thomas-Alyea, Electrochemical Systems, in, Wiley-VCH Verlag GmbH & Co. KGaA, New Jersey (2004).

28. M. Doyle, T. F. Fuller, and J. Newman, Modeling of Galvanostatic Charge and Discharge of the Lithium/Polymer/Insertion Cell, *Journal of The Electrochemical Society*, **140**, 1526–1533 (1993) http://jes.ecsdl.org/cgi/doi/10.1149/1.2221597.

29. T. S. Chadha, B. Suthar, D. Rife, V. R. Subramanian, and P. Biswas, Model Based Analysis of One-Dimensional Oriented Lithium-Ion Battery Electrodes, *Journal of The Electrochemical Society*, **164**, E3114–E3121 (2017) https://iopscience.iop.org/article/10.1149/2.0141711jes.

30. J. Landesfeind and H. A. Gasteiger, Temperature and Concentration Dependence of the Ionic Transport Properties of Lithium-Ion Battery Electrolytes, *Journal of The Electrochemical Society*, **166**, A3079–A3097 (2019) http://jes.ecsdl.org/lookup/doi/10.1149/2.0571912jes.

3.2.2 Li-Ion Battery Material Impedance Analysis I: NMC 111 Kinetic Theory and Experiment

The manuscript entitled "Li-Ion Battery Material Impedance Analysis I: NMC 111 Kinetic Theory and Experiment" will be submitted to a peer-reviewed journal.

To describe Li-ion battery active material kinetics, Newman and co-workers devised a mathematical model which altered the established fundamental Butler-Volmer Kinetics equation to adjust for the arising difference for insertion materials.[8,9] The model takes into account the change in state-of-charge (SOC) within the active material by adding a term for the filled and empty space which is/can be occupied by the Li^+. To understand if modern battery active materials follow the kinetic behavior predicted by Newman, we measured the NMC 111 kinetics with respect to SOC and electrolyte concentration, as well as the solid diffusion resistance of lithium in the NMC 111 material.

First, the impedance of NMC 111 electrodes was measured for different areal capacities to a frequency of 1 mHz. The measurement showed that areal capacities around 0.5 mAh/cm² are best suited to analyze the kinetics of the active material, especially the solid diffusion resistance. The SOC-dependent analysis of the charge transfer resistance shows how the general U-shape of the curve matches Newmans model but requires adjustment of the transfer coefficients. Also, as the model is designed for full lithiation and delithiation, the SOC for this measurement is defined as the lithium which could reversibly be extracted from the material if it would not show the structural changes at higher potentials (i.e., ~280 mAh/g). The SOC shaped trend as the kinetics, and due to the limited cycling window this leads to asymmetric kinetics in NMC 111. During delithiation both the charge transfer and diffusion resistance decrease, while on the reverse pathway, i.e., lithiation, they significantly increase. This is also reflected in the electrodes performance, which shows improved delithiation capacities compared to lithiation at high C-rates. Analyzing the change in kinetics with electrolyte concentration only follows the proposed theory for concentrations between 30 mM and 1.5 M, with the expected decrease in R_{ct} with increasing salt concentration. Above 1.5 M, R_{ct} increases again. This can be explained by viewing the electrolyte similarly to an active material, in that, too much or too little Li^+ has an adversarial effect on the kinetics.

_____

The manuscript shows how closely the proposed theory for insertion material matches the experiments, but that careful adjustments need to be made to ensure a proper representation of the material.

Author contributions

R.M. performed the measurements and evaluated the data. B.S. provided insights into the battery theory and the diffusion resistance analysis and revised the theory sections. R. M. wrote the manuscript. R.M., B.S., and H.A.G. discussed the results and revised the manuscript.

Li-Ion Battery Material Impedance Analysis I: NMC 111 Kinetic Theory and Experiment

Robert Morasch[a]*, Bharatkumar Suthar[b], and Hubert A. Gasteiger[a]

[a] Chair of Technical Electrochemistry, Department of Chemistry and Catalysis Research Center, Technical University of Munich, Munich, Germany

[b] Department of Chemical Engineering, Indian Institute of Technology Bombay, Mumbai 400076, India

*Corresponding author

Abstract

The expression for the exchange current density to describe the intercalation kinetics of Li-ion batteries proposed by Newman and coworkers is now used extensively for battery modeling, however their applicability to existing battery materials needs to be thoroughly validated. Here we show an electrochemical impedance spectroscopy (EIS) analysis of the kinetic behavior of NMC 111 as a function of electrolyte salt concentration and state-of-charge (SOC) and compare it to the proposed theory. An areal capacity dependent EIS analysis first gives insight into the feasibility of measuring kinetic and transport parameters, including the solid diffusion resistance, showing how lower areal capacities are required to predominantly probe the material. We then show how the charge transfer kinetics follow a Butler-Volmer type concentration dependent behavior for lower concentrated electrolytes (≤1.5 M) but deviate from the proposed theory at higher salt concentrations. A further SOC dependent analysis shows how NMC 111 generally follows the proposed theory of U-shaped symmetric kinetics, but the limited oxidative stability window leads to practically asymmetric kinetics for charging and discharging. This asymmetry is visible in lithiation and delithiation rate tests, where upon lithiation the kinetics generally become slower for higher degrees of lithiation, limiting the performance.

Introduction

There are a variety of factors that influence the performance of commercial Li-Ion batteries, e.g., cell design, electrode-, or active material properties. While measurement probing the electrode's geometric microstructure, i.e., tortuosity, has become standard practice,[1–3] accurately measuring and modeling kinetic and transport parameters of battery materials is more difficult and many parameters are either fitted or assumed.[4] Most notably, Doyle, Fuller and Newman[5,6] put forth an expression for the exchange current density which incorporated the state-of-charge (SOC) dependence (i.e., the change in concentration of the species in the solid active material) into the Butler-Volmer equation for Li-ion batteries (see equation 5 in the section below). The equation is used to model a variety of battery materials, even though popular materials can drastically differ in the way the Li-insertion occurs. The equation is extensively used for commonly available battery materials such as Graphite or cathodes of the NMC family, without validation of the applicability of such expressions for these materials, due to lack of experimental data. For instance, a popular battery material is nanometer sized $LiFePO_4$ (LFP) which exhibits a phase change behavior rather than a typical intercalation, as the lithiated phase is in the form of $LiFePO_4$ and the delithiated phase is $FePO_4$ with unfavorable intermediate stages.[7,8] The analysis of individual electrode particles has shown that the particles are either present in their lithiated or delithiated stage and very few particles in an intermediate stage.[9] This difference requires an adaptation of the kinetic theory and model to describe the material.[10] $Li(Ni_{1/3}Mn_{1/3}Co_{1/3})O_2$ (NMC 111) on the other hand can be seen as an intercalation material in the classical sense, where the material can attain a continuous range of intermediately lithiated stages and where the material transport inside the particle can be described by classical diffusion. Negative aspects of the material are its electrochemical stability, which

does not allow for a full delithiation of the material.[11] Due to the widespread use of NMC materials, we chose to study the NMC 111 material kinetics as a baseline to assess whether the expression for the exchange current density along with the commonly used parameters can correctly describe the kinetic aspects of the material or whether they need to be extended/modified.

To measure kinetic parameters, electrochemical impedance spectroscopy (EIS) can be a useful tool when it comes to discerning individual resistances. An important factor to consider in analyzing battery electrode impedances is the porous electrode impedance, i.e., the change in spectrum due to the porous nature of an electrode. How to analyze porous electrode EIS spectra and extract individual parameters has been addressed in multiple publications.[2,12–17] The porous pathways in battery electrodes of conventional areal capacities (~ 3 mAh/cm^2) leads to mass transport losses at higher currents, changing the local Li$^+$ concentration in the liquid electrolyte. It is therefore important to understand how the material's kinetics change for a changing electrolyte salt concentration. To simplify this analysis, it is first necessary to reduce the influence of the geometric properties of the electrode (achieved by using a thin electrode) to highlight the inherent material properties. Tsai et al.[18] performed single-particle impedance measurements of NMC 111, with an NMC particle attached to a tungsten tip, arguing that the successful extraction of material properties requires such an extreme approach. While this analysis allowed a binder-free application, such a setup still raises concerns about the electrical connection between the tip and particle. Additionally, microstructural changes due to particle cracking may drastically change the material over the first few cycles, making an analysis of the material after several initial cycles in a practical setup more relevant.[19,20] In this publication we therefore first examine the influence of areal capacity (or areal mass loading) on the

impedance spectrum of NMC 111 electrodes. This allows us to find a suitable areal capacity for further studies and enables us to focus on the kinetic aspects of the material. A rate test study at different areal capacities is used to determine when the electrode performance is affected by the porous nature of the electrode, i.e., changes in the electrolyte concentration across the electrode due to mass transport losses in the liquid phase or other influences such as electrical resistances across the electrode. By measuring the charge transfer kinetics of NMC 111 at different electrolyte concentrations, we show the influence such concentration gradients can have on the charge transfer kinetics, which to our knowledge has not been presented in literature to this extent before. We additionally provide activation energies for the measured resistances. The material parameters, both charge transfer resistance and, qualitatively, the solid diffusion resistance, are then determined as a function of state-of-charge (SOC). The electrolyte salt concentration- and SOC -dependent kinetic behavior is also compared to expected values from the Newman model. Finally, we show the importance of the SOC dependent change in kinetics on the C-rate performance of the material by comparing the performance of low areal capacity electrodes in charging and discharging direction.

Experimental

Slurry preparation and drying.— Li(Ni$_{1/3}$Mn$_{1/3}$Co$_{1/3}$)O$_2$ (NMC 111, BASF, BET 0.3 m^2/g), conductive graphite (SFG6L, Timcal), Super C65 and polymer binder (polyvinylidene fluoride (PVDF), Arkema) at a ratio of 90:2:3:5 (wt.) were mixed with N-Methyl-2-pyrrolidone (NMP, Sigma Aldrich, anhydrous, 99.5 %) at a solid:liquid ratio of 1:1 (wt:wt) in a planetary mixer (Thinky ARV-310) at 2000 rpm for five minutes. The prepared slurry was coated onto an aluminium current collector foil (MTI, 11 μm) attached to a glass plate using a gap bar coater (RK PrintCoat Instruments, UK) at a wet film thicknesses of 30 μm,

4

60 μm, 120 μm and 250 μm for the capacities of 0.37, 0.7, 1.6 and 2.9 mAh/cm^2 respectively (based on a reversible capacity of 145 mAh/g), and dried in an oven at 50 °C. The dried electrodes were punched out to a diameter of 10.95 mm (equating to an area of ~0.94 cm^2) using an electrode punch (Hohsen Corp. OSAKA, Japan).

Cell assembly and cycling.— For electrochemical impedance analysis, a three-electrode cell setup (Swagelok® T-cell) with a gold-wire reference electrode (GWRE, described in more detail in Fig. 1b in Ref. [21]) was used. The cells were built inside an argon filled glove box (MBraun, 25 °C ± 1 °C, oxygen and water content <0.1 ppm, Ar 5.0, Westfalen). All cell parts were dried at 120 °C in a vacuum oven (Büchi, Switzerland) for 8 h before being transferred into an Ar-filled glovebox, with the exception of the separators which were dried at 300 °C.

The cells were assembled with a NMC 111 working electrode, two porous glass fiber separators with a diameter of 11 mm (VWR, 250 μm uncompressed thickness, 90% porosity), and a counter electrode consisting of a free-standing graphite electrode firmly attached to the metallic lithium foil (as described in Ref. [22]). 80 μl of electrolyte were added to the cells. The self-mixed electrolyte was made using LiPF$_6$ (BASF, battery grade) in EC:EMC 3:7 (wt:wt), battery grade, Gelon, China). Base solutions of 0.1 M, 1 M and 3 M electrolyte were mixed and diluted to attain additional electrolyte concentrations of 0.03, 0.5, 1.5, 2 and 2.5 M. Additionally, commercial electrolyte (Gotion, USA, battery grade) of nominally the same composition for concentrations of 0.1, 1 and 2.5 M was used. Hydrogen Fluoride was measured using the TitroLine 7000 (SI Analytics).

Using a potentiostat (Bio-Logic Science Instruments, France), the gold-wire reference electrode was lithiated at 150 nA for 1 h via the counter electrode in a temperature-controlled chamber (25 °C, Binder). The cycling protocol started with a 3 h open circuit

voltage phase to allow for complete wetting of the electrode. 5 initial cycling steps at C/5 were performed galvanostatically (constant current delithiation) between 2.5 V and 4.2 V, (additionally to 4.4 V and 4.6 V for SOC dependent measurements) vs Li$^+$/Li with a 1h constant potential hold at the respective final charge potential depending on the measurement. The electrodes were then brought to the desired potential/SOC at C/10 and rested for 1h or kept at the measured potential for 1h prior to the impedance measurement. Potentiostatic electrochemical impedance spectroscopy measurements were performed at either a stated potential or SOC from 30 kHz to 0.1 Hz or 0.001 Hz and with an excitation of 10 mV. For temperature dependent measurement the cells were placed in a temperature-controlled chamber (Espec, Japan) and the impedance measurement was performed 2h after the chamber reached the target temperature.

The C/5 cycling to 4.2 V, 4.4 V and 4.6 V reached reversible capacities of 145 mAh/g, 171 mAh/g and 195 mAh/g, respectively. For the rate test the electrodes were (after the initial C/5 cycles) brought to 100% SOC (4.2 V) or 0% SOC (2.5 V) for the lithiation and delithiation rate test (from C/10 to 5C rates), respectively, via constant current at the same C-rate as the rate test, but not faster than 1C, with a subsequent potential hold for 1h. The rate test was then performed by applying a constant current with a potential cutoff of 4.2 V or 2.5 V vs Li$^+$/Li for delithiation and lithiation rate tests, respectively.

Electrochemistry fundamentals and theory

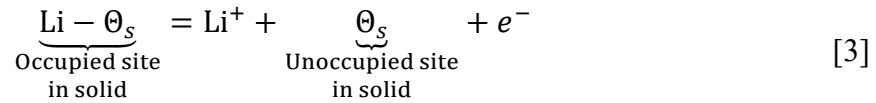*Butler-Volmer Kinetics for Intercalation Materials:*

To capture the intercalation kinetics, following set of equations were proposed by Newman and coworkers [5,6,23,24]

$$i = i_0 \left[\exp\left(\frac{\alpha_a F(\phi_1 - \phi_2 - U)}{RT} \right) - \exp\left(-\frac{\alpha_c F(\phi_1 - \phi_2 - U)}{RT} \right) \right] \qquad [1]$$

with i_0 as the exchange current density, α_a and α_c as the anodic and cathodic transfer coefficients, F as Faraday's constant, R as the universal gas constant, ϕ_1 as solid potential, ϕ_2 as the solution (electrolyte) potential and U as the open circuit voltage of the interface. The exchange current density is given by the following expression:[23]

$$i_0 = i_{0,\text{ref}} \prod_i \left(\frac{c_i}{c_{i,\text{ref}}} \right)^{\gamma_i} \qquad [2]$$

Here, $i_{0,\text{ref}}$ is the exchange current density at reference concentration ($c_{i,\text{ref}}$). For complex reactions, γ_i, α_c, and α_a may be a complicated function of the symmetry factor and γ_i can even be unrelated to the α_c and α_a. The intercalation reaction is given as follows:

$$\underbrace{\text{Li} - \Theta_s}_{\substack{\text{Occupied site} \\ \text{in solid}}} = \text{Li}^+ + \underbrace{\Theta_s}_{\substack{\text{Unoccupied site} \\ \text{in solid}}} + e^- \qquad [3]$$

Lacking experimental data, Newman and coworkers assumed the intercalation reactions to be a first order reaction and the following expression for the exchange current density was proposed (by replacing $\gamma_{\text{Li}^+} = \alpha_a$, $\gamma_{c_s} = \alpha_a$ and $\gamma_{(c_{s,\text{max}} - c_s)} = \alpha_c$):

$$i_0 = Fk(T)(c_{s,\text{max}} - c_s)^{\alpha_c}(c_s)^{\alpha_a}(c_l)^{\alpha_a} \qquad [4]$$

Where k contains the Arrhenius type temperature dependence, c_s is the concentration of lithium in the solid host, $c_{s,\text{max}} - c_s$ is the concentration of unoccupied sites and c_l is the concentration of lithium ions in the liquid electrolyte. For polymer electrolytes, the solubility of lithium in the electrolyte also plays a role since the available space for Li^+ in polymer electrolytes is limited. The proposed expression by Newman for the exchange

current density of polymer electrolyte incorporates this limitation in a similar way as it incorporates the concentration limitation of unoccupied sites in the solid phase (i.e., $(c_{\text{sat}} - c_{\text{l}})^{\alpha_c}).$[24]

Eq. 4 (with $\alpha_a = \alpha_c = 0.5$) is extensively used in the battery modeling community for common, liquid electrolyte battery materials and systems, though, the experimental validity of Eq. 4 is not rigorously established. For small voltage perturbations (≤ 10 mV) of the kinetic overpotential $\eta \equiv (\phi_1 - \phi_2 - U)$, Eq. 1 can be linearized using $\exp(x) = 1 + x$ (also using $\alpha_a + \alpha_c = 1$), resulting in

$$i = k\,(c_{\text{l}})^{\alpha_a}(c_{\text{max}} - c_{\text{s}})^{\alpha_a} c_{\text{s}}^{\alpha_c}\,\frac{F}{RT}\eta \qquad [5]$$

Which can be transformed into an equation for the charge transfer resistance for small kinetic overpotentials

$$R_{\text{ct}} \equiv \lim_{\eta \to 0}\frac{\eta}{i} = \frac{RT}{Fi_0} = \frac{RT}{Fk} \times \frac{1}{c_{\text{l}}^{\alpha_a}} \times \frac{1}{(c_{\text{max}} - c_{\text{s}})^{\alpha_a} c_{\text{s}}^{\alpha_c}} \qquad [6]$$

The term $(c_{\text{max}} - c_{\text{s}})^{\alpha_a}$ is a measure of the available free sites for intercalation, and therefore the state-of-charge (SOC) for a cathode active material, resulting in slower kinetics (larger R_{ct}) when the material approaches its maximum concentration. On the other hand, the term $c_{\text{s}}^{\alpha_c}$ describes the available Li for the cathodic reaction, and therefore the state-of-discharge (SOD), resulting in slower kinetics when the material approaches an empty state. This leads to a U-shaped charge transfer resistance curve over SOC (shown in Fig. 1) with poor kinetics at high and low SOCs. Such a description is plausible when considering the potential profile of most intercalation materials. When the potential profile is steep at high and low SOCs, no charge can be extracted, and the electrode is under so

called blocking conditions, where the kinetics of the electrode get too slow for practical applications.[14] This can be seen in the shape of TiS₂ shown by West et al.,[25] which served as the template for the initial Newman model. TiS₂ shows a symmetric, steep potential drop towards lower SOCs when the material is lithiated. Not every material can be reversibly fully depleted or refilled, as shown later with the SOC dependent NMC 111 analysis, and therefore one must take care when using equation [4] to describe battery kinetics. Fig. 1a shows the SOC dependent charge transfer resistance as expressed in equation [6], normalized to a resistance value of 1 for the minimum resistance, and with $R_{ct} \propto$

$\frac{1}{(c_{max}-c_s)^{\alpha_a} \times c_s^{\alpha_c}}$. Assuming $\alpha_a + \alpha_c = 1$, $\alpha_a = 0.5$ (black line) gives symmetric U-shaped kinetics with the minimum resistance at 50% SOC. The change in resistance is less than a factor 2 between 10 and 90% SOC and only starkly increases at SOCs below or above those, respectively. Changing α_a to 0.3 or 0.7 leads to asymmetric SOC dependent kinetics and the resistance minimum is shifted to a higher SOC ($\alpha_a = 0.3$, blue line) or a lower SOC ($\alpha_a = 0.7$, red line). Fig. 1b shows the concentration dependent change in kinetics, with R_{ct} normalized to 1 for a concentration of 1 M. The resistance is correlated to the electrolyte as $R_{ct} \propto \frac{1}{c_l^{\alpha_a}}$, leading to lower resistances for higher salt concentrations.
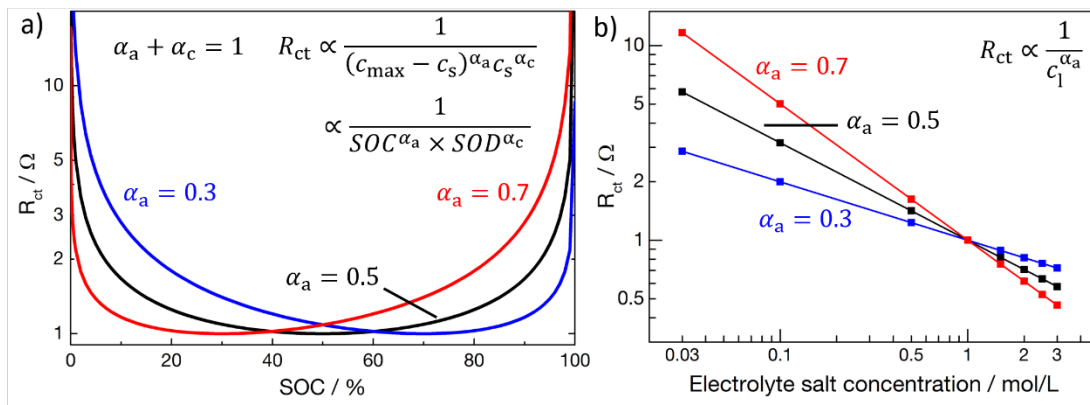

Figure 1 Kinetic theory for intercalation materials as expressed in Eqn. 6. a) SOC dependent charge transfer kinetics for different combinations of α_a and α_c. When both coefficients are the same value, the kinetics are

symmetric; if the coefficients differ, the resistance minimum shifts from 50%. Resistances normalized to a 1 Ω resistance in their respective minimum b) Li^+ electrolyte concentration dependent kinetics normalized to a value of 1 Ω at a 1M concentration for different values of α_a, predicting an increase in resistance with decreasing salt concentration.

Results and Discussion

Validation of EIS measurements on NMC 111 electrodes at various areal capacities—

This subsection discusses the influence of electrode areal capacity on the impedance spectra of NMC 111 electrodes (working electrode impedance spectra measured via gold-wire reference electrode), as well as capacity dependent charging (delithiation) rate tests. It serves to find the proper areal capacity and validate the later performed EIS analysis of the material kinetics to ensure influences of, e.g., the electrode geometry are minimal.

Fig. 2a depicts the equivalent circuit model for a porous electrode. The circuit consists of two backbones, the left side represents electrical resistance elements (r_{el}) with an additional electrical contact resistance R/Q element at the current-collector/electrode interface (bottom left). The electrical resistance is considered negligible in this study due to the addition of sufficient conductive carbon and graphite in the porous electrode, but small influences on the spectra cannot be excluded. Some EIS spectra shown in Fig. 2 show the end of a semi-circle at the highest frequencies, which is attributed to an electrical contact resistance (visible as a semi-circle in the kHz regime[14,26]) but cannot be resolved due to the frequency limitation of the GWRE above 30 kHz. The influence of electrical resistances on the blocking impedance of porous electrodes is described in Ref.27. The right backbone consist of the pore resistance in the porous electrode, coupled with individual Warburg elements in the pores (r_p; w_i). Since local electrode current densities are dependent on the ratio of pore resistance to charge transfer resistance,[28] different concentration overpotentials can be expected at different electrode depths. Hence the pore

resistance Warburg elements may be individually different. The ionic resistance and Warburg diffusion resistance in the separator are shown in the top right corner. The two backbones are connected via a charge transfer reaction element in series with the finite length solid diffusion Warburg, coupled with the constant phase element from the electrochemical double layer at the electrode material surface ($w_s + [r_{ct}/q_{ct}]$).

Fig. 2b shows the EIS spectra of NMC 111 electrodes of different areal capacities at 4V ($\approx$ 80% SOC). All cells were cycled to 4.2 V vs Li$^+$/Li. The lowest areal capacity of 0.37 mAh/cm^2 shows the largest semi-circle, associated with the charge transfer reaction R_{ct}, with a resistance value of $\approx$ 7.5 Ωcm^2. The kinetic resistance decreases with increasing areal capacity. In Fig. 2c, a small pore resistance R_{ion} of $\approx$ 2 Ωcm^2 is visible as $\frac{1}{3} \times$ 2 Ωcm^2 between the high- and low frequency intercept in the blocking impedance of the 0.37 mAh/cm^2 sample, obtained at OCV before any current was applied to the cell, (for blocking impedance analysis see Ref. 1,2). The R_{ion} is also visible in the non-blocking spectrum due to the low value of R_{ion} compared to R_{ct}. Increasing the areal capacity decreases R_{ct} due to the increase in active surface area, but the simultaneously increasing pore resistance transforms the spectrum and the pore resistance needs to be evaluated additionally to extract R_{ct}.[28] Fig. 2d shows the impedance of the highest areal capacity electrode with 2.9 mAh/cm^2, both under blocking conditions and at 4V vs Li$^+$/Li. The extracted R_{ion} is $\approx$ 8.5 Ωcm^2. The 1 Hz low-frequency resistance (LFR$_{1Hz}$) and high-frequency resistance (HFR) intercepts give an electrode resistance (LFR$_{1Hz}$-HFR, no semi-circle fit) of $\approx$ 3 Ωcm^2. Analyzing the spectra according to Ref. 28 gives a resulting charge transfer resistance of $\approx$ 1 Ωcm^2, i.e., significantly smaller than the 3 Ωcm$^2_{geom}$ electrode resistance, but in accordance with the $\approx$ 8 fold increase in active material from 0.37 to 2.9 mAh/cm^2.
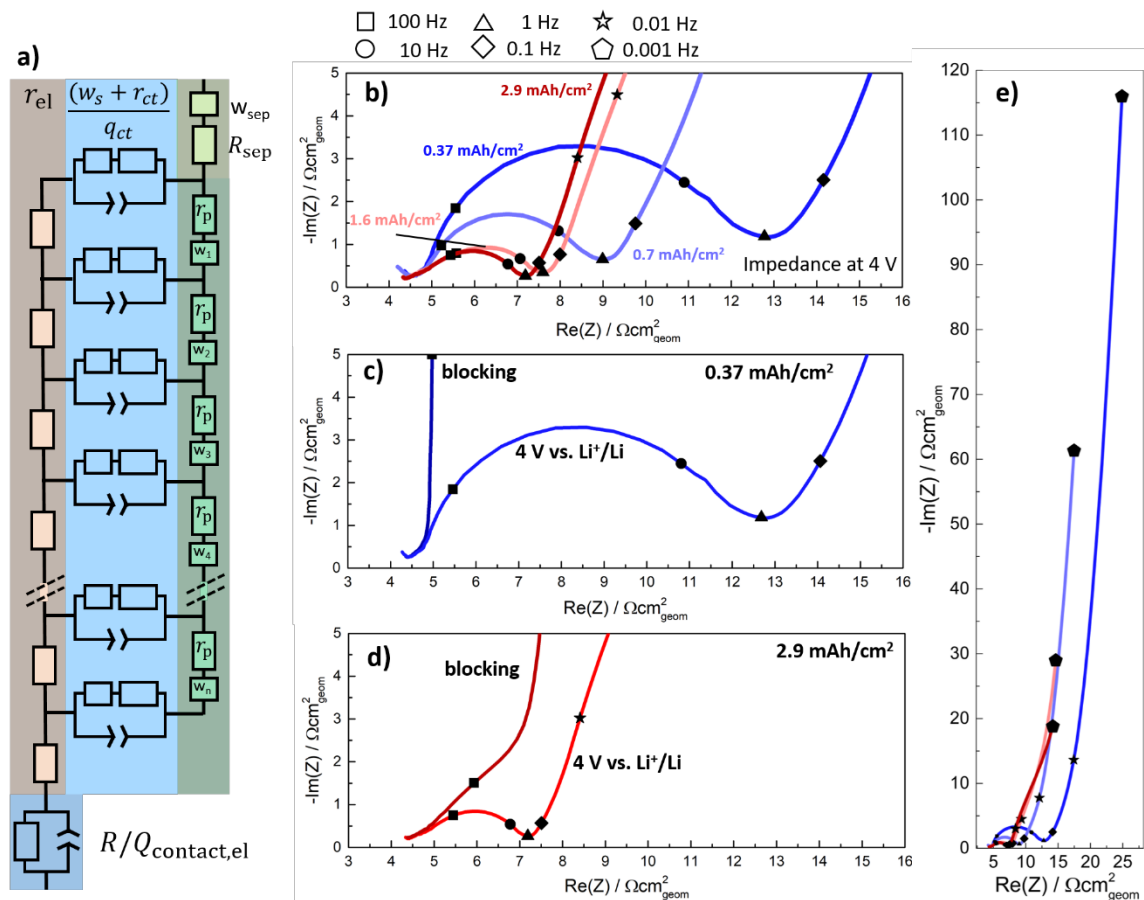
Figure 2 Equivalent circuit model and Impedance spectra of NMC 111 electrodes at different areal capacities. Impedance data aligned in the x-axis to correct for minor differences in the HFR for better visibility; a) Porous Equivalent circuit model for porous electrodes with two backbones: one for electrical resistance (left) with electrical contact resistance (bottom left) and one for electrolyte pore resistance (right, electrolyte pore- and Warburg diffusion resistance) including the separator elements (top right), connected via an element for the charge transfer reaction with solid diffusion Warburg element. b) EIS comparison of areal capacities of 0.37, 0.7, 1.6 and 2.9 mAh/cm² measured at 4V vs Li⁺/Li. The semi-circle representing the charge transfer resistance decreases drastically with increasing loading but stagnates at higher loading in accordance with the porous electrode impedance response. c) and d) shows the lowest and highest loading EIS spectra in addition to their blocking impedance (measured at OCV after cell assembly), showing the change in pore resistance with loading. e) Full impedance spectra with low frequency datapoints to 1 mHz.

Fig. 2 e) shows the full EIS spectra down to 1 mHz. The capacitive behavior at lower frequencies (between 10 mHz and 1 mHz) is mostly attributed to the solid phase finite length (reflective) Warburg.[16,17] The impedance analysis thus gives two distinct capacitance values (not counting the capacitance from a contact resistance semi-circle), i)

the electrochemical double layer capacitance from the electrode/electrolyte interface, which scales with electrode surface area (i.e., active and passive materials) and ii) the capacitance relating to the charge storage capacity (active material areal capacity) which also depends on the local slope of the OCV.[29]

To validate whether the low frequency (<10 mHz) capacitance can be correlated to the extracted charge of an electrode, and thus the diffusion resistance, we compared the measured capacitance to the charge which could be extracted in the region of the NMC 111 OCV potential profile around 4V from the electrode's C/5 cycle before the impedance measurement, i.e., the charge that was extracted between 3.99 V and 4.01 V vs Li$^+$/Li during slow cycling. The later discussed charge rate test in Figure 4 shows that at C/5 the cell reached over 99% capacity, suggesting that the overpotential for all cells was low enough to assume sufficiently low overpotentials and a full extraction of charge at this C-rate, i.e., it is close to the OCV potential, a necessary prerequisite for the comparison to the EIS analysis. Assuming perfect capacitive behavior, the low frequency datapoints were converted to an electrical charge value via $C_{\mathrm{EIS}} = \frac{1}{\omega \cdot \mathrm{Im}(Z)} \Delta U$ with ω as the angular frequency and $\Delta U = 20$ mV. Fig. 3a and b illustrates the analysis method of C_{OCV}, which was determined by extracting the charge at the potential between 3.99 and 4.01 V (i.e., $\Delta U = 20$ mV) and extracting the experimentally obtained capacity in this potential window. Fig 3c shows $C_{\mathrm{EIS}}/C_{\mathrm{OCV}}$ as a function of frequency and areal capacity. The lower areal capacities approach the charge extracted from the potential up to $\approx$ 89 %, meaning the imaginary resistance in the EIS measurement is slightly higher than expected and thus gives slightly lower calculated capacitance values compared to the extracted OCV capacity values. However, the convergence towards a value of 1 with varying electrode capacities from 0.37 to 2.9 mAh/cm^2 suggests that the assumption of probing the material properties

(as opposed to the electrode or separator properties) holds true. The reason for the discrepancy of 11 % is not known and might be either a systematic error in evaluating the data (e.g., the assumption of perfect capacitive behavior) or not yet fully completed diffusion, both supported by the impedance data as the capacitive branch has not reached a perfect 90° upward angle. Yet the lowest capacity seems sufficient to probe the material at a frequency of 1 mHz and only little further improvement may be obtained by decreasing the electrode capacity. Probing the electrode to even lower frequency would result in impractically long measurement times. The substantial discrepancy of the 2.9 mAh/cm^2 electrode can be expected, as a higher areal capacity results in a reduced low frequency imaginary resistance due to the capacitive nature of the 10 mHz to 1 mHz frequency resistance regime. The spectrum is thus more likely to be disturbed by other diffusion phenomena (e.g., from the separator liquid diffusion which is a constant contribution in all measurements), and the assumption of a dominating solid diffusion resistance becomes invalid at such high capacities. Additionally, a diffusion resistance in the thicker, porous electrode might arise, which, if not yet fully completed at the lowest frequency of 1 mHz, still adds to the imaginary part of the impedance spectrum. The electrolyte in the electrode pores can have significant influence on the low frequency impedance spectra, which we aim to decrease here, which has been shown in Ref. 17. This shows that a lower areal capacity is useful when analyzing the kinetics and solid diffusion of electrode materials, as both resistances become enlarged and dominant in their respective frequency domain. A more detailed analysis of the diffusion resistance and charge transfer kinetics over SOC is detailed further below.
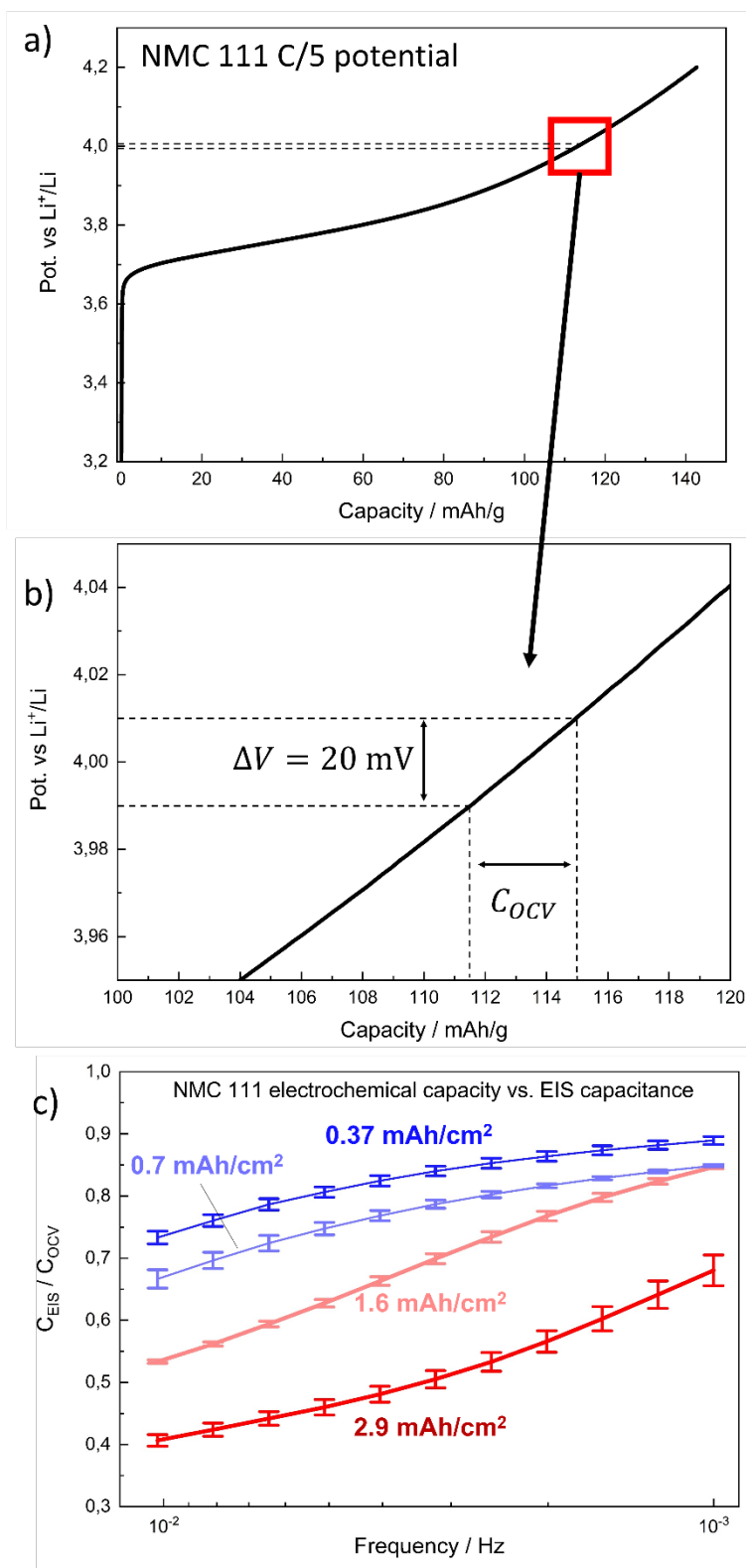
Figure 3 Comparison of the charge calculated from EIS spectra at different frequencies and the charge extracted from the linearized potential profile of the individual electrodes to validate the assumption of probing mainly the solid diffusion branch of the electrode; a) Potential profile of NMC 111 with dotted lines highlighting where the diffusion resistance measurement and capacity analysis of C_{OCV} was obtained; b) zoom of the potential at which the EIS measurement and capacity analysis was performed; c) C_{EIS}/C_{OCV} as

a function of EIS measurement frequency. The lower areal capacities approach the expected value of 1, indicating that the lower capacity improves the visibility of the diffusion resistance analysis.

The electrode areal capacity can have great impact on the electrode behavior, e.g., through the increase in thickness of the electrode, which can lead to changes in local Li^+ concentration in the electrolyte, due to mass transport losses during cycling. Such changes are expected to change the electrode charge transfer resistance and are described by Eqns. 2 and 4. To understand which areal capacity is affected by the liquid electrolyte transport, the electrodes underwent a delithiation rate test as shown in Fig. 3. The lower areal capacities of 0.37 and 0.7 mAh/cm^2 show the same high capacities reached even for C-rates up to 5C. This is because the mass transport overpotential of the electrode is negligibly small and the performance is mainly limited by the material properties, e.g., the kinetics or the solid diffusion resistance. The high capacities achieved up to 5C show that the material is only weakly limited in these aspects. Increasing the areal capacity decreases the achieved electrode capacities drastically for higher C-rates. The electrode now becomes limited in the electrolyte transport (electrical resistances are assumed small due to the high amount of conductive additive in the electrodes, see experimental section), leading to strong concentration gradients across the electrode. To study the effect of the Li^+ concentration in the electrolyte on the electrode kinetics, we measured the material kinetics at different electrolyte concentrations.
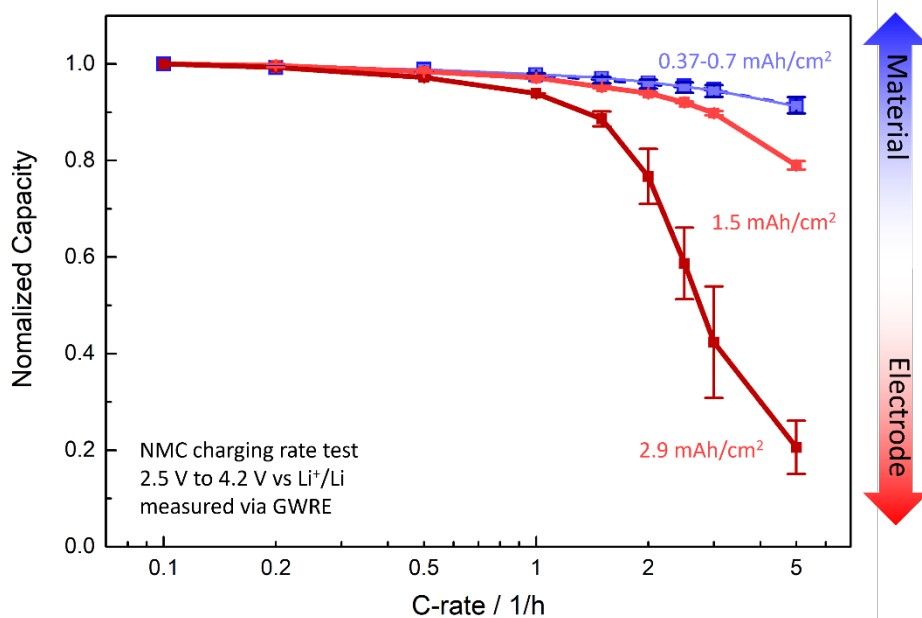
Figure 4 Charging (delithiation) rate test of NMC 111 electrodes at different areal capacities. The change in performance with areal capacity is attributed to mass transport losses in the electrode pores due to electrolyte concentration gradients. The 0.37 and 0.7 mAh/cm^2 electrodes are overlapping, suggesting no influence from mass transport on both measurements and thus a predominant limitation of the material kinetics. The 1.5 mAh/cm^2 shows initial signs of additional losses at C-rates of 2C, while the 2.9 mAh/cm^2 electrodes already show initial limitations at 1C, with the most drastic performance drop off among all samples. Rate test performed between 2.5 V and 4.2 V vs Li$^+$/Li in a T-cell setup with GWRE.

Kinetics of NMC 111 at varying LiPF$_6$ concentrations— This subsection shows the results of the NMC 111 EIS analysis using LiPF$_6$ salt concentrations between 0.03 M and 3 M in EC:EMC 3:7 (wt.:wt.). NMC 111 half-cells with GWREs were assembled using different electrolyte concentrations and cycled 5 times between 2.5 and 4.2 V at C/5 (including a 1h potential hold at 4.2 V) before measuring impedances at various steps between 3.7 V and 4.2 V vs Li$^+$/Li. For the concentration dependent impedance analysis in Fig. 5, a self-mixed electrolyte was used (see experimental section) while for a later analysis, commercial electrolyte pre-mixed at varying salt concentrations was used to ensure the results obtained here were not the result of improper material handling. Both sets of electrolytes gave comparatively similar results, as explained in this section.

The above described BV and Newman kinetics for liquid electrolytes predict a correlation of the exchange current density with the Li$^+$ electrolyte concentration to be $c_l^{\alpha_a}$, assuming all other parameters are constant. This includes the concentration of the reduced species intercalated in the solid, which is taken care of when measuring at the same SOC. Since the reference electrode is also immersed in the same electrolyte as the working electrode, the analysis and potentials all shift equally with changing electrolyte concentration according to the Nernst equation and the cycling and measuring protocol does not need to be adjusted. Fig. 5a shows the concentration-dependent charge transfer resistance, normalized to the Materials BET surface area (0.3 m^2/g), ranging from $3.7 - 4.2$ V vs Li$^+$/Li. For concentrations from 0.03 M to 1.5 M, the charge transfer resistance R_{ct} shows a logarithmically linear change with concentration, following a behavior which can be described with an α_a coefficient of 0.5 (grey dashed line given as guide for the eye). This behavior follows the expected trend predicted by both the Newman and BV equations. For higher electrolyte concentrations above 1.5 M, R_{ct} increases, contradictory to the expected theoretical behavior for liquid electrolyte.
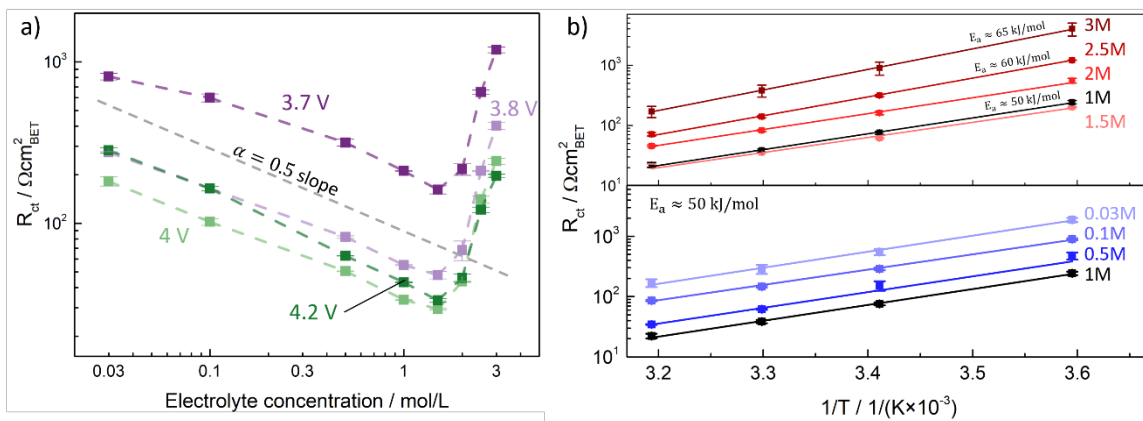
Figure 5 a) charge transfer resistance R_{ct} of NMC 111 measured for different electrolyte concentrations extracted from EIS spectra and normalized to a material BET surface area of 0.3 m^2/g. While at lower concentrations the behavior is as expected, the resistance increases contrary to the usually applied BV-theory.; b) The charge transfer resistance measured at 4V at different salt concentrations and different temperatures. For concentrations between 0.03 M to 2 M the activation energy is $\approx$ 50 kJ/mol and increases to 60 and 65 kJ/mol for the 2.5 and 3 M measurements, respectively.

18

Fig. 5b shows the temperature dependent resistances. The activation energies for the kinetics at 4 V at concentrations between 0.03 M and 2 M was measured to be around 50 kJ/mol but deviates at high concentrations to 60 kJ/mol and 65 kJ/mol for the 2.5 M and 3 M concentrated electrolyte, respectively. The deviation from the expected BV-type behavior can be caused by a plethora of reasons, e.g., the effect a high salt concentration may have on the electrolyte properties. A review of Li-ion battery electrolytes can be found in Ref. [30].

To first ensure that the observed behavior is not an artefact of the self-mixed electrolyte and any impurities such as hydrogen fluoride (HF) that might arise from mixing high concentrated electrolytes, we re-measured the NMC 111 kinetics using commercially available high and low concentrated electrolytes. The commercial electrolyte was tested for its HF content via a HF titration (see experimental section) and determined to be 44 ppm for the 2.5 M concentrated electrolyte, compared to 39 ppm for the 1M concentrated electrolyte. Thus, we assume no additional influence coming from HF which could damage the NMC surface.

Fig. 6a shows the impedance response of NMC 111 at 4V, measured in a 0.1, 1 and 2.5 M commercial electrolyte. The resistance increases by a factor ~3 from the 1 M to 0.1 M R_{ct} is as expected for an α-value of 0.5, and thus gives the same result as the self-mixed electrolyte. The 2.5 M commercial electrolyte measurement also shows an increased resistance, as observed for the self-mixed electrolyte, suggesting that this is not an artefact from the electrolyte preparation. The 2.5 M impedance response shows what appears to be an additional semi-circle feature below 1 Hz, not found in the other spectra with lower concentrations (but found in both self-mixed and commercial electrolyte). There are at least

two possible sources for the impedance deviation and additional features: i) the feature is part of the electrolyte impedance response alone, i.e., not connected to the kinetics (e.g. electrolyte diffusion) at such high concentrations and overlaps with the actual kinetics, and thus could be described by some other polarization phenomena; ii) it arises from the interface and electrolyte interaction therewith and is therefore connected to the kinetics. The first hypothesis is easily tested, as any property which solely arises from the electrolyte would be visible, and reasonably constant, when using other electrodes of, e.g., higher areal capacity, similar to, e.g., the HFR which is not a function of any electrode state or property. The 1.5 mAh/cm^2 electrode measured in the 2.5 M electrolyte shows a similar impedance spectra deviation in the same frequency range but significantly decreased in magnitude. Comparing the shape of the 1.6 mAh/cm^2 impedances from Fig. 2 with the 1.5 mAh/cm^2 impedance in Fig. 6 shows that the impedances in Fig. 2 measured in a 1 M electrolyte show a minimum around 1 Hz, whereas the 2.5 M impedance shows an additional stretched out feature, which could arise from an underlying semi-circle. It can therefore be concluded that the feature visible in the 2.5 M measurement is not from the electrolyte itself but is rather related to the electrode active material interface and the large semi-circle is still representing the material kinetics.

The influence of high salt concentrations on the material interface have been studied in the literature as well. Steinrück et al.[31] studied the electrolyte-metal oxide interface and found that high concentrated electrolyte builds a more ordered electrochemical double layer around metal oxides. Tatara et al.[32] show similarly increased kinetic resistances for high electrolyte concentrations in NMC 811, but also show that additional delithiation outside of the materials usual stability window (in their case from 4.3 V and upwards for the NMC

811) shows lower degradation when using higher salt concentrations. This was explained by a reduced electrolyte reactivity due to the higher salt concentration.

To see if the effect of the high concentrated electrolyte is permanent, the electrodes cycled in 2.5 M electrolyte were harvested, washed in diethyl carbonate (DEC) and re-measured in a 1 M electrolyte (see Fig. 6b). Measuring the 4 V impedance in the first cycle shows a reduction in resistance and in the subsequent cycles the impedance is reduced to the same value as the NMC 111 electrode measured solely in a 1M electrolyte. The effects from the electrolyte therefore do not appear permanent but were also not immediately washed off during the washing step. This however suggests a non-destructive interplay between the material and the electrolyte, and thus the kinetics shown in Fig. 5 appear to be valid also for the high concentrated electrolyte. It can be mentioned that, as shown by Tatara et al., the effect a high concentrated electrolyte has on the cathode depends also on the type of salt, as, e.g., $LiBF_4$ has a lower EC coordination compared to $LiPF_6$ and thus a comparison of two electrolytes using different salts (or the same salt but different concentrations of EC in the solvent) is expected to yield different outcomes.[32]
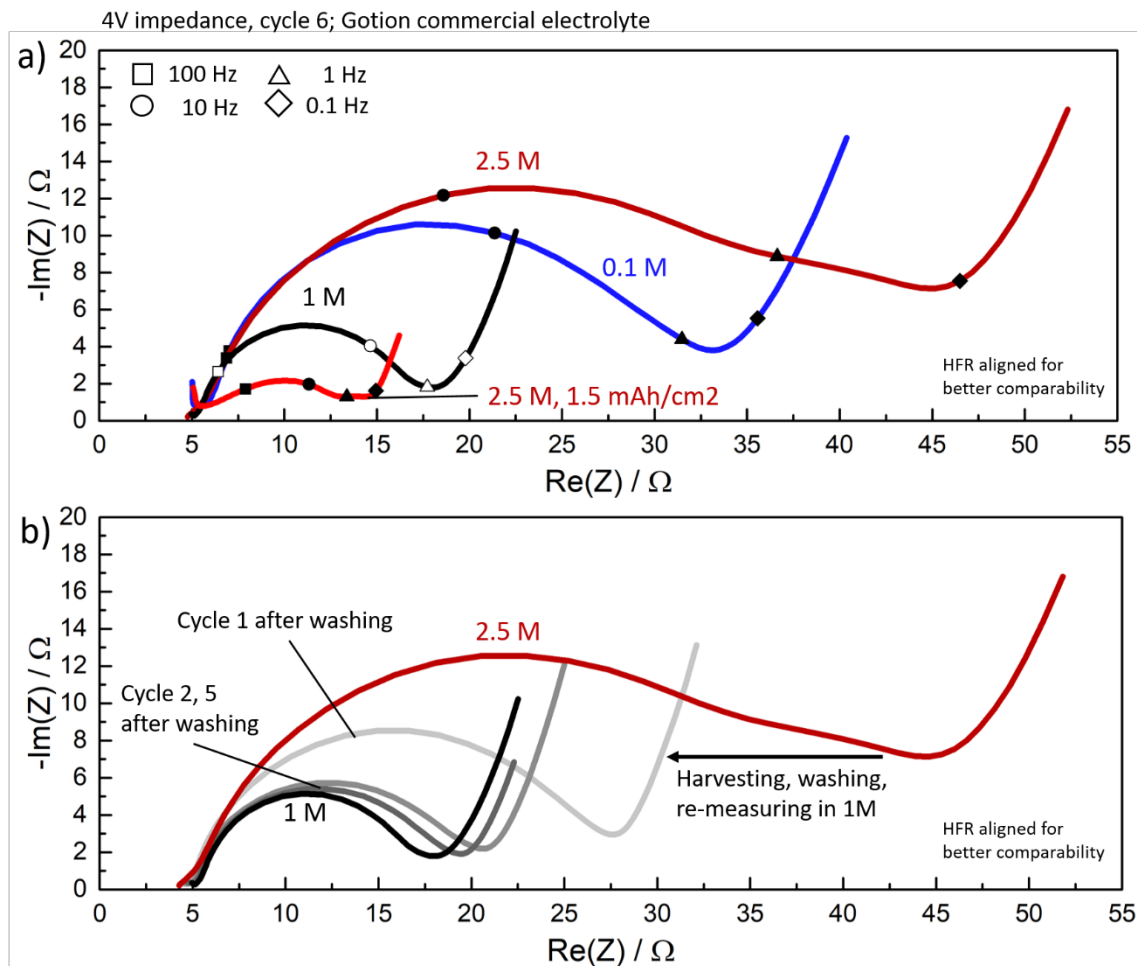
Figure 6 NMC 111 impedance date measured at 4 V vs Li$^+$/Li. a) Impedance data measured in a 0.1, 1 and 2.5 M commercial electrolyte. The resistance change from the 1M to the 0.1 M electrolyte is as expected from the BV/Newman theory. The increased resistance for the high-concentrated 2.5 M electrolyte is not predicted by the theory and the additional measurement at a higher areal capacities shows that the additional feature around 1 Hz is linked to the electrode surface area, and thus, the kinetics. b) replots the 1M and 2.5 M impedances from a) and shows the impedance of the electrode cycled in 2.5 M after washing, measured in a 1M concentrated electrolyte. The resistance is reduced and after two cycles decreased to the expected value of the 1 M concentrated electrolyte, suggesting no permanent surface change has occurred.

An alternative explanation for the increase in kinetics for strongly increased electrolyte salt concentration is the solubility limit of the electrolyte, i.e., the maximum dissociated salt concentration achievable for a given electrolyte composition, which could lead to a similar behavior of the electrolyte dependent kinetics compared to the SOC dependent active material kinetics. As Li$^+$ requires free solvent molecules (EC) to be dissociated in the electrolyte, a high concentration of Li$^+$ at the electrode/electrolyte interface could hinder

22

further solvation of Li^+. Fig. 7 plots the charge transfer resistance linearly over concentration, with the grey line representing the same equation used for the change in kinetics of the solid material, but now with c_{sat} representing the saturation limit of the electrolyte, here assumed as 3 M as this appeared to be the highest achievable salt concentration during mixing. A similar theory has been proposed by Newman for polymer electrolytes, which are limited in the amount of Li^+ which can be inserted into the polymer electrolyte.[6,24] The shape of the experimental data appears asymmetric, with still a minimum at half the assumed maximum salt concentration, which is not a trend that can be represented by the equation used for the grey line. Thus, further investigation into high salt concentration kinetics and a variation in the equation are necessary to find a proper mathematical representation of the here shown phenomenon.
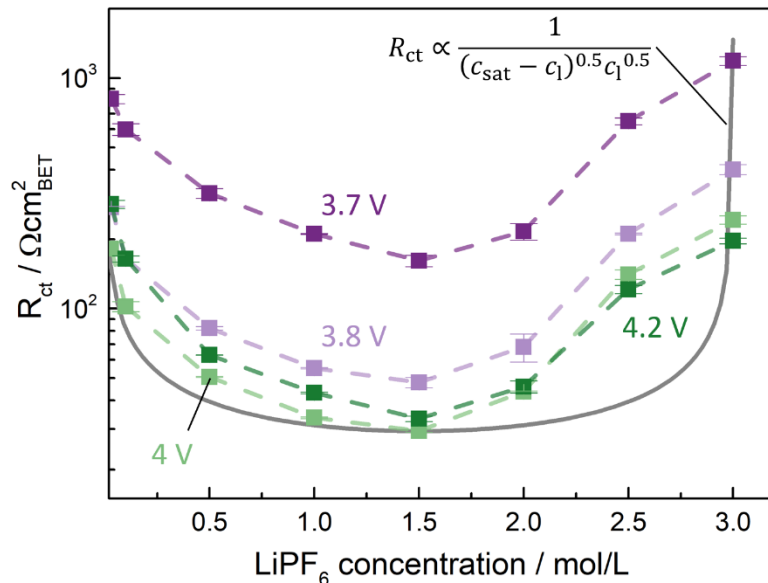

Figure 7 Charge transfer kinetics from Fig. 5 replotted with a linear relationship to the electrolyte salt concentration. The grey line plots the charge transfer resistance if the electrolyte concentration dependent kinetics behave similarly to the theory for active material (Eqn. 4), with a solubility limit in concentration c_{sat} (here assumed as 3 M).

This analysis shows that the NMC 111 kinetics cannot be described by the simple relationship of $R_{ct} \sim \frac{1}{c_l^{\alpha_a}}$ but requires an additional term for higher-concentrated electrolytes or an adaptation of the equations, incorporating an electrolyte solubility limit. An additional method to determine the transfer coefficients α_a and α_c is by applying high currents and measuring the kinetic overpotential to extract the tafel kinetics. Generously extrapolating the kinetic resistance of an electrode from the capacity dependent impedance in Fig. 2 gives a maximum of 40 Ωcm^2 kinetic resistance for a 0.1 mAh/cm^2 electrode. Calculating the overpotential at 1 C (0.1 mA/cm^2) gives 4 mV overpotential acc. to ohms law, which is valid as such low overpotentials are in the linear BV-regime. To accurately measure the kinetic resistances at high overpotentials would require currents far beyond 10 C, which for cell setups such as the T-cell setup used here are impractical as these currents lead to additional losses across the separator. The loading dependent rate test (Fig. 4) also shows that the limitation in electrolyte transport does not allow for currents far outside of the linear BV-regime for practical applications of Li-ion batteries.

SOC dependent EIS analysis of R_{ct} and diffusion resistances of NMC 111— This subsection shows the SOC dependent analysis of the charge transfer kinetics as well as the low frequency diffusion resistance measured down to 1 mHz.

Fig. 8a shows an impedance spectrum of the NMC 111 at 3.8 V and the equivalent circuit for a thin electrode at the top of the figure. As a 0.37 mAh/cm^2 electrode has a mass loading of less than 3 mg/cm^2, it can be considered a flat electrode, and the main contributions to the resistance are the high-frequency separator resistance offset, the charge transfer resistance (red semi-circle) as well as diffusion resistances (blue). For such an electrode, R_{ct} can directly be extracted from the impedance spectra without the use of a transmission line model. The measured diffusion resistance however has two contributions, the liquid

diffusion in the separator and the solid diffusion in the active material. Measuring the low frequency impedance at different SOC would thus only change the active material diffusion resistance and the charge transfer resistance. The separator diffusion resistance can then be assumed constant as it is not a function of the active material SOC.
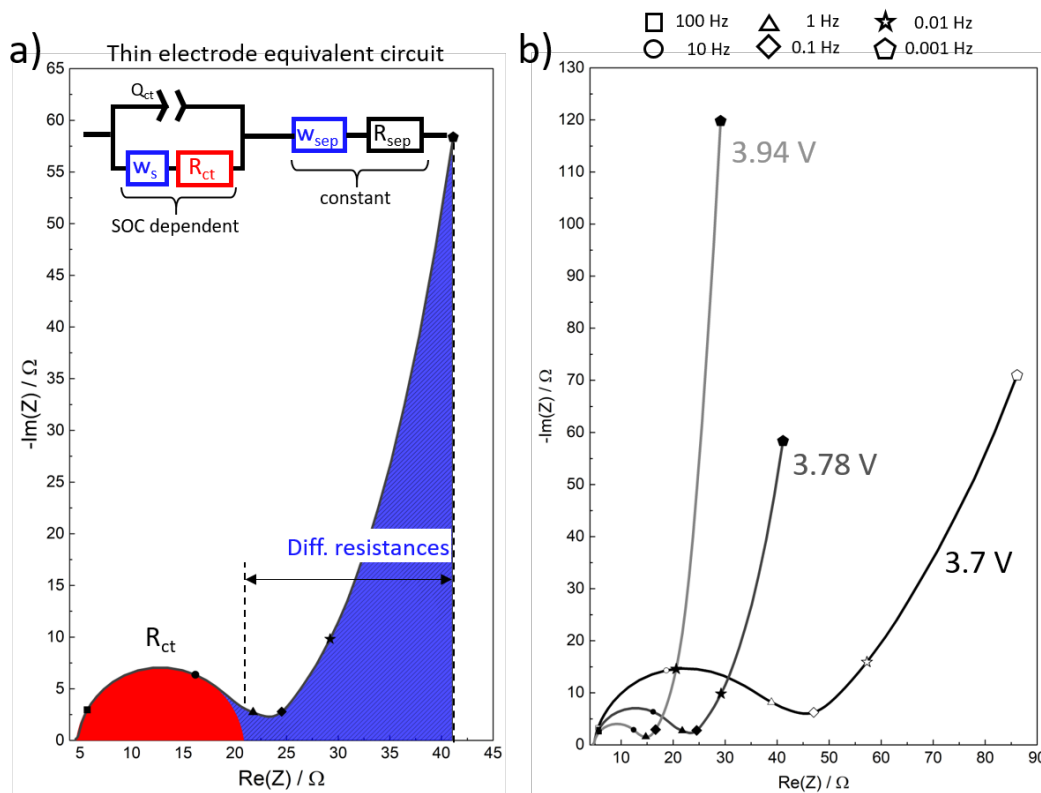

Figure 8 Nyquist plots for NMC electrodes of 0.37 mAh/cm^2 measured to 1 mHz. a) example plot showing the contribution of the kinetic and diffusion resistance. The diffusion resistance includes both the resistance from the reflective solid Warburg diffusion as well as the transmissive Warburg diffusion resistance from the liquid electrolyte in the separator, the latter can be taken constant over all SOCs. b) example impedance plots depicting the low frequency impedance of the NMC 111 electrode at 3.7 V (~10% SOC), 3.78 V (~40% SOC) and 3.94 V (~80 % SOC) showing both a decrease in charge transfer kinetics and diffusion resistance with increasing SOC.

Fig. 8b shows exemplary NMC impedance spectra at different potentials, from 30 kHz to 1 mHz. At 3.7 V the impedance plot has not yet reached the capacitive behavior (close to a 90° slope) and thus the diffusion resistance measured is underestimated. The other two spectra at higher potentials have reached a (mostly) capacitive behavior and can be evaluated for their diffusion resistance. The analysis was performed using the x-axis

(Re(Z)) value of the 1 mHz datapoint and subtracting both HFR and R_{ct}. The remaining resistance value constitutes the diffusion in the separator and the impedance response of the spherical diffusion in the solid active material.

Fig. 9 shows the SOC dependent charge transfer kinetics of the NMC electrodes for different cut-off potentials. As discussed earlier, the Newman kinetics were designed for a full insertion/removal of the active species into the material. This is not possible for NMC 111 due to the instability of the material at higher potentials. NMC 111 can usually be cycled to a potential of 4.2 V or 4.4 V vs Li$^+$/Li, and we additionally cycled the material to 4.6 V to understand the kinetic behavior over a wider SOC range, even though the material is not stable for long term cycling at this potential.[11] All cells were cycled 5 times at C/5 to the respective cut-off potential before the SOC-dependent impedance measurement was performed. Fig. 9a shows R_{ct} normalized to the BET surface area as a function of lithium-content. All materials have an initial Li-loss due to the slow kinetics for re-insertion, visible in the increase in charge transfer resistance at higher lithium concentrations (low SOC), which could be recovered by applying a low potential to the material for several hours (assuming the material has not undergone substantial irreversible changes).[33]
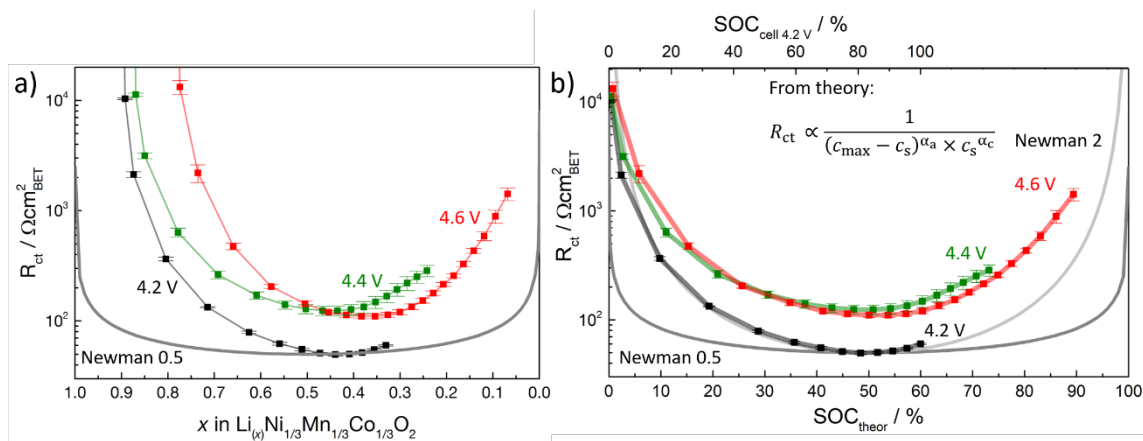

Figure 9 SOC dependent kinetics. a) Charge transfer resistance as a function of Li-content in the material for different cutoff potentials. The general shape is that of the kinetics predicted by Newman (For both $\alpha = 0.5$) but the material shows stronger changes with SOC and the minima are shifted to lower degrees of

lithiation. All materials have previously been cycled to the respective cutoff potential. b) re-plots the date of a) but redefining SOC_theor such that 0% SOC_theor corresponds to the practically full material after the irreversibly lost lithium and 100 % SOC_theor correspond to a theoretically complete delithiation of the material. For reference, the top axis shows the cell SOC for a cutoff of 4.2 V, as it might be defined for practical applications. The materials now show their minimum resistance at 50 % SOC and the kinetics can be described by the Newman equation using both $\alpha = 2$ (grey line labeled Newman 2).

The impedances show a U-shaped trend with a minimum resistance at a lithium content of ~0.44 for a cut-off of 4.2 V and 4.4 V and 0.38 for the NMC cycled to 4.6 V. The electrodes cycled to 4.2 V show an overall lower R_{ct} compared to 4.4 V and 4.6 V. The Newman predicted kinetics show the U-shaped form but for $\alpha = 0.5$ the expected minimum resistance should be at $x = 0.5$. More drastically different however is the change in kinetics with Li-content. The Newman kinetics equation predicts significantly less change in kinetics over SOC compared to the experimental measurement.

To correct the kinetics for the (practically) irreversible capacity loss, Fig. 9b changes the x-Axis plot to adjust for these losses, described as SOC_theor. Here, 0% SOC_theor corresponds to the material in its fullest state when charged at C/10 (practically full), however 100% SOC_theor still represents the materials full delithiation (theoretically empty). The thus normalized kinetics now show their kinetic minimum at ~50% of their theoretical SOC, regardless of cut-off potential or initial irreversible losses, and are closer represented by the Newman kinetics. The Newman kinetics (Eqn. 6) shown in the two figures were calculated using the relationship $R_{ct} \propto \frac{1}{(c_{max}-c_s)^{\alpha_a} \times c_s^{\alpha_c}}$ and then adjusting the remaining offset such that the minimum resistances overlap. The curves described as Newman 0.5 show the change in SOC with both α coefficients as 0.5. The Newman 2 curve was calculated with the coefficients set to 2, changing the curvature of the kinetics, which now overlap much closer to the experimentally obtained data. The analysis shows that for SOC dependent kinetics, different transfer coefficients from those used for the electrolyte-

dependent data need to be used. Adjusting for these differences, the material still shows a remarkable similarity to the Newman model. Also, the 4.4 V and 4.6 V cycled cells show almost identical resistances when plotted over a normalized plot in Fig. 9b. Both are expected to have undergone some form of surface reconstruction, and additional growth of structurally different layers into the material due to, in this case, oxygen loss,[11] are not reflected in R_{ct} as it is measured at the particle surface alone and the thickness of such a layer should be irrelevant.

Fig. 10 shows the SOC dependent diffusion resistance in blue (as defined in Figure 7a, including both liquid and solid phase diffusion resistances) over the adjusted theoretical SOC. This diffusion resistance measured here is only of a qualitative nature, as the analysis for actual diffusion would require detailed knowledge about the particle shape and size distribution and requires an appropriate model, as, e.g., shown in Ref 34. Assuming that the diffusion behavior in solid particles will ultimately lead to a vertical line (pure capacitive behavior) and not a tilted line (as obtained in CPE) the defined diffusion resistance can be considered as underestimates, especially at lower SOCs as described above.[29] Since individual measurements to low frequencies take around 10h of measurement time, this analysis was only done for the cut-off potential of 4.2 V.

The diffusion resistance for such a thin electrode (where the electrode can be approximated as flat) represent the sum of i) the liquid Warburg resistance of the separator (as estimated in the appendix A) and ii) $1/5^{th}$ of the Warburg resistance of the solid spherical particle R_{part} (equation 7 below). In the separator, 1 Ωcm^2 electrolyte HFR would cause an additional 1.33 Ωcm^2 diffusion resistance, which can then be subtracted from the measurement (see Appendix for detailed explanation). In this case the observed 4 Ω HFR (on a T-cell surface area of 0.94 cm^2) resistance would result in 5.32 Ω (or 5.7 Ωcm^2)

diffusion resistance, can make up a third of the total diffusion resistance measured and is therefore not negligible. The particle diffusion resistance R_{part} with the Warburg resistance of the solid particles is defined as:[29,35]

$$R_{\text{part}} = 5 \times R_{\text{meas}} \times A_{\text{part}} = \frac{\partial U}{\partial c_s} \frac{r_s}{F D_s} \qquad [7]$$

Where R_{meas} is the experimentally measured diffusion resistance of the projected diffusion surface area A_{part}, $\frac{\partial U}{\partial c_s}$ is the slope of the open circuit potential (OCV) over the solid concentration change, r_s the particle radius and D_s the diffusion resistance in the solid phase.

To calculate a diffusion coefficient, the projected diffusion area of the spherical particles, i.e., the area measured if the surface of the particles was perfectly smooth, therefore not the BET surface area, is needed. With 0.37 mAh/cm^2 and 145 mAh/g, this gives an areal loading of $\approx$ 2.6 mg/cm^2 of NMC. With a density of 4.7 g/cm^3, the NMC 111 volume gives 0.55×10^{-3} cm$^3_{\text{part}}$/cm^2. Assuming a uniform particle radius of 10 μm (spheres), gives a volume of 4.2×10^{-9}cm^3 per particle and thus 1.3×10^5 particles and a total surface area A = 1.6 cm$^2_{\text{part}}$/cm^2. For comparison, the BET surface area would have yielded 7.8 cm^2.

Correcting the experimentally measured diffusion resistance at ~40% SOC$_{\text{theor}}$ (around 60% SOC$_{\text{cell}}$; ~16 Ωcm^2) for the liquid Warburg (5.7 Ωcm^2) gives $R_{\text{meas}} \approx$ 10.3 Ωcm^2, and thus, $R_{\text{part}} \approx$ 82 Ωcm$^2_{\text{part}}$. Taking the local slope at this SOC (1.9×10^{-5} V/mol/m$^3_{\text{part}}$), the diffusion coefficient for this SOC is calculated to 2.4×10^{-13} m^2/s, similar to a previously reported value for NMC 111.[34] Assuming this diffusion coefficient to be constant over SOC would result in a theoretically measured diffusion resistance which now only depends on the OCV slope. The brown line in Fig. 10 shows the diffusion resistance which would

theoretically be measured if the diffusion coefficient was constant, i.e., the resistance would only depend on the local OCV slope. It shows a distinct minimum in resistance at low SOC, in a region where the experimentally measured resistance is highest. The difference between the theoretically expected diffusion resistance (red line) and the experimentally measured resistance (grey line) can be interpreted as an effective change in diffusion coefficient, assuming the particle morphology is constant (i.e., no reversible particle breathing). Thus, the NMC 111 diffusion coefficient is decreasing by one order of magnitude between the higher and lower SOC, respectively.

Comparing the diffusion resistance with the charge transfer kinetics, their minima are somewhat aligned between 40-50% SOC_{theor}, and their shape over SOC is similarly U-shaped with an increase in resistance towards higher degrees of lithiation. A proper diffusion analysis of NMC materials can be difficult, as this material is composed of secondary particles containing small primary particles. Particle breathing over SOC and cracking over cycling changes the effective diffusion length and any analysis would only give an effective diffusion coefficient which might contain additional diffusion from liquid penetrating the particle.[19,36] A thorough analysis of the material diffusion would require spherical single crystal NMC particles of a narrow particle range to get accurate information on the diffusion coefficient. Charbonneau et al.[34] have measured polycrystalline diffusion coefficients via EIS by applying such a model, however only measured the first cycle and the 50th cycle and neglected a correction for the liquid diffusion. This correction is especially necessary if the electrode loading is such that the measured diffusion resistance is in the same order of magnitude as the cell separator resistance, as was the case here for parts of the measured spectra, even though the areal capacity is already considered very low.
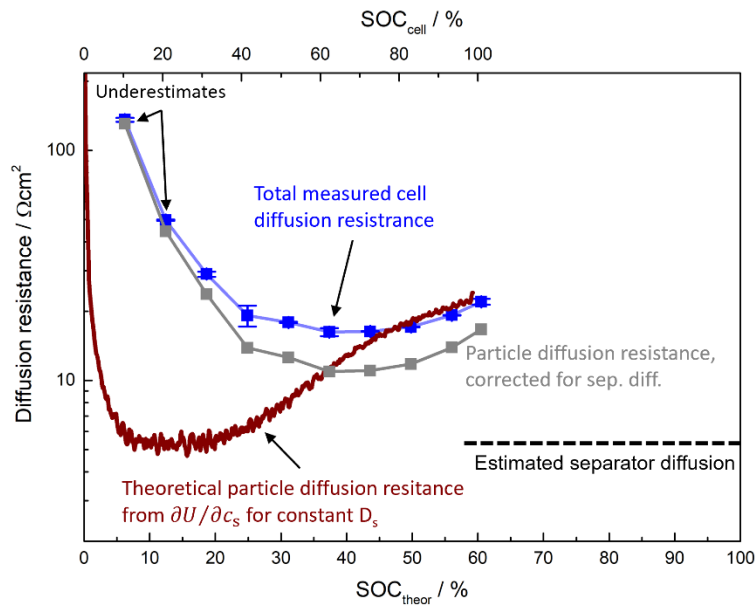
Figure 10 Blue: Diffusion resistance extracted from the low frequency impedance analysis, containing both the separator and particle diffusion resistance. The estimated separator diffusion is 5.7 Ωcm^2 and is independent of the electrode SOC. 0% SOC_{theor} is defined as the reversibly available SOC whereas 100% SOC is the theoretically attainable SOC if the material was stable at these degrees of delithiation. The particle diffusion resistance (grey) was corrected for the separator diffusion resistance and (for spherical particles) corresponds to $1/5^{th}$ of the total particle diffusion resistance. Assuming a constant diffusion resistance of 2.2×10^{-13} m²/s the brown line shows the change in diffusion resistance due to the material specific changes in the potential slope. The first two resistances at low SOC were obtained from spectra which did not show a capacitive behavior at the lowest frequency and are thus considered underestimates.

The SOC dependent analysis shows the change in kinetics over SOC, which practically become asymmetric due to the partial usage of the material. To understand the influence of the asymmetric kinetics on the materials rate capability, we performed charging (delithiation) and discharging (lithiation) rate test with electrodes of very low areal capacity, 0.37 mAh/cm². Fig 11a shows the potential profile of the C/10 and 5C charging (delithiation, green) and discharging (lithiation, red) rate test. As seen previously in Fig. 9 and Fig. 10, towards low SOC the kinetic- and diffusion resistances of NMC 111 increase starkly, whereas these resistances decrease towards higher SOCs, which becomes visible in the decrease in overpotential between the C/10 and 5C delithiation curves over the course of charging (green curves). The opposite effect is visible more severely in the lithiation curves, where the measured capacity is limited much more significantly and the

difference between the C/10 and 5C curves (red) increases drastically towards the end of discharge. Fig 11b shows the overall reached capacities of C-rates up to 5C.
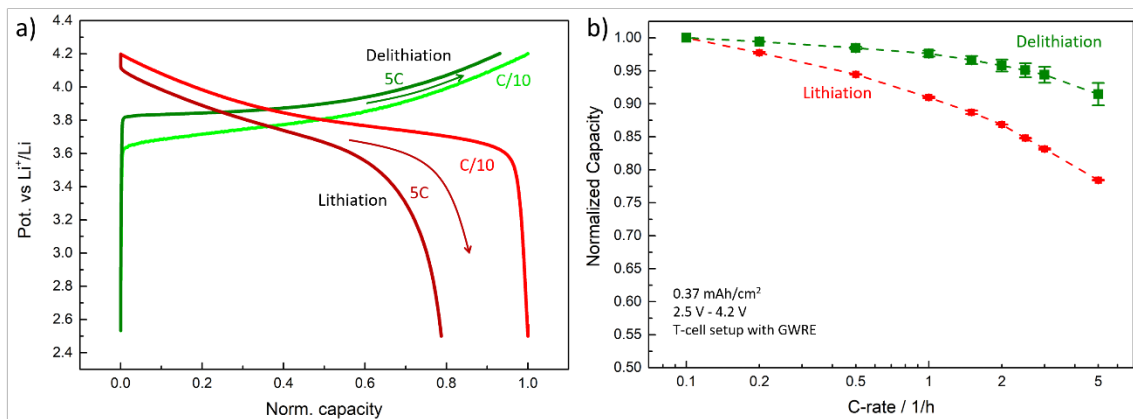

Figure 11 Rate test of thin NMC electrodes with a capacity of ~0.37 mAh/cm^2. a) lithiation and delithiation potential curves at C/10 and 5C showing the discrepancy in performance. During delithiation the kinetics generally become faster while during lithiation both the charge transfer and diffusion resistance increase towards higher degrees of lithiation leading to significantly increased overpotentials. b) capacities reached between C/10 and 5 C for lithiation and delithiation.

Conclusions

This work shows an EIS based kinetic analysis of NMC 111 electrodes. We first give an overview over the kinetic theory which was adapted by Newman for intercalation materials, and served as the basis for comparison throughout the rest of this work. To find a suitable electrode design for the analysis, we then demonstrated the impact of areal capacity on the impedance spectra, especially with regards to the 1 mHz low frequency impedance, showing how lowering areal capacity improves probing the charge transfer kinetics and solid diffusion resistance, which especially for the latter case is sufficient around 0.37 mAh/cm^2. Rate tests showed that at lower areal capacities the electrode performance becomes independent of the electrode mass loading, once mass transport limitations become negligible and the material properties dominate.

The first step in the kinetics analysis was the electrolyte salt concentration dependent analysis. Generally, the change in kinetics with concentration are described by $R_{ct} \propto \frac{1}{c_l^{\alpha_a}}$ which we show is true for lower electrolyte concentrations between 0.03 M and 1.5 M LiPF$_6$. At higher salt concentrations, up to 3M, the kinetic resistance increases contrary to the popularly used expression for liquid electrolytes, but in line with other observations in literature. To understand if the resistance change is a result of a permanent destruction of the NMC 111 surface, we harvested electrodes which were cycled in a 2.5 M electrolyte, washed them, and re-measured them in a 1M electrolyte. The electrodes regained a lower charge transfer resistance, in line with expected measurements of a 1M electrolyte, showing that the effect is indeed a kinetic effect and not permanent and therefore needs to be incorporated into the kinetic model. The observations could also be described by a model which incorporates a solvation limit into the electrolyte, similar to the proposed theory for the solid active material. As this effect of increasing resistance may be linked to the EC coordination of the salt,[32] our results are only valid for a LiPF$_6$ electrolyte with a 3:7 ratio (wt. : wt.) of EC to EMC. The lower electrolyte concentrations (0.03 M to 2 M) showed the same activation energy of 50 kJ/mol, while at higher salt concentrations (2.5-3 M) the activation energy increased up to 65 kJ/mol.

The SOC dependent analysis of the charge transfer kinetics, predicted as $R_{ct} \propto \frac{1}{(c_{max} - c_s)^{\alpha_a} \times c_s^{\alpha_c}}$, showed U-shaped kinetics over the theoretically achievable SOC similar to the predicted values from the Newman model, but showed a significantly steeper slope. Adjusting the definition for SOC due to the practically irreversible capacity loss of the material, but incorporating the theoretically achievable maximum capacity, showed kinetics which were more closely in line with the Newman model. They exhibited symmetric kinetics with a minimum at 50% SOC$_{theor}$, but still require adjustment of the

kinetic transfer coefficients α from 0.5 to the, less physically defined but experimentally measured, value of 2. The diffusion resistance also follows a U-shaped trend, which, when considering the limited available SOC window of the NMC 111, leads to asymmetric kinetics of the material in practical use. The diffusion and charge transfer resistance increase for higher degrees of lithiation limits the electrode capacity during discharge, as demonstrated in rate capability lithiation and delithiation rate tests.

The measurements showed that in the case of NMC 111, the kinetic transfer coefficients for the liquid phase behave independently of the transfer coefficients for the solid phase and thus must be treated separately, rather than using one set of parameters for both.

Acknowledgments

Appendix

Assuming that the Warburg resistance of the separator placed between two thin electrodes will be similar to the Warburg resistance of the same separator placed between two flat lithium foils, we can use the Li-separator-Li setup and associated equations to calculate the potential difference due to diffusion overpotential across the separator. From the diffusion overpotential, we can calculate the Warburg resistance. The Li-Seperator-Li system has the following boundary condition on each side corresponding to the faradaic reaction (i.e., at the interface between liquid electrolyte and Li electrode)

$$-D_{\text{eff}} \frac{\partial c_l}{\partial x}\bigg|_{x=0,\,d_{sep}} = \frac{I(1 - t_+)}{F} \qquad \text{[A1]}$$

Where x is the axial coordination going from 0 to the thickness of the separator d_{sep}, t_+ is the transference number and I is the applied current. In this system, at steady state, the concentration gradient in the entire separator will be the same everywhere and can be given by (assuming that applied current is small enough so that the concentration difference across the separator is tiny hence the transport parameters will not vary substantially)

$$\frac{\partial c_l}{\partial x} = -\frac{I(1 - t_+)}{F D_{\text{eff}}} \qquad \text{[A2]}$$

The charge balance equation applicable to the system is given below.[5]

$$\frac{\partial \phi_2}{\partial x} = -\frac{I}{\kappa_{\text{eff}}} + \frac{\frac{2RT}{F}(\text{TDF})(1 - t_+)}{c_l}\frac{\partial c_l}{\partial x} \qquad \text{[A3]}$$

Here, ϕ_2 is electrolyte potential, $\kappa_{\text{eff}} \equiv \kappa \varepsilon / \tau$ is the effective electrolyte conductivity which is given by bulk conductivity, electrode porosity and tortuosity, TDF is the thermodynamic factor. The second term on the RHS can be modified using the concentration gradient given by A2 as below.

$$\frac{\partial \phi}{\partial x} = -\frac{I}{\kappa_{\text{eff}}} - \frac{I}{\underbrace{\frac{c D_{eff} F^2}{2RT(TDF)(1 - t_+)^2}}_{W}} \qquad \text{[A3]}$$

While the first term is thought to give the potential drop due to limited conductivity of the electrolyte, the second term in Eq. A3 can be used to give the potential drop due to diffusion overpotential, hence the Warburg resistance can be calculated using the second term of Eqn. A3 as below.

$$R_{\text{w}} = \frac{d_{\text{sep}}}{W A} = \frac{d_{\text{sep}}}{\left(\frac{c_l D_{\text{eff}} F^2}{2RT(TDF)(1 - t_+)^2}\right) A} \qquad \text{[A4]}$$

Using Landesfeind et al[37] for TDF =1.5 , $\kappa = 8.9$ mS/cm, D=3E−10m^2/s and $t_+ = 0.25$ at 298 K, a 1 cm^2 area of 89µm thickness filled with electrolyte would result in a 1 Ω high frequency resistance (resulting from the electrolyte conductivity). The resulting diffusion resistance would be an additional 1.33 Ω, i.e., every 1 Ω in separator high frequency resistance results in an additional 1.33 Ω in diffusion resistance.

References

1. I. V. Thorat, D. E. Stephenson, N. A. Zacharias, K. Zaghib, J. N. Harb, and D. R. Wheeler, Quantifying tortuosity in porous Li-ion battery materials, *Journal of Power Sources*, **188**, 592–600 (2009).

2. J. Landesfeind, J. Hattendorff, A. Ehrl, W. A. Wall, and H. A. Gasteiger, Tortuosity

Determination of Battery Electrodes and Separators by Impedance Spectroscopy, *Journal of The Electrochemical Society*, **163**, A1373–A1387 (2016).

3. T.-T. Nguyen, A. Demortière, B. Fleutot, B. Delobel, C. Delacourt, and S. J. Cooper, The electrode tortuosity factor: why the conventional tortuosity factor is not well suited for quantifying transport in porous Li-ion battery electrodes and what to use instead, *npj Computational Materials*, **6**, 123 (2020).

4. A. Falconi, Electrochemical modeling of lithium-ion cell behaviour for electric vehicles, thesis, (2017).

5. T. F. Fuller, M. Doyle, and J. Newman, Simulation and Optimization of the Dual Lithium Ion Insertion Cell, *Journal of The Electrochemical Society*, **141**, 1–10 (1994).

6. M. Doyle, T. F. Fuller, and J. Newman, Modeling of Galvanostatic Charge and Discharge of the Lithium/Polymer/Insertion Cell, *Journal of The Electrochemical Society*, **140**, 1526–1533 (1993).

7. M. Farkhondeh, M. Pritzker, M. Fowler, M. Safari, and C. Delacourt, Mesoscopic modeling of Li insertion in phase-separating electrode materials: Application to lithium iron phosphate, *Physical Chemistry Chemical Physics*, **16**, 22555–22565 (2014).

8. M. Z. Bazant, Theory of chemical kinetics and charge transfer based on nonequilibrium thermodynamics, *Accounts of Chemical Research*, **46**, 1144–1160 (2013).

9. M. Wagemaker, D. P. Singh, W. J. H. Borghols, U. Lafont, L. Haverkate, V. K. Peterson, and F. M. Mulder, Dynamic solubility limits in nanosized olivine LiFePO4, *Journal of the American Chemical Society*, **133**, 10222–10228 (2011).

10. V. Srinivasan and J. Newman, Discharge Model for the Lithium Iron-Phosphate Electrode, *Journal of The Electrochemical Society*, **151**, A1517 (2004).

11. R. Jung, M. Metzger, F. Maglia, C. Stinner, and H. A. Gasteiger, Oxygen Release and Its Effect on the Cycling Stability of $LiNi_xMn_yCo_zO_2$ (NMC) Cathode Materials for Li-Ion Batteries, *Journal of The Electrochemical Society*, **164**, A1361–A1377 (2017).

12. N. Ogihara, S. Kawauchi, C. Okuda, Y. Itou, Y. Takeuchi, and Y. Ukyo, Theoretical and Experimental Analysis of Porous Electrodes for Lithium-Ion Batteries by Electrochemical Impedance Spectroscopy Using a Symmetric Cell, *Journal of The Electrochemical Society*, **159**, A1034–A1039 (2012).

13. N. Ogihara, Y. Itou, T. Sasaki, and Y. Takeuchi, Impedance spectroscopy characterization of porous electrodes under different electrode thickness using a symmetric cell for high-performance lithium-ion batteries, *Journal of Physical Chemistry C*, **119**, 4612–4619 (2015).

14. J. Landesfeind, D. Pritzl, and H. A. Gasteiger, An Analysis Protocol for Three-Electrode Li-Ion Battery Impedance Spectra: Part I. Analysis of a High-Voltage Positive Electrode, *Journal of The Electrochemical Society*, **164**, A1773–A1783 (2017).

15. N. Meddings, M. Heinrich, F. Overney, J. S. Lee, V. Ruiz, E. Napolitano, S. Seitz, G. Hinds, R. Raccichini, M. Gaberšček, and J. Park, Application of electrochemical impedance spectroscopy to commercial Li-ion cells: A review, *Journal of Power Sources*, **480**, 228742 (2020).

16. J. Moškon, J. Žuntar, S. Drvarič Talian, R. Dominko, and M. Gaberšček, A Powerful Transmission Line Model for Analysis of Impedance of Insertion Battery Cells: A Case Study on the NMC-Li System, *Journal of The Electrochemical Society*, **167**, 140539 (2020).

17. J. Moškon and M. Gaberšček, Transmission line models for evaluation of impedance response of insertion battery electrodes and cells, *Journal of Power Sources Advances*, **7**,

100047 (2021).

18. P. C. Tsai, B. Wen, M. Wolfman, M. J. Choe, M. S. Pan, L. Su, K. Thornton, J. Cabana, and Y. M. Chiang, Single-particle measurements of electrochemical kinetics in NMC and NCA cathodes for Li-ion batteries, *Energy and Environmental Science*, **11**, 860–871 (2018).

19. S. Oswald, D. Pritzl, M. Wetjen, and H. A. Gasteiger, Novel Method for Monitoring the Electrochemical Capacitance by In Situ Impedance Spectroscopy as Indicator for Particle Cracking of Nickel-Rich NCMs: Part I. Theory and Validation, *Journal of The Electrochemical Society*, **167**, 100511 (2020).

20. S. Oswald, D. Pritzl, M. Wetjen, and H. A. Gasteiger, Novel Method for Monitoring the Electrochemical Capacitance by In Situ Impedance Spectroscopy as Indicator for Particle Cracking of Nickel-Rich NCMs: Part II. Effect of Oxygen Release Dependent on Particle Morphology, *Journal of The Electrochemical Society*, **168**, 120501 (2021).

21. S. Solchenbach, D. Pritzl, E. J. Y. Kong, J. Landesfeind, and H. A. Gasteiger, A Gold Micro-Reference Electrode for Impedance and Potential Measurements in Lithium Ion Batteries, *Journal of The Electrochemical Society*, **163**, A2265–A2272 (2016).

22. R. Morasch, B. Suthar, and H. A. Gasteiger, Simple Way of Making Free-Standing Battery Electrodes and their Use in Enabling Half-Cell Impedance Measurements via μ-Reference Electrode, *Journal of The Electrochemical Society*, **167**, 100540 (2020).

23. J. Newman and K. E. Thomas-Alyea, Electrochemical Systems, in, Wiley-VCH Verlag GmbH & Co. KGaA, New Jersey (2004).

24. R. M. Thomas, K.E., Newman, J. and Darling, Mathematical modeling of lithium batteries. In Advances in lithium-ion batteries, Mathematical modeling of lithium batteries.

In Advances in lithium-ion batteries, p. 35–43, (2002).

25. K. West, T. Jacobsen, and S. Atlung, Modeling of Porous Insertion Electrodes with Liquid Electrolyte, *Journal of The Electrochemical Society*, **129**, 1480–1485 (1982).

26. M. Gaberscek, J. Moskon, B. Erjavec, R. Dominko, and J. Jamnik, The importance of interphase contacts in Li ion electrodes: The meaning of the high-frequency impedance arc, *Electrochemical and Solid-State Letters*, **11**, A170 (2008).

27. J. Landesfeind, M. Ebner, A. Eldiven, V. Wood, and H. A. Gasteiger, Tortuosity of Battery Electrodes: Validation of Impedance-Derived Values and Critical Comparison with 3D Tomography, *Journal of The Electrochemical Society*, **165**, A469–A476 (2018).

28. R. Morasch, J. Keilhofer, H. A. Gasteiger, and B. Suthar, Methods—Understanding Porous Electrode Impedance and the Implications for the Impedance Analysis of Li-Ion Battery Electrodes, *Journal of The Electrochemical Society*, **168**, 080519 (2021).

29. J. Song and M. Z. Bazant, Effects of Nanoparticle Geometry and Size Distribution on Diffusion Impedance of Battery Electrodes, *Journal of The Electrochemical Society*, **160**, A15–A24 (2013).

30. K. Xu, Electrolytes and interphases in Li-ion batteries and beyond, *Chemical Reviews*, **114**, 11503–11618 (2014).

31. H. G. Steinrück, C. Cao, Y. Tsao, C. J. Takacs, O. Konovalov, J. Vatamanu, O. Borodin, and M. F. Toney, The nanoscale structure of the electrolyte-metal oxide interface, *Energy and Environmental Science*, **11**, 594–602 (2018).

32. R. Tatara, Y. Yu, P. Karayaylali, A. K. Chan, Y. Zhang, R. Jung, F. Maglia, L. Giordano, and Y. Shao-Horn, Enhanced Cycling Performance of Ni-Rich Positive Electrodes (NMC) in Li-Ion Batteries by Reducing Electrolyte Free-Solvent Activity, *ACS Applied Materials*

and Interfaces, **11**, 34973–34988 (2019).

33. I. Buchberger, S. Seidlmayer, A. Pokharel, M. Piana, J. Hattendorff, P. Kudejova, R. Gilles, and H. A. Gasteiger, Aging Analysis of Graphite/LiNi$_{1/3}$ Mn$_{1/3}$ Co$_{1/3}$ O$_2$ Cells Using XRD, PGAA, and AC Impedance, *Journal of The Electrochemical Society*, **162**, A2737–A2746 (2015).

34. V. Charbonneau, A. Lasia, and G. Brisard, Impedance studies of Li+ diffusion in nickel manganese cobalt oxide (NMC) during charge/discharge cycles, *Journal of Electroanalytical Chemistry*, **875**, 113944 (2020).

35. J. P. Meyers, M. Doyle, R. M. Darling, and J. Newman, The Impedance Response of a Porous Electrode Composed of Intercalation Particles, *Journal of The Electrochemical Society*, **147**, 2930 (2000).

36. A. O. Kondrakov, A. Schmidt, J. Xu, H. Geßwein, R. Mönig, P. Hartmann, H. Sommer, T. Brezesinski, and J. Janek, Anisotropic Lattice Strain and Mechanical Degradation of High- and Low-Nickel NCM Cathode Materials for Li-Ion Batteries, *Journal of Physical Chemistry C*, **121**, 3286–3294 (2017).

37. J. Landesfeind and H. A. Gasteiger, Temperature and Concentration Dependence of the Ionic Transport Properties of Lithium-Ion Battery Electrolytes, *Journal of The Electrochemical Society*, **166**, A3079–A3097 (2019).

3.2.3 Li-Ion Battery Material Impedance Analysis II: Graphite and Solid Electrolyte Interphase Kinetics

The manuscript entitled "Li-Ion Battery Material Impedance Analysis II: Graphite and Solid Electrolyte Interphase Kinetics" will be submitted to a peer-reviewed journal.

Understanding the kinetics of graphite requires understanding the kinetics of the solid electrolyte interphase (SEI), which is formed during the first charge on the graphite surface. To understand the properties of the SEI, copper films were measured via EIS before and after formation in LP57 (EC:EMC 3:7 + 1M LiPF$_6$) and LP57-2 (+2% Vinylene carbonate, VC) electrolyte and showed that the SEI is dynamic, decreasing its resistance for a decreasing potential (towards 0V vs. Li$^+$/Li). Such a behavior is unexpected, as classically described solid electrolytes do not change their resistance with the applied potential. Studies have shown that solid electrolytes can form space charge layers, i.e., layers enriched or depleted of charge carriers, which could explain the behavior observed for the SEI.[98,99] Additional analysis of thin graphite electrodes showed that the SEI resistance is the main contribution to the graphite kinetics, with the charge transfer resistance becoming negligible above ~10% SOC.

To understand the impact of changing electrolyte concentration on the SEI resistance, electrodes underwent formation in a 1M LiPF$_6$ electrolyte, were then harvested, washed and re-measured in electrolyte of different salt concentrations between 0.03 M and 3 M. The analysis showed decreasing SEI resistances for increasing salt concentrations, which hints at an interplay between the SEI and the electrolyte. Analogously, performing the formation step in electrolytes with different salt concentrations has a similar effect on the SEI. To understand the influence of the SEI on the Li-plating kinetics, graphite electrodes which showed distinctly differing SEI resistances were brought to 10 mV vs. Li$^+$/Li for 1h to ensure that the material is fully lithiated. A subsequent Li-plating current of 1 mA showed that the SEI resistance is visible in the Li-plating reaction overpotential as an initial offset, but the additional nucleation overpotential is the same for both reactions.

The analysis shows that the SEI is dynamic and behaves similarly to a charge transfer resistance, in that it shows a potential dependence and a dependence on

the electrolyte concentration. Since the R_{ct} is negligibly small, the graphite electrode can be modeled by one kinetic element alone.

Author contributions

R.M. performed the measurements and evaluated the data. R.M. and B.S. discussed the analysis and interpretation of the data. R. M. wrote the manuscript. R.M., B.S. and H.A.G. discussed the results and revised the manuscript.

Li-Ion Battery Material Impedance Analysis II: Graphite and Solid Electrolyte Interphase Kinetics

Robert Morasch[a]*, Bharatkumar Suthar[b] and Hubert A. Gasteiger[a]

[a] Chair of Technical Electrochemistry, Department of Chemistry and Catalysis Research Center, Technical University of Munich, Munich, Germany

[b] Department of Chemical Engineering, Indian Institute of Technology Bombay, Mumbai 400076, India

*Corresponding author

Abstract

Li-ion battery graphite electrodes form a solid-electrolyte-interphase (SEI) which is vital in protecting the stability and efficiency of the cell. The SEI properties have been studied extensively in the context of formation and additives, however studying its kinetic features after formation have been neglected. In this study we show the dynamic resistive behavior of the SEI after formation. Via electrochemical impedance spectroscopy measurements on Cu-foil after SEI formation we show how the SEI shows a potential-dependent resistance which can be explained by a change in charge carriers (Li^+) in the SEI. Additional measurements on graphite exhibit a similar behavior and allow us to separate the charge transfer kinetics from the SEI resistance, showing that the SEI resistance is the dominating resistance in the graphite kinetics. Measurements on pre-formed electrodes also show how the SEI resistance changes when in contact with electrolyte of different $LiPF_6$ salt concentrations, with the resistance decreasing for increasing salt concentrations. Ultimately, we show that the SEI resistance affects Li-plating by acting as an offset to the plating reaction but does not affect the nucleation overpotential itself.

157

Introduction

The solid-electrolyte-interphase (SEI) in Li-ion batteries is a protective layer formed by the decomposition of electrolyte on an electrode surface, allowing the transport of ions while blocking any further exchange of electrons with the electrolyte.[1,2] Studying the properties and composition of the SEI is a difficult task, as its composition and thickness depends on the individual components of the electrolyte, the applied potential profile and temperature during formation and aging history of the layer.[3–7] It is proposed to consist of a compact inner layer and a porous outer layer, the latter allowing interactions with the electrolyte.[8–10] As Electrochemical impedance spectroscopy (EIS) analysis of e.g. Li-metal electrodes, which immediately form an SEI when they come in contact with electrolyte, show at least one semi-circle feature, the proposed equivalent circuit of the SEI consists of R/C elements, i.e., a resistor and a capacitor in parallel.[2,10] The capacitor can also be replaced by a constant phase element (Q) to account for the imperfect capacitive behavior. Li metal however is not well suited to study all aspects of the SEI via EIS, as no custom formation procedure can be applied. Additionally, the measured resistance contains both the Li-plating charge transfer kinetics as well as the SEI resistance. To study the effect of formation and additives on the SEI resistance, multiple studies have used electrode surfaces (e.g. copper or nickel) or applied potentials which allow the analysis in the absence of any faradaic reactions.[8,11–16] These studies and others show that electrolyte additives can greatly change the anode resistance, which can thus be attributed to a change in SEI composition.[17–19] This complicates any fundamental analysis of the SEI behavior, as changes in composition could lead to changes in the layers properties. Additionally, no thorough studies have been conducted to study the properties of a fully formed SEI on graphite and its impact on the EIS spectra with respect to understanding and deconvoluting

the effect of the SEI as well as the charge transfer resistance. Similarly, the SEI properties in the context of the electrode kinetic theory such as the effect of Li^+ concentration changes on the fully formed SEI resistance are unknown. While previous publications showed the EIS response of half cells, the use of a reference electrode in combination with an EIS analysis of thin graphite electrodes has not been shown.

This study first shows EIS measurements on Copper and Nickel metal foils either before or after three full formation cycles using LP57 or LP57 + 2% (wt.) vinylene carbonate (VC). We show the changes in the SEI resistance with respect to potential which occur even after all electrodes have undergone the same formation procedure, and correlate them to changes in the capacitance related to the SEI but also to the capacitance at the metal/SEI interface. This is followed by EIS measurements on thin graphite electrodes at different potentials. The thin electrode is necessary to highlight the interface resistance (SEI and R_{ct}) while avoiding contributions of the porous pathway which would show in electrodes of higher mass loadings.[20] Additionally, we show the impact of a changing electrolyte salt concentration on the SEI resistance of graphite electrodes which all underwent the formation step in the same electrolyte and compare them to the resistance of electrodes which underwent formation in electrolytes of different salt concentration. Finally, we correlate the measured SEI resistance to the Li-plating overpotential on graphite electrodes.

Experimental

Slurry preparation and drying.— Graphite (T311, Timcal, 19 μm D50, 3 m^2/g) and polymer binder (polyvinylidene fluoride (PVDF), Kynar, Arkema) at a ratio of 95:5 (wt:wt) were mixed with N-Methyl-2-pyrrolidone (NMP, Sigma Aldrich, anhydrous, 99.5%) at a solid:liquid ratio of 5:4 (wt:wt) or 5:5 (higher amounts of liquid are used to achieve lower

electrode loadings) in a planetary mixer (Thinky ARV-310) at 2000 rpm for five minutes. The prepared graphite slurries were coated onto a copper current collector foil (MTI, 10 μm) attached to a glass plate using a gap bar coater (RK PrintCoat Instruments, UK) at a wet film thickness of 30 μm, resulting in electrodes of ~250 to ~350 μAh/cm² (referenced to a nominal graphite capacity of 350 mAh/g$_G$), and dried in an oven at 50 °C. The dried electrodes were punched out to a diameter of 10.95 mm (equating to an area of ~0.94 cm²) using an electrode punch (Hohsen Corp. OSAKA, Japan), and compressed in a press using a pressure of ~ 100 MPa.

Cell assembly, formation and impedance measurement.— For electrochemical impedance analysis, a three-electrode cell setup (Swagelok® T-cell) with a gold-wire reference electrode (GWRE; described in more detail in Fig. 1b in Ref. [21]) was used. The cells were built inside an argon filled glove box (MBraun, 25 °C ± 1 °C, oxygen and water content <0.1 ppm, Ar 5.0, Westfalen). All cell parts were dried at 120 °C in a vacuum oven (Büchi, Switzerland) for 8 h before being transferred into the glovebox.

The cells were assembled with a graphite working electrode, two porous glass fiber separators with a diameter of 11 mm (VWR, 250 μm uncompressed thickness, 90% porosity), and a counter electrode consisting of a free-standing graphite electrode that was firmly attached to the metallic lithium foil (0.45 mm thickness and 11 mm diameter, Rockwood Lithium), as described in Ref.[22]. 80 μl of LP57 electrolyte (1 M LiPF$_6$ in EC:EMC 3:7 (wt:wt) (battery grade, Gotion, USA) or with the addition of 2 wt% vinylene carbonate (battery grade, Gotion, USA) were added to the cells. Additionally, for concentration dependent measurements two sets of electrolyte were used: An in house mixed electrolyte solution with 0.03, 0.1, 0.5, 1, 2, 2.5 and 3 M LiPF$_6$ in EC:EMC 3:7

(Battery grade, Gelon, China) or commercially available electrolyte of 0.1, 1 and 2.5 M LiPF6 in EC:EMC 3:7 (Battery grade, Gotion, USA).

Using a potentiostat (Bio-Logic Science Instruments, France), the gold-wire reference electrode was lithiated at 150 nA for 1 h via the counter electrode in a temperature-controlled chamber (25 °C, Binder). The cycling protocol started with a 3 h open circuit voltage phase to allow for complete wetting of the electrode. Three formation cycles for the graphite working electrode were performed galvanostatically at C/10 (referenced to a nominal specific capacity of 350 mAh/g$_G$) between 2V and 40 mV vs. Li$^+$/Li. For the metal foil formation, three cyclic voltammetry formation cycles were performed, with the reduction half cycle in the following steps: 500 mV/min from 2V to 0.9 V, 18 mV/min from 0.9 V to 0.2 V, 0.5 mV/min from 0.2 to 80 mV and 0.15 mV/min from 80 mV to 50 mV. The oxidation step was done in the reverse order.

Potentiostatic electrochemical impedance measurements were performed at open circuit voltage (OCV) or the specified potential from 30 kHz to 0.1 Hz with an excitation of 10 mV; the use of the micro-reference electrode (i.e., the GWRE) allowed for a rigorous determination of the impedance response of the graphite electrode. Impedance fitting was performed using the Bio-Logic instrument software EC-Lab.

Results and Discussion

SEI equivalent circuit description.— SEI equivalent circuit models of the SEI show it as a series of R/C elements, as e.g. also done for conventional solid electrolytes.[2, 10,23] For such equivalent circuits, multiple semi-circles are only visible in the spectrum if the processes they describe are sufficiently different in their frequency distribution of the R/C elements and it can depend on the SEI composition whether one or many semi-circle

161

features are visible. The number of R/C elements is not defined, as every solid electrolyte grain in the SEI could be modeled by a not quantifiable number of R/C elements in series, followed by another grain boundary. The SEI measured in this work however only gives rise to one semi-circle, which does not mean that other setups or SEI compositions may not show additional features related to individual transport mechanisms (e.g. inter- vs intra-grain conduction or the Li^+ transfer from the electrolyte into the SEI). We therefore describe the SEI with one R/Q element (shown in Fig. 1) for both experimental setups, the metal foil electrodes (Fig. 1a) as well as the graphite electrodes (Fig. 1b), with the latter additionally containing charge transfer and diffusion phenomena, since graphite allows a faradaic reaction. The interpretation of seeing only one semi-circle will be discussed at a later part of this publication.
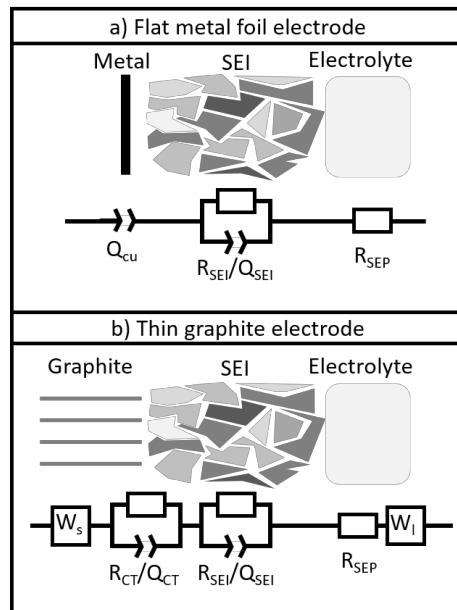
Figure 1 Equivalent circuit models for the SEI analysis. a) metal foil equivalent circuit containing a constant phase element for the capacitive metal/SEI interface (Q_{cu}), one R/Q element describing the SEI and the separator high frequency offset (**R_{sep}**). b) thin graphite electrode equivalent circuit with an R/Q element for each the charge transfer kinetics and SEI resistance, as well as the solid and liquid Warburg elements and the separator solution resistance.

162

***Influence of the solid electrolyte interphase on EIS spectra.*—** This subsection describes the EIS analysis of copper/nickel foil which have undergone SEI formation. All data presented here were recorded either before or after three formation cycles. This analysis serves to show the impact of the SEI on impedance spectra in the absence of faradaic reactions. Fig. 2a shows the formation procedure of the metal foil electrodes. After formation, EIS spectra on the metal foils were recorded every 200 mV from 2 V to 0.2 V and back to 2V for 3 cycles with a 15 min potential hold before each measurement (potential stepping shown in Fig. 3a). Fig. 2b shows exemplary impedance spectra of a copper foil before formation (grey) and after formation in LP57 (dark green) during the first potential stepping cycle. Before formation the impedance response is dominated by the capacitive behavior of the Cu foil and shows no other distinguishable features. After formation a semi-circle appears, which is a result of the SEI formation and has been observed and analysed similarly in previous publications.[8,11–14] Since no faradaic process is possible at the metal foil, it can be described by a capacitive element alone (Fig. 1a), whereas the SEI is represented by an R/Q element, visible as a depressed semi-circle (but overlapped by the capacitive branch).
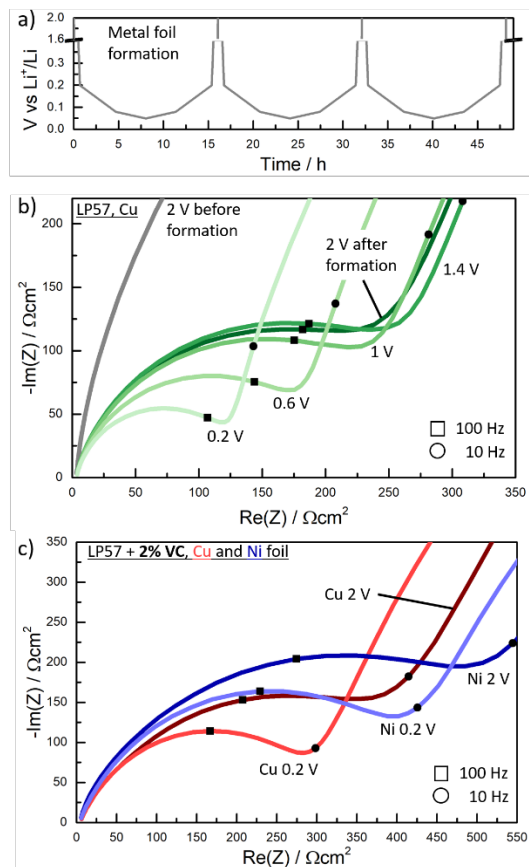
Figure 2 Metal foil impedance analysis. All data was measured either before or after the formation procedure shown in a) (details in the experimental section). b) Nyquist plots of the Cu foil electrode measured in LP57 at different potentials. All EIS curves measured after three formation cycles except the grey curve c) Cu and Ni foil measurements in LP57 + 2% VC after formation at the highest (2 V) and lowest (0.2 V) potential measured.

At 2 V (vs Li^+/Li) after formation, the SEI resistance shown in Fig. 2b is highest with ~250 Ωcm^2 and does not change significantly between 2 and 1 V. Only below 1 V the resistance starts to significantly change and decreases, shown exemplary in the 0.6 V and 0.2 V spectra, the latter reaching a minimum of ~115 Ωcm^2. A similar behavior was observed when VC was added to the electrolyte (Fig. 2c, red), with the highest resistance on the Cu foil at ~350 Ωcm^2 and the lowest resistance ~270 Ωcm^2. Additionally to the Cu foil, Ni foil was also measured which showed the same qualitative behavior as Cu (Fig. 2c, blue) but with higher overall resistances, e.g. due to differences in surface roughness.

Fig. 3 shows the full analysis of the Cu foil measurements over the whole potential stepping range of the impedance spectra which were fitted with the equivalent circuit shown in Fig. 1a. Fig. 3b shows the resistance extracted from the spectra fit. The analysis shows a reversible change in SEI resistance for both LP57 (green squares) and LP57 +2% VC (red triangles). Starting from 2V the resistance is almost constant between 2V and 0.8 V but changes more drastically between 0.8 V and 0.2 V. On the reverse pathway, changing the potential from 0.2 V to 2 V this step behavior is not visible anymore, and the change in resistance is close to linear, resulting in a hysteresis in SEI resistance with potential. The LP57 resistance is continuously increasing over time by ~60% when comparing the resistances at 2V and by 40% for the 0.2 V resistances, i.e., the gap between 2V and 0.2 V is widening, making the pathway dependent analysis more difficult. The addition of VC results in higher overall resistances but the change in resistance over cycling is minimal and the SEI thus appears significantly more stable. The VC data shows the same path dependency with a minimal change in resistance from 2V to 0.8 V, a strong change from 0.8 V to 0.2 V and again a linear change on the reverse pathway from 0.2 V to 2 V. Additional information can be gained when analyzing the two capacitances, Q_{sei} and Q_{Cu}, although such an analysis must be done with caution, as it is not clear where Q_{sei} arises. Viewing the SEI as a classical solid electrolyte, it can be seen as a series of R/Q elements and thus the calculated capacitance can be viewed as an effective capacitance of the entire layer rather than pinpoint a specific interface. Additionally, the capacitance could arise at the SEI/electrolyte interface, which would be in parallel to the desolvation resistance, i.e., the resistance describing the transfer of solvated Li^+ from the electrolyte into the SEI, a process which requires the stripping of the solvation shell. As there is only one semi-circle visible, the desolvation resistance and SEI resistance are either not discernible in their frequency (i.e., are present in the same timescale) or one of the two is negligibly small.

Seeing as the SEI resistance is greatly influenced by the addition of additives, a desolvation resistance is ruled out as a possible source in our analysis. Analyzing the SEI capacitance (Fig. 3c) shows a similar potential dependent trend, as however expected for a double layer capacitance, but only changes by ~20% between the highest and lowest potential for both samples. The capacitances also do not exactly track the change in resistance. Before formation, the copper foil capacitance (at the Cu/electrolyte interface) showed a value of 5 ± 0.2 $\mu Fs^{\alpha-1}$, a value consistent with the low geometric surface area of the 0.94 cm^2 copper film. After formation, the capacitance at the Cu/SEI interface (~ 0.4 mFs$^{\alpha-1}$, see Fig. 3d) is two orders of magnitude higher than at the before measured Cu/electrolyte interface and more than an order of magnitude higher than the SEI capacitance, which could be explained by the lack of a solvation shell for the conducting ions at this interface, possibly allowing a higher charge carrier (Li$^+$) density. When changing the potential, Q_{cu} very closely tracks the simultaneous change in resistance, best visible in the measurement containing VC.

The interpretation of this data should be done cautiously as the conduction mechanisms of the SEI are not well understood. Assuming that the only mobile charge in the SEI is Li$^+$,(i.e., a transference number (t$_+$) of one, typical for a solid electrolyte) both changes in capacitance must be connected to an increase in charge carriers (Li$^+$) in the SEI and at the Cu/SEI interface, with the only source available being the electrolyte. Similar to the field effect in semiconductors (see e.g. Ref [26]) or the space charge layer at an electrode/solid electrolyte interface (see Refs. [27–29]) where an applied potential changes the conduction resistance through the material via the accumulation of charges, accumulated Li$^+$ from the electrolyte could cause a change in resistance in the SEI. This also has implications on the analysis of SEI resistances on metal interfaces for formation studies. When performing formation trials by holding electrodes at various constant potentials, the impedance

166

10

analysis on the individual electrodes needs to then be performed at the same potential (practically a higher potential) to exclude any potential dependencies of the SEI in the measured resistance.
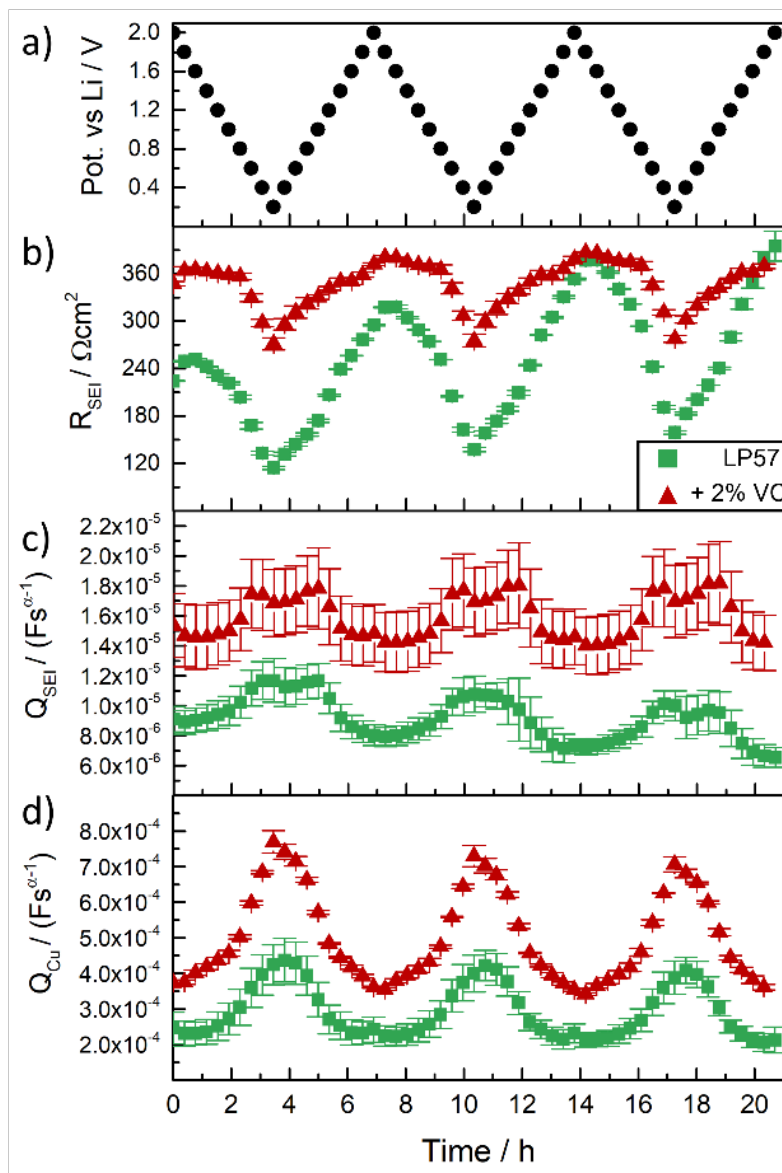
Figure 3 Analysis of the impedances on Cu foil using only LP57 (green squares) or additionally 2% VC (red triangles). Electrodes measured after three formation cycles via reference electrode a) potential steps for the impedance analysis; b) SEI resistance extracted from the spectrum fit; c) capacitance of the SEI (semi-circle capacitance in the spectrum); d) capacitance at the Cu/SEI interface.

Influence of the solid electrolyte interphase on impedance spectra of graphite anode.—

When analyzing graphite EIS spectra, the analysis of the kinetic resistance of the electrode

167

is more complex than a metal foil as the graphite allows the insertion of Li^+ and thus includes additional R/Q element to consider. To understand and deconvolute the SEI resistance (i.e., transport through the SEI) from the actual intercalation resistance (intercalation into graphite at the graphite/SEI interface), we analyzed the EIS spectra of thin graphite electrodes measured between 2V and 0.04 V. At 2 V, the available capacity from graphite electrodes is zero and thus must show a practically infinitely large kinetic resistance (blocking conditions),[25,30] a similar behaviour as the previously discussed metal foils. At lower potentials though, the kinetic resistance must decrease when the intercalation into the material becomes viable. The aim of this analysis is to show the change in EIS spectra with a step-by-step reduction in potential to track the shrinking kinetic resistance features as well as the SEI features.
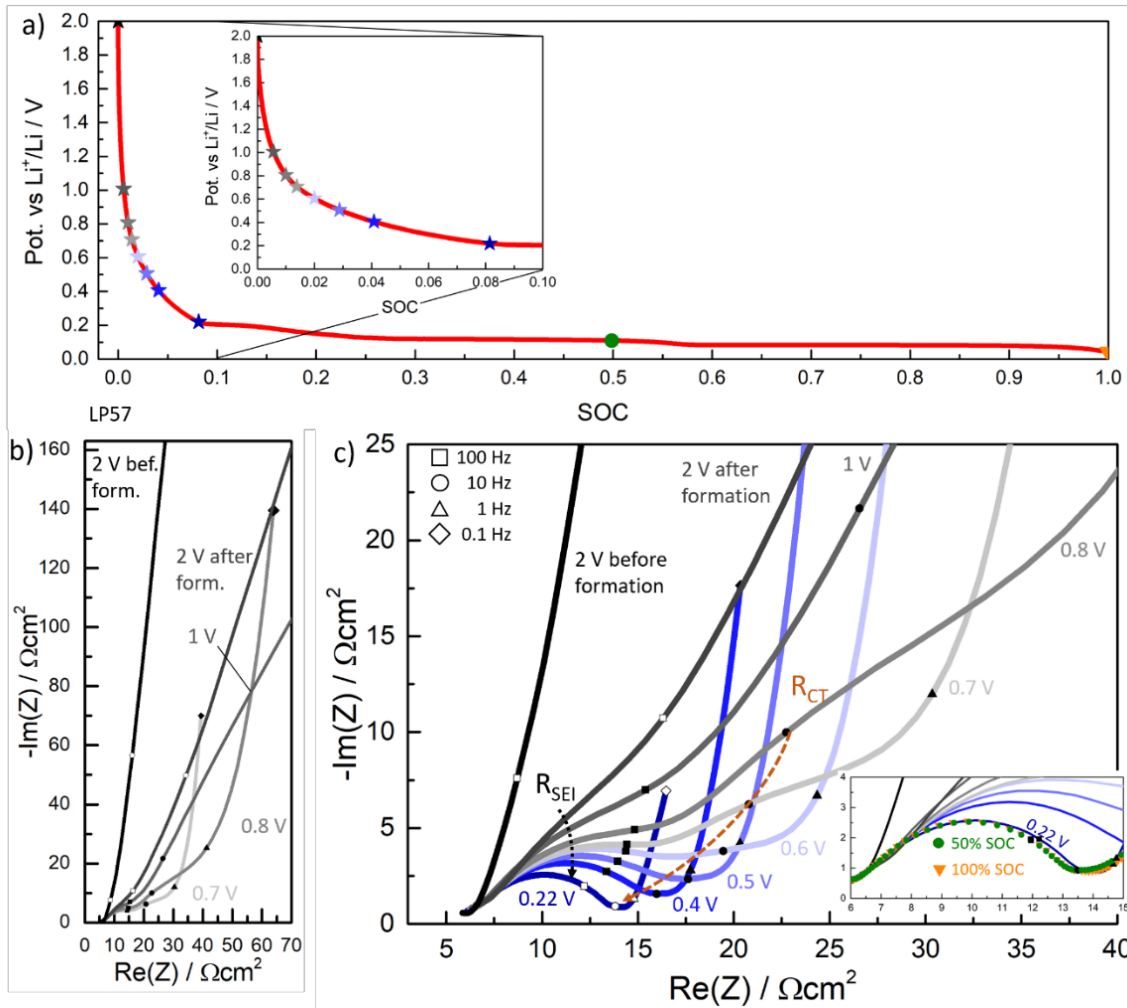
168

Figure 4 Graphite impedance analysis. a) Graphite potential with the zoom into the first 10% SOC, with markings at which impedance measurements are shown. b) Graphite impedance spectra before and after formation between 2 V and 0.7 V vs Li$^+$/Li; c) Zoomed in graphite impedance spectra showing both SEI and charge transfer resistance and their evolution between 2 V and 0.22 V. The bottom right zoom also shows the impedance at 50 and 100% SOC. Graphite electrode of ~0.3 mAh/cm^2 measured via GWRE in T-cell three electrode setup.

Figure 4a shows the graphite potential profile, with the inset showing the first 10% SOC zoomed in. Fig 4b and c show the Impedance data of a graphite electrode with an areal capacity of ~0.3 mAh/cm^2. The low capacity was chosen to avoid influences from the electrode pore resistance, which can be considered negligible in this analysis. Before formation at 2 V (black) the impedance shows a purely capacitive behavior without any significant pore resistance, as expected for a thin electrode. The capacitance of the

169

electrode before formation was found to be ~0.4 $mFs^{\alpha-1}$. After formation the electrode still shows a capacitive (blocking) behavior but includes the underlying SEI resistance semi-circle, just like the copper foil experiment. The SEI semi-circle, visible in the region above 100 Hz, is not as pronounced compared to the copper foil measurement, as it is superimposed with the capacitive branch of the graphite/SEI interface after formation. With ~0.71 $mFs^{\alpha-1}$ (meas. at 2 V) the increase in capacitance from the graphite/electrolyte to the graphite/SEI interface is less than a factor 2, significantly different compared to the ~100-fold increase seen for the Cu foil. Additionally, the SEI capacitance is around 0.35 $mFs^{\alpha-1}$, only a factor 2 lower than the graphite/SEI interface, thus resulting in a stronger overlap of the semi-circle and capacitance resulting in a more stretched semi-cirlce and a lesser distinction between the two spectral features. The SEI resistance at 2 V was found to be ~11 Ωcm^2. At this potential the charge transfer resistance is too high to allow the faradaic reaction to occur but decreasing the potential should reduce the charge transfer resistance and eventually allow the deconvolution of the two resistances. Between 2V and 1V the impedance analysis only showed minor changes to the spectra since the electrode is still under blocking conditions at these potentials. At 1 V the SEI semi-circle is better visible due to the increased low frequency capacitance of the electrode, which should still reflect the graphite/SEI interface. This potential also marks the onset of the faradaic reaction, below which the majority of the exchanged charge can be associated to a reaction rather than capacitive effects, visible in the distinct change in potential slope around this potential (see Fig. 4a). While at higher potentials the capacitance could be associated with an electrochemical double-layer capacitance, the graphite now allows a limited reaction which shifts the low frequency capacitive behavior to the solid diffusion and the exchanged faradaic charge, and thus the low frequency capacitive behavior becomes a function of the locally probed potential slope.

The impedance at 0.8 V now shows a second semi-circle around 10 Hz (i.e., one order of magnitude higher in capacitance) which we attribute to the charge transfer reaction. Both semi-circles are still stretched due to the overlapping solid diffusion resistance. Those features also don't allow a proper fitting of the two semi-circles, as the underlying diffusion resistance stretches the spectrum to an unknown amount, giving rise to a multitude of possible spectra. Thus the analysis of these features is only of a qualitative nature. At 0.7 V both semi-circles are still visible, with the apparent top frequency point of the R_{ct} semi circle of ~ 10 Hz. Upon further decreasing the potential this semi-circle is not visibly anymore and is superimposed with the diffusion resistance. When tracking the 100 Hz and 10 Hz datapoints over the course of the measurements, it appears as if the kinetic resistance becomes negligibly small and from 0.4 V onward, corresponding to ~ 4% SOC, the majority of the remaining kinetic resistance of the graphite electrode is the SEI resistance. A possibility for the low value of R_{ct} could be the local Li^+-concentration at the Graphite/SEI interface. In liquid electrolytes, following Butler-Volmer, an increased salt (i.e., available Li^+) concentration decreases the kinetic resistance. Similarly here, without a solvation shell Li^+ might accumulate in greater concentration at the graphite/SEI interface, which in turn drastically decreases the charge transfer resistance and is visible in the distinctly larger capacitance. This follows the above mentioned theory about accumulating charge-carriers similarly also decreasing the SEI resistance, albeit to a much lesser degree.

The inset in Fig 4c shows the impedance spectra at 8% (0.22 V), 50% and 100% SOC which shows no change in resistance. This is in line with the assumption that the resistance is in fact SEI and not the charge transfer kinetics, which e.g. in cathodes show a strong U-shaped SOC-dependence.[30,31] The charge transfer kinetics might show a similar U-shape, which is just not visible in the spectra as R_{ct} is vanishingly small for most SOCs. This also

explains why the graphite electrode cannot be brought to blocking conditions at 100% SOC. The potential profile does not appear steep enough to warrant an assumption of a blocking behavior where R_{ct} increases drastically, and with the SEI resistance practically representing the total kinetic resistance of the anode, its resistance appears to be SOC independent. The graphite kinetics can therefore be considered constant over SOC, as they are fully made up of the SEI resistance in any practical use. The impedance of the graphite electrode can also, for all practical applications, be described by one semi-circle instead of two,, which simplifies any analysis on porous graphite electrodes. In this case, from 0.22 V and lower, the SEI resistance is ~7 Ωcm^2 and therefore ~40% lower than the resistance measured at 2 V. Its capacitance is now ~0.45 $mFs^{\alpha-1}$ with an α value of 0.75 and a top frequency of ~350 Hz. Among others, Gasberscek et al.[24] have shown that the SEI is sometimes associated with a semi-circle visible in the kHz frequency region in full cell measurements, which in fact is rather associated with the electrical contact resistance of the cathode.[25] The SEI resistance measured here also lies in the higher frequency range in the range of 0.1 kHz, sufficiently different to make a distinction between the two if measured in a full cell. The capacitance of the graphite/SEI interface cannot be measured accurately but can be approximated by estimating an R/Q element of 0.5 Ωcm^2 charge transfer resistance with a top freqeuency of 10 Hz, an α of 0.9, and using $Q = 1/((2\pi f)^{\alpha} \times R)$ (see figure 4c, dark blue spectra corresponding to 0.22 V). Such calculation would yield a capacitance of 24 $mFs^{\alpha-1}$, one order of magnitude higher that the SEI capacitance. In our setup the charge transfer semi-circle is only visible due to the low resistance of the SEI in LP57. Adding VC to the electrolyte starkly increases the resistance, as seen in Fig. 5. Here the 2 V impedance before and after formation better shows the SEI semi-circle, giving ~ 64 Ωcm^2 SEI resistance. The 0.8 V impedance shows no second semi-

circle, which is not surprising as it can be noted from Fig. 4 that the estimated R_{ct} at 0.8 V

appears not larger than 20 Ωcm^2 and is additionally strongly distorted by the underlying

capacitive feature. In Fig. 5 it is therefore most probably superimposed with the other

resistances to the point that its features are not visible anymore. Between 0.4 V and 100%

SOC, only the SEI semi-circle is visible, which in the latter case gives a resistance of ~ 45

Ωcm^2, i.e., decreased by 30% from the resistance measured at 2 V. The significantly

different increase in resistance of the SEI with the addition of VC suggests that its

resistance is mostly due to the conduction of ions into and through the SEI but not a

desolvation/stripping of the EC solvation shell from the Li$^+$ directly, as this process should

be independent of the SEI composition.
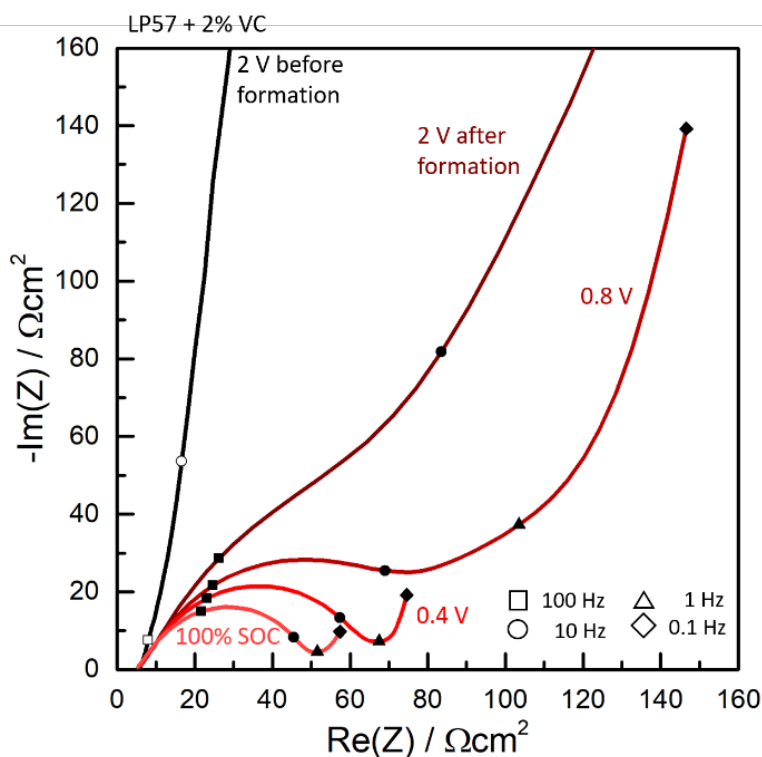
Figure 5: Graphite impedance analysis similar to Figure 4c but using LP57+2% VC. As expected, the addtion of 2% VC leads to higher SEI resistance to the point where the second semi-circle corresponding the charge-transfer resistance in not longer distinctly visible (e.g. compare 0.8 V spectra with the impedance spectra plotted in Figure 4c at the same OCV). Graphite electrode of ~0.3 mAh/cm^2 measured via GWRE in T-cell three electrode setup.

Kinetic behavior of the electrode in the presence of the SEI.— Having a protective layer made of solid electrolyte around an electrode raises the question of the kinetic behavior of the electrode, as the actual reaction is still only taking place at the electrode/SEI interface. For example, in the case of a "classical" solid electrolyte (SE) (i.e., fixed amount of charges in the SE which don't allow concentration changes/gradients), which is several μm in thickness, the notion of an adjacent SE/liquid interface influencing the bulk properties of the SE would be questionable and the reaction kinetics should therefore be independent of the properties of the liquid electrolyte. The SEI however is only a few nm in thickness with a possible change in Li^+ in the solid electrolyte, as shown above. Hence the question of the effect of the electrolyte on the SEI properties and subsequently on the charge transfer reaction arises.

To better understand the kinetic behavior of the SEI we performed experiments using different electrolyte concentrations. For this, graphite electrodes underwent three formation cycles in a custom mixed LP57 electrolyte (used for the analysis in Fig. 6 and Fig. 7a; see experimental section for further details) to ensure that the SEI composition was the same in all cases. The graphite was fully delithiated to 2 V, harvested, rinsed in diethyl carbonate and reassembled in 0.03, 0.1, 0.5, 1, 2, 2.5 and 3M custom mixed $LiPF_6$ in EC:EMC 3:7 (i.e., the solvent mixture of LP57 with varying salt concentration). The electrodes were then brought to 100% SOC and their impedance was measured at 5, 20, 30 and 40°C. Fig. 6a shows the extracted SEI resistance at 20°C of the electrodes. The analysis shows that the electrolyte change has the same effect on the SEI resistance as predicted by the Butler-Volmer kinetics with a kinetic transfer coefficient α_a of 0.5 $(1/R) \propto c_l^{0.5}$ shown in the dotted line using the 1M resistance as reference point). This shows that there is a link between the electrolyte and the SEI resistance, as also observed by Lu et al.,[9] who showed

that there is an exchange between the electrolyte and the SEI. Temperature dependent measurements (Fig. 6b) show that for both higher and lower electrolyte concentrations the activation energy is the same (~ 60 kJ/mol indicated by the grey dashed lines).
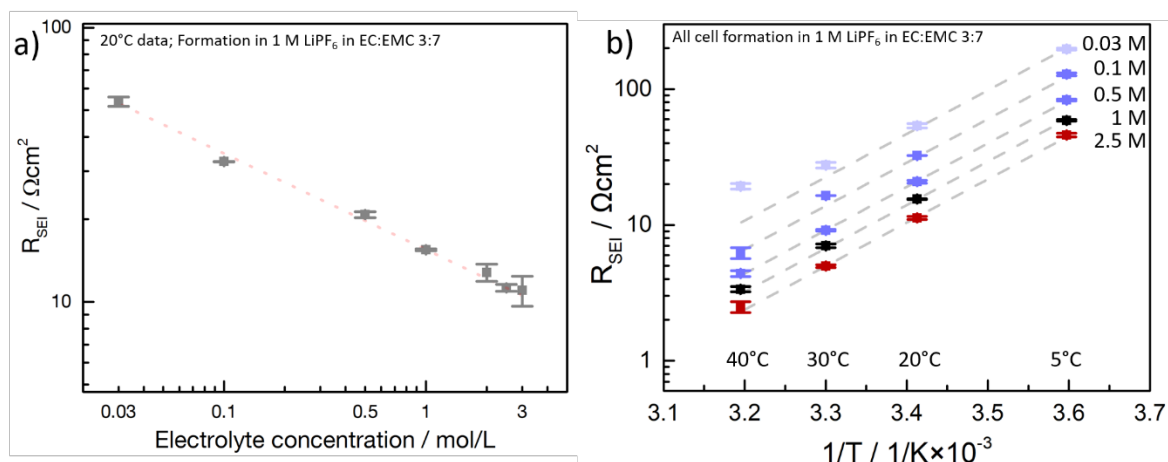

Figure 6 SEI resistance extracted from EIS measurements. All cells underwent formation in a 1M solution of LiPF6 in EC:EMC 3:7, harvested, washed and reassembled in the respective electrolyte. a) extracted SEI resistance at 20°C and 100% SOC over concentration. The dotted line represents the change in resistance assuming $1/R_{ct} \propto c_l^{0.5}$. b) temperature dependent measurements showing an activation energy for selected concentrations to be ~60 kJ/mol, indicated by the dashed lines.

Fig 7a shows the corresponding impedance spectra of the data shown in Fig. 6a, which was collected at 20°C and in a frequency range from 30 kHz to 50 mHz. The data is shifted in the real axis to allow a better comparison of the electrodes. The increase in resistance with decreasing electrolyte concentration is clearly visible. Fig. 7b shows electrodes which were also measured in the respective electrolyte, (here at 25 °C) but, unlike the data in Fig. 7a, also underwent their formation in the respective electrolyte (commercially available electrolyte of the same nominal composition). The analysis shows a very similar trend, with an increased resistance for the electrode in the 0.1 M electrolyte of a factor ~3.5 which is close to the expected value of 3.16 for if the resistance was to follow the relationship $\frac{1}{R} \propto c_l^{0.5}$. This relationship would also predict a resistance decrease of 40% for the 2.5 M

electrolyte, whereas here the resistance appears decreased by ~60 %. Correlating the results from Fig. 7a to Fig. 7b should be done cautiously as the formation mechanism for both electrodes may be fundamentally different when the electrolyte salt concentration during the formation procedure is drastically different. The change in concentration may change the SEI formation kinetics similarly as a change in temperature. As this cannot be proven in the context of this work, the mechanism behind the findings in Fig. 7b requires further analysis.
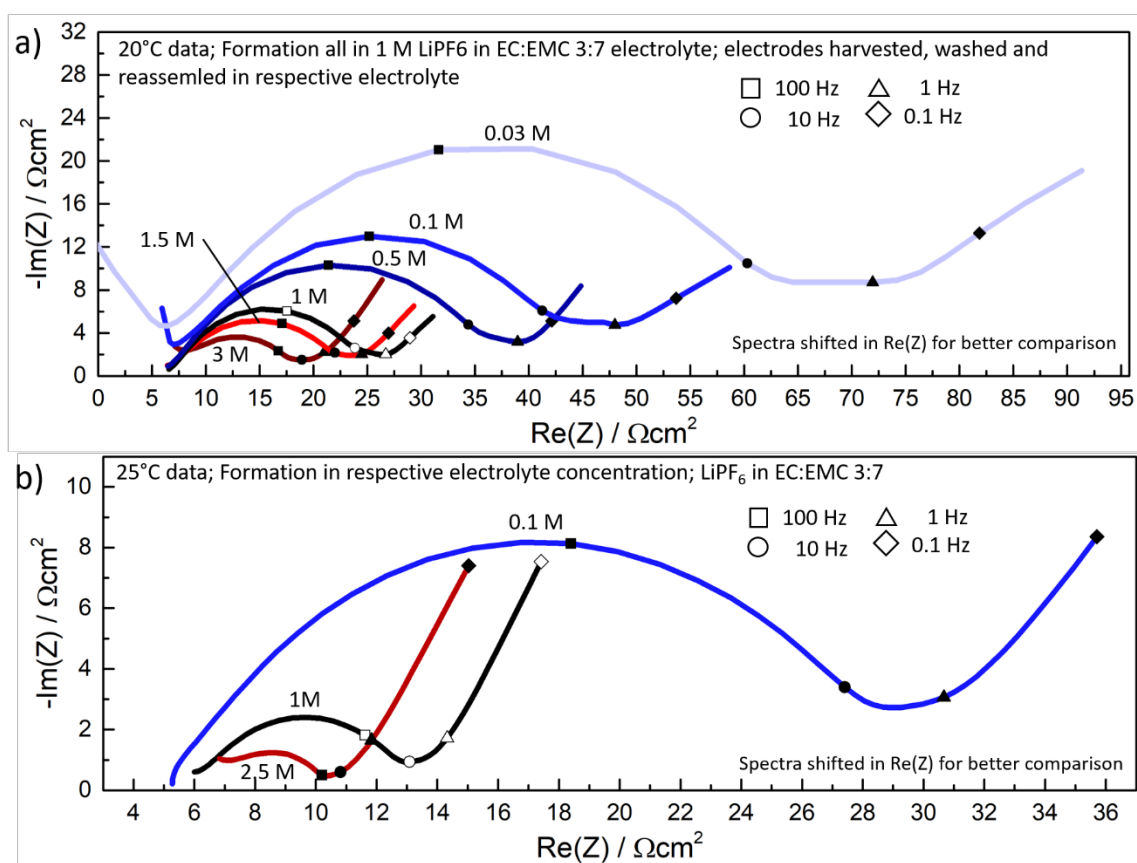
Figure 7 a) EIS spectra of the data presented in Fig. 6a; electrodes were preformed in 1M LiPF$_6$ in EC:EMC 3:7 (LP57), harvested, washed and re-measured in the respective custom mixed elcetrolytes. Data shown at 20°C and 100% SOC. b) Impedance measurements of electrodes with the formation in the respective electrolyte (commercially available mixtures of the same composition as Fig. 7a). All spectra were shifted in the x-axis to allow a better comparison of the data.

All of the SEI impedance analyses only showed one semi-circle for the SEI resistance, yet there are multiple mechanisms connected to the SEI which are briefly discussed here.

Possible sources of resistance are the desolvation (stripping of the solvation shell), Li^+ transport through an outer SEI and subsequently an inner SEI, and possible inter- and intra grain conduction mechanisms. Given the large influence that small electrolyte additives have on the SEI resistance suggests one dominant resistive feature. The resistance of a porous SEI can also be described as minimal when estimating the following model: Conservatively assuming e.g. a porosity (ε) of 10% for an outer SEI (which could be described as barely porous) filled with electrolyte (conductivity σ = 8.9 mS/cm) and thickness (d) of 1μm (excessively large for an SEI) on a $1cm^2$ smooth electrode surface area (A) with tortuosity (τ) 5, using the relationship $R = \frac{\tau}{\varepsilon}\frac{d}{\sigma A}$ gives a resistance of $\approx 0.5\ \Omega$ for such a hypothetical outer SEI. The resistance would be significantly less than any measured value reported in our work. This does not negate the existence of such a layer, but the low resistance of a thin layer which can be described as porous in the sense that it might be partially filled with electrolyte would make it virtually invisible to the measurement.

Another important aspect to consider is the timeframe in which the above measurements take place. While in the absence of an SEI a change in Li^+ concentration should directly change the charge transfer resistance, the interactions between the SEI and the electrolyte may take a significant amount of time, as shown by Lu et al.[8] where the interactions of the SEI with the electrolyte was on the order of several minutes. In our measurements the cells were harvested in their delihiated state and measured at the earliest after the 10h charging step, giving ample time for any interactions between the SEI and the electrolyte. For many practical applications where changes in the electrolyte salt concentration might actually occur, e.g., fast charging or discharging of a cell, the SEI resistance might not actually

behave as described in Fig. 6 if the timeframe of the measurement is shorter than the required interaction time.

***Impact of SEI resistance on Li-plating.*—** If the measured resistance (i.e. the semicircle reistance as summarized in Fig. 6a) actually corresponds to the SEI resistance, it would therefore also impact the Li-plating overpotential. Li-plating is not restricted to homogeneous plating on the graphite surface area, as the plating forms dendrites which offer additional surface area for the plating reaction, But the initiation of the plating reaction will require overcoming the SEI resistance. For this Li-plating analysis, two uncompressed, thin graphite electrodes with a capacity of 0.35 mAh/cm^2 underwent formation with LP57 and LP57+2% VC. Fig. 8a shows the EIS spectrum of the two electrodes at 100% SOC, here not normalized to the surface area so their resistance can be directly correlated to the overpotential from the later applied 1 mA plating current. As also shown from the previous analysis, the addition of VC increases the SEI resistance drastically. After the EIS analysis the electrodes were brought to 0.01 V and kept at this potential for 1 h to ensure that the graphite is at its maximum SOC without causing Li-plating. Then the 1mA lithiation current was applied, which should cause an overpotential of 1 mV/Ω.
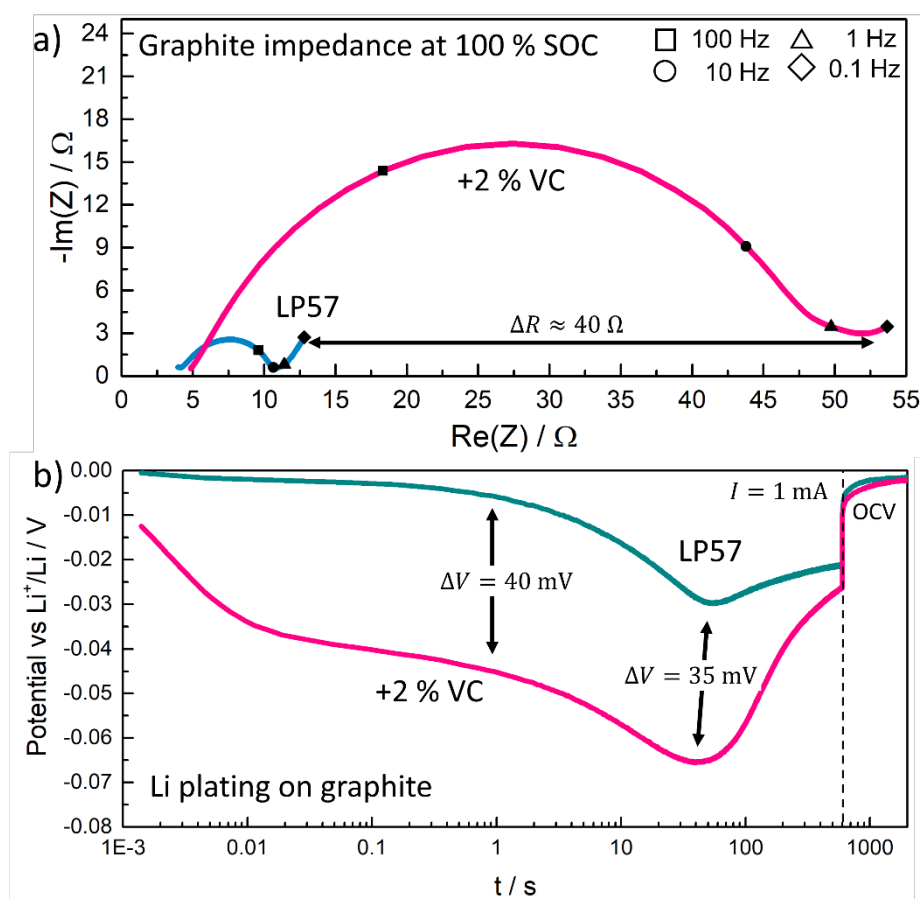
Figure 8: a) Nyquist plot showing the impedance of graphite electrode of 0.35 mAh/cm² in LP57 and LP57+2% VC electrolyte at 100% SOC. b) Potential response of the graphite electrodes after a potential hold at 0.01 V vs Li+/Li and a subsequent 1mA lithiation current to force Li-plating on the electrode. The difference in the mesured resistance is clearly visible as a difference in plating current. Both electrodes appear to have a similar nucleation overpotential. Potential measured via GWRE in a T-cell three electrode setup.

Fig. 8b shows the electrode potential after the current was applied. The capacitive effect of the R/Q element is visible at time scales below 0.01 s. At the 1 s mark, the 40 mV difference in overpotential corresponds to the 40 Ω difference in SEI resistance for the electrodes. Considering the starting potential of 0.01 V, the net initial overpotential of the electrode after 1 s is 16 mV and 55 mV for the LP57 and LP57+2% VC sample, respectively, correlating with the total cell resistance measured in EIS. Both overpotentials increase up until ~40s and then decrease, as expected for an increased surface area from the ongoing Li-plating. The difference in the peak overpotential (occurs at ~40 s in this case) is ~35 mV

179

and the difference between the potentials decreases as the plating continues, most probably caused by an increase in surface area. A higher SEI resistance therefore closely correlates to the measured Li-plating overpotential at early stages of Li-plating. A similar observation was made by Liu et al.[32] who have shown that higher anode resistances correlate with a later onset of Li-plating in a full cell setup, but did not employ a reference electrode to track the overpotential. Comparing the 1s overpotential from the maximum peak overpotential at ~40 s leads to an additional overpotential of ~23 mV and 20 mV for LP57 and the +2% VC samples (i.e., a resistance of 23 Ω or 20 Ωcm^2). The electrolyte diffusion resistance can be assumed equal for both measurements which suggests the Li-plating nucleation overpotential (at the electrode/SEI interface) is independent of the SEI resistance and the SEI only acts as an offset to this reaction.

Conclusions

The influence of the solid-electrolyte-interphase (SEI) on impedance spectra and its kinetic behavior is described in the context of this work. All analysis was done before or after three formation cycles, highlighting the dynamic nature of the SEI resistance. We first showed how the SEI resistance on metal foils changes with the applied potential even after the formation was done. The resistance decreased for decreasing potential, which was correlated to changes in the SEI capacitance and the capacitance at the Cu/SEI interface, showing how the SEI capacitance only changes very little but the capacitance at the Cu electrode closely tracks the changes in resistance of the SEI with potential. A mechanism of changing charge carriers which change both the capacitance and the resistance has been proposed. Further analysis of thin graphite electrodes shows that the SEI resistance is the

dominating kinetic resistance for all practical applications, and the actual charge transfer resistance is vanishingly small.

We further studied the effect of electrolyte concentration on the SEI resistance. Electrodes which have been pre-formed in a 1M LiPF$_6$ concentrated electrolyte still exhibited a concentration dependent resistance when measured between 0.1 and 3 M concentrated electrolytes following the relationship $\frac{1}{R_{sei}} \propto c_l^{0.5}$. This was explained by the interaction of the electrolyte with the SEI which has been described in literature.[9] Performing the graphite formation in differently concentrated electrolytes showed a similar trend in resistance. The SEI resistance was then correlated to the Li-plating overpotential. It was found that the plating reaction initially requires overcoming the SEI resistance, but the overpotential for the plating nucleation was the same independent of the SEI resistance.

Acknowledgments

References

1. E. Peled, *The Electrochemical Behavior of Alkali and Alkaline Earth Metals in Nonaqueous Battery Systems—The Solid Electrolyte Interphase Model*, (1979), p. 2047–2051.

2. E. Peled, D. Golodnitsky, and G. Ardel, *Advanced Model for Solid Electrolyte Interphase Electrodes in Liquid and Polymer Electrolytes*, (1997), p. L208–L210.

3. S. K. Heiskanen, J. Kim, and B. L. Lucht, *Generation and Evolution of the Solid Electrolyte Interphase of Lithium-Ion Batteries*, Elsevier Inc., (2019), p. 2322–2333.

4. A. L. Michan, M. Leskes, and C. P. Grey, *Voltage Dependent Solid Electrolyte Interphase Formation in Silicon Electrodes: Monitoring the Formation of Organic Decomposition Products*, (2016), p. 385–398.

5. L. Wang, A. Menakath, F. Han, Y. Wang, P. Y. Zavalij, K. J. Gaskell, O. Borodin, D. Iuga, S. P. Brown, C. Wang, K. Xu, and B. W. Eichhorn, *Identifying the components of the solid–electrolyte interphase in Li-ion batteries*, Springer US, (2019), p. 789–796.

6. C. Delacourt, A. Kwong, X. Liu, R. Qiao, W. L. Yang, P. Lu, S. J. Harris, and V. Srinivasan, *Effect of Manganese Contamination on the Solid-Electrolyte-Interphase Properties in Li-Ion Batteries*, (2013), p. A1099–A1107.

7. Z. Zhuo, P. Lu, C. Delacourt, R. Qiao, K. Xu, F. Pan, S. J. Harris, and W. Yang, *Breathing and oscillating growth of solid-electrolyte-interphase upon electrochemical cycling*, Royal Society of Chemistry, (2018), p. 814–817.

8. P. Lu, C. Li, E. W. Schneider, and S. J. Harris, *Chemistry, impedance, and morphology evolution in solid electrolyte interphase films during formation in lithium ion batteries*, (2014), p. 896–903.

9. P. Lu and S. J. Harris, *Lithium transport within the solid electrolyte interphase*, Elsevier B.V., (2011), p. 1035–1037.

10. A. Zaban, E. Zinigrad, and D. Aurbach, *Impedance spectroscopy of Li electrodes. 4. A general simple model of the Li-solution interphase in polar aprotic systems*, (1996), p. 3089–3101.

11. H. Schranzhofer, J. Bugajski, H. J. Santner, C. Korepp, K. C. Möller, J. O. Besenhard, M. Winter, and W. Sitte, *Electrochemical impedance spectroscopy study of the SEI formation on graphite and metal electrodes*, (2006), p. 391–395.

12. W. Huang, D. T. Boyle, Y. Li, Y. Li, A. Pei, H. Chen, and Y. Cui, *Nanostructural and Electrochemical Evolution of the Solid-Electrolyte Interphase on CuO Nanowires Revealed by Cryogenic-Electron Microscopy and Impedance Spectroscopy*, (2019), p. 737–744.

13. P. G. Kitz, M. J. Lacey, P. Novák, and E. J. Berg, *Operando investigation of the solid electrolyte interphase mechanical and transport properties formed from vinylene carbonate and fluoroethylene carbonate*, (2020), p. 0–8.

14. P. G. Kitz, M. J. Lacey, P. Novák, and E. J. Berg, *Operando EQCM-D with*

Simultaneous in Situ EIS: New Insights into Interphase Formation in Li Ion Batteries, (2019), p. 2296–2303.

15. S. Kranz, T. Kranz, A. G. Jaegermann, and B. Roling, *Is the solid electrolyte interphase in lithium-ion batteries really a solid electrolyte? Transport experiments on lithium bis(oxalato)borate-based model interphases*, Elsevier, (2019), p. 138–146.

16. S. Solchenbach, X. Huang, D. Pritzl, J. Landesfeind, and H. A. Gasteiger, *Monitoring SEI Formation on Graphite Electrodes in Lithium-Ion Cells by Impedance Spectroscopy*, The Electrochemical Society, (2021), p. 110503.

17. R. Petibon, E. C. Henry, J. C. Burns, N. N. Sinha, and J. R. Dahn, *Comparative Study of Vinyl Ethylene Carbonate (VEC) and Vinylene Carbonate (VC) in LiCoO 2 /Graphite Pouch Cells Using High Precision Coulometry and Electrochemical Impedance Spectroscopy Measurements on Symmetric Cells* , (2014), p. A66–A74.

18. R. Petibon, C. P. Aiken, N. N. Sinha, J. C. Burns, H. Ye, C. M. VanElzen, G. Jain, S. Trussler, and J. R. Dahn, *Study of Electrolyte Additives Using Electrochemical Impedance Spectroscopy on Symmetric Cells*, (2013), p. A117–A124.

19. D. Pritzl, S. Solchenbach, M. Wetjen, and H. A. Gasteiger, *Analysis of Vinylene Carbonate (VC) as Additive in Graphite/LiNi 0.5 Mn 1.5 O 4 Cells* , (2017), p. A2625–A2635.

20. J. Moškon and M. Gaberšček, *Transmission line models for evaluation of impedance response of insertion battery electrodes and cells*, (2021), p. 100047.

21. S. Solchenbach, D. Pritzl, E. J. Y. Kong, J. Landesfeind, and H. A. Gasteiger, *A Gold Micro-Reference Electrode for Impedance and Potential Measurements in Lithium Ion Batteries*, (2016), p. A2265–A2272.

22. R. Morasch, B. Suthar, and H. A. Gasteiger, *Simple Way of Making Free-Standing Battery Electrodes and their Use in Enabling Half-Cell Impedance Measurements via μ -Reference Electrode* , IOP Publishing, (2020), p. 100540.

23. I. V. Krasnikova, M. A. Pogosova, A. O. Sanin, and K. J. Stevenson, *Toward Standardization of Electrochemical Impedance Spectroscopy Studies of Li-Ion Conductive Ceramics*, (2020), p. 2232–2241.

24. M. Gaberscek, J. Moskon, B. Erjavec, R. Dominko, and J. Jamnik, *The importance of interphase contacts in Li ion electrodes: The meaning of the high-frequency impedance arc*, (2008), p. A170.

25. J. Landesfeind, D. Pritzl, and H. A. Gasteiger, *An Analysis Protocol for Three-Electrode Li-Ion Battery Impedance Spectra: Part I. Analysis of a High-Voltage Positive Electrode*, (2017), p. A1773–A1783.

26. B. Razavi, (2001).

27. S. Braun, C. Yada, and A. Latz, *Thermodynamically Consistent Model for Space-Charge-Layer Formation in a Solid Electrolyte*, (2015), p. 22281–22288.

28. J. Haruyama, K. Sodeyama, L. Han, K. Takada, and Y. Tateyama, *Space-charge layer effect at interface between oxide cathode and sulfide electrolyte in all-solid-state lithium-ion battery*, (2014), p. 4248–4255.

29. Y. Nomura, K. Yamamoto, T. Hirayama, S. Ouchi, E. Igaki, and K. Saitoh, *Direct*

Observation of a Li-Ionic Space-Charge Layer Formed at an Electrode/Solid-Electrolyte Interface, (2019), p. 5346–5350.

30. D. Pritzl, J. Landesfeind, S. Solchenbach, and H. A. Gasteiger, *An Analysis Protocol for Three-Electrode Li-Ion Battery Impedance Spectra: Part II. Analysis of a Graphite Anode Cycled vs. LNMO*, (2018), p. A2145–A2153.

31. V. Charbonneau, A. Lasia, and G. Brisard, *Impedance studies of Li+ diffusion in nickel manganese cobalt oxide (NMC) during charge/discharge cycles*, Elsevier B.V., (2020), p. 113944.

32. T. Teufl, D. Pritzl, S. Solchenbach, H. A. Gasteiger, and M. A. Mendez, *Editors' Choice—State of Charge Dependent Resistance Build-Up in Li- and Mn-Rich Layered Oxides during Lithium Extraction and Insertion*, (2019), p. A1275–A1284.

33. Q. Q. Liu, R. Petibon, C. Y. Du, and J. R. Dahn, *Effects of Electrolyte Additives and Solvents on Unwanted Lithium Plating in Lithium-Ion Cells*, (2017), p. A1173–A1183.

184

4 Conclusions

This thesis explored various topics around the application and interpretation of electrochemical impedance spectra measured in Li-ion batteries.

A major advantage in the rapid screening of battery electrodes is the use of half-cells, i.e., using Li-metal as counter electrode. However, as shown in 3.1.1, the use of the gold-wire reference electrode (GWRE) showed artefacts in the EIS spectra when using half-cells. By building a mock-battery out of circuit elements we showed that the artefacts were not caused by any electrochemical phenomena, but by the combination of i) a very high resistance of the GWRE in the range of MΩ and ii) significantly differing impedances of the working and counter electrode, which presumably influenced the circuitry of the potentiostat. This could be mitigated by attaching a free-standing graphite electrode on top of the Li-metal, yielding a low resistance counter electrode at 0V vs Li$^+$/Li while still supplying a practically unlimited lithium inventory for the cell. This setup was used for all following EIS measurements, apart from symmetric cells, in this work.

The simplest analysis of porous battery electrodes is the measurement of tortuosity under blocking conditions in a symmetric cell, as it involves no faradaic reactions and allows the user the quantification of the pore resistance. Usually, the blocking Nyquist plot is used to extrapolate the low- and high-frequency resistance, the difference of which corresponds to 1/3 of the ionic pore resistance (R_{ion}). As shown in 3.1.2, this analysis is only valid for homogeneous distributions of the pore resistance. Using drying trials and energy-dispersive X-ray spectroscopy measurements on electrode cross-sections, we showed that rapid drying of electrodes causes binder migration. The ensuing inhomogeneous distribution of binder can then be linked to an inhomogeneity in the electrode's pore resistance.

As was shown in this thesis, the tortuosity measurement is a measurement with reflective boundary conditions, and thus it is sensitive to inhomogeneities. Higher resistances at the separator interface lead to higher measured electrode resistances, as all the ionic current passes through this interface.

When measuring porous electrodes under faradaic (non-blocking) conditions, the measurement can also be sensitive to inhomogeneities. For such a measurement, it is important to know the ratio of kinetic resistance to the transport resistance, as this ratio determines the electrodes utilization during the EIS measurement. In 3.1.3 it was shown that if the kinetic resistance (R_{ct}) of an electrode is dominating, the electrode is used mostly homogeneously and the Nyquist plot features a prominent semi-circle. However, if the transport resistance (R_{ion}) is dominating, the electrode is only partially used and the EIS measurement is only representative of the part of the porous electrode which is close to the separator interface. Under such conditions, any attempt at correctly fitting the spectra does not yield accurate information about the electrode unless the pore resistance can be determined by an independent measurement.

A comparison between graphite and silicon electrodes gave a good example of how kinetic and transport resistances can limit an electrode's performance, as shown in 3.2.1. Silicon electrodes are generally significantly thinner than graphite electrodes as the use of silicon improves the specific capacity of the electrode. On the other hand, the kinetic resistance of the silicon electrode is higher compared to that of graphite. Thus, when comparing their resistances at different temperatures, silicon electrodes show a higher resistance compared to graphite when measured at low temperatures due to the higher activation energy of the kinetic resistance but show a significantly lower resistance when measured at higher temperatures. An overpotential analysis of charge ratecapability tests at different temperatures highlighted how kinetic resistances create a shift on the OCV curve, while transport resistances cause downward sloping potential profiles.

While the ionic resistance in an electrode can be assumed mostly constant during charge or discharge, the kinetics of the active material usually are not. Their dependency on SOC and electrolyte concentration has been modelled extensively, most commonly using the Newman model, but a thorough study of the kinetic

aspects of active materials is missing. Thus, in 3.2.2 NMC 111 cathode active material was probed for its kinetic resistances, which were then compared to the prevalent theory. In lithium-ion battery modelling, usually a kinetic transfer coefficient of 0.5 is assumed, which leads to symmetric SOC dependent kinetics with a minimum resistance at 50% SOC. The kinetic resistance of NMC 111 was found to follow this trend if its SOC window in the model was defined such that i) 0% SOC being defined as however much lithium could be reinserted into the material at a reasonable current during discharge, to reach a practically fully lithiated material (e.g., a potential of 3.0 V at C/10 current, even though the material could be lithiated more for longer wait times)[100] and ii) 100% SOC being defined as whatever charge could still be extracted from the material's theoretical maximum capacity after the irreversible losses. This was shown to be true whether the material was previously cycled to 4.2, 4.4, or 4.6 V vs Li^+/Li. For the liquid electrolyte concentration dependence, NMC 111 half-cells were cycled in electrolyte made of $LiPF_6$ in EC:EMC 3:7 (wt.:wt.) in salt concentrations c_l between 30 mM and 3 M. The prevalent theory predicts a change in kinetic resistance following $c_l^{0.5}$. This was observed between electrolyte concentrations of 30 mM and ~1.5 M, above which the kinetic resistance increased, contrary to the theory. The trend appeared to show a similar U-shape as the SOC-dependent kinetics, which appears reasonable when considering that the amount of Li^+ which can be inserted/extracted into/out of the electrolyte should be similarly limited as the charge in active materials. An additional low-frequency EIS analysis showed how the NMC diffusion resistance is highest at low SOCs, which in combination with the high kinetic resistance at low SOCs limits the discharge capacity of NMC 111 more than its charge capacity, since during fast charging the kinetics improve with time while during discharging the kinetics slow down.

Attempting a similar analysis on graphite adds the complexity of having the solid electrolyte interphase (SEI) in between the electrolyte and the charge transfer reaction. 3.2.3 shows an EIS analysis on Cu-foil, which gave insight into the dynamic resistance behavior of the SEI, and showed reversible changes in its resistance between 2.0 V and 0.2 V vs Li^+/Li. A decrease in potential came with a decrease in resistance, and, concurrently, an increase in the capacitance measured at the Cu-SEI interface as well as within the SEI. Since an increase in capacitance can only be achieved by an increase in charge density, and assuming Li^+ is the only mobile

charge in the SEI, this data was interpreted as an increase in Li$^+$ within the SEI that would then result in a decrease in resistance. Following this, a very thin graphite electrode with ~0.35 mAh/cm^2 was measured before and after the formation step to identify the two resistances, R_{ct} and R_{sei}, in the EIS spectrum. At 2.0 V vs Li$^+$/Li, R_{ct} is practically infinitely large and the SEI semi-circle resistance is the only one remaining. Stepwise decreasing the potential showed a decreasing second semi-circle, interpreted as a decreasing R_{ct} value, which then became vanishingly small for practical SOCs above 10%. Ultimately, for practical applications, the SEI resistance was the only remaining resistance, especially visible in the significant change in SEI resistance when using VC as additive. Graphite electrodes with the same areal capacity which underwent formation in LP57 were harvested and re-measured via EIS using differently concentrated electrolyte between 0.03 M and 3 M. The analysis showed that the SEI resistance behaves according to $c_l^{0.5}$, which is a somewhat unexpected dependence of the SEI resistance on the electrolyte concentration. Lastly, graphite electrodes formed in LP57 without and with the addition of 2% VC (wt) were tested for their Li-plating overpotential. The overpotential closely tracked the measured SEI resistance, which naturally must be overcome for the Li-plating reaction to occur.

Figure 4.1 shows a sketch summarizing the key findings of this thesis.

In 3.1.1 a setup which enabled half-cell EIS measurements via μ-reference electrode was successfully developed.

Furthermore, the existing understanding and analysis of porous electrodes was expanded. 3.1.2 showed how EIS spectra of blocking electrodes change in spectral shape when becoming inhomogeneous in their binder-, and thus, tortuosity-distribution across the electrode, an effect arising from the electrode production. 3.1.3 further extended the understanding of non-blocking EIS measurements on porous electrodes, which were previously performed under the assumption of dominating kinetic resistances (R_{ct}), to the regime of a dominating transport resistance (R_{ion}) and gave new insights into the electrode's inhomogeneous utilization during the EIS measurement. A practical analysis of this method was shown in 3.2.1, where silicon and graphite electrodes were analyzed for their kinetic and transport resistance, which showed that the difference in geometry (i.e.,

thickness, and thus transport resistance) was a dominating contributor to the charge rate capability difference of the electrodes.
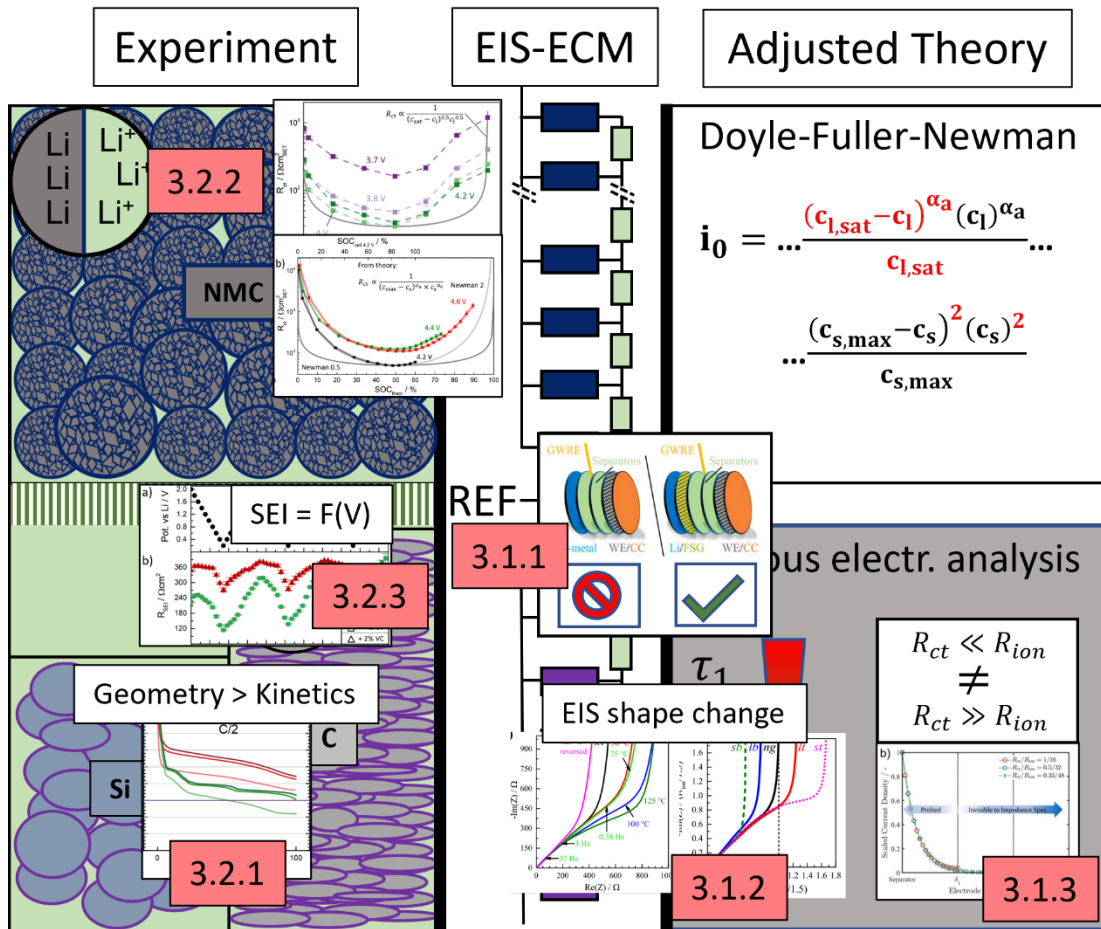

Figure 4.1 Summary of the key findings of this thesis in a variation plot of Figure 1.1: 3.1.1 showed the origin of EIS artefacts when using a μ-reference electrode in half-cell measurements and a practical solution. 3.1.2 illustrated how binder migration causes inhomogeneities in tortuosity and the effect on the blocking EIS spectrum. 3.1.3 showed how the analysis of porous electrodes needs to be adjusted if the ionic resistance dominates the resistive behavior; 3.2.1 showed how the difference in electrode thickness is a major contributor to the performance difference in silicon and graphite electrodes; 3.2.2 gave new insights into how to describe the electrolyte-salt-concentration- and state-of-charge-dependent kinetics of NMC111; 3.2.3 gave insights into the dynamic behavior of the solid electrolyte interphase

Further investigation was done on battery active material kinetics. In 3.2.2 it was shown that NMC 111 kinetics only partly follow the widely used theory. The $LiPF_6$ salt-concentration-dependent kinetics required adjustment in the form of a saturation limit, similarly to the limits for battery active materials, with a concentration saturation limit. The SOC dependent kinetics required adjustments in the transfer coefficient, resulting in larger changes in resistance with SOC compared to the proposed theory. The graphite kinetics analysis shown in 3.2.3

gave insights into the behavior of the SEI, most prominently its dynamic resistance which can change as a function of applied potential or electrolyte salt concentration.

Especially the last two projects, the cathode active material kinetics and the SEI kinetics, should in the future be further studied. For cathode materials, a wider comparison of cathode active material SOC-dependent kinetics could give insight into the mechanism for the SOC-dependent behavior. Materials could include, e.g., $LiFePO_4$, TiS_2 (which is not in use anymore but was the experimental basis of the Newman-model)[9,101] or other materials from the NMC-family. Additionally, further studies on the electrolyte-salt concentration for, e.g., other electrolyte compositions might yield insights into the apparent Li^+-saturation limit of electrolytes which was observed in this work. On the anode side, a similar analysis as was done here for graphite could be conducted for silicon, to understand its resistance dependence on the electrolyte formulation and on the applied potential. Generally, a proper study of the silicon kinetics must be completed to understand the behavior of the partially lithiated material and how to properly model such a system.

References

1. K. Mizushima, P. C. Jones, P. J. Wiseman, and J. B. Goodenough, Li_xCoO_2 (0<x<-1): A new cathode material for batteries of high energy density, *Materials Research Bulletin*, **15**, 783–789 (1980).

2. M. S. Whittingham, Electrical Energy Storage and Intercalation Chemistry, *Science*, **192**, 1126–1127 (1976).

3. Y. Liu, R. Zhang, J. Wang, and Y. Wang, Current and future lithium-ion battery manufacturing, *iScience*, **24**, 102332 (2021).

4. A. Kwade, W. Haselrieder, R. Leithoff, A. Modlinger, F. Dietrich, and K. Droeder, Current status and challenges for automotive battery production technologies, *Nature Energy*, **3**, 290–300 (2018).

5. V. Sulzer, P. Mohtat, A. Aitio, S. Lee, Y. T. Yeh, F. Steinbacher, M. U. Khan, J. W. Lee, J. B. Siegel, A. G. Stefanopoulou, and D. A. Howey, The challenge and opportunity of battery lifetime prediction from field data, *Joule*, **5**, 1934–1955 (2021).

6. W. Wang, J. Wang, J. Tian, J. Lu, and R. Xiong, Application of Digital Twin in Smart Battery Management Systems, *Chinese Journal of Mechanical Engineering (English Edition)*, **34** (2021).

7. N. G. Panwar, S. Singh, A. Garg, A. K. Gupta, and L. Gao, Recent Advancements in Battery Management System for Li-Ion Batteries of Electric Vehicles: Future Role of Digital Twin, Cyber-Physical Systems, Battery Swapping Technology, and Nondestructive Testing, *Energy Technology*, **9**, 1–17 (2021).

8. T. F. Fuller, M. Doyle, and J. Newman, Simulation and Optimization of the Dual Lithium Ion Insertion Cell, *Journal of The Electrochemical Society*, **141**, 1–10 (1994).

9. M. Doyle, T. F. Fuller, and J. Newman, Modeling of Galvanostatic Charge and Discharge of the Lithium/Polymer/Insertion Cell, *Journal of The Electrochemical Society*, **140**, 1526–1533 (1993).

10. J. Moškon and M. Gaberšček, Transmission line models for evaluation of

impedance response of insertion battery electrodes and cells, *Journal of Power Sources Advances*, **7**, 100047 (2021).

11. J. Moškon, J. Žuntar, S. Drvarič Talian, R. Dominko, and M. Gaberšček, A Powerful Transmission Line Model for Analysis of Impedance of Insertion Battery Cells: A Case Study on the NMC-Li System, *Journal of The Electrochemical Society*, **167**, 140539 (2020).

12. K. Mc Carthy, H. Gullapalli, K. M. Ryan, and T. Kennedy, Review—Use of Impedance Spectroscopy for the Estimation of Li-ion Battery State of Charge, State of Health and Internal Temperature, *Journal of The Electrochemical Society*, **168**, 080517 (2021).

13. K. Mc Carthy, H. Gullapalli, and T. Kennedy, Online state of health estimation of Li-ion polymer batteries using real time impedance measurements, *Applied Energy*, **307**, 118210 (2022).

14. A. Y. Kallel, V. Petrychenko, and O. Kanoun, State-of-Health of Li-Ion Battery Estimation Based on the Efficiency of the Charge Transfer Extracted from Impedance Spectra, *Applied Sciences (Switzerland)*, **12** (2022).

15. D. Deng, Li-ion batteries: Basics, progress, and challenges, *Energy Science and Engineering*, **3**, 385–418 (2015).

16. Y. Zhang, T. T. Zuo, J. Popovic, K. Lim, Y. X. Yin, J. Maier, and Y. G. Guo, Towards better Li metal anodes: Challenges and strategies, *Materials Today*, **33**, 56–74 (2020).

17. Z. Luo, X. Qiu, C. Liu, S. Li, C. Wang, G. Zou, H. Hou, and X. Ji, Interfacial challenges towards stable Li metal anode, *Nano Energy*, **79**, 105507 (2021).

18. X. Q. Zhang, X. B. Cheng, and Q. Zhang, Advances in Interfaces between Li Metal Anode and Electrolyte, *Advanced Materials Interfaces*, **5**, 1–19 (2018).

19. D. Jantke, R. Bernhard, E. Hanelt, T. Buhrmester, J. Pfeiffer, and S. Haufe, Silicon-Dominant Anodes Based on Microscale Silicon Particles under Partial Lithiation with High Capacity and Cycle Stability, *Journal of The Electrochemical Society*, **166**, A3881–A3885 (2019).

20. F. Ozanam and M. Rosso, Silicon as anode material for Li-ion batteries, *Materials*

Science and Engineering B: Solid-State Materials for Advanced Technology, **213**, 2–11 (2016).

21. M. Gu, Y. He, J. Zheng, and C. Wang, Nanoscale silicon as anode for Li-ion batteries: The fundamentals, promises, and challenges, *Nano Energy*, **17**, 366–383 (2015).

22. M. Wetjen, S. Solchenbach, D. Pritzl, J. Hou, V. Tileli, and H. A. Gasteiger, Morphological Changes of Silicon Nanoparticles and the Influence of Cutoff Potentials in Silicon-Graphite Electrodes, *Journal of The Electrochemical Society*, **165**, A1503–A1514 (2018).

23. Q. Shi, J. Zhou, S. Ullah, X. Yang, K. Tokarska, B. Trzebicka, H. Q. Ta, and M. H. Rümmeli, A review of recent developments in Si/C composite materials for Li-ion batteries, *Energy Storage Materials*, **34**, 735–754 (2021).

24. M. Wetjen, D. Pritzl, R. Jung, S. Solchenbach, R. Ghadimi, and H. A. Gasteiger, Differentiating the Degradation Phenomena in Silicon-Graphite Electrodes for Lithium-Ion Batteries, *Journal of The Electrochemical Society*, **164**, A2840–A2852 (2017).

25. S. Solchenbach, X. Huang, D. Pritzl, J. Landesfeind, and H. A. Gasteiger, Monitoring SEI Formation on Graphite Electrodes in Lithium-Ion Cells by Impedance Spectroscopy, *Journal of The Electrochemical Society*, **168**, 110503 (2021).

26. M. Nie, J. Demeaux, B. T. Young, D. R. Heskett, Y. Chen, A. Bose, J. C. Woicik, and B. L. Lucht, Effect of Vinylene Carbonate and Fluoroethylene Carbonate on SEI Formation on Graphitic Anodes in Li-Ion Batteries, *Journal of The Electrochemical Society*, **162**, A7008–A7014 (2015).

27. E. Peled, D. Golodnitsky, and G. Ardel, Advanced Model for Solid Electrolyte Interphase Electrodes in Liquid and Polymer Electrolytes, *Journal of The Electrochemical Society*, **144**, L208–L210 (1997).

28. E. Peled, The Electrochemical Behavior of Alkali and Alkaline Earth Metals in Nonaqueous Battery Systems—The Solid Electrolyte Interphase Model, *Journal of The Electrochemical Society*, **126**, 2047–2051 (1979).

29. P. Lu and S. J. Harris, Lithium transport within the solid electrolyte interphase,

References

──

Electrochemistry Communications, **13**, 1035–1037 (2011).

30. N. Nitta, F. Wu, J. T. Lee, and G. Yushin, Li-ion battery materials: Present and future, *Materials Today*, **18**, 252–264 (2015).

31. R. Jung, M. Metzger, F. Maglia, C. Stinner, and H. A. Gasteiger, Oxygen Release and Its Effect on the Cycling Stability of $LiNi_xMn_yCo_zO_2$ (NMC) Cathode Materials for Li-Ion Batteries, *Journal of The Electrochemical Society*, **164**, A1361–A1377 (2017).

32. S. S. Zhang, Problems and their origins of Ni-rich layered oxide cathode materials, *Energy Storage Materials*, **24**, 247–254 (2020).

33. U. H. Kim, G. T. Park, P. Conlin, N. Ashburn, K. Cho, Y. S. Yu, D. A. Shapiro, F. Maglia, S. J. Kim, P. Lamp, C. S. Yoon, and Y. K. Sun, Cation ordered Ni-rich layered cathode for ultra-long battery life, *Energy and Environmental Science*, **14**, 1573–1583 (2021).

34. Z. H. Sun, Z. F. Chen, Q. W. Fu, and X. Y. Jiang, Aluminum alloy anode materials for Li-ion batteries, *IOP Conference Series: Materials Science and Engineering*, **182**, 012011 (2017).

35. A. Gabryelczyk, S. Ivanov, A. Bund, and G. Lota, Corrosion of aluminium current collector in lithium-ion batteries: A review, *Journal of Energy Storage*, **43**, 103226 (2021).

36. H. Yang, G. V. Zhuang, and P. N. Ross, Thermal stability of $LiPF_6$ salt and Li-ion battery electrolytes containing $LiPF_6$, *Journal of Power Sources*, **161**, 573–579 (2006).

37. X. Zhang and T. M. Devine, Factors That Influence Formation of AlF_3 Passive Film on Aluminum in Li-Ion Battery Electrolytes with $LiPF_6$, *Journal of The Electrochemical Society*, **153**, B375 (2006).

38. X. Huang, Separator technologies for lithium-ion batteries, *Journal of Solid State Electrochemistry*, **15**, 649–662 (2011).

39. X. Zhang, E. Sahraei, and K. Wang, Li-ion Battery Separators, Mechanical Integrity and Failure Mechanisms Leading to Soft and Hard Internal Shorts, *Scientific Reports*, **6**, 1–9 (2016).

40. M. F. Lagadec, R. Zahn, and V. Wood, Characterization and performance

evaluation of lithium-ion battery separators, *Nature Energy*, **4**, 16–25 (2019).

41. K. Xu, Nonaqueous liquid electrolytes for lithium-based rechargeable batteries, *Chemical Reviews*, **104**, 4303–4417 (2004).

42. J. C. Bachman, S. Muy, A. Grimaud, H. Chang, N. Pour, S. F. Lux, O. Paschos, F. Maglia, S. Lupart, P. Lamp, L. Giordano, and Y. Shao-Horn, Inorganic Solid-State Electrolytes for Lithium Batteries: Mechanisms and Properties Governing Ion Conduction, *Chemical Reviews*, **116**, 140–162 (2016).

43. F. Zheng, M. Kotobuki, S. Song, M. O. Lai, and L. Lu, Review on solid electrolytes for all-solid-state lithium-ion batteries, *Journal of Power Sources*, **389**, 198–213 (2018).

44. T. Kim, K. Kim, S. Lee, G. Song, M. S. Jung, and K. T. Lee, Thermal Runaway Behavior of Li_6PS_5Cl Solid Electrolytes for $LiNi_{0.8}Co_{0.1}Mn_{0.1}O_2$ and $LiFePO_4$ in All-Solid-State Batteries, *Chemistry of Materials* (2022).

45. Y. Meesala, A. Jena, H. Chang, and R. S. Liu, Recent Advancements in Li-Ion Conductors for All-Solid-State Li-Ion Batteries, *ACS Energy Letters*, **2**, 2734–2751 (2017).

46. K. E. Thomas-Alyea, C. Jung, R. B. Smith, and M. Z. Bazant, In Situ Observation and Mathematical Modeling of Lithium Distribution within Graphite, *Journal of The Electrochemical Society*, **164**, E3063–E3072 (2017).

47. M. Z. Bazant, Theory of chemical kinetics and charge transfer based on nonequilibrium thermodynamics, *Accounts of Chemical Research*, **46**, 1144–1160 (2013).

48. D. R. Baker and M. W. Verbrugge, Intercalate Diffusion in Multiphase Electrode Materials and Application to Lithiated Graphite, *Journal of The Electrochemical Society*, **159**, A1341–A1350 (2012).

49. J. Li, N. Lotfi, R. G. Landers, and J. Park, A Single Particle Model for Lithium-Ion Batteries with Electrolyte and Stress-Enhanced Diffusion Physics, *Journal of The Electrochemical Society*, **164**, A874–A883 (2017).

50. X. Han, M. Ouyang, L. Lu, and J. Li, Simplification of physics-based electrochemical model for lithium ion battery on electric vehicle. Part I: Diffusion

simplification and single particle model, *Journal of Power Sources*, **278**, 802–813 (2015).

51. B. Y. Liaw, G. Nagasubramanian, R. G. Jungst, and D. H. Doughty, Modeling of lithium ion cells - A simple equivalent-circuit model approach, *Solid State Ionics*, **175**, 835–839 (2004).

52. X. Lai, W. Gao, Y. Zheng, M. Ouyang, J. Li, X. Han, and L. Zhou, A comparative study of global optimization methods for parameter identification of different equivalent circuit models for Li-ion batteries, *Electrochimica Acta*, **295**, 1057–1066 (2019).

53. S. Tamilselvi, S. Gunasundari, N. Karuppiah, A. Razak Rk, S. Madhusudan, V. M. Nagarajan, T. Sathish, M. Z. M. Shamim, C. A. Saleel, and A. Afzal, A review on battery modelling techniques, *Sustainability (Switzerland)*, **13**, 1–26 (2021).

54. J. Landesfeind, J. Hattendorff, A. Ehrl, W. A. Wall, and H. A. Gasteiger, Tortuosity Determination of Battery Electrodes and Separators by Impedance Spectroscopy, *Journal of The Electrochemical Society*, **163**, A1373–A1387 (2016).

55. A. Lasia, Electrochemical Impedance Spectroscopy and its Applications, Electrochemical Impedance Spectroscopy and its Applications, p. 1–367, Springer New York, New York, NY, (2014).

56. V. F. Lvovich, Impedance Spectroscopy, Impedance Spectroscopy, John Wiley & Sons, Inc., Hoboken, NJ, USA, (2012).

57. S. Solchenbach, D. Pritzl, E. J. Y. Kong, J. Landesfeind, and H. A. Gasteiger, A Gold Micro-Reference Electrode for Impedance and Potential Measurements in Lithium Ion Batteries, *Journal of The Electrochemical Society*, **163**, A2265–A2272 (2016).

58. N. Meddings, M. Heinrich, F. Overney, J. S. Lee, V. Ruiz, E. Napolitano, S. Seitz, G. Hinds, R. Raccichini, M. Gaberšček, and J. Park, Application of electrochemical impedance spectroscopy to commercial Li-ion cells: A review, *Journal of Power Sources*, **480**, 228742 (2020).

59. R. Raccichini, M. Amores, and G. Hinds, Critical review of the use of reference electrodes in li-ion batteries: A diagnostic perspective, *Batteries*, **5**, 1–24 (2019).

60. M. Gaberscek, J. Moskon, B. Erjavec, R. Dominko, and J. Jamnik, The importance of interphase contacts in Li ion electrodes: The meaning of the high-frequency

impedance arc, *Electrochemical and Solid-State Letters*, **11**, A170 (2008).

61. J. Landesfeind, D. Pritzl, and H. A. Gasteiger, An Analysis Protocol for Three-Electrode Li-Ion Battery Impedance Spectra: Part I. Analysis of a High-Voltage Positive Electrode, *Journal of The Electrochemical Society*, **164**, A1773–A1783 (2017).

62. J. P. Meyers, M. Doyle, R. M. Darling, and J. Newman, The Impedance Response of a Porous Electrode Composed of Intercalation Particles, *Journal of The Electrochemical Society*, **147**, 2930 (2000).

63. S. Oswald, D. Pritzl, M. Wetjen, and H. A. Gasteiger, Novel Method for Monitoring the Electrochemical Capacitance by In Situ Impedance Spectroscopy as Indicator for Particle Cracking of Nickel-Rich NCMs: Part I. Theory and Validation, *Journal of The Electrochemical Society*, **167**, 100511 (2020).

64. S. Oswald, D. Pritzl, M. Wetjen, and H. A. Gasteiger, Novel Method for Monitoring the Electrochemical Capacitance by In Situ Impedance Spectroscopy as Indicator for Particle Cracking of Nickel-Rich NCMs: Part II. Effect of Oxygen Release Dependent on Particle Morphology, *Journal of The Electrochemical Society*, **168**, 120501 (2021).

65. S. Oswald, M. Bock, and H. A. Gasteiger, Elucidating the Implications of Morphology on Fundamental Characteristics of Nickel-Rich NCMs: Cracking, Gassing, Rate Capability, and Thermal Stability of Poly- and Single-Crystalline NCM622, *Journal of The Electrochemical Society*, **169**, 050501 (2022).

66. J. Landesfeind and H. A. Gasteiger, Temperature and Concentration Dependence of the Ionic Transport Properties of Lithium-Ion Battery Electrolytes, *Journal of The Electrochemical Society*, **166**, A3079–A3097 (2019).

67. M. Schönleber, Verfahren zur Charakterisierung des Niederfrequenzverhaltens von Lithium-Ionen Batterien, Verfahren zur Charakterisierung des Niederfrequenzverhaltens von Lithium-Ionen Batterien, KIT Scientific Publishing, Karlsruhe, (2018).

68. C. Ho, I. D. Raistrick, and R. A. Huggins, Application of A-C Techniques to the Study of Lithium Diffusion in Tungsten Trioxide Thin Films, *Journal of The Electrochemical Society*, **127**, 343–350 (1980).

69. N. Ogihara, S. Kawauchi, C. Okuda, Y. Itou, Y. Takeuchi, and Y. Ukyo, Theoretical and Experimental Analysis of Porous Electrodes for Lithium-Ion Batteries by Electrochemical Impedance Spectroscopy Using a Symmetric Cell, *Journal of The Electrochemical Society*, **159**, A1034–A1039 (2012).

70. M. Adamič, S. D. Talian, A. R. Sinigoj, I. Humar, J. Moškon, and M. Gaberšček, A Transmission Line Model of Electrochemical Cell's Impedance: Case Study on a Li-S System, *Journal of The Electrochemical Society*, **166**, A5045–A5053 (2019).

71. R. Morasch, J. Landesfeind, B. Suthar, and H. A. Gasteiger, Detection of Binder Gradients Using Impedance Spectroscopy and Their Influence on the Tortuosity of Li-Ion Battery Graphite Electrodes, *Journal of The Electrochemical Society*, **165**, A3459–A3467 (2018).

72. J. Landesfeind, M. Ebner, A. Eldiven, V. Wood, and H. A. Gasteiger, Tortuosity of Battery Electrodes: Validation of Impedance-Derived Values and Critical Comparison with 3D Tomography, *Journal of The Electrochemical Society*, **165**, A469–A476 (2018).

73. F. Pouraghajan, H. Knight, M. Wray, B. Mazzeo, R. Subbaraman, J. Christensen, and D. Wheeler, Quantifying Tortuosity of Porous Li-Ion Battery Electrodes: Comparing Polarization-Interrupt and Blocking-Electrolyte Methods, *Journal of The Electrochemical Society*, **165**, A2644–A2653 (2018).

74. I. V. Thorat, D. E. Stephenson, N. A. Zacharias, K. Zaghib, J. N. Harb, and D. R. Wheeler, Quantifying tortuosity in porous Li-ion battery materials, *Journal of Power Sources*, **188**, 592–600 (2009).

75. T.-T. Nguyen, A. Demortière, B. Fleutot, B. Delobel, C. Delacourt, and S. J. Cooper, The electrode tortuosity factor: why the conventional tortuosity factor is not well suited for quantifying transport in porous Li-ion battery electrodes and what to use instead, *npj Computational Materials*, **6**, 123 (2020).

76. M. Ebner and V. Wood, Tool for Tortuosity Estimation in Lithium Ion Battery Porous Electrodes, *Journal of The Electrochemical Society*, **162**, A3064–A3070 (2015).

77. J. Huang and J. Zhang, Theory of Impedance Response of Porous Electrodes: Simplifications, Inhomogeneities, Non-Stationarities and Applications, *Journal of*

198

The Electrochemical Society, **163**, A1983–A2000 (2016).

78. N. Ogihara, Y. Itou, T. Sasaki, and Y. Takeuchi, Impedance spectroscopy characterization of porous electrodes under different electrode thickness using a symmetric cell for high-performance lithium-ion batteries, *Journal of Physical Chemistry C*, **119**, 4612–4619 (2015).

79. N. Ogihara and Y. Itou, Impedance Analysis Using Symmetric Cells for Understanding Electrochemical Behaviour of Porous Electrodes for Lithium-ion Batteries, *R&D Review of Toyota CRDL*, **48**, 17–24 (2017).

80. A. Zaban, E. Zinigrad, and D. Aurbach, Impedance spectroscopy of Li electrodes. 4. A general simple model of the Li-solution interphase in polar aprotic systems, *Journal of Physical Chemistry*, **100**, 3089–3101 (1996).

81. S. Jaiser, J. Kumberg, J. Klaver, J. L. Urai, W. Schabel, J. Schmatz, and P. Scharfer, Microstructure formation of lithium-ion battery electrodes during drying – An ex-situ study using cryogenic broad ion beam slope-cutting and scanning electron microscopy (Cryo-BIB-SEM), *Journal of Power Sources*, **345**, 97–107 (2017).

82. S. Jaiser, M. Müller, M. Baunach, W. Bauer, P. Scharfer, and W. Schabel, Investigation of film solidification and binder migration during drying of Li-Ion battery anodes, *Journal of Power Sources*, **318**, 210–219 (2016).

83. M. Müller, L. Pfaffmann, S. Jaiser, M. Baunach, V. Trouillet, F. Scheiba, P. Scharfer, W. Schabel, and W. Bauer, Investigation of binder distribution in graphite anodes for lithium-ion batteries, *Journal of Power Sources*, **340**, 1–5 (2017).

84. J. B. Habedank, J. Endres, P. Schmitz, M. F. Zaeh, and H. P. Huber, Femtosecond laser structuring of graphite anodes for improved lithium-ion batteries: Ablation characteristics and process design, *Journal of Laser Applications*, **30**, 032205 (2018).

85. M. Mangang, H. J. Seifert, and W. Pfleging, Influence of laser pulse duration on the electrochemical performance of laser structured $LiFePO_4$ composite electrodes, *Journal of Power Sources*, **304**, 24–32 (2016).

86. P. Smyrek, J. Pröll, H. J. Seifert, and W. Pfleging, Laser-Induced Breakdown Spectroscopy of Laser-Structured $Li(NiMnCo)O_2$ Electrodes for Lithium-Ion

Batteries, *Journal of The Electrochemical Society*, **163**, A19–A26 (2016).

87. W. Pfleging, M. Mangang, Y. Zheng, and P. Smyrek, Laser structuring for improved battery performance, *SPIE Newsroom*, **1**, 10–12 (2016).

88. W. Pfleging, A review of laser electrode processing for development and manufacturing of lithium-ion batteries, *Nanophotonics*, **7**, 549–573 (2017).

89. J. B. Habedank, J. Kriegler, and M. F. Zaeh, Enhanced Fast Charging and Reduced Lithium-Plating by Laser-Structured Anodes for Lithium-Ion Batteries, *Journal of The Electrochemical Society*, **166**, A3940–A3949 (2019).

90. J. B. Habedank, L. Kraft, A. Rheinfeld, C. Krezdorn, A. Jossen, and M. F. Zaeh, Increasing the Discharge Rate Capability of Lithium-Ion Cells with Laser-Structured Graphite Anodes: Modeling and Simulation, *Journal of The Electrochemical Society*, **165**, A1563–A1573 (2018).

91. J. B. Habedank, F. J. Günter, N. Billot, R. Gilles, T. Neuwirth, G. Reinhart, and M. F. Zaeh, Rapid electrolyte wetting of lithium-ion batteries containing laser structured electrodes: in situ visualization by neutron radiography, *International Journal of Advanced Manufacturing Technology*, **102**, 2769–2778 (2019).

92. T. Tsuda, N. Ando, S. Nakamura, Y. Ishihara, N. Hayashi, N. Soma, T. Gunji, T. Tanabe, T. Ohsaka, and F. Matsumoto, Improvement of high-rate discharging performance of $LiFePO_4$ cathodes by forming micrometer-sized through-holed electrode structures with a pico-second pulsed laser, *Electrochimica Acta*, **296**, 27–38 (2019).

93. J. Park, S. Hyeon, S. Jeong, and H. J. Kim, Performance enhancement of Li-ion battery by laser structuring of thick electrode with low porosity, *Journal of Industrial and Engineering Chemistry*, **70**, 178–185 (2019).

94. B. Suthar, J. Landesfeind, A. Eldiven, and H. A. Gasteiger, Method to Determine the In-Plane Tortuosity of Porous Electrodes, *Journal of The Electrochemical Society*, **165**, A2008–A2018 (2018).

95. L. H. J. Raijmakers, M. J. G. Lammers, and P. H. L. Notten, A new method to compensate impedance artefacts for Li-ion batteries with integrated micro-reference electrodes, *Electrochimica Acta*, **259**, 517–533 (2018).

96. S. Jaiser, A. Friske, M. Baunach, P. Scharfer, and W. Schabel, Development of a three-stage drying profile based on characteristic drying stages for lithium-ion battery anodes, *Drying Technology*, **35**, 1266–1275 (2017).

97. J. Landesfeind, A. Eldiven, and H. A. Gasteiger, Influence of the Binder on Lithium Ion Battery Electrode Tortuosity and Performance, *Journal of The Electrochemical Society*, **165**, A1122–A1128 (2018).

98. Y. Nomura, K. Yamamoto, T. Hirayama, S. Ouchi, E. Igaki, and K. Saitoh, Direct Observation of a Li-Ionic Space-Charge Layer Formed at an Electrode/Solid-Electrolyte Interface, *Angewandte Chemie*, **131**, 5346–5350 (2019).

99. S. Braun, C. Yada, and A. Latz, Thermodynamically Consistent Model for Space-Charge-Layer Formation in a Solid Electrolyte, *Journal of Physical Chemistry C*, **119**, 22281–22288 (2015).

100. I. Buchberger, S. Seidlmayer, A. Pokharel, M. Piana, J. Hattendorff, P. Kudejova, R. Gilles, and H. A. Gasteiger, Aging Analysis of Graphite/LiNi$_{1/3}$ Mn$_{1/3}$ Co$_{1/3}$ O$_2$ Cells Using XRD, PGAA, and AC Impedance, *Journal of The Electrochemical Society*, **162**, A2737–A2746 (2015).

101. K. West, T. Jacobsen, and S. Atlung, Modeling of Porous Insertion Electrodes with Liquid Electrolyte, *Journal of The Electrochemical Society*, **129**, 1480–1485 (1982).

Acknowledgements

I did it all by myself…

… obviously kidding.

There are no guidelines that I am aware of on how to write the acknowledgement, especially the order of people seems in part arbitrary. Since this is a more personal note, I would have preferred to thank people in order of their appearance in the parts of my life which led me to doing my thesis, to avoid any assumptions on importance depending on rank. However there seems to be a trend to thank the supervising professor first, which is understandable giving the enormous role such a person usually plays. So I will follow the trend, starting with the supervisor who will be the only one named including his title, but the order afterwards is then of a more arbitrary nature.

So my first thank you then has to go out to **Professor Hubert A. Gasteiger** (a.k.a. Chief, Chef, Mon Colonel, Mon général, Sir, Professor or just Hubert) of the Chair for Technical Electrochemistry (TEC). This thank you is not for you doing your job, which I guess is to provide some structure (e.g., money) for PhDs to do their job. It is for going far beyond what can be expected from a supervisor every day of the year. Covering all aspects for which I have to thank you seems like an impossible task, there is just too much. I started out as an intern and already there realized that the environment you created for your PhD students was exceptional. The independence you allow them and the respect you show them lets your students create their own world, especially an environment in which scientific criticism is welcomed by students amongst each other. You set the highest standards for scientific rigor, which can be infuriating and inspiring at the same time. Presentations getting stuck on the second slide because you are already asking questions I myself just never thought of at first can be a frustrating experience, but that's just because I had to adapt to the world you just opened my mind up to. Usually such meetings would start late, which is often because you just need to give some more attention to what has just been presented to you. I already miss the late-night meetings of, e.g., fighting over how to interpret EIS spectra. It is not easy to find someone willing to spend another hour at work, foregoing their long-planned swim, just to understand exactly what is going on in those measurements. And in all those meetings you are never stuck on an idea, which I think is one of your biggest gifts. You are willing to be wrong and acknowledge it with zero resistance, a trait all too rare in the scientific community. Thank you for teaching me to always dig

deeper, for giving me the opportunity to do my thesis not only at your group but with you as my fiercest critic. Thank you for that and for so much more!

Next I would like to thank **Roland Jung** (a.k.a. Rolando, or Kazinder). You were the first person I worked with at TEC during my internship. You taught me the basics of Li-ion batteries, with great passion but also with patience I only hope to ever achieve. You always took your time and I learned a lot from you about electrochemistry and the fun of cathode material screening, which introduced me to so much more and still helps me understand Li-ion battery chemistry to this day. I still cherish our time together in Cambridge and I am happy to call you my friend. Thank you Roland!

Once I started my PhD I was paired with **Johannes Landesfeind**, whom I have to thank immensely for teaching me to focus! Describing our relationship is somewhat difficult. On the one hand you were some form of mentor, explaining the intricacies of EIS, transmission line models and electrolyte theory (or simply pointing to your paper). Whenever there might have been chemistry involved you managed to simplify the experiment to avoid those influences, because who cares about the pesky chemistry. Because you knew how to focus(!) and so you allowed this electrical engineer (me) to get a foothold in a topic more suitable for my background and taught me what is important and what can (probably) be ignored for the sake of efficiency. On the other hand you were also a great sparring partner, someone to bounce ideas off of and whom proving wrong or be proven wrong by was either way an enjoyable experience because each way I could learn something. I am happy to call you my friend and that we kept in contact for all this time. Thank you Johannes!

Johannes and I were soon joined by **Bharatkumar Suthar** (a.k.a. Sir, Professor or just Bharat). Bharat takes the philosophy part of his PhD more serious than most other people. You have a drive to not only find the solution to a problem but to understand it to the point of developing an intuition for mathematical connections far beyond the average researcher. Your influence on my work was undoubtably the largest when it came to supplying the fundamentals of battery theory. Our relationship could really be described as symbiotic, evident in your name being on all my manuscripts and publications. While I was performing the experiments, you took lead in finding and explaining the theory behind it. Knowing how an

experiment should turn out is the best way of understanding the experimental data afterwards, and especially enjoyable if we were right as well. I miss our lunches where could sit for hours discussing how we think an experiment would turn out, drawing graphs of potentially Nobel prize winning advancements (if our theories were true), just to end in "yeah, someone should do that". You also challenged my personal beliefs with philosophical questions, shaping my mindset and forcing me to verbalize and quantify beliefs which otherwise would have been just washed-up ideas. I am grateful to you for all this and so much more. Thank you Bharat!

More thanks go out to my ExZellTUM/SurfaLib project partners, especially **Tanja Zünd**, who tirelessly tried to make something out of the project that I could never see in it. You actually tried to save the world and made an inspiring effort to improve everything that came out of ExZellTUM. A lot of the work and passion you put into the project probably went uncredited, but in my mind no professor or subgroup leader who was part of that project was willing to do what you did, bring (or force) everyone together. We sometimes clashed and were not always on the best terms but we managed to stay friends in the end, and I am grateful for that. Thank you Tanja!

Far away from batteries, I made a friend in the fuel cell subgroup, **Ana Marija Damjanović** (Eaanaaaa, Marija [non-silent j], Marija [Rolling r and spanish j as in e.g. Jesús]). Once we got to talking I think we quickly became friends and stayed that way ever since, bonding mostly over our weirdness or over sharing secrets and gossip from the opposing subgroup. It was great to have a "neutral" friend among the colleagues and someone who just gets it. You know what I am talking about. I am also grateful to have shared my only fuel cell project with you, which taught me a lot. Thank you Ana!

Another thanks goes to **Mohammad Fathi Tovini** (a.k.a. Momo), thank you for great conversations and being a friend along the way. Thank you bro!

Further thanks go to **Franziska Friedrich** (a.k.a. Franziskar, Francine, Juanzi, Frau Friiiiiiedrich but rarely Franzi). I do like to believe that I chose you when I came into your office and told you that, since Bharat is on vacation, you are now my replacement friend. Things went only uphill from there. There are a ton of things I can thank you for, like our shared dinners with great conversations, but if I had to

_____

choose I would say you were my moral compass. Whenever I struggled with how to deal with situations properly and fairly, you always gave me great advice. Your words never fell on deaf ears with me and I am grateful that we shared our time at TEC together and are still as close as we were when it ended. You also introduced me to **Tim Friedrich** whom I would also like to thank for many great dinners and conversations! Thank you both!

I also have to thank **Veronika Pichler** for all her efforts in explaining the paperwork necessary so we all got paid and got things done. I apologize for all the holidays I missed in my timesheets and am grateful for your patience in solving everyones paperwork troubles. Thank you Vroni!

Further thanks go to **Johannes Wandt** and **Sophie Solchenbach**, who I only shared little time with at TEC but who even beyond their PhD were always interested and motivated to participate in meetings and shared their passion. Such a commitment is a great motivator and I am thankful to have shared great scientific discussions with the both of you!

I am similarly grateful for all the new people who joined. **Lennart Reuter**, who shared a passion for SEI analysis and taught me a great deal about the chemistry aspect of it. Your scientific rigor and relentlessness impressed me greatly and I very much enjoyed our time in the BMW project together! **Clara Berg**, who showed a great interest in EIS analysis, I had a lot of fun learning about silicon electrodes with you. And **Simon Helmer**, who took over some of my projects and who I enjoyed working with and hope to hear more from in the time to come. Thank you all!

More thanks go to my former students, especially **Josef Keilhofer** and **Mahla Bakshi** who I had the privilege of supervising a masters thesis with. I learned a lot from both of you.

Furthermore I would like to thank **Jonas Dickmanns**, **Robin Schuster**, **Moritz Bock**, **Leon Reinschlüssel**, **Christian Sedlmeier**, **Rebecca Wilhelm, Maximilian Graf** and **Stefan Oswald** for great conversations and the great atmosphere you created in the office or hallways of TEC. I would generally like to thank **all members of TEC**, past and present who have shaped my time there. Thank you all!

I would also like to thank **Pyae Phyo** for accompanying me for large parts of this thesis. Your own journey to a PhD was rocky but you never gave up and were an inspiration to me in many frustrated days. Thank you Pyae!

I would like to thank my gaming friends, **Thomas Aigner**, **Lukas Häubl** and **Fabian Hertwig** for many hours of distraction and laughter. It was a blast!

And lastly, I would like to thank my family. My brother **Matthias Morasch** who made sure I knew he had a Nature publication and his PhD before me, my brother **Michael Morasch** who stoically goes his own way towards a PhD and for all the fun we had playing Stellaris and my sister **Julia Morasch** and her children for many family events she initiated. Also many thanks to my father **Ulrich Morasch** for supporting my career at all its ups and downs. Lastly thank you **Ursula Morasch**, my mother, for all the support you gave me. Whether it was financial support for 8 months spent in Cambridge, enabling me to have my first contact with electrochemistry, or giving me a place to stay when I came back for my PhD position at TEC, I could not have done it without you. Thank you all!

Scientific Contributions

Published and submitted articles

- **Robert Morasch**, Josef Keilhofer, Hubert Gasteiger and Bharatkumar Suthar "Methods—Understanding Porous Electrode Impedance and the Implications for the Impedance Analysis of Li-Ion Battery Electrodes" Morasch et al 2021 J. Electrochem. Soc.
- **Robert Morasch**, Bharatkumar Suthar, and Hubert A. Gasteiger "Simple Way of Making Free-Standing Battery Electrodes and their Use in Enabling Half-Cell Impedance Measurements via μ- Reference Electrode" Journal of The Electrochemical Society, 2020 167 100540;
- **Robert Morasch**, Johannes Landesfeind, Bharatkumar Suthar, and Hubert A. Gasteiger "Detection of Binder Gradients Using Impedance Spectroscopy and Their Influence on the Tortuosity of Li-Ion Battery Graphite Electrodes" Journal of The Electrochemical Society, 165 (14) A3459-A3467 (2018);
- R. Jung, **R. Morasch**, P. Karayaylali, K. Phillips, F. Maglia, C. Stinner, Y. Shao-Horn, and H. A. Gasteiger, Effect of Ambient Storage on the Degradation of Ni-Rich Positive Electrode Materials (NMC811) for Li-Ion Batteries, Journal of The Electrochemical Society, 165, A132–A141 (2018).
- **R. Morasch**, D. G. Kwabi, M. Tulodziecki, M. Risch, S. Zhang, and Y. Shao-Horn, Insights into Electrochemical Oxidation of NaO_2 in Na-O_2 Batteries via Rotating Ring Disk and Spectroscopic Measurements, ACS Applied Materials and Interfaces, 9, 4374–4381 (2017).
- Clara Berg=, **Robert Morasch**=, Maximilian Graf and Hubert A. Gasteiger "Comparison of Silicon and Graphite Anodes on their Temperature-Dependent Impedance and Rate Performance", *submitted*

Articles in preparation

- **Robert Morasch**, Bharatkumar Suthar, and Hubert A. Gasteiger „Li-Ion Battery Material Impedance Analysis I: NMC 111 Kinetic Theory and Experiment"
- **Robert Morasch**, Bharatkumar Suthar, and Hubert A. Gasteiger „Li-Ion Battery Material Impedance Analysis II: Graphite and Solid Electrolyte Interphase Kinetics"
- Simon Helmer, **Robert Morasch**, Hubert A. Gasteiger and Bharatkumar Suthar, "LiC_6 mobility in HOPG"
- Simon Helmer, **Robert Morasch**, Sven Friedrich and Hubert A. Gasteiger, "Methods - Identification of contact resistances in multilayer pouch cells using impedance spectroscopy"

- Ana Marija Damjanović, **Robert Morasch**, Robin Girod, Dario Mauth, Hubert A. Gasteiger, "Investigation and Quantification of Ionomer Gradient in Cathode Catalyst Layer for PEMFC Application"
- Lennart Reuter, **Robert Morasch**, Jonas Dickmanns, Filippo Maglia, Roland Jung and Hubert A. Gasteiger, "Temperature Dependent Formation of the Graphite SEI with Vinylene Carbonate Electrolyte Additive"

Oral presentations

- **Robert Morasch**, Bharatkumar Suthar and Hubert A. Gasteiger „A critical analysis of impedance derived tortuosities – Decoupling the influence of homogeneity, film resistance and pore resistance on the impedance response of li-ion battery electrodes" ModVal 2019, Braunschweig, Germany
- **Robert Morasch**, Johannes Landesfeind, Bharatkumar Suthar, and Hubert A. Gasteiger "Facile Detection of Binder Gradients using Impedance Spectroscopy and their Influence on the Tortuosity of Li-Ion Battery Electrodes" AiMES 2018, Cancun, Mexiko
- **Robert Morasch**, Bharatkumar Suthar, Jan B. Habedank, Johannes Landesfeind and Hubert A. Gasteiger „Experimental Validation of Simulated Ionic Resistances in Laser-Structured Electrodes" ModVal 2018, Aarau, Switzerland

Poster presentations

- **Robert Morasch**, Bharatkumar Suthar, and Hubert A. Gasteiger "Butler-Volmer Kinetics in Li-Ion battery electrodes: A concentration-dependent impedance analysis" Gordon Research Conference 2020, Ventura, USA
- **Robert Morasch**, Johannes Landesfeind, Bharatkumar Suthar, and Hubert A. Gasteiger "Detection of Binder Migration using Impedance Spectroscopy and its Influence on the Tortuosity of Li-Ion Battery Electrodes" Batterieforum 2019, Berlin, Germany. 1st place Poster Award